energies

MDPI

Article

Multi-DOF WEC Performance in Variable Bathymetry Regions Using a Hybrid 3D BEM and Optimization

Markos Bonovas [1], Kostas Belibassakis [1] and Eugen Rusu [2,*]

[1] School of Naval Architecture and Marine Engineering, National Technical University of Athens, 15780 Athens, Greece; markosbonovas@hotmail.gr (M.B.); kbel@fluid.mech.ntua.gr (K.B.)

[2] Department of Mechanical Engineering, University Dunarea de Jos of Galati, 800008 Galați, Romania

* Correspondence: erusu@ugal.ro; Tel.: +40-740-205-534

Received: 9 April 2019; Accepted: 29 May 2019; Published: 1 June 2019

Abstract: In the present work a hybrid boundary element method is used, in conjunction with a coupled mode model and perfectly matched layer model, for obtaining the solution of the propagation/diffraction/radiation problems of floating bodies in variable bathymetry regions. The implemented methodology is free of mild-slope assumptions and restrictions. The present work extends previous results concerning heaving floaters over a region of general bottom topography in the case of generally shaped wave energy converters (WECs) operating in multiple degrees of freedom. Numerical results concerning the details of the wave field and the power output are presented, and the effects of WEC shape on the optimization of power extraction are discussed. It is demonstrated that consideration of heave in combination with pitch oscillation modes leads to a possible increase of the WEC performance.

Keywords: renewable energy; marine environment; wave energy converters; variable depth effects; multi-DOF WECs; design optimization

1. Introduction

Renewable energy from the oceans is increasingly attracting the interest of the scientific and industrial society. Wave energy converters are constantly being deployed in areas characterized by increased potential, and a recent review concerning point absorber wave energy harvesters is presented in [1]. The performance of the devices installed in the nearshore and coastal environment, where the bottom terrain may present significant variations, can be evaluated by formulating and solving interaction problems of free surface gravity waves, floating bodies, and the seafloor; see, e.g., Wehausen [2] and Mei [3]. A thorough presentation of the interaction between waves and oscillating energy systems can be found in Falnes [4]. Models describing coupling methodologies for numerical modelling of near and far-field effects of wave energy converter arrays are presented in various works; see, e.g, [5–7].

The power efficiency and the operation of the WECs is affected by the bottom topography due to the local entrapped modes and of their impact on the wave propagation, with non-negligible results, especially in array layouts; see [5,8,9]. This is also demonstrated in wave propagation over variable seabed topographies or abrupt bathymetries including coastal structures; see, e.g., [10,11].

The numerical method implemented in this work for the treatment of the hydrodynamic problems simulating the WEC operation is a hybrid boundary element method coupled with a perfectly matched layer (BEM-PML) technique, which is used in conjunction with a coupled mode system for the simulation of the propagating waves over general seabed topography, as presented and validated in [12,13]. For the calculation of the propagation wave field over general 3D bottom topographies, including possibly steep parts, the coupled mode model (CMM), developed in [14] and extended for the 3D-domains in [15,16], is applied. The latter method is validated by comparisons against experimental

data [17,18] and calculations obtained by the phase-averaged wave model SWAN (simulating waves nearshore) [19]. The boundary element method is then implemented for the calculation of the excitation loads on the floating body, along with the hydrodynamic coefficients of added mass and damping by utilizing the 3D Green's Function, while the perfectly matched layer model is numerically treating the behavior of the outgoing radiating waves at large distances from the floating body [20].

The present method is applied to derive numerical results concerning the details of the wave field and the power output. Different axisymmetric WEC-shapes and power take off (PTO) configurations are examined, and the effects on the optimization of wave energy extraction are discussed. Following previous investigations, as reported in detail by Falnes [4], the consideration of additional degrees of freedom could significantly enhance the performance of a oscillating floating WEC. By using the present hybrid BEM, it is demonstrated that consideration of heave in combination with pitch modes leads to a substantial increase of the WEC performance, up to 300%. What is more important is that the consideration of additional degrees of freedom has an important effect on the determination of the optimal shape of the floater. Finally, the present model supports the application to more complex optimization problems, associated with multi DOF (degree of freedom) WEC performance, which are expected to be excited in variable bathymetry due to general wave incidence, in conjunction with depth inhomogeneity effects.

2. Formulation

2.1. Heaving Cylinder over Variable Bathymetry

We first consider a vertical cylindrical WEC of radius a and draft T, operating in a nearshore environment, characterized by a depth-transition from an incidence-subregion of constant depth $h = h_1$, to a transmission-subregion of constant depth $h = h_3$, with the depth $h_2(\mathbf{x})$ in the middle subdomain exhibiting an arbitrary variation with respect to the horizontal coordinates $\mathbf{x} = (x, y)$. The motion of the floating body is excited by a harmonic wave of angular frequency ω propagating with an incident angle θ. Under the assumption that the wave slope is relatively small, the wave potential and the free-surface elevation are expressed by

$$\Phi(\mathbf{x}, z; t) = \mathrm{Re}\left\{-\frac{igH}{2\omega}\varphi(\mathbf{x}, z; \mu) \cdot \exp(-i\omega t)\right\} \tag{1}$$

$$\eta(\mathbf{x}; t) = \mathrm{Re}\left\{\frac{H}{2}\varphi(\mathbf{x}, z; \mu) \cdot \exp(-i\omega t)\right\} \tag{2}$$

where H is the incident wave height, g is the gravity acceleration, $\mu = \omega^2/g$ is the frequency parameter, and $i = \sqrt{-1}$ is the imaginary unit. According to the hydrodynamic theory of floating bodies (see, e.g., [7]), the complex wave potential is decomposed on several components, namely the propagating wave potential $\varphi_P(\mathbf{x}, z)$, defined without the effect of the body, the diffraction potential $\varphi_D(\mathbf{x}, z)$ due to the presence of the rigid motionless body, and the radiation potential $\varphi_R(\mathbf{x}, z)$, related to the oscillations in the six degrees of freedom of the floater

$$\varphi(\mathbf{x}, z) = \varphi_P(\mathbf{x}, z) + \varphi_D(\mathbf{x}, z) + \frac{2\omega^2}{gH}\varphi_R(\mathbf{x}, z) \tag{3}$$

$$\varphi_R(\mathbf{x}, z) = \sum_{\ell=1}^{6} \xi_\ell \varphi_\ell(\mathbf{x}, z) \tag{4}$$

The boundary conditions on the wetted surface of the body are

$$\partial\varphi_D(\mathbf{x}, z)/\partial n = -\partial\varphi_P(\mathbf{x}, z)/\partial n, \quad \partial\varphi_\ell(\mathbf{x}, z)/\partial n = n_\ell, \quad \ell = 1, 2, \ldots 6, \tag{5}$$

where $\mathbf{n} = (n_1, n_2, n_3)$ denotes the normal vector with direction inwards the body, and n_ℓ is the ℓ-component of the generalized normal vector. Moreover, the wave potential (all components) should satisfy the bottom boundary condition on the variable seabed topography

$$\partial\varphi(\mathbf{x}, z)/\partial z + \nabla_2 h(\mathbf{x})\nabla_2\varphi(\mathbf{x}, z) = 0, \quad z = -h(\mathbf{x}) \tag{6}$$

where $\nabla_2 = \left(\partial_x, \partial_y\right)$ denotes the horizontal gradient.

In particular, the heave response of the cylinder is obtained as

$$\xi_3 = (X_P + X_D)/A \tag{7}$$

where X_P and X_D are the Froude–Krylov and diffraction exciting vertical forces due to propagation and diffraction potentials, respectively, defined as follows

$$X_P = \frac{\rho g H}{2} \iint\limits_{\partial D_B} \phi_P n_3 dS \tag{8}$$

$$X_D = \frac{\rho g H}{2} \iint\limits_{\partial D_B} \phi_D n_3 dS \tag{9}$$

The complex coefficient $A(\omega)$ involved in Equation (7) is given by

$$A(\omega) = -\omega^2(M + a_{33}) - i\omega(B_S + b_{33}) + (C_S + c_{33}) \tag{10}$$

where the hydrodynamic coefficients α_{33} and b_{33} (added mass and damping coefficient of the body) are calculated by integrating the heaving radiation potential on the wetted surface of the WEC:

$$a_{33} - \frac{1}{i\omega} b_{33} = \rho \iint\limits_{\partial D_B} \varphi_3 n_3 dS \tag{11}$$

Also, c_{33}=$\rho g A_{WL}$ is the hydrostatic coefficient in heave motion and A_{WL} denotes the waterline surface. The coefficients Bs and Cs are characteristic parameters of the PTO system. Finally, the time-average WEC power output, considering only the ξ_3-heave mode, is calculated by

$$P(\omega, \theta) = \frac{1}{2}\eta_{eff}\omega^2\left|B_S(\xi_3)^2\right| \tag{12}$$

where η_{eff} denotes the efficiency of the PTO. The power output obviously depends on the frequency ω, the direction θ, and the height H of the incident wave, as well as on the characteristics of the PTO installed in the specific environment. Furthermore, the overall performance of the device is dependent on the wave conditions as they are described by the incident directional wave spectrum.

2.2. Propagation Wave Field

The coupled mode model, developed by Athanassoulis and Belibassakis [14] and extended to 3D by Belibassakis et al [15], is appropriate for the efficient numerical simulation of wave propagation problems over a varying sea bottom topography that may contain steep parts, where analytic solutions are not available. The propagation potential over a variable bathymetry, in the absence of the floating body-scatterer, is based on the following local-mode representation

$$\varphi_P(\mathbf{x}, z) = \varphi_{-1}(\mathbf{x})Z_{-1}(z; \mathbf{x}) + \sum_{n=0}^{\infty} \varphi_n(\mathbf{x})Z_n(z; \mathbf{x}) \tag{13}$$

where the vertical functions Z_n $(z;\ x)$ are obtained as eigenfunctions of regular Sturm–Liouville problems, formulated at the local depth, and the system is enhanced by appropriate additional terms in order to consistently satisfy the boundary conditions on the sloping seabed. The functions $\varphi_n(x)$ are the complex amplitude of the n^{th}-mode, and are found as the solution of the following coupled mode system (CMS)

$$\sum_{n=-1} \mathbf{A}_{mn}(\mathbf{x})\nabla^2\varphi_n(\mathbf{x}) + \mathbf{B}_{mn}(\mathbf{x})\nabla\varphi_n(\mathbf{x}) + \mathbf{C}_{mn}(\mathbf{x})\varphi_n(\mathbf{x}) = 0 \tag{14}$$

where the matrix coefficients $\mathbf{A}_{mn}$, $\mathbf{B}_{mn}$, and $\mathbf{C}_{mn}$ are defined in terms of the vertical eigenfunctions and are listed in Table 1 of Reference [15]. An important feature of the above CMS is that it can be naturally reduced to well-known simplified models when the environmental parameters permit such simplification. In fact, keeping only the propagating mode ($n = 0$) in Equation (14), the system reduces to a one-equation model, which is exactly the modified mild-slope equation; see [10]. The CMS is also supplemented by appropriate boundary conditions for treating incident, reflection, and transmission phenomena in general bathymetry regions.

2.3. Diffraction and Radiation Potentials

The evaluation for the 3D diffraction and radiation potentials associated with the floating WEC will be treated by the BEM method developed by Belibassakis et al [21] and described in more detail in [13]. In this model, the induced potential and velocity from the collection of the 4-node quadrilateral elements, which are used to discretize all parts of the boundary surface (body, free-surface, seabed surface etc.), is given by

$$\varphi(\mathbf{r}) = \sum_p F_p \Phi_p(\mathbf{r}) \tag{15}$$

$$\nabla\varphi(\mathbf{r}) = \sum_p F_p \mathbf{U}_p(\mathbf{r}) \tag{16}$$

where the summation refers to all panels and Φ_p and U_p denote, respectively, the induced potential and velocity from the p$^{\text{th}}$ element with unit singularity distribution to the field point $\mathbf{r} = (x, y, z)$. The induced potential and velocities from each element are obtained by a semi-analytical method, and the discrete solution is finally obtained using the collocation method, used to satisfy the boundary conditions at the centroid of each panel of the geometrical configuration.

2.4. PML Implementation

The domain and the radiating behavior of the diffraction and radiation fields in the far field at large distances from the floating body are numerically simulated by means of an absorbing layer technique, based on a perfectly matched layer (PML) applied all around the borders of the free-surface computational domain; see, e.g., [22]. In the present model, the free-surface boundary condition is expressed by the following formula (see also [12,13,21]):

$$\frac{\partial\Phi}{\partial n} - \mu(\omega)\Phi = 0, \quad r \in \partial D_F \tag{17}$$

where

$$\mu(\omega) = \left\{ \begin{array}{ll} \frac{\omega^2}{g}, & R < R_a \\ \frac{\omega^2}{g}\left(1 + i\widetilde{c}\frac{(R-R_a)^n}{\lambda^n}\right)^2, & R \geq R_a \end{array} \right\} \tag{18}$$

The efficiency of the above technique to damp the outgoing waves with minimal back-scattering is dependent on various parameters of the present PML, including the layer thickness, its activation point R_a, and the coefficient $\widetilde{c}$. The latter are optimized by systematic investigation using as objective function the minimization of the error of the numerical solution against analytical results available in the case of floating vertical cylindrical bodies in constant depth; see, e.g., [23]. This procedure is

evaluated in detail in [12], and is shown to provide satisfactory results proving the reliability of the present hybrid BEM-PML-CMS numerical scheme.

2.5. Mesh Generation

In computational hydrodynamic problems, mesh generation is an issue of utmost importance. From this perspective, in the present problem, every part of the boundary surface is discretized by distribution of the panels (4-node quadrilateral elements), satisfying perfect junction of various sub-meshes, and ensuring global continuity of geometry. A cylindrical arrangement of panels in all boundary parts is used, as shown in Figure 1, which is found to be suitable for the representation of the radiating behavior of the diffraction and radiation fields; see also [12]. In the example illustrated in Figure 1, the mesh resolution is: 10×88 for the cylindrical WEC (with the first index representing vertical and the second azimuthal discretization). A domain extent of 4 wavelengths on the free surface is discretized into $(4N/\lambda) \times 88$ and 26×88 elements on the bottom surface, respectively, where N denotes the number of elements per wavelength for discetizing the domain. A finer mesh on the floating body corresponding to 18×88 elements is also used for examining the convergence of calculated results.

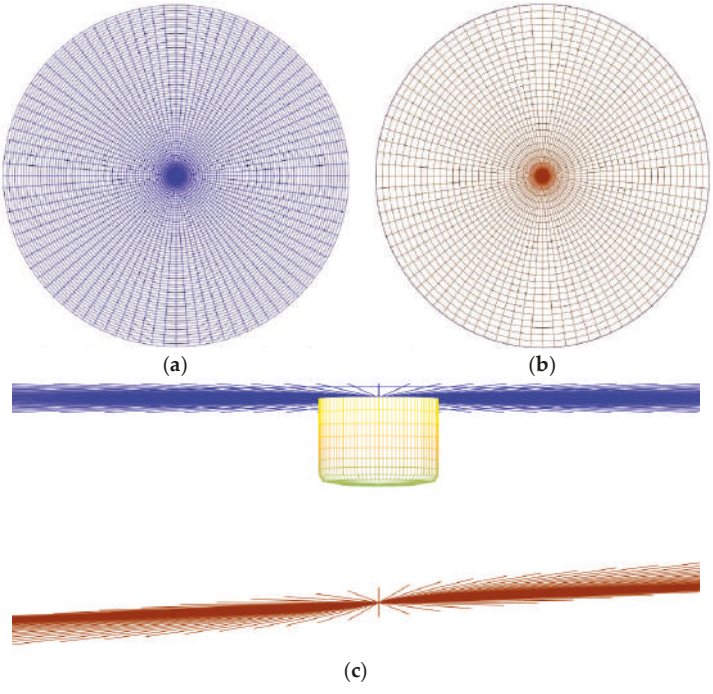

Figure 1. Computational meshes on (**a**) free surface, (**b**) bottom, and (**c**) WEC surface.

2.6. Variable Bathymetry

In this work, the effect of sloping seabeds on the WEC performance is examined by considering an operation over a smooth but steep shoaling region. The seabed profile exhibits a monotonic variation along the x-axis, described as follows

$$h(x) = h_m - 0.5(h_1 - h_3)\tanh(\alpha_{bot}\pi(x - x_{mean})) \tag{19}$$

where the mean depth is: $h_m = 0.5(h_1 + h_3)$ and x_{mean} is the center of the domain span along x-axis, where the WEC is also located. The coefficient α_{bot} controls the bottom slope. The region is characterized by constant depths at infinity, in particular h_1 and h_2.

2.7. 2-DOF WEC Problem Formulation

The idea of combining more than one degree of freedom for harnessing the available power provided by the incident wave is another perspective on improving the WEC efficiency. In this case, the device is able to absorb a higher amount of incident wave power and presents improved grid stability [13,24–26]. Considering the floating WEC operating in two power modes, namely heaving and pitching with amplitudes ξ_{30}, ξ_{50}, respectively, the responses are obtained from the solution of the following system of coupled equations

$$D_{33}\xi_{30} + D_{35}\xi_{50} = X_{P3} + X_{D3} \tag{20}$$

$$D_{53}\xi_{30} + D_{55}\xi_{50} = X_{P5} + X_{D5} \tag{21}$$

where

$$D_{33} = \left(-\omega^2(M + A_{33}) + i\omega(B_{33} + B_{S3}) + C_{33}\right),\ D_{35} = \left(-\omega^2(A_{35} + I_{35}) + i\omega B_{35} + C_{35}\right) \tag{22}$$

$$D_{53} = \left(-\omega^2(A_{53} + I_{53}) + i\omega B_{53} + C_{53}\right),\ D_{55} = \left(-\omega^2(A_{55} + I_{55}) + i\omega(B_{55} + B_{S5}) + C_{55}\right) \tag{23}$$

The hydrodynamic coefficients of added mass and damping, as well as the excitation Froude–Krylov and diffraction heave-forces and pitch-moments in the right-hand side of Equations (20) and (21), are calculated by the present BEM solver. As regards the rest of the included coefficients in the above expressions, the fact should be considered that the center of gravity is coincident to the center of the circular waterline of radius a. A typical mass distribution near the surface of the WEC is assumed, corresponding to radius of gyration $R_{yy} = 0.7a$ and thus, $I_{55} = MR_{yy}^2$. Also, $C_{33} = \rho g \pi a^2$, $C_{35} = C_{53} = 0$, and $C_{55} = 0.25\rho g \pi a^4 + M \cdot GB$, where M denotes the mass of the body and GB the vertical distance between the center of buoyancy and the center of gravity. In the present work we have assumed a fixed location of CG coincident the center of buoyancy (GB = 0) for all WEC shapes examined (operating in one or more DOF) in order to provide a first comparative evaluation. It should be mentioned that, even in the latter case, substantial stability concerning the pitch motion is still offered by the available metacentric height. The latter in the case of the cylindrical WEC examined in the paper is 12% of the draft, while for the nailhead, WEC becomes 3.7 times the draft due to increased waterline area. Additional stability is offered by the PTO damping. Based on the above, in conjunction with the fact that in extreme cases a cut-off system is used to ensure safety, the simplified assumption GB = 0 is made and used for the examples considered here in order to illustrate the developed method to calculate the WEC performance and optimization. The consideration of variable mass distributions and different CGs would lead to a substantially more complicated multidimensional optimization problem that is left to be examined in future work. Finally, the coefficients D_{35} and D_{53} are found, for every geometry, to be quite small, compared with D_{33} and D_{55}, and therefore the coupling between the two oscillatory modes is weak.

3. Design Assessment Features

3.1. Geometries Generation

Many different WEC shapes are currently operating in coastal areas all over the world, used both for research purposes and commercial applications. Geometries like the conical, the semi-spherical, and the elliptical, as well as many other shapes, have been examined in a variety of studies (see, e.g., [27–29] and the references cited there). Based on the relevant industry trends and research activities, eight different axisymmetric body shapes have been examined. The geometrical details can

be found in [12]. At this point, it should be mentioned that very sophisticated designs and shapes, which are normally accompanied with high R&D (research and development) and manufacturing costs, are not examined. The generation of the above shapes, as well as other axisymmetric geometries, is handled by a parametric model based on a spline representation of the profiles controlled by a set of nodes. As an example, the profile of the nailhead-shaped WEC is shown in Figure 2, and the body surface is obtained by 360 degrees rotation. One significant feature of the present WEC shape model is that it is in compliance with the constant-mass constraint. If the same material is considered for the construction of the considered point absorbers with the same mass distribution, then the radius and the draft of each shape can be calculated in order to maintain the submerged vertical cross section area equal to the area of the reference cylindrical WEC design corresponding to a/h = 1/3.5, T/a = 3/2, and d/h = 4/7, where a is the radius, T is the draft, h repreents the water depth, and consequently d = h-T is the bottom clearance below the WEC. For a more unbiased comparison between designs, the assumption of constant-mass is adopted as a basic reference feature for all the tested geometries.

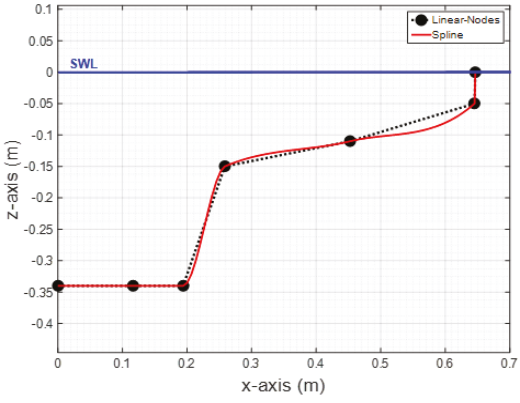

Figure 2. Generating spline of the nailhead-shaped WEC wetted surface.

The above parametric model could be exploited for directly finding the most efficient design. However, in order to reduce the computational cost, a particular set of variants was studied and specific details can be found in Reference [12].

3.2. PTO Damping Configuration

For the evaluation of the absorbed power output by the devices, a typical PTO has been assumed. The heave-PTO coefficient B_{S3} is taken C_{PTO3}-times the mean value of hydrodynamic damping $\overline{b}_{33}$ over the frequency range, $B_{S3} = C_{PTO3}\overline{b}_{33}$, which for the cylindrical WEC considered here is estimated as $2\pi\overline{b}_{33}M\omega_{R3} = 0.12$, and the corresponding resonance frequency is $\omega_{R3}\sqrt{a/g} = 0.7$. A similar PTO assumption is considered for the pitch motion, where the PTO damping is taken C_{PTO5}-times the mean value of hydrodynamic damping $\overline{b}_{55}$ over frequency, which is estimated as $2\pi\overline{b}_{55}M\omega_{R5} = 0.01$, where the corresponding resonance frequency is $\omega_{R5}\sqrt{a/g} = 0.45$. The values for the coefficients C_{PTO3} and C_{PTO5} are selected over a wide range, according to the geometry, contextually, and more detailed investigation of their operational restrictions. Very low values of the PTO coefficients, both for heave and pitch mode, are not considered either because they are incompatible with the current industry standards, or because they lead to high resonance amplitudes which are not permitted due to operational limits and survivability restrictions. These limits are decided after a careful examination of the relevant responses and performances. The damping coefficient of the power take off system is a decisive parameter for the performance of the devices, and after fine tuning and optimization is expected to provide significant improvements concerning the overall WEC performance.

3.3. Performance Index Definition

The averaged power-P output of the device, normalized with respect to the incident wave power, is plotted in Figure 3 in the case of the cylindrical-shaped WEC. According to the selection of PTO damping, there are cases of concentrated power maximization in the near-resonance frequency bandwidth, or cases of lower power levels, corresponding to responses covering wider frequency bandwidth. The curve with the largest area below defines the optimum PTO damping value. The latter behavior concerning the extraction of incident wave energy is exploited in the definition of an index quantifying the performance of different designs, which is based on the area below the "most-efficient-curve" of normalized power output. The result will be used, in normalized form with respect to incident power, to quantify the overall performance of the WEC and will be called performance index (PI%).

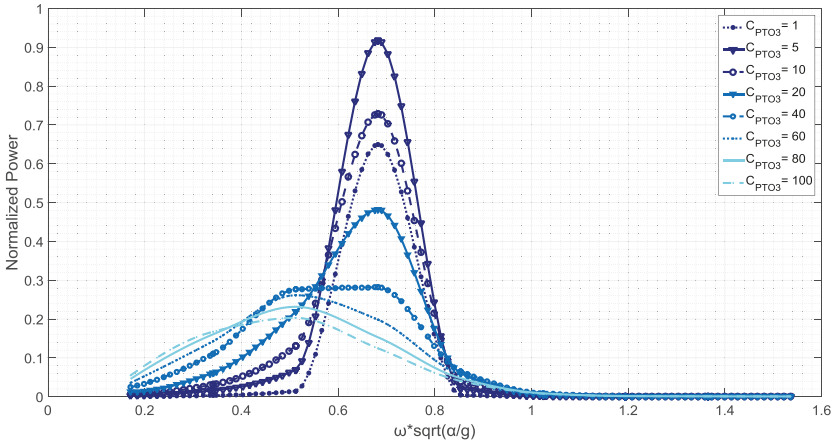

Figure 3. Normalized power output by the reference cylindrical heaving WEC (a/h = 1/3.5, T/a = 3/2, d/h = 4/7) over the variable bottom (h_1 = 1.2 m, h_3 = 0.8 m, α_{bot} = 0.5) for different PTO damping configurations. Indicative values of the $C_{PTO3} = B_{S3}/\bar{b}_{33}$ considered here are C_{PTO3} = [1, 5, 10, 20, 40, 80, 100].

In more detail, each WEC design corresponds to a different waterline radius due to mass-constraint implementation. Therefore, the operational bandwidth of non-dimension angular frequency varies among the WECs. In order to obtain a reliable index for assessing their performance, the P.I. is defined as the ratio of the area below the power curve for the optimum PTO damping to the area of the rectangle [0,1] and [0.2, max($\omega\sqrt{a/g}$)], representing the total available power for absorption by the system. It should be considered that the fact for this rectangle is that the horizontal axis span differs to the efficiency frequency bandwidth, commonly used in WEC evaluations, a fact that can be observed with a closer look of Figure 3, where this difference is apparent. It should also not be overlooked that even if this index takes small values, almost insignificant compared with the capture width ratio (CWR) of WEC devices, however, as its definition explains, is a totally different index and every alteration of its value, caused for example by a variable-depth seafloor, is countable. For the extension of the latter definition to the 2-DOF WEC, the total power output, calculated as the summation of the contribution by each mode individually, will be used as the performance index.

4. Numerical Results and Discussion

4.1. Heaving Cylindrical WEC over Variable Bathymetry

The investigation of the heaving response of the reference cylindrical WEC over a variable seabed is discussed in this section. As an example, the cylindrical WEC with a/h = 1/3.5, T/a = 3/2, and d/h = 4/7 operates over a variable bottom topography described by Equation (19), with h_1 = 1.5 m, h_3 = 0.5 m, and α_{bot} = 0.5. The propagation field, evaluated by the CMS, is illustrated in Figure 4 in the case of normally incident waves of frequency $\omega\sqrt{a/g} = 0.7$ (resonance frequency). The corresponding bathymetric non-dimensional frequency of the waves is $\omega\sqrt{h/g} = 1.3$. It is clearly observed that the propagating field is diffracted and reflected, and the bottom boundary condition is consistently satisfied, by the fact that the equipotential lines intersect perpendicularly in the seabed profile. In Figure 4, the illustration of the free-surface elevation is also indicated by using solid black line.

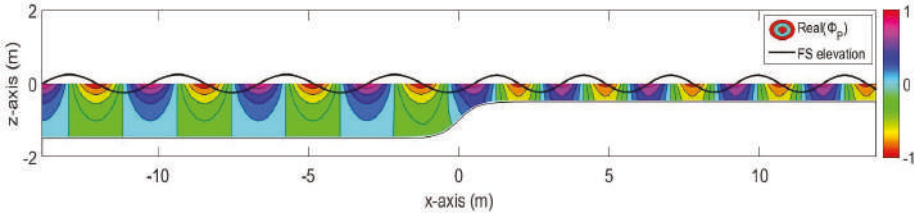

Figure 4. Propagating field (real part) over a smooth shoal on the vertical plane as calculated by the CMS for normally incident waves $\omega\sqrt{h/g} = 1.3$ θ = 0 degrees. Variable bottom (h_1 = 1.5 m, h_3 = 0.5 m, α_{bot} = 0.5).

Using the data concerning the propagating wave field and its normal derivative over the motionless WEC-scatterer, the diffraction field is calculated by the present BEM-PML solver which is illustrated in Figure 5, where the bottom contours are also plotted using dashed lines and the body's position is indicated with the white disk in the center of the domain. The heave radiation field on the free surface for WEC frequency $\omega\sqrt{a/g} = 0.7$ over the variable bottom topography (h_1 = 1.5 m, h_3 = 0.5 m, α_{bot} = 0.5), is shown in Figure 6 as calculated by the present method. The bottom contours are indicated by using dashed lines. Furthermore, the calculated radiation potentials related to the rest oscillation modes (except of yaw, which is not excited) are presented in Figure 7 for the same frequency as before. The details of the radiated wave pattern are clearly observed in these plots, as well as the effects of variable seabed topography, resulting in an amplification of wave amplitudes in the shallower region due to shoaling effects. The effectiveness of the present PML model is clear in these plots by noticing the damping of the outgoing waves after the PML-activation point, which in the cases considered is set at a radius of three wavelengths away from the floating body.

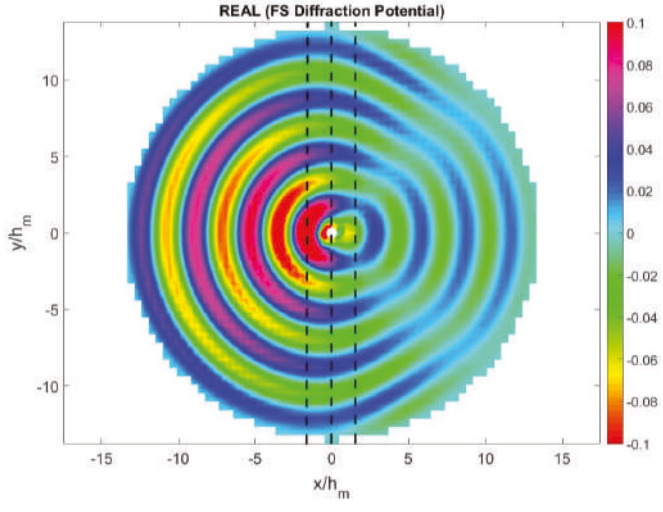

Figure 5. Diffraction field (real part) on the free surface for normally incident waves $\omega\sqrt{a/g} = 0.7$ θ = 0 degrees as calculated by the present hybrid BEM over the variable bottom topography (h_1 = 1.5 m, h_3 = 0.5 m, α_{bot} = 0.5). The bottom contours are indicated by using dashed lines.

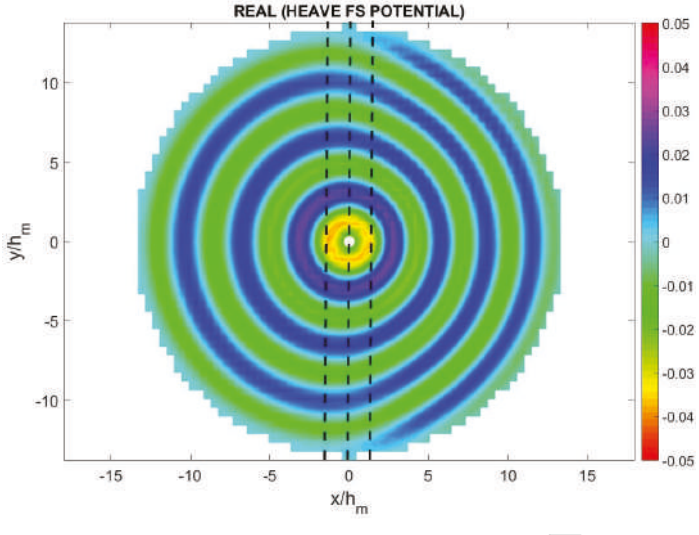

Figure 6. Heave radiation field on the free surface for WEC frequency $\omega\sqrt{a/g} = 0.7$ over the variable bottom topography (h_1 = 1.5 m, h_3 = 0.5 m, α_{bot} = 0.5), as calculated by the present method. The bottom contours are indicated by using dashed lines.

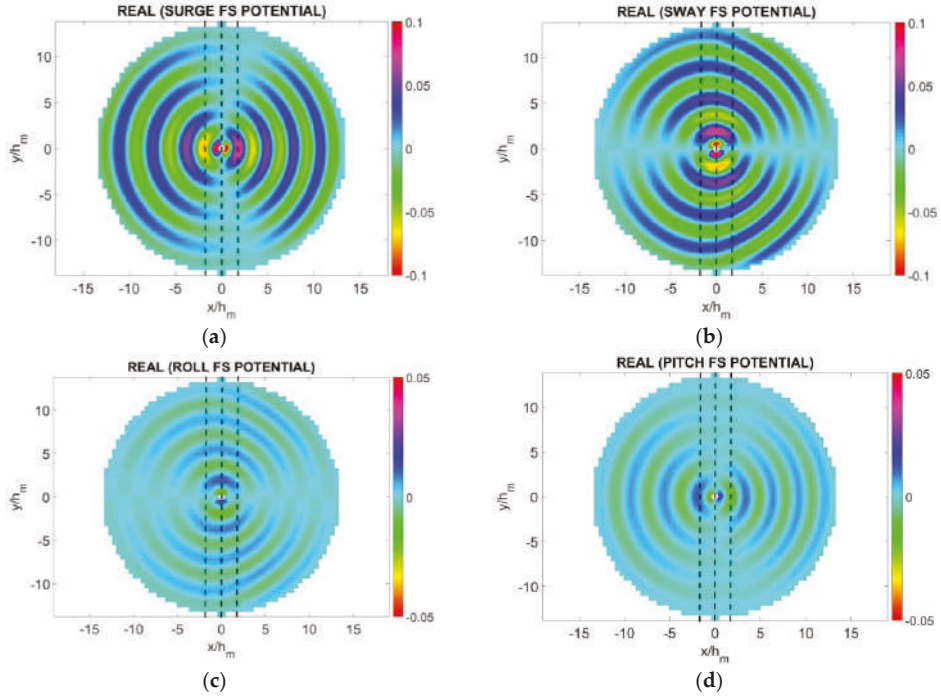

Figure 7. Radiation fields on the free surface for WEC frequency $\omega\sqrt{a/g} = 0.7$ over the variable bottom topography (h_1 = 1.5 m, h_3 = 0.5 m, α_{bot} = 0.5), as calculated by the present method. (**a**) surge, (**b**) sway, (**c**) roll, (**d**) pitch.

4.2. Heaving (1-DOF) WECs over Variable Bathymetry

In order to examine the effect of variable seabed topography on the WEC performance over shoaling bottom topography, the responses are evaluated for the eight different WEC shapes which have been presented and discussed in detail in Reference [12]. Except for the steep bottom profile considered in the previous section, a second less steep bathymetric profile was initially examined, which is also described by Equation (19), for h_1 = 1.2 m, h_3 = 0.8 m, and α_{bot} = 0.5. Both seabed geometries have the same mean depth, h_m = 1 m, but the maximum bottom slope decreases from 0.7 to 0.3.

The main aim of the present work is the assessment of the performance of the devices by means of the achieved performance index. The damping of the PTO is set initially, for the assessment of the designs, as: C_{PTO3} = [1, 5, 10, 50, 100, 250, 500, 750, 1000]. The latter configuration will be optimized in the sequel in order to estimate the value of the exact PTO damping coefficient providing the best performance. Numerical results concerning the performance index are presented in Table 1 for each WEC design over a flat bottom and variable bottom topography. We observe that the conical WEC is selected as the design with the best performance, among all the investigated alternative designs in the case of an 1-DOF device and this holds true for both of the examined depth configurations. Furthermore, comparison between the two most efficient shapes, i.e. the conical and the semi-spherical, is also performed in [28] and concludes again in the superiority of the conical WEC against the semi-spherical one.

Moreover, the shoaling sea bottom topography is shown to affect the performance of every WEC-design, and more specifically it causes an increase of the device's ability for harnessing wave energy. The highest upgrade is detected for the disk-shaped WEC, being equal to almost +3.3%.

However, it should be taken under consideration the fact that the performance index (P.I.) used in the present work to quantify the overall WEC performance, accounts for the whole frequency bandwidth and not only the efficient bandwidth of each WEC operation. For example, in the case of the cylindrical WEC, it is clearly observed in Figure 3 that the efficient bandwidth is $0.2 < \omega\sqrt{a/g} < 1$ while the total bandwidth extends in the range $0 < \omega\sqrt{a/g} < 1.8$. The latter is used because the efficient frequency bandwidth of other WEC shapes is different but it is included in the extended range. The above has the effect that changes of the calculated PI due to bathymetry remain rather small.

Results like this are very promising and may be a first indication for installations of WECs over a deliberately sloping seabed, with man-made constructions and interventions that could be combined with water wave lenses producing the focusing of the wave energy in the location of the WEC or WEC-array and contributing to achieve higher power absorption by the devices. Further studies of this effect and optimization will be subjects of future work.

Table 1. 1-DOF WEC shapes and PI for flat and variable bottom topographies (h_1 = 1.2 m, h_3 = 0.8 m, α_{bot} = 0.5).

WEC Design	Max {Performance Index} Flat Bottom	Max {Performance Index} Variable Bottom
Cylindrical	11.29%	11.41%
Nailhead-shaped	15.38%	15.74%
Disk-shaped	13.66%	14.11%
Elliptical	14.73%	15.11%
Egg-shaped	10.63%	10.82%
Conical	17.70%	17.92%
Floater-shaped	9.87%	10.10%
Semi-spherical	13.30%	13.39%

Proceeding to the determination of the optimal PTO damping values for the conical WEC, it is found by finer discretization of the parameters that a performance index of 17.95% is achieved for a PTO coefficient equal to C_{PTO3} = 77 in the case of the flat bottom. The latter index has further improved to 18.10% with C_{PTO3} = 80 over the smooth shoal, Equation (19). This result is more proof of the significance of the effects by a varying topography in the design-task of the WECs.

4.3. 2-DOF WECs over Variable Bathymetry

The accomplished performance index by the 1-DOF WEC design may be appreciably upgraded by considering the device operating in 2-DOFs (heave and pitch). These modes of operation are normally coupled with surge oscillation mode and all those three degrees of freedom determine the maximum possible energy absorption by a wave device, according to [4]. However, in this study, surge power mode is omitted, with the WEC assumed to be properly moored. Moreover, surge motion is strongly affected by more complex phenomena such as wave drift forces and thus this assumption is in compliance with the complexity of the developed hydrodynamic theory. The same procedure for the selection of the most efficient shape and the optimal PTO damping coefficient is followed, using the subsequent values of PTOs coefficients C_{PTO3} = [1, 5, 10, 20:10:340] and C_{PTO5} = [50:10:400], resulting in the data presented in Table 2.

In this case, the two qualified designs are the cylindrical WEC and the nailhead-shape WEC, which are expected to be the best performing designs in the case of heaving-pitching body due to its larger waterline area. The results summarizing the performance over flat and sloping seabed topography are listed in Table 3. It is observed that the effect induced by the variable seafloor is sometimes constructive, for example, as for the Disk-shaped device (+0.27%), and other times destructive, as it happens in the case of the cylindrical device (−0.43%).

As stated previously, the impact of the seabed profile is now not so simple and affects the performance of the device in a more complicated way. The PTOs used for harnessing power from the

sea environment are exhibiting different damping values. Thus, the optimization of the PTO coefficients is investigated with respect to three principal design parameters: (i) the geometry of the WEC, (ii) the heave-PTO damping coefficient, and (iii) the pitch-PTO damping coefficient. The calculated values of the performance index for the cylindrical and the nailhead-shape WECs operating over a flat bottom topography are plotted in Figure 8, allowing the prompt comparison and the determination of the optimal PTO damping coefficients.

Table 2. 2-DOFs WEC shapes and PI for flat and variable bottom topographies (h_1 = 1.2 m, h_3 = 0.8 m, α_{bot} = 0.5).

WEC Design	Max {Performance Index (Heave+Pitch)} Flat Bottom	Max {Performance Index (Heave+Pitch)} Variable Bottom
Cylindrical	32.43%	32.00%
Nailhead-shaped	29.00%	29.08%
Disk-shaped	22.04%	22.31%
Elliptical	27.12%	27.26%
Egg-shaped	26.25%	25.84%
Conical	21.99%	22.07%
Floater-shaped	19.65%	19.59%
Semi-spherical	13.44%	13.60%

Table 3. Optimum WEC designs, P.I., and PTO damping for flat and variable bottom topography in the case of smooth shoal (h_1 = 1.2 m, h_3 = 0.8m, α_{bot} = 0.5).

Design & Performance		Cylindrical WEC	Nailhead-Shaped WEC
Max{Performance Index (Heave+Pitch)}	Flat	32.47%	29.00%
	Variable	32.04%	29.08%
PTO damping coefficient: [C_{PTO3}, C_{PTO5}]	Flat	[4, 50]	[261, 214]
	Variable	[4, 50]	[276, 213]

Finally, the bathymetry also affects the optimal values of PTO damping for each device, and this can be studied considering it as an additional design constraint. The effects on the WEC performances by the variable bathymetry in the case of the smooth shoal defined by Equation (19) are presented in Figure 9, with the strongest influence detected for the pitch power mode of the cylindrical WEC and the heave power mode of the nailhead-shaped WEC.

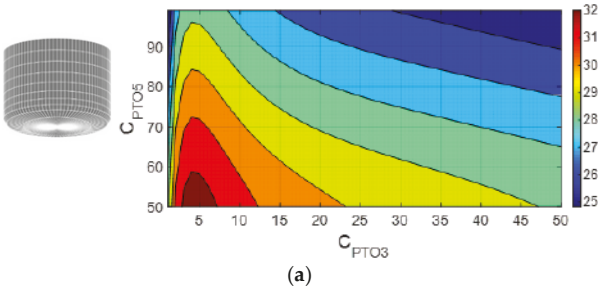

(**a**)

Figure 8. *Cont.*

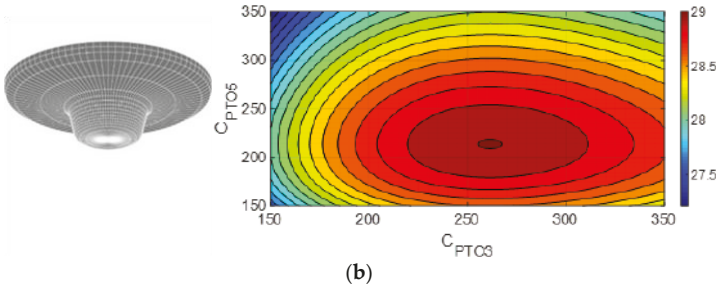

(**b**)

Figure 8. Isoperformance curves of (**a**) Cylindrical WEC and (**b**) Nailhead-shaped WEC over flat bottom.

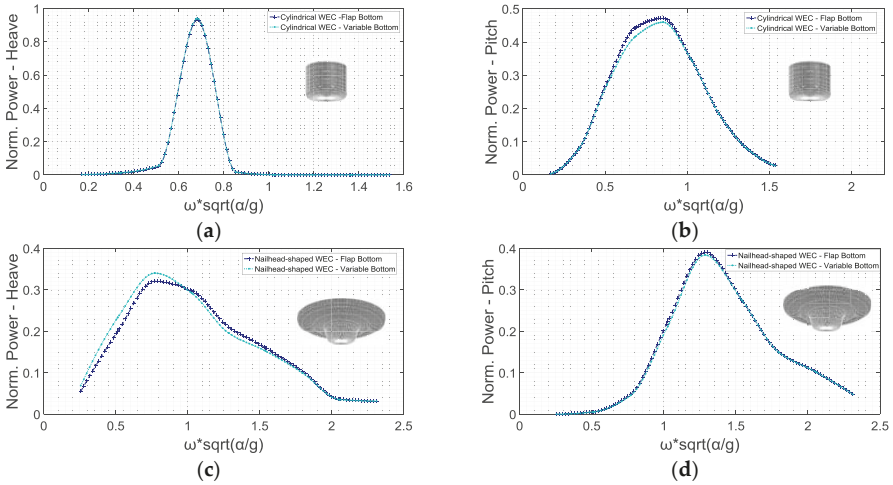

Figure 9. Normalized power output over flat and variable bottom topography (h_1 = 1.2 m, h_3 = 0.8 m, α_{bot} = 0.5) using the optimized PTO. Cylindrical WEC in (**a**) heave mode and (**b**) pitch mode, and nailhead-shaped WEC in (**c**) heave mode and (**d**) pitch mode.

5. Sloping Seabed Effect

In order to better illusrate the effect of the sloping seabed on the performance of WECs, a second, steeper, bottom topography is considered, with bathymetric profile defined by Equation (19) for h_1 = 1.5 m, h_3 = 0.5 m, and α_{bot} = 0.5; see Figure 4. The results, presented in Table 4 for the optimum heaving-WECs and 2-DOF WECs, prove that the effects by the seabottom cannot be predicted a priori. For the heaving WEC, a slight increase of PI is observed, while for the 2-DOF systems, an increase for the cylindrical WEC is obtained. The nailhead-shaped design performance index seems almost unaffected by the bottom topography. Again, the small changes of P.I. values are due to the bandwidth extent that has been considered for the definition of the index in order to enable comparison between various WEC shapes characterized by different resonant frequencies.

Table 4. Optimum WEC designs, P.I. over flat and sloping seabeds with increased steepness.

Type	Geometry	P.I. % Flat	δ P.I. % Steep vs Flat	δ P.I. % Steep vs Variable
Heaving WECs	Cylindrical	11.3%	6.2%	5.2%
	Conical	17.7%	3.1%	0.8%
2-DOF WECs	Cylindrical	32.4%	0.3%	1.6%
	Nailhead-shaped	29.0%	0.1%	0.4%

6. Conclusions

In the present work, several aspects related to the performance of wave energy converters of the type of point absorbers are studied, using a boundary element method for solving the associated hydrodynamic problems. In particular, a hybrid BEM coupled with a perfectly matched layer model is used for calculating the diffraction and radiation fields, based on information concerning the wave conditions around the floating bodies derived from a coupled mode model. The present method is shown to provide useful information, being able to treat general body geometry of the floating body operating in various oscillation modes over flat or sloping seabeds. Subsequently, it is systematically applied to numerically simulate the WEC performance in variable bathymetry regions. For the assessment and comparison of various designs, a specific performance index was defined as a useful indicator for the estimation of the power absorbing capacity. Regarding the PTO damping, which is exhibiting various constraints, this was found to be very important concerning the optimum performance of a WEC. From the results of the present study, it is concluded that the conical floater appears to be the most efficient design in the case of a heaving WEC, while the cylindrical and the nailhead-shaped forms are the ones exhibiting the highest performance operating as 2-DOF devices in coupled heaving and pitching modes. It is demonstrated that multiple DOF systems could substantially increase the levels of the extracted wave energy, and that the sloping seabed could also have an effect on the overall behavior of the devices and it should be taken into account. Future extensions of the present work include the examination of the performance and optimization of WEC arrays in more than two power modes in variable bathymetry, as well as the investigation of viscosity effects.

Author Contributions: The main idea of this work belongs to K.B. and M.B., while the main draft of the text and numerical simulations were handled by M.B.; E.R. participated in verification of the results, operated various corrections and acted as corresponding author. All authors agreed with the final form of this article.

Funding: The work of the corresponding author was carried out in the framework of the research project REMARC (Renewable Energy extraction in MARine environment and its Coastal impact), supported by the Romanian Executive Agency for Higher Education, Research, Development and Innovation Funding – UEFISCDI, grant number PN-III-P4-IDPCE-2016-0017.

Conflicts of Interest: The authors declare no conflict of interest.

Abbreviations

BC	Boundary Condition
BEM	Boundary Element Method
CMM	Coupled-Mode Model
CMS	Coupled-Mode System
DOF	Degree Of Freedom
FS	Free Surface
PI	Performance Index
PML	Perfectly Matched Layer
PTO	Power Take Off
RAO	Response Amplitude Operator
R&D	Research & Development
SWAN	Simulating Waves Nearshore
SWL	Sea Water Level
WEC	Wave Energy Converter

Nomenclature

a	Waterline radius
A	Hydrodynamic matrix
a_{bot}	Bottom slope coefficient
a_{ij}	Added mass coefficient (i, j=1, … ,6)
b_{ij}	Hydr. damping coefficient (i, j=1, … ,6)
B_{mn}	CMS coefficient
B_s	PTO damping coefficient
c_{ij}	Hydrostatic coefficient (i, j=1, … ,6)
C_{mn}	CMS coefficient
C_{PTOi}	PTO mean-damping multiplier
C_s	PTO hydrostatic coefficient
d	Bottom clearance
D_{ij}	Coupling coefficient of i-j modes
F_P	Source strength of p^{th} element
g	Gravity acceleration
GB	Center of buoyancy
H	Wave height
h	Depth
i	Imaginary unit
M	Mass
N	Number of elements per wavelength
n_i	Normal vector of i-mode (i=1, … ,6)
P	Power
$P.I.$	Performance Index
R	Radial distance
r	Position vector
R_a	PML activation radius
R_{yy}	Radius of gyration
t	Time
T	Draft
U_P	Induced velocity by p^{th} element
x	x-Coordinate
X_D	Diffraction excitation forces
X_P	Froude Krylov excitation forces
y	y-Coordinate
z	z-Coordinate
Z_n	Vertical function of n^{th}-mode (n=-1, 0, 1, …)
A_{mn}	CMS coefficient
η	Free surface elevation
η_{eff}	PTO efficiency
λ	Wavelength
μ	Frequency parameter
ξ_i	Response amplitude of i-mode (i=1, … ,6)
ρ	Water density
Φ	Wave potential
φ_d	Diffraction potential
φ_i	Radiation potential of i-mode (i=1, … ,6)
φ_n	Amplitude of n^{th}-mode (n=-1, 0, 1, …)
φ_p	Propagation potential
Φ_P	Induced potential by p^{th} element
φ_R	Radiation potential
ω	Angular frequency
ω_R	Resonance angular frequency

References

1. Al Shami, E.; Zhang, R.; Wang, X. Point Absorber Wave Energy Harvesters: A Review of Recent Developments. *Energies* **2019**, *12*, 47. [CrossRef]
2. Wehausen, J.V. The Motion of Floating Bodies. *Annu. Rev. Fluid Mech.* **1971**, *3*, 237–268. [CrossRef]
3. Mei, C.C. *The Applied Dynamics of Ocean Surface Waves*; World Scientific: Singapore, 1989.
4. Falnes, J. *Ocean Waves and Oscillating Systems: Linear Interactions including Wave Energy Extraction*; Cambridge University Press: Cambridge, UK, 2004.
5. Verao Fernandez, G.; Balitsky, P.; Stratigaki, V.; Troch, P. Coupling Methodology for Studying the Far Field Effects of Wave Energy Converter Arrays over a Varying Bathymetry. *Energies* **2018**, *11*, 2899. [CrossRef]
6. Balitsky, P.; Quartier, N.; Verao Fernandez, G.; Stratigaki, V.; Troch, P. Analyzing the Near-Field Effects and the Power Production of an Array of Heaving Cylindrical WECs and OSWECs Using a Coupled Hydrodynamic-PTO Model. *Energies* **2018**, *11*, 3489. [CrossRef]
7. Fernández, G.V.; Stratigaki, V.; Troch, P. Irregular Wave Validation of a Coupling Methodology for Numerical Modelling of Near and Far Field Effects of Wave Energy Converter Arrays. *Energies* **2019**, *12*, 538. [CrossRef]
8. Charrayre, F.; Peyrard, C.; Benoit, M.; Babarit, A. A Coupled Methodology for Wave-Body Interactions at the Scale of a Farm of Wave Energy Converters Including Irregular Bathymetry. In Proceedings of the 33rd International Conference on Ocean, Offshore and Arctic Engineering (ASME 2014), San Francisco, CA, USA, 8–13 June 2014.
9. McCallum, P.; Forehand, D.; Sykes, R. On the Performance of an Array of Floating Wave Energy Converters for Different Water Depths. In Proceedings of the 33rd International Conference on Ocean, Offshore and Arctic Engineering (ASME 2014), San Francisco, CA, USA, 8–13 June 2014.
10. Massel, S.R. Extended refraction-diffraction equation for surface waves. *Coast. Eng.* **1993**, *19*, 97–126. [CrossRef]
11. Touboul, J.; Rey, V. Bottom pressure distribution due to wave scattering near a submerged obstacle. *J. Fluid Mech.* **2012**, *702*, 444–459. [CrossRef]
12. Belibassakis, K.; Bonovas, M.; Rusu, E. A Novel Method for Estimating Wave Energy Converter Performance in Variable Bathymetry Regions and Applications. *Energies* **2018**, *11*, 2092. [CrossRef]
13. Bonovas, M. WECs over General Bathymetry: A Novel Approach for Performance Evaluation and Optimization. Master's Thesis, National Technical University of Athens, Athens, Greece, 2019.
14. Athanassoulis, G.A.; Belibassakis, K.A. A consistent coupled-mode theory for the propagation of small-amplitude water waves over variable bathymetry regions. *J. Fluid Mech.* **1999**, *389*, 275–301. [CrossRef]
15. Belibassakis, K.A.; Athanassoulis, G.A.; Gerostathis, T.P. A coupled-mode model for the refraction-diffraction of linear waves over steep three-dimensional bathymetry. *Appl. Ocean Res.* **2001**, *23*, 319–336. [CrossRef]
16. Belibassakis, K.A.; Gerosthathis, T.P.; Athanassoulis, G.A. A Coupled-Mode Model for the Transformation of Wave Systems Over Inhomogeneous Sea/Coastal Environment. In Proceedings of the 29th International Conference on Offshore Mechanics and Arctic Engineering (OMAE2010), Shanghai, China, 6–11 June 2010; pp. 471–478. [CrossRef]
17. Berkhoff, J.C.W.; Booij, N.; Radder, A.C. Verification of numerical wave propagation models for simple harmonic linear water waves. *Coast. Eng.* **1982**, *6*, 255–279. [CrossRef]
18. Vincent, C.L.; Briggs, M.J. Refraction–diffraction of irregular waves over a mound. *J. Waterw. Port Coast. Ocean Eng.* **1989**, *115*, 269–284. [CrossRef]
19. Booij, N.; Ris, R.C.; Holthuijsen, L.H. A third-generation wave model for coastal regions: 1. Model description and validation. *J. Geoph. Res.* **1999**, *104*, 7649–7666. [CrossRef]
20. Ryszard, M.S. *Ocean Surface Waves: Their Physics and Prediction*; World Scientific: Singapore, 1996.
21. Belibassakis, K.A.; Gerostathis, T.P.; Athanassoulis, G.A. A 3D-BEM coupled-mode method for WEC arrays in variable bathymetry. In *Progress in Renewable Energies Offshore, Proceedings of the 2nd International Conference on Renewable Energies Offshore (RENEW2016), Lisbon, Portugal, 24–26 October 2016*; CRC Press: Boca Raton, FL, USA, 2016; p. 365.
22. Turkel, E.; Yefet, A. Absorbing PML boundary layers for wave-like equations. *Appl. Numer. Math.* **1998**, *27*, 533–557. [CrossRef]
23. Yeung, R. Added mass and damping of a vertical cylinder in finite depth waves. *Appl. Ocean Res.* **1981**, *3*, 119–133. [CrossRef]

24. Brooke, J. *Wave Energy Conversion*; Elsevier Science: Amsterdam, The Netherlands, 2003.
25. Davis, A.F.; Thomson, J.; Mundon, T.R.; Fabien, B.C. Modeling and Analysis of a Multi Degree of Freedom Point Absorber Wave Energy Converter. In Proceedings of the 33rd International Conference on Ocean, Offshore and Arctic Engineering (ASME 2014), San Francisco, CA, USA, 8–13 June 2014. [CrossRef]
26. Sergiienko, N.Y. Three-Tether Wave Energy Converter: Hydrodynamic Modelling, Performance Assessment and Control. Ph.D. Thesis, University of Adelaide, Adelaide, Australia, 2018.
27. Backer, G. Hydrodynamic Design Optimization of Wave Energy Converters Consisting of Heaving Point Absorbers. Ph.D. Thesis, University of Gent, Ghent, Belgium, 2009.
28. Blommaert, C. Composite Floating Point Absorbers for Wave Energy Converters: Survivability Design, Production Method and Large-Scale Testing. Ph.D. Thesis, University of Gent, Ghent, Belgium, 2018.
29. Franzitta, V.; Curto, D.; Rao, D.; Viola, A. Hydrogen Production from Sea Wave for Alternative Energy Vehicles for Public Transport in Trapani (Italy). *Energies* **2016**, *9*, 850. [CrossRef]

energies

MDPI

Article

Sealing Performance Analysis of an End Fitting for Marine Unbonded Flexible Pipes Based on Hydraulic-Thermal Finite Element Modeling

Liping Tang [1], Wei He [1], Xiaohua Zhu [1,*] and Yunlai Zhou [2]

[1] School of Mechatronic Engineering, Southwest Petroleum University, Chengdu 610500, China; lipingtang@swpu.edu.cn (L.T.); hewei@stu.swpu.edu.cn (W.H.)
[2] Department of Civil and Environmental Engineering, The Hong Kong Polytechnic University, Hong Kong 00852, SAR, China; YunLai.zhou@alumnos.upm.es
* Correspondence: zhuxh@swpu.edu.cn

Received: 11 May 2019; Accepted: 30 May 2019; Published: 10 June 2019

Abstract: End fittings are essential components in marine flexible pipe systems, performing the two main functions of connecting and sealing. To investigate the sealing principle and the influence of the temperature on the sealing performance, a hydraulic-thermal finite element (FE) model for the end fitting sealing structure was developed. The sealing mechanism of the end fitting was revealed by simulating the sealing behavior under the pressure penetration criteria. To investigate the effect of temperature, the sealing behavior of the sealing ring under different temperature fields was analyzed and discussed. The results showed that the contact pressure of path 1 (i.e., metal-to-polymer seal) was 31.7 MPa, which was much lower than that of path 2 (metal-to-metal seal) at 195.6 MPa. It was indicated that the sealing capacities were different for the two leak paths, and that the sealing performance of the metal-to-polymer interface had more complicated characteristics. Results also showed that the finite element analysis can be used in conjunction with pressure penetration criteria to evaluate the sealing capacity. According to the model, when the fluid pressures are 20 and 30 MPa, no leakage occurs in the sealing structure, while the sealing structure fails at the fluid pressure of 40 MPa. In addition, it was shown that temperature plays a significant role in the thermal deformation of a sealing structure under a temperature field and that an appropriately high temperature can increase the sealing capacity.

Keywords: end fitting; unbonded flexible pipe; sealing performance; pressure penetration; temperature

1. Introduction

The development of offshore resources has traditionally relied on floating production systems, such as floating production storage and offloading (FPSO) units and semi-submerged ships [1]. The hydrocarbons produced by an FPSO or from nearby subsea templates are transported through a pipeline or offloaded onto a tanker [2,3]. In terms of offshore pipes, submarine pipelines, which are buried in a trench or laid on the seabed, are commonly used [4,5]. Compared with conventional steel pipes, flexible pipe systems have the characteristics of higher flexibility, greater applicability, and enhanced recyclability [6]. Flexible pipes can be classified into two primary types: bonded flexible pipes and unbonded flexible pipes [7,8]. An unbonded flexible pipe usually comprises an outer polymeric layer, helical tensile armor, anti-wear layers, pressure armor layers, and an inner carcass layer [9], as shown in Figure 1. With the rapid development of techniques for exploiting deep-water resources, unbonded flexible pipes now play a significant role in transferring oil and gas resources from offshore platforms to onshore facilities.

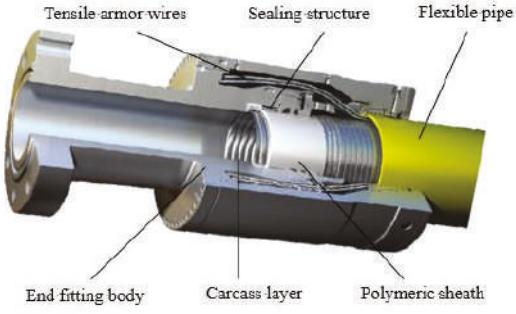

Figure 1. Typical cross-section of flexible pipeline end fitting [9].

Connecting the subsea infrastructure to surface facilities and transporting hydrocarbon products are the major applications of flexible pipes in the offshore oil and gas industry [10]. However, the harsh deep-sea environment imposes significant challenges on flexible pipes, necessitating higher mechanical response and performance characteristics [11]. According to the American Petroleum Institute (API), the terminations of a flexible pipe are defined as end fittings (as shown in Figure 2), of which the functions are: (1) to provide a transition between the pipe body and the connecting component and (2) to transmit the loads acting on the pipe without allowing the pipe to fail [12]. The widespread use of flexible pipes under more demanding operational conditions makes the safety performance of end fittings particularly important [13].

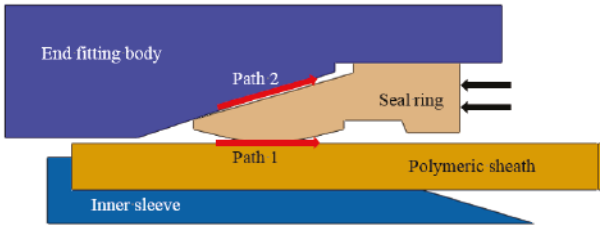

Figure 2. Schematic illustration of the sealing structure.

Experiences in offshore environments have shown that the end fitting of a flexible pipe may be the weakest point [13]. In service, end fittings will be subjected to similar environmental loads and conditions as the pipe, such as axial tension, inner pressure, and external hydrostatic pressure [14]. Apart from mechanical load, the end fitting has to offer thermal insulation and be leak-proof [13]. Therefore, if the sealing capacity of the end fitting is insufficient, there will be a risk of oil and gas leakage, which can have serious consequences. Because the composite structure of flexible pipe consists of many independent concentric metallic and polymeric layers, the structure of the end fitting is also multifaceted and complex [15]. To ensure that the end fitting has adequate sealing performance, it is necessary to investigate its sealing capacity.

In general, existing studies related to the sealing performance of a structure have concentrated on the sealing rings [16]. Typical examples are "O" rings, although these are different from the structure of an end fitting sealing assembly. In addition, a number of studies have focused on the mechanical behavior of flexible pipe, such as the instability of the armor wire [17], the collapse of the carcass layers [18], and fatigue reliability analysis [19]. Although the sealing behavior of the end fitting is unlike the mechanical behavior of the flexible pipe body or the layers inside the end fitting, which have been extensively investigated [8,20], there has been relatively little research on the sealing performance of the end fittings themselves.

The composite materials used in flexible pipe have different properties to metallic materials in terms of anisotropy, thermal expansion coefficient, thermal conductivity, and stiffness. Indeed, the structural properties of composite materials are more complex than those of metallic materials. This may lead to interface failure, such as when the composite material separates from the metallic material, thus losing the ability to maintain leak-tight integrity. Hatton et al. [15] studied the design of sealing assemblies in different types of end fittings using finite element (FE) analysis and laboratory testing.

To understand the sealing performance of a mechanical connector in a subsea pipeline, Wang et al. [21] investigated the critical condition of the sealing structure and created a new method to analyze the contact pressure of the sealing surface by examining the static metal sealing mechanism. An optimized design for a new subsea pipeline mechanical connector was proposed and an approach for determining the contact pressure of various dimensions was provided.

For an end fitting in a high-pressure pipe, it is challenging to create the necessary sealing performance. Fernando et al. [22] developed an FE model of a flexible pipe end fitting and presented a method of evaluating the sealing performance of the sealing assembly and the design requirements for the sealing assembly of the end fitting. In their work, FE analysis was conducted using specially established leak criteria. In addition, an ultrasonic technique was used to measure the contact pressure at the metal-to-metal interface, which showed that their method had significant promise.

Li et al. [23] considered the sealing performance of the sealing assembly in a deep-water flexible pipe end fitting and established an FE model using the ABAQUS software (6.11). They studied the key parameters under different conditions, providing further references for research on flexible pipe end fittings. By summarizing the general sealing criteria, Zhang [24] introduced the concept of "contact pressure amplification factor" to evaluate the sealing capability of end fittings, while Marion et al. [25] investigated the suitability of end fittings for high-temperature thermal cycling conditions using specially designed pipe samples and facilities that satisfy the API specifications.

Previous studies have analyzed and optimized the sealing criteria and the geometric parameters of the sealing assembly. However, there have been few studies related to the sealing behavior. In general, research on the sealing performance of the end fittings is not comprehensive. In this study, FE methods were used to develop a two-dimensional axisymmetric numerical model of the sealing structure of an end fitting, including the temperature field. The pressure penetration criteria were applied to this model to analyze the performance of the sealing structure.

2. Sealing Analysis

2.1. Sealing Structure

According to the API SPEC 17J and 17B standards [12,26], the sealing structure of a typical flanged unbonded flexible pipe end fitting is as illustrated in Figure 2. As can be seen in the figure, the functional structure of the sealing system is mainly composed of four parts: the inner sleeve, polymeric sheath, sealing ring, and end fitting body. The inner sleeve is the innermost component of the end fitting. This plays a supporting role in the whole structure and is used to bear the radial force while in service. The polymeric sheath of the flexible pipe is pressed on the outer side of the inner sleeve, and is one of the most important parts of the sealing structure. The end fitting body is the outermost part of the sealing structure, and is used to protect all components in the end fitting. The wedge sealing ring provides the critical sealing capacity through axial extrusion.

The sealing ring is designed in advance according to the specifications of the flexible pipe and end fitting. The sealing assembly in an end fitting is usually formed by swaging a metallic sealing ring into the area between the polymeric layer and the end fitting body. During assembly, the contact surface between the sealing ring and the end fitting body and between the sealing ring and the polymeric sheath creates two leakage paths [14,22]. Path 2 is the metal-to-metal microscopic gap between the end fitting body and the sealing ring, where a higher contact pressure ensures better sealing capacity. Path 1 refers to the metal-to-polymer contact interface between the sealing ring and the polymeric

sheath of the flexible pipe. This path involves complex interactions such as elastic–plastic deformation and nonlinear contact. The contact pressure is lower than in path 1, so leaks are more likely to occur through this path.

2.2. Sealing Criteria

Sealing can be either dynamic or static. The contact sealing between the sealing ring and the polymeric material in the inner layer of the flexible pipe is a type of static sealing [27]. In engineering applications, the performance of this type of sealing is evaluated by comparing the contact pressure and the length of the two contact surfaces. To obtain good sealing capacity, it is necessary to achieve a relatively large contact pressure, and so the length of the contact surface should be as long as possible. Of course, the premise is that the physical properties of the material itself cannot be destroyed.

For the sealing to remain valid, the contact pressure of the sealing path must be greater than the critical failure pressure. However, calculating the critical failure pressure is complicated, and the influence of the material and the medium should be considered. In a previous study [22], the nominal critical failure pressure was expressed as

$$p_c = \alpha p_f + (1 - \alpha)\sigma_\gamma \tag{1}$$

where p_c is the critical failure pressure and p_f is the fluid pressure in the sealing system, σ_Y is the smaller yield stress of the two materials in contact, and α is the ratio of the length of the fluid infiltrating into the contact surface to the length of the contact path. However, in practical applications, the geometry and roughness of the contact surface exert significant influences, so this formula is not exact.

In this study, to simulate the real process of fluid intrusion, a pressure penetration module was employed in the FE software [28,29]. The loading principle of the pressure penetration criteria is illustrated in Figure 3. On the two contact surfaces, the surface with elements 3 and 4 is defined as the master surface, and that with elements 1 and 2 is defined as the slave surface. Nodes 11 and 12 belong to element 1 on the side of the contact surface.

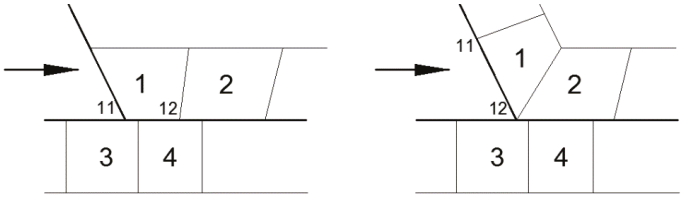

(**a**) Initial loading (**b**) Critical loading

Figure 3. Pressure penetration criteria diagram.

As shown by the arrows in this figure, when the fluid penetrates from left to right, the fluid pressure load will be applied normal to the surface from left to right. Node 11 is the first node exposed to the fluid pressure. If the contact pressure of node 11 is higher than the applied fluid pressure, the pressure penetration stops and node 11 becomes the critical node for the contact pressure (Figure 3a). If the contact pressure of node 11 is less than the fluid pressure, the pressure penetration will continue to load along the contact surface until a new critical contact pressure node is reached (Figure 3b). In addition, if no critical node exists, the contact path cannot provide the sealing capacity under this fluid pressure. The application of pressure penetration can identify the critical node dynamically along the path and determine whether the sealing capacity is sufficient [30].

2.3. Thermal Sealing Analysis

High temperatures will lead to thermal expansion and material deformation, which will change the contact behavior and affect the sealing performance [31]. However, in previous studies on the

sealing performance of end fittings, temperature has seldom been taken into account. Over recent years, operating temperatures and pressures have risen as water depths have continued to increase, making the design, manufacture, and installation of flexible pipe a complex challenge. Therefore, the thermal sealing performance at different temperatures is investigated in this paper. Changes in temperature should follow the basic thermal conduction equation. According to the law of conservation of energy, this can be calculated as follows [32]:

$$\rho c \frac{\partial \theta}{\partial t} = \frac{\partial}{\partial x}(\mathrm{k}\frac{\partial \theta}{\partial x}) + q(x,t) \tag{2}$$

At the same time, the FE method has the ability to model heat transfer with convection. Based on the work of Yu and Heinrich [33,34], the formulation can be obtained by the following expression:

$$\int \delta\theta\left[\rho c\left\{\frac{\partial \theta}{\partial t} + V \cdot \frac{\partial \theta}{\partial x}\right\} - \frac{\partial}{\partial x} \cdot \left(k \cdot \frac{\partial z}{\partial x}\right) - q\right] dV + \int_{Sq} \partial\theta\left[n \cdot k \cdot \frac{\partial \theta}{\partial x} - q_s\right] dS = 0 \tag{3}$$

where $c(\theta)$ is the specific heat capacity of the fluid, $\rho(\theta)$ is the fluid density, $\theta(x, t)$ is the temperature at a spatial position x at time t, $k(\theta)$ is the conductivity of the fluid, $q(x, t)$ is the heat added per unit volume from external sources, $\delta\theta(x, t)$ is an arbitrary variational field, q_s is the heat flowing into the volume across the surface on which the temperature is not prescribed (S_q), and n is the outward normal to the surface.

The boundary condition of this thermal equilibrium equation is that $\theta(x)$ is prescribed over some part of the surface S_θ, and that the heat flux per unit area entering the domain across the rest of the surface, $q_s(x)$, is defined by convection or radiation conditions. In the conditions considered in this study, the boundary term in the equation defines

$$q_s = -n \cdot k \cdot \frac{\partial \theta}{\partial x} \tag{4}$$

This implies that q_s is the flux associated with conduction across the surface only; any convection of energy across the surface is not included in q_s.

2.4. Mechanical Analysis

Based on the analysis of the flexible pipe end fitting sealing structure in the preceding section, the polymeric sheath is squeezed between the inner sleeve and the end fitting body when assembled. Thus, in the FE model, the axial degrees of freedom at both ends of the polymeric sheath are restrained to prevent axial motions, but radial free expansion and contraction are not affected. When variations in temperature lead to thermal deformation of the polymeric sheath, the expansion can only happen in the radial direction. In previous studies on the deformation of polymeric material [27], the radial deformation of the seal can be calculated by converting the deformation in the axial direction to a deformation in the radial direction. Based on the principle of volume invariance, the deformation relation between the radial direction and the axial direction for a cylinder specimen can be described as

$$\frac{\pi d^2}{4}(l + \Delta l) = \frac{\pi(d + \Delta d)^2}{4} l \tag{5}$$

where d is the diameter of the cylinder specimen before the deformation, l is the length of the cylinder specimen before deformation, and Δd and Δl are the radial and axial increments, respectively, of the cylinder specimen after deformation.

3. FE Modeling Procedures

Considering the geometry and axisymmetric load characteristics of the sealing system, a two-dimensional plane axisymmetric solid model is employed to predict the seal performance. This section describes a thermal coupling sealing structure model of a flexible pipe with a design pressure of 20 MPa. This model was developed using FE with the ABAQUS software. Note that the factory acceptance test pressure is 1.5 times the design pressure, so the critical pressure acting on the end fitting is 30 MPa in service [12]. The model comprises the inner sleeve, polymeric sheath, sealing ring, and end fitting body, from inside to outside. The inner and outer diameters of the flexible pipe are 139.7 mm and 209.5 mm, respectively, and the thickness of the polymeric sheath is 5 mm. The basic physical properties of each component are listed in Table 1.

Table 1. Materials and properties for each part of the model.

Component	Young's Modulus (GPa)	Poisson's Ratio	Yield Strength (MPa)
End fitting body	210	0.3	355
inner sleeve	210	0.3	355
Sealing ring	191	0.3	758
Polymeric sheath	0.571	0.45	20.74

In addition, the polymeric sheath of the flexible pipe is usually made from high-molecular-weight polymeric materials, such as high-density polyethylene (HDPE) [35]. In this study, the polymeric material parameters were taken from the work of Malta and Martins [36], and the elastic–plastic properties are illustrated in Figure 4.

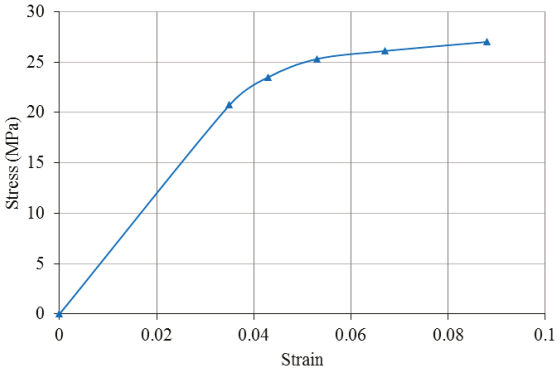

Figure 4. Stress versus strain curve for the polymeric material [36].

To model the incompressible or quasi-incompressible characteristics of these materials, the planar axisymmetric hybrid element CAX4H is selected. Structured and sweep meshing techniques are used in each part of the model, and the mesh is refined around the contact area to improve the accuracy of the simulation. Because of the nonlinear contact characteristics of metallic and polymeric materials, the Mohr-Coulomb friction criterion is employed to describe the contact relationship (i.e., normal contact is "hard" and tangential contact incurs a penalty under a friction coefficient of 0.1) [37].

To simulate the sealing process of the sealing ring, full constraints are applied to the inner sleeve, end fitting body, and polymeric sheath of the flexible pipe, while the sealing ring is free to undergo axial displacement. Pressure penetration is then applied to predict the effectiveness of the sealing. When analyzing the parameter sensitivity of the sealing structure, a temperature field is applied to the model. In addition, an implicit solver is used to obtain improved solution convergence and performance. The FE model of the sealing structure is illustrated in Figure 5.

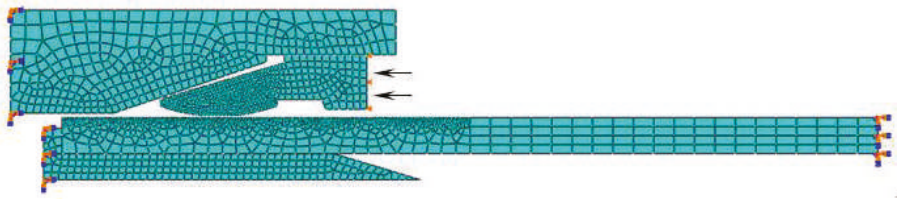

Figure 5. Description of the finite element (FE) model.

4. Results and Discussion

4.1. Simulation of Sealing Principle

According to the design specifications and assembly requirements of the end fitting, axial displacement is applied to the sealing ring to achieve an interference fit. In this section, the von Mises stress and the contact pressure of the model are investigated to analyze the sealing performance of the sealing structure. The von Mises stress distribution of the sealing structure after assembly at 20 °C is shown in Figure 6.

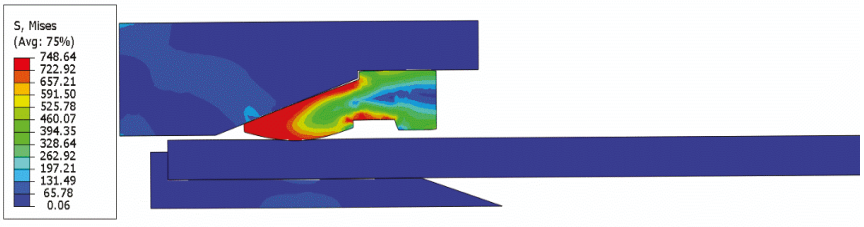

(**a**) Von Mises stress in the seal region

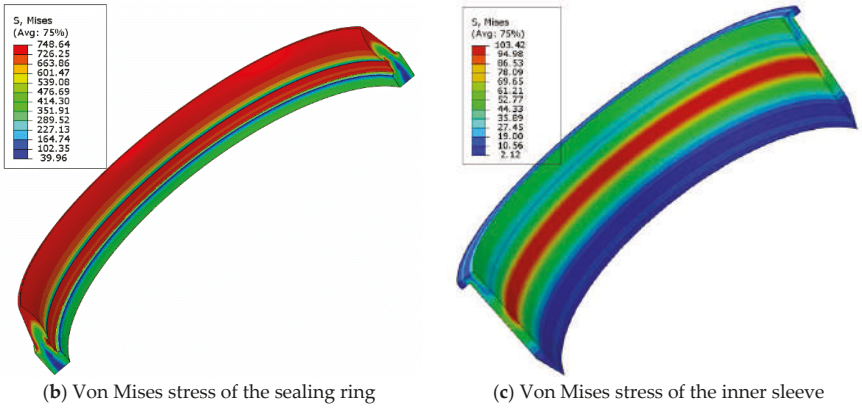

(**b**) Von Mises stress of the sealing ring (**c**) Von Mises stress of the inner sleeve

Figure 6. Von Mises stress distribution of the FE model.

As can be seen from Figure 6a, the von Mises stress of the model is mainly concentrated on the wedge sealing ring, and so the stress of the inner sleeve and the end fitting body is relatively small. The closer to the tip of the sealing ring, the greater the von Mises stress, because the tip is subjected to a greater pressure. A three-dimensional von Mises stress contour distribution of the sealing ring, obtained by rotating the planar sealing ring, is shown in Figure 6b. The maximum von Mises stress of the wedge sealing ring is 748.6 MPa in the FE model, which does not exceed the yield stress of the material. This shows that no plastic deformation occurs in the sealing ring and the property of the material itself is not destroyed. In addition, some stress concentration occurs in the contact area of

the inner sleeve (as shown in Figure 6c), but the maximum stress is still less than the yield stress of the material.

To clarify the characteristics of the contact pressure distribution in the sealing structure, the three-dimensional contact pressure contour distribution of the FE model is presented in Figure 7. On the polymeric sheath of the flexible pipe, some contact pressure occurs on the outer side of the contact region, although the contact pressure on the inner side is lower. For the sealing ring, the contact pressure is higher on the outer interface close to the end fitting body (i.e., path 2), whereas the contact pressure is lower on the inner interface close to the polymeric sheath (i.e., path 1). This may be caused by the property of the materials along the contact paths.

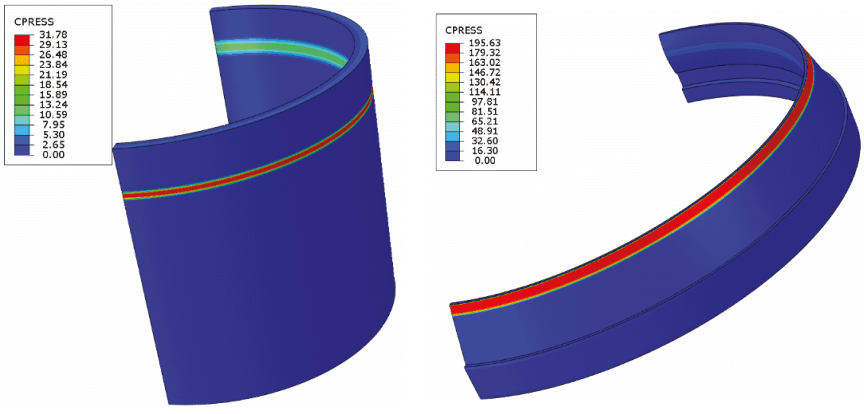

(**a**) Contact pressure of the polymeric sheath (**b**) Contact pressure of the sealing ring

Figure 7. Contact analysis of the sealing structure.

Based on the FE model of the sealing structure, the contact pressure distributions on the nodes along the two paths were obtained. They are illustrated in Figure 8. The maximum contact pressure along path 1 is 31.74 MPa, which is slightly greater than the test pressure of 30 MPa. The maximum contact pressure along path 2 is 195.6 MPa, which is much larger than the design pressure and test pressure of the end fitting. This indicates that there will be no seal leakage along this path, which is consistent with the results of previous works [22,23]. Hence, we focus on path 1 in the following analysis.

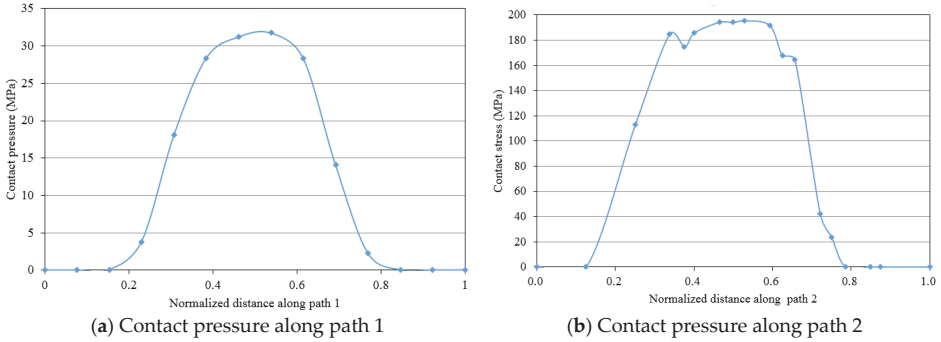

(**a**) Contact pressure along path 1 (**b**) Contact pressure along path 2

Figure 8. Comparison of the sealing performance along the two paths.

4.2. Analysis of Pressure Penetration

The pressure penetration criteria can be applied to evaluate the sealing capacity of the sealing assembly. According to the design pressure and the maximum test pressure of the end fitting, the sealing performance of the sealing structure along path 1 was analyzed at fluid pressures of 20, 30, and 40 MPa at a temperature of 20 °C. The contact pressure on the polymeric sheath reflects the variation in the pressure penetration, and Figure 9 shows the contact pressure of the polymeric sheath under the different fluid pressures. With an increase in fluid pressure, the contact pressure on one side of the inner surface of the polymeric sheath increases, whereas the pressure on the outer surface gradually decreases. This is because when the fluid acts along path 1, the contact surface between the sealing ring and the polymeric sheath is continuously penetrated by the pressure, causing these components to separate from each other. On the contrary, the contact surface between the sheath and the inner sleeve is squeezed and shrunken along the radial direction.

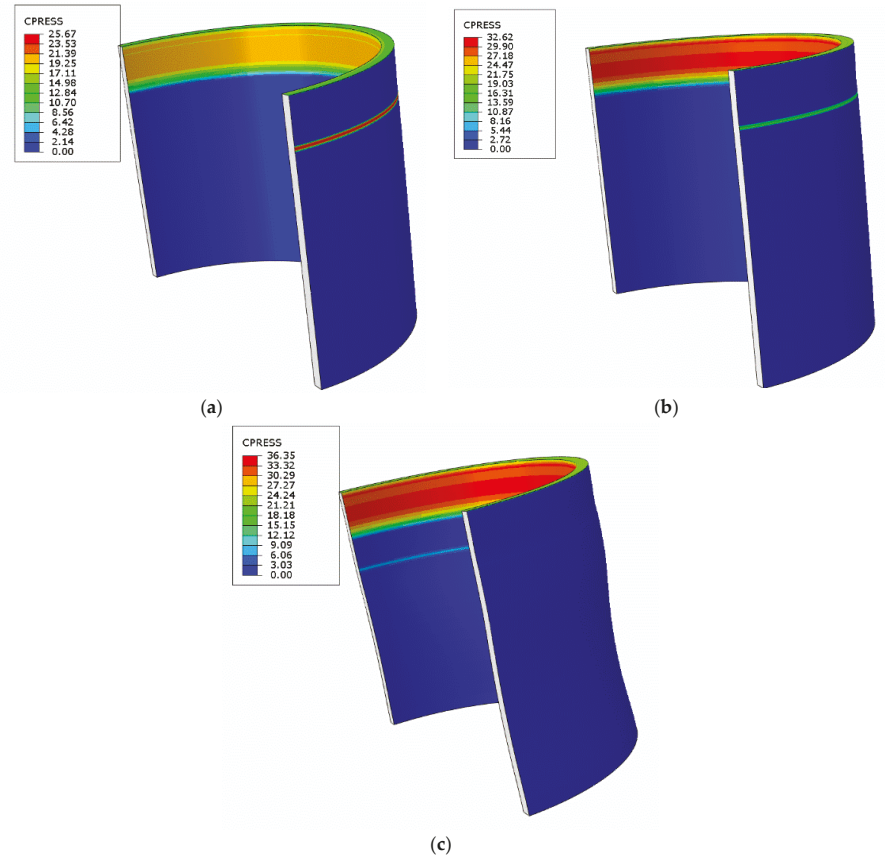

Figure 9. Contact pressure of polymeric sheath under different fluid pressures: (**a**) 20 MPa; (**b**) 30 MPa; (**c**) 40 MPa.

Figure 10 shows the contact pressure distribution of the nodes along path 1. When no pressure penetration is applied, the maximum contact pressure is 31.7 MPa. At fluid pressures of 20 and 30 MPa, the maximum contact pressure and contact length decrease, and the pressure distribution moves to

the right. At this time, the existence of the contact pressure indicates that no leakage will occur in the sealing structure.

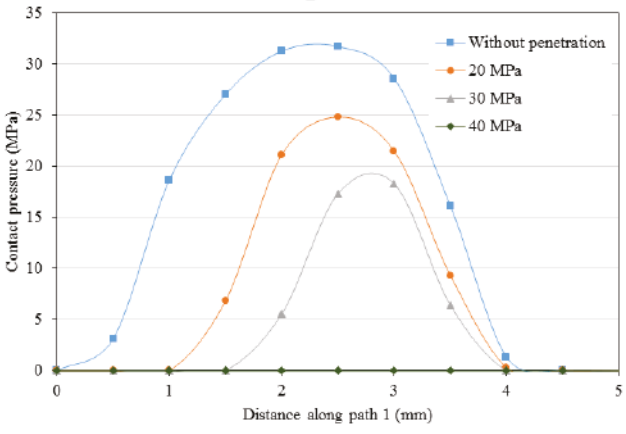

Figure 10. Contact pressure under different fluid pressure.

When the fluid pressure is 40 MPa, the contact pressure along path 1 becomes 0 MPa, which indicates that the fluid pressure is too high, and the sealing structure fails. As shown in Figure 9, the fluid leakage through this path flows around the annulus of the flexible pipe, acting to compress the polymeric sheath and make it collapse. In addition, leakage accidents may occur if the sealing structure fails. It should be emphasized that, after many simulation calculations and predictions, the sealing structure was found to leak at a fluid pressure of 35.5 MPa. In other words, the critical fluid pressure of the sealing structure in this study is 35.5 MPa.

4.3. Analysis of the Thermal Sealing

Under the actual working conditions of flexible pipe end fittings, the hydrocarbon products transported along the pipe can reach high temperatures, so thermal effects in the sealing structure cannot be ignored. This section reports the changes in sealing performance of the sealing structure under temperature fields of 20, 50, 60, 70, and 80 °C in the model [38].

Compared with metallic materials, the polymeric materials in the flexible pipe will be more strongly influenced by temperature. Therefore, after applying different temperature fields to the FE model of the sealing structure, the contact pressure distributions of the polymeric sheath were recorded (as shown in Figure 11). From the perspective of deformation, an increase in temperature deforms the polymeric sheath and causes the flexible pipe to expand. Regarding the contact pressure along path 1, as the temperature increases from 20–80 °C, the maximum contact pressure increases from 31.7–41.3 MPa—a rise of 30% (as shown in Figure 12). In addition, the contact length increases because the material expands at higher temperatures, increasing the number of contactable nodes.

From the results in Table 2, the maximum von Mises stress of the model exhibits a continuous increase, becoming close to the yield strength of the material at 80 °C. The contact pressures along the two paths gradually increase, which indicates that the sealing capacity is also increasing. In summary, thermal effects can enhance the sealing performance, but the temperature should not exceed the rated temperature of the material, otherwise failure will occur.

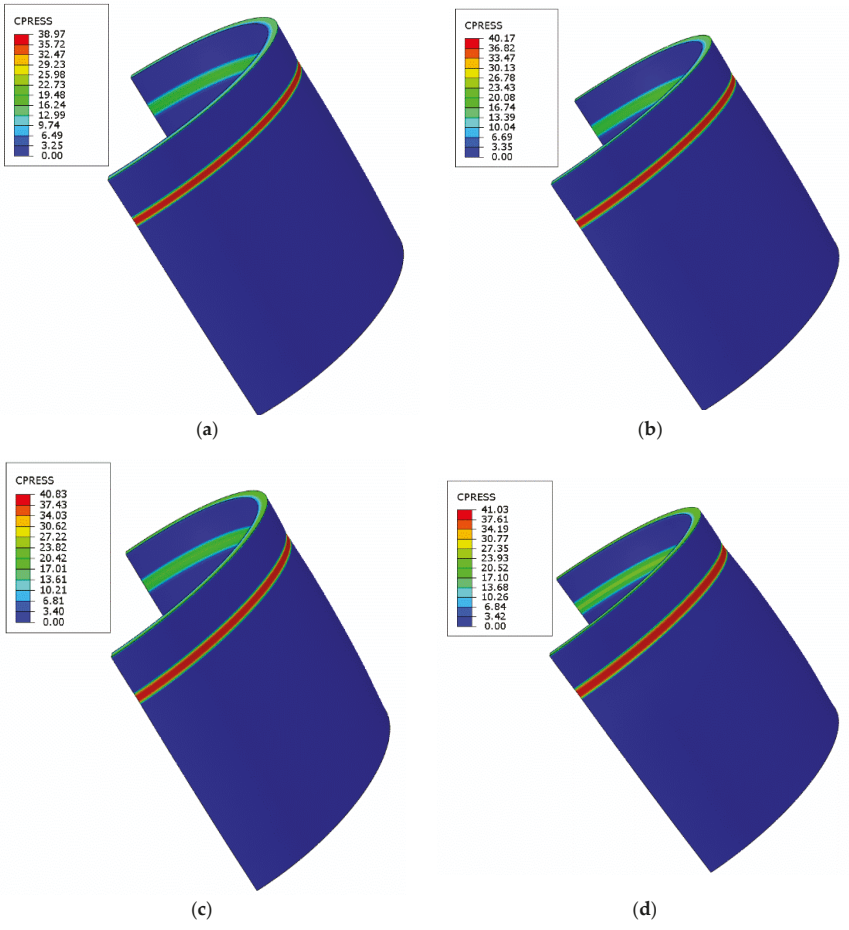

Figure 11. Contact pressure distribution of the polymeric sheath: (**a**) 50 °C; (**b**) 60 °C; (**c**) 70 °C; (**d**) 80 °C.

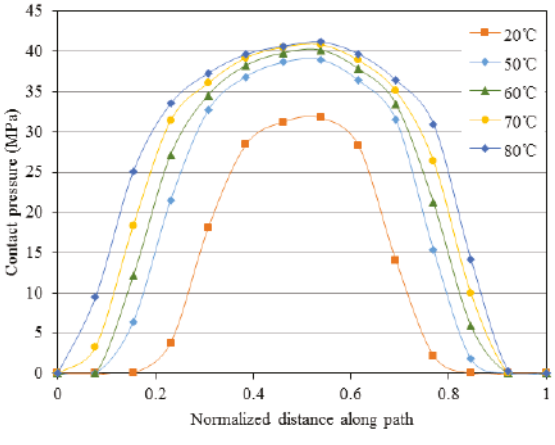

Figure 12. Contact pressure along path 1.

Table 2. Results of the FE model at different temperatures.

Temperature (°C)	20	50	60	70	80
Von Mises stress (MPa)	748.6	750.1	751.6	753.7	756.8
Contact pressure in path 1 (MPa)	31.7	38.9	40.1	40.8	41.3
Contact pressure in path 2 (MPa)	195.6	199.7	227.3	229.4	234.5

5. Conclusions

A classical unbonded flexible pipe is a combination of polymeric and metallic layers. An end fitting with reliable sealing properties is a precondition of a successful flexible pipe application. In this study, a hydraulic-thermal FE model was developed to investigate the sealing performance of a flexible pipe end fitting. The FE model employed the pressure penetration criterion and considered the temperature field, which is suitable for real applications. Using this model, the sealing principle was simulated and the influence of thermal effects on the sealing capacity was investigated.

The results showed that the maximum von Mises stress occurs on the sealing ring during the sealing process, whereas the stresses on the other components are relatively small. In terms of the contact pressure distribution, the maximum value appears in the sealing region, and is higher along path 2. By introducing pressure penetration, the sealing performance could be predicted and the dynamical pressure critical node was identified. In the model described in this paper, the critical fluid pressure of the end fitting is 35.5 MPa, which means that leakage occurs when the working pressure exceeds this value. In previous studies, thermal effects were usually omitted. The results in this paper, however, show that temperature is an important factor in the sealing performance of the sealing assembly, and should not be neglected. Thermal effects cause the components of the sealing structure to deform and expand. By increasing the contact length and contact pressure, the sealing ability of the sealing structure can be improved. Of course, very high temperatures are not appropriate, because the strain on the sealing ring should be considered in actual applications.

Author Contributions: L.T. contributed significantly to analysis and manuscript writing; W.H. performed the numerical simulation and data analyses; X.Z. contributed to the conception of the investigation; Y.Z. helped perform the analysis with constructive discussions.

Funding: This research was funded by the China Postdoctoral Science Foundation (43XB3793XB), National Key Research and Development Program (2018YFC0310204), National Natural Science Foundation of China (No. 51674214), and Scientific Innovation Group for Youths of Sichuan Province (No. 2019JDTD0017). And The APC was funded by National Key Research and Development Program (2018YFC0310204).

Conflicts of Interest: This article does not involve conflicts of interest.

References

1. Moan, T.; Amdahl, J.; Ersdal, G. Assessment of ship impact risk to offshore structures-New NORSOK N-003 guidelines. *Mar. Struct.* **2019**, *63*, 480–494. [CrossRef]
2. Yang, C.K.; Kim, M.H. Numerical assessment of the global performance of spar and FPSO connected by horizontal pipeline bundle. *Ocean Eng.* **2018**, *159*, 150–164. [CrossRef]
3. Zhang, J.M.; Li, X.S.; Chen, Z.Y.; Zhang, Y.; Li, G.; Yan, K.F.; Lv, T. Gas-Lifting characteristics of methane-water mixture and its potential application for self-eruption production of marine natural gas hydrates. *Energies* **2018**, *11*, 240. [CrossRef]
4. Guha, I.; White, D.J.; Randolph, M.F. Subsea pipeline walking with velocity dependent seabed friction. *Appl. Ocean Res.* **2019**, *82*, 296–308. [CrossRef]
5. Zhang, P.; Huang, Y.F.; Wu, Y. Springback coefficient research of API X60 pipe with dent defect. *Energies* **2018**, *11*, 3213. [CrossRef]
6. Paiva, L.F.; Vaz, M.A. An empirical model for flexible pipe armor wire lateral buckling failure load. *Appl. Ocean Res.* **2017**, *66*, 46–54. [CrossRef]

7. Anderson, T.A.; Vermiyea, M.E.; Dodds, V.J.N.; Finch, D.; Latto, J.R. Qualification of flexible fiber-reinforced pipe for 10,000-foot water depths. In Proceedings of the Offshore Technology Conference, Houston, TX, USA, 6–9 May 2013.
8. Pham, D.C.; Sridhar, N.; Qian, X.; Sobey, A.J.; Achintha, M. A review on design, manufacture and mechanics of composite risers. *Ocean Eng.* **2016**, *112*, 82–96. [CrossRef]
9. Dahl, C.S.; Andersen, B.; Groenne, M. Developments in managing flexible risers and pipelines, a suppliers perspective. In Proceedings of the Offshore Technology Conference, Houston, TA, USA, 2–5 May 2011.
10. Ebrahimi, A.; Kenny, S.; Hussein, A. Radial buckling of tensile armor wires in subsea flexible pipe—Numerical assessment of key factors. *ASME J. Offshore Mech. Arct. Eng.* **2016**, *138*, 031701. [CrossRef]
11. Drumond, G.P.; Geovana, P.; Pasqualino, I.P.; Pinheiro, B.C.; Estefen, S.F. Pipelines, risers and umbilicals failures: A literature review. *Ocean Eng.* **2017**, *148*, 412–425. [CrossRef]
12. API 17B. *Recommended Practice for Flexible Pipe*, 5th ed.; American Petroleum Institute: Washington, DC, USA, 2014.
13. Campello, G.C.; Sousa, J.R.M.; Vardaro, E. An analytical approach to predict the fatigue life of flexible pipes inside end fittings. In Proceedings of the Offshore Technology Conference, Houston, TX, USA, 2–5 May 2016.
14. Fernando, U.S.; Nott, P.; Graham, G.; Roberts, A.E.; Sheldrake, T. Experimental evaluation of the metal-to-metal seal design for high-pressure flexible pipes. In Proceedings of the Offshore Technology Conference, Houston, TX, USA, 30 April–3 May 2012.
15. Hatton, S.; Rumsey, L.; Biragoni, P.; Roberts, D. Development and qualification of end fittings for composite riser pipe. In Proceedings of the Offshore Technology Conference, Houston, TX, USA, 6–9 May 2013.
16. Peng, G.; Zhang, Z.; Li, W. Computer vision algorithm for measurement and inspection of O-rings. *Measurement* **2016**, *94*, 828–836. [CrossRef]
17. Liu, X.; Li, G.; Yue, Q.; Oberlies, R. Acceleration-oriented design optimization of ice-resistant jacket platforms in the Bohai Gulf. *Ocean Eng.* **2009**, *36*, 1295–1302. [CrossRef]
18. Tang, M.; Lu, Q.; Yan, J.; Yue, Q. Buckling collapse study for the carcass layer of flexible pipes using a strain energy equivalence method. *Ocean Eng.* **2016**, *111*, 209–217. [CrossRef]
19. Cour, D.; Kristensen, C.; Nielsen, N.J.R. Managing fatigue in deepwater flexible risers. In Proceedings of the Offshore Technology Conference, Houston, TX, USA, 5–8 May 2008.
20. Li, X.; Jiang, X.; Hopman, H. A review on predicting critical collapse pressure of flexible risers for ultra-deep oil and gas production. *Appl. Ocean Res.* **2018**, *80*, 1–10. [CrossRef]
21. Wang, L.Q.; Wei, Z.L.; Yao, S.M.; Guan, Y.; Li, S.K. Sealing performance and optimization of a subsea pipeline mechanical connector. *Chin. J. Mech. Eng.* **2018**, *31*, 1–14. [CrossRef]
22. Fernando, U.S.; Karabelas, G. Analysis of end fitting barrier seal performance in high pressure un-bonded flexible pipes. In Proceedings of the 33rd ASME International Conference on Ocean, Offshore and Arctic Engineering, San Francisco, CA, USA, 8–13 June 2014.
23. Li, X.; Du, X.; Wan, J.; Xiao, H. Structure analysis of flexible pipe end fitting seal system. In Proceedings of the 34th ASME International Conference on Ocean, Offshore and Arctic Engineering, St John's, NL, Canada, 31 May–5 June 2015.
24. Zhang, L.; Yang, Z.; Lu, Q.; Yan, J.; Chen, J.; Yue, Q. Numerical simulation on the sealing performance of serrated teeth inside the wedgy sealing ring of end fitting of marine flexible pipeline. *Oil Gas Storage Transp.* **2017**, *37*, 108–115. (In Chinese)
25. Marion, A.; Rigaud, J.; Werth, M.; Martin, J. γ-Flex®: A new material for high temperature flexible pipes. In Proceedings of the Offshore Technology Conference, Houston, TX, USA, 6–9 May 2002.
26. API 17J. *Specification for Un-Bonded Flexible Pipe*, 4th ed.; American Petroleum Institute: Washington, DC, USA, 2014.
27. Yan, H.; Zhao, Y.; Liu, J.; Jiang, H. Analyses toward factors influencing sealing clearance of a metal rubber seal and derivation of a calculation formula. *Chin. J. Aeronaut.* **2016**, *29*, 292–296. [CrossRef]
28. Gorash, Y.; Dempster, W.; Nicholls, W.D.; Hamilton, R. Fluid pressure penetration for advanced FEA of metal-to-metal seals. *Proc. Appl. Math. Mech.* **2015**, *15*, 197–198. [CrossRef]
29. Zhao, B.; Zhao, Y.; Wu, X.; Xiong, H. Sealing performance analysis of P-shape seal with fluid pressure penetration loading method. *IOP Conf. Ser. Mater. Sci. Eng.* **2018**, *397*, 012126. [CrossRef]

30. Slee, A.J.; Stobbart, J.; Gethin, D.T.; Hardy, S.J. Case study on a complex seal design for a high pressure vessel application. In Proceedings of the ASME Pressure Vessels and Piping Conference, Anaheim, CA, USA, 20–24 July 2014.
31. Wang, B.; Peng, X.; Meng, X. A thermo-elastohydrodynamic lubrication model for hydraulic rod O-ring seals under mixed lubrication conditions. *Tribol. Int.* **2019**, *129*, 442–458. [CrossRef]
32. Deng, D.; Zhang, C.; Pu, X.; Liang, W. Influence of material model on prediction accuracy of welding residual stress in an austenitic stainless steel multi-pass buttwelded joint. *J. Mater. Eng. Perform.* **2017**, *26*, 1494–1505. [CrossRef]
33. Yu, C.; Heinrich, J. Petrov-Galerkin methods for the time-dependent convective transport equation. *Int. J. Numer. Meth. Eng.* **1986**, *23*, 883–902. [CrossRef]
34. Yu, C.; Heinrich, J. Petrov-Galerkin method for multidimensional, time-dependent, Convective-Diffusive equations. *Int. J. Numer. Meth. Eng.* **1987**, *24*, 2201–2215. [CrossRef]
35. Yu, R.; Yuan, P. Structure and research focus of marine un-bonded flexible pipes. *Oil Gas Storage Transp.* **2016**, *35*, 1255–1260. (In Chinese)
36. Malta, E.; Martins, C. Finite element analysis of flexible pipes under axial compression: Influence of the sample length. *ASME J. Offshore Mech. Arct. Eng.* **2017**, *139*, 011701. [CrossRef]
37. Cuamatzi-Melendez, R.; Castillo-Hernandez, O.; Vazquez-Hernandez, A.O.; Vaz, M.A. Finite element and theoretical analyses of bisymmetric collapses in flexible risers for deepwaters developments. *Ocean Eng.* **2017**, *140*, 195–208. [CrossRef]
38. Pethrick, R.A.; Banks, W.M.; Brodesser, M. Ageing of thermoplastic umbilical hose materials used in a marine environment 1-Polyethylene. *Proc. Inst. Mech. Eng. Part L J. Mater. Des. Appl.* **2014**, *228*, 45–62. [CrossRef]

energies

MDPI

Article

An Assessment of Wind Energy Potential in the Caspian Sea

Florin Onea and Eugen Rusu *

Department of Mechanical Engineering, Faculty of Engineering, Dunarea de Jos University of Galati, 47 Domneasca Street, 800008 Galati, Romania

* Correspondence: eugen.rusu@ugal.ro; Tel.: +40-740-205-534

Received: 10 June 2019; Accepted: 25 June 2019; Published: 1 July 2019

Abstract: At this time, there are plans to develop offshore wind projects in the Caspian Sea. The aim of the present work was to estimate the possible benefits coming from such a project. As a first step, the wind profile of this region was established by considering reanalysis data coming from the ERA-Interim project, the time interval covered being between January 1999 and December 2018. According to these results, significant resources have been noticed in the northern part where the wind speed frequently reached 8 m/s, being identified also as a hot-spot south of Olya site. In the second part, the performances of some offshore wind turbines were established. These were defined by rated capacities ranging from 3 MW to 8.8 MW. The downtime period of some generators can reach 90% in the central and southern sectors, while for the capacity factor, the authors expected a maximum of 33.07% for a turbine rated at 4.2 MW. From a financial point of view, the values of the levelized cost of energy (LCOE) indicated that the sites from the north and central parts of the Caspian Sea have been defined by an average LCOE of 0.25 USD/kWh. Thus, they can represent viable locations for wind farm projects.

Keywords: Caspian Sea; wind speed; offshore turbines; capacity factor; LCOE

1. Introduction

The wind energy market is a dynamic sector that is continuously expanding. Nevertheless, this evolution will finally reach saturation, taking into account that the range of suitable sites for such projects will reduce. As an alternative, one of the best locations to develop a wind project is near the coastal areas, which can easily support the development of either onshore and offshore projects. At this time, there is growing interest to develop systems capable of operating in deep water areas, the floating platforms being the most viable solution [1,2]. A significant percentage of the projects have operated in Europe (almost 409 projects), being estimated that in 2018, only 18 projects were added to the grid. Per total, the operating projects are defined by a capacity of 18.5 GW, this value being supported by 11 countries, such as UK, Germany, Denmark, Norway or Portugal, as being more relevant. One of the largest wind turbines connected at this moment is the Haliade 150-6 MW (Merkur project, Germany), with the mention that some other projects currently under construction may include systems defined by comparable capacity, or even higher [3].

Most of the research is focused on the coastal areas facing the ocean environment [4–6], since the wind resources are more consistent in such areas. During recent years, the enclosed sea basins were also considered for investigation [7–9]. More advanced progress is related to the Mediterranean Sea, where a pilot farm of 24.8 MW will be developed off the coast of Gruissan in the Aude region, France. It is expected that through four wind turbines, it is possible to generate approximately 100 million kWh/year, which should be enough to cover the annual electricity consumption of more than 50,000 inhabitants [10]. Other sources indicate that a 30 MW wind project will be installed in front

of the Taranto Harbour, Puglia, Southern Italy, which will consider ten wind turbines produced by Senvion [11]. The French coastal area located in this region seems to present important wind resources, and the implementation of several floating projects is expected in the near future [12].

As for the Caspian Sea wind resources, there is some research focused in this aspect. In the research by Amirinia et al [13], the distribution of the wind and wave resources associated to the southern area was evaluated. By considering various databases (including in-situ measurements) and the characteristics of a 3 MW wind turbine, it was found that more promising results have been reported in the eastern part of this region. In Rusu and Onea [8], the wind and wave regime from this region were also assessed, and more energetic conditions in the centre and northern regions were observed, with an average wind speed of 6 m/s (at 80 m height). In addition, observations of the bathymetric map of the Caspian Sea highlight that the entire northern area is defined by a lower water depth, which is very suitable for the development of the wind projects. In Onea and Rusu [14], the performances of some wind turbines that may operate in the coastal areas of the Black and Caspian seas were discussed. The turbines were reported to an operating hub height of 80 m, while the power output of the particular systems were estimated using a Betz coefficient of 0.5. By applying these simplifications, it appears that the performances of some wind turbines have been overestimated, resulting in capacity factors of 70%, compared to the usual capacity factor values between 20 and 40%. An important aspect, which is highlighted in this work, is related to the diurnal and nocturnal fluctuations of the wind conditions. Kerimov et al [15] analysed the long term distribution of wind resources, also proposed some suitable sites, and evaluated the associated costs required to couple some wind generators to the electrical grid. According to these results, one of the best sites to implement an offshore wind project is located in the northern part of Absheron peninsula (Azerbaijan). Here, a suitable connection grid was also identified. Although, this region is an enclosed sea defined by moderate conditions, there is some research focused on the local wave resources that brings into discussion the viability of a commercial wave farm in this environment, especially considering hybrid wind-wave approaches [16–18].

On the other hand, it is well known that the Caspian Sea region is defined by important oil reserves and therefore, at this time, it seems that the interest for a renewable project is not very high [19]. Nevertheless, taking into account that there are problems with the oil pollution in this region [20,21], some changes are expected to occur. Thus, at this moment there are plans to develop a 200 MW offshore wind farm in the coastal areas of Azerbaijan, which will significantly increase the existing wind capacity (66.7 MW) of this country. It is estimated that the project will cost 392 million euro. This is one of the multiple wind parks proposed for this area, and more likely will be developed close to the capital, Baku [22,23].

In this context, the objective of the present work is to provide a more complete picture of the wind resources in the Caspian Sea in order to identify some suitable sites for the development of a wind project, and also to establish the performances of some state-of-the-art wind turbines that may operate in the vicinity of some major cities from this region.

2. Materials and Methods

2.1. The Target Area

Figure 1 presents a first perspective of the Caspian Sea. Thus, Figure 1a,b presented the distribution of the water depth, in general, and for the reference sites considered for evaluation. Regarding the northern sector, this is defined by lower water depths that do not exceed 50 m, compared to the southern side, where the water depth values easily reach 500 m, and even higher, if the Nowshahr site as a reference is considered. Several distances from the shoreline are taken into account (5 km, 25 km and 50 km) in order to identify the variations from the nearshore to offshore. Furthermore, in Table 1 the characteristics of the sites located near the shore are presented. A total of 10 reference sites are considered for evaluation, the main selection criteria being related to the fact that they are important port cities capable of easily offering the infrastructure and technical support for the development of a

wind project. The sites located at 5 km, are defined by lower water depths (<50 m), but going towards the 50 km limit, these values significantly increase. This is the case of the Iranian sites of Babolsar, Nowshahr, Anzali and Astara, where the depths can easily exceed 400 m. The 50 km limit was not arbitrarily selected, and represents an acceptable threshold at which a renewable project can still be competitive [24].

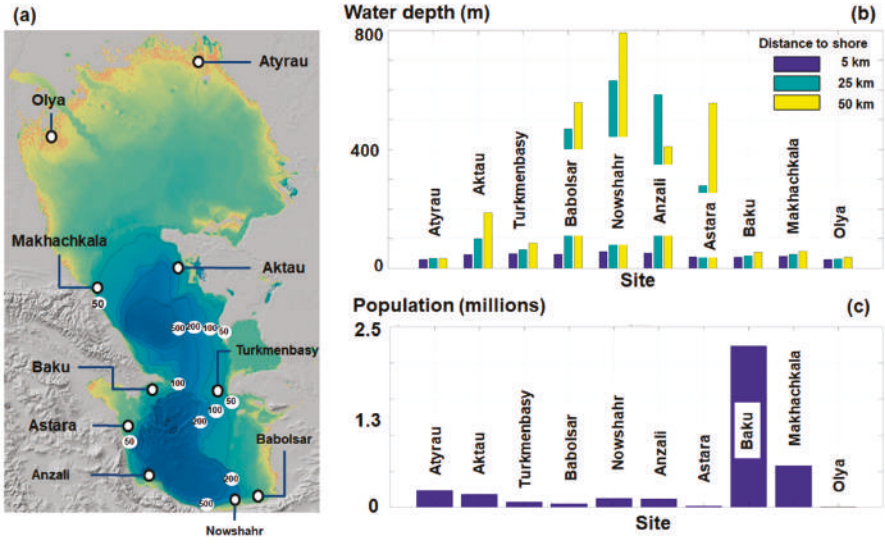

Figure 1. The Caspian Sea and the reference sites considered for assessment, where: (**a**) bathymetry map [25]; (**b**) water depths corresponding to each reference site [25]; (**c**) number of inhabitants corresponding to the reference area considered [26].

Table 1. The main characteristics of the considered sites located at a distance of 5 km from shore.

No.	Site	Country	Long (°)	Lat (°)	Water Depth (m)
P1	Atyrau	Kazakhstan	51.745	46.680	30
P2	Aktau	Kazakhstan	51.101	43.615	46
P3	Türkmenbasy	Turkmenistan	52.714	39.994	50
P4	Babolsar	Iran	52.643	36.759	48
P5	Nowshahr	Iran	51.492	36.705	56
P6	Anzali	Iran	49.512	37.519	52
P7	Astara	Iran	48.938	38.425	38
P8	Baku	Azerbaijan	49.889	40.324	37
P9	Makhachkala	Russia	47.584	42.997	41
P10	Olya	Russia	48.136	45.269	30

The port of Baku is the capital of Azerbaijan and one of the largest cities in the Caucasus, this aspect being reflected by the number of its inhabitants (Figure 1c), of almost 2.5 million, being followed by the Makhachkala city with 0.6 million inhabitants and Atyrau with 0.24 million.

2.2. Wind Dataset

ERA-Interim Reanalysis Data

The ERA-Interim wind product has been considered for assessment, this being a project maintained by the European Center for Medium-Range Weather Forecasts (ECMWF). This global model covers the time interval from 1979 to the present, being defined by a temporal resolution of 6h per day

(00-06-12-18 UTC). In the near future, this model may be replaced by the ERA5 product defined by 1h resolution and some others significant improvements [27,28]. For the present work, only the data covering the 20-year time interval from January 1999 to December 2018 are used, considering a spatial resolution of $0.125° \times 0.125°$ (the highest one). The *U* and *V* components of the wind speed are reported to a 10 m height above the sea level, and in this case, the wind speed is denoted as *U10*. Apart from the assessment of the wind energy potential, another objective of the present work is to estimate the performance of some offshore wind turbines, and therefore the *U10* values need to be adjusted to the hub height of a particular system. This is indicated as [29,30]:

$$U_{turbine} = U10\frac{\ln(z_{turbine}) - \ln(z_{10})}{\ln(z_{10}) - \ln(z_0)} \quad (1)$$

where, $U_{turbine}$—wind speed at hub height, $U10$—initial wind speed (at 10 m), z_0—roughness factor (calm sea surface −0.0002 m), z_{10} and $z_{turbine}$—reference heights.

2.3. Wind Turbines

Several offshore wind turbines are considered for evaluation, their characteristics being presented in Table 2. The rated power of the generators is in the range of 3–8.8 MW, with the systems rated below 6 MW currently in operation, compared to the others that are the next generation turbines and are being implemented at this moment. In general, the cut-in values are approximately 3–3.5 m/s. The system, Adwen AD 5-135, has a lower rated speed value of 11.4 m/s, which means that this turbine will reach his rated capacity quicker. Each turbine is defined by a particular hub height, some of them being specifically indicated by the manufacturers, but in most of the cases these are mentioned as site specific, being possible to develop in this way multiple scenarios. A minimum of 65 m corresponds to the system Vestas V90-3.0 MW, while a maximum value of 140 m corresponds to Vestas V164-8.0 MW.

Table 2. The main characteristics of the wind turbines considered [31].

Turbine	Rated Power (MW)	Cut-in Speed (m/s)	Rated Speed (m/s)	Cut-out Speed (m/s)	Diameter (m)	Hub Height (m)
Vestas V90-3.0	3	3.5	15	25	90	65–105
Vestas V112-3.45	3.45	3	13	25	112	84
Siemens SWT-3.6-120	3.6	3.5	12	25	120	90
Siemens SWT-3.6-107	3.6	4	13.5	25	107	80 or site specific
Siemens SWT-4.0-130	4	5	12	25	130	89.5
Envision EN 136-4.2	4.2	3	10.5	25	136	80/90/110
Areva M5000-116	5	4	12.5	25	116	site specific
Adwen AD 5-135	5.05	3.5	11.4	30	135	site specific
Siemens SWT-6.0-154	6	4	13	25	154	site specific
Senvion 6.2M126	6.15	3.5	14	30	126	85/95
Siemens SG 7.0-154	7	3	13	25	154	site specific
Siemens SG 8.0-167	8	3	12	25	167	site specific
Vestas V164-8.0	8	4	13	25	164	105/140
Vestas V164-8.8	8.8	4	13	25	164	site specific

The annual electricity production (*AEP*) indicator is frequently used to quantify the electricity output expected in a particular system. In the present work, the following expression was considered for this indicator [32]:

$$AEP = T \cdot \int_{cut-in}^{cut-out} f(u)P(u)du \quad (2)$$

where, AEP—in MWh, T—average hours per year (8760 hr/year), $f(u)$—Weibull probability density function, $P(u)$—power curve of a turbine, cut-in and cut-out values of a turbine.

One way to estimate the overall performances of a particular system is through the capacity factor (C_f), that can be defined as [32]:

$$C_f = \frac{P_E}{R_P} \cdot 100, \quad (3)$$

where: P_E is the electric power expected to be generated and R_P represents the rated power of the system.

3. Results

3.1. Verification of the Reanalysis Data

The ERA-Interim data were obtained through numerical simulations and therefore the accuracy of these data for this enclosed sea area need to be discussed. One way is to use the satellite measurements provided by the AVISO (Archiving, Validation and Interpretation of Satellite Oceanographic Data) project that include daily multi-mission measurements [33]. This dataset was defined by only one measurement per day (*U*10 values), and for the current work the values corresponding to the interval January 2010 and December 2017 were processed. Figure 2 presents a direct comparison between AVISO and ERA-Interim data, including a quality check of the satellite measurements. A common problem associated to the altimeter data, has been represented by the accuracy of these systems to measure the marine resources at the land-water interface. As can be seen from Figure 1a, a maximum of 50.46% corresponded to the site of Atyrau, compared to a minimum of 20.76% indicated for Baku, while a constant distribution of 41% was noticed close to the sites Babolsar, Nowshahr and Anzali, respectively.

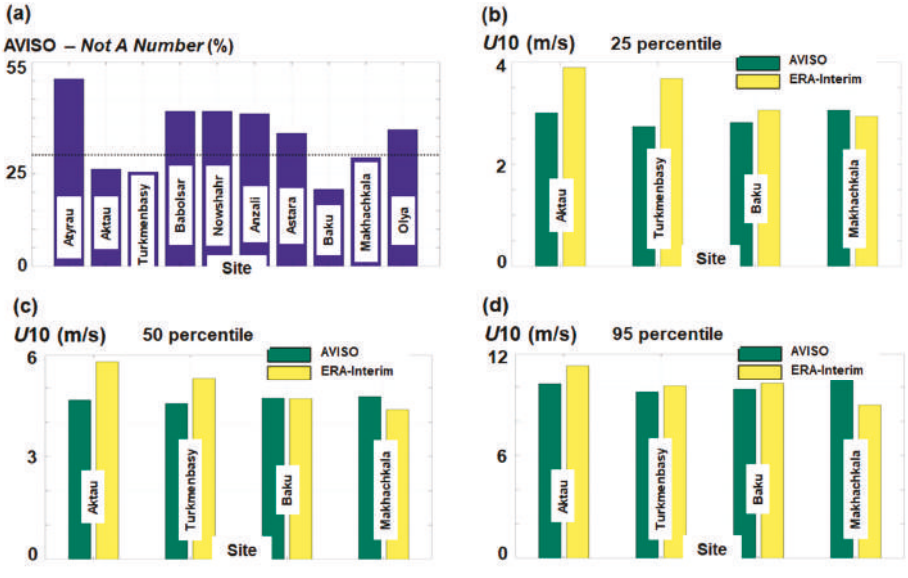

Figure 2. The comparisons between the AVISO measurements and the ERA–Interim reanalysis data for the time interval 2010–2017. The results are structured in: (**a**) NaN corresponding to the AVISO measurements; (**b**) 25 percentile; (**c**) 50 percentile; (**d**) 95 percentile.

In order to compare the two datasets, only the sites defined by much lower NaN (not a number) occurrences were considered for evaluation, and for this work, the ones chosen did not exceed 30% (indicated by dotted line). From the percentile analysis (25, 50 and 95), the ERA-Interim indicated higher values than the satellite measurements, this aspect being valid only for the sites Aktau, Türkmenbasy and Baku located in the eastern and southern sectors. The Aktau site was defined by more significant

variations, and a difference of 0.9 m/s (25 percentile), 1.16 m/s (50 percentile) and 1.12 m/s (95 percentile) was observed. A reverse pattern corresponded to the Makhachkala site (west coast–north of Baku), where ERA-Interim slightly underestimated the wind resources, with a maximum difference of 1.62 m/s for the 95 percentile.

3.2. Analysis of the Wind Speed

A first perspective of the wind distribution is presented in Figure 3, including the full time distribution (denoted as the total time) and the four main seasons that include: spring (March-April-May), summer (June-July-August), autumn (September-October-November) and winter (December-January-February). Regardless the period taken into account, it is clear that the northern part of the Caspian Sea is defined by more important wind resources. For the total time, a maximum value of 8.5 m/s was noticed in the southern regions of Olya site (north-west), and on an axis that crosses the northern area of this basin. The values significantly decreased towards the centre of this target area, the eastern part being defined by more important resources that can reach 6 m/s. The areas located in the centre-west and south seem to be defined by hot-spot regions where the wind conditions frequently indicated values of approximately 2 m/s, which meant that they are not very attractive for a wind project.

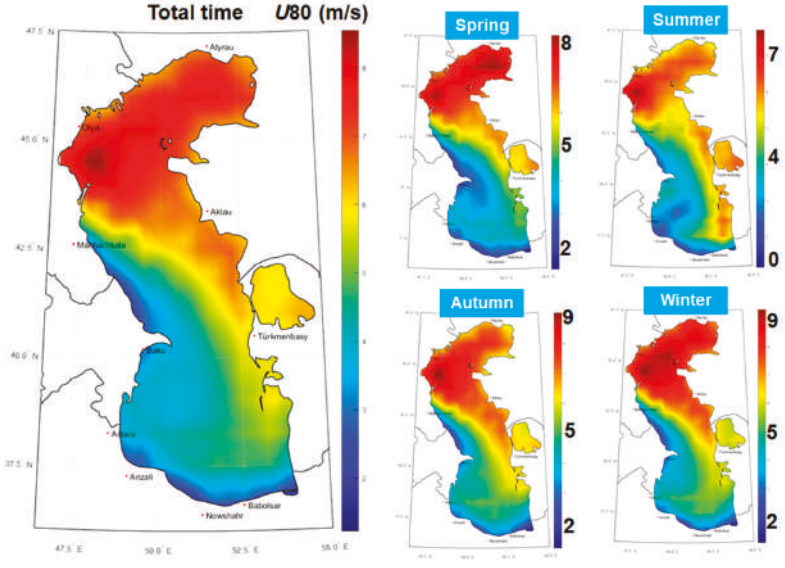

Figure 3. Spatial distribution of the *U80* parameter (average values) considering the 20-year time interval (January 1999 to December 2018) of ERA-Interim data.

During the springtime, the spatial distribution was similar to the total time, where the maximum values can increase to 8 m/s. As for the summer season, moderate conditions were noticed and the hot-spot area located near the Olya site was identified, where the wind speed reached a maximum value of 7.3 m/s. For the rest of the regions, the conditions decreased below 6 m/s, with a significant percentage of the southern part did not exceed 4 m/s. During autumn and winter, the wind strength significantly increased, and more frequent wind speeds of 9 m/s were observed.

Figure 4 presents a slightly better representation of the seasonal variations, where the average values corresponding to each season are reported to the total time distribution. Various patterns were noticed. During spring, in the north, wind conditions increased approximately 10% and a decrease of the resources to almost 20% was observed close to the Absheron Peninsula (Baku site). During

summer, the entire region indicated a decrease of the values to almost 30%. There is a hot spot close to the Babolsar site (south-east) where the wind speed may increase to 30%. During autumn, a wind farm located close to the Absheron Peninsula may have indicated better performances with an expected increase of the wind speed to almost 20%. The northern and centre regions indicated, in general, a slight increase of the values that may reach a maximum of 10%. During winter, the wind conditions presented a constant increase in intensity (≈15%), and in some sites, the balance was close to zero. In this case, the eastern area of Babolsar indicated a 15% decrease of the values.

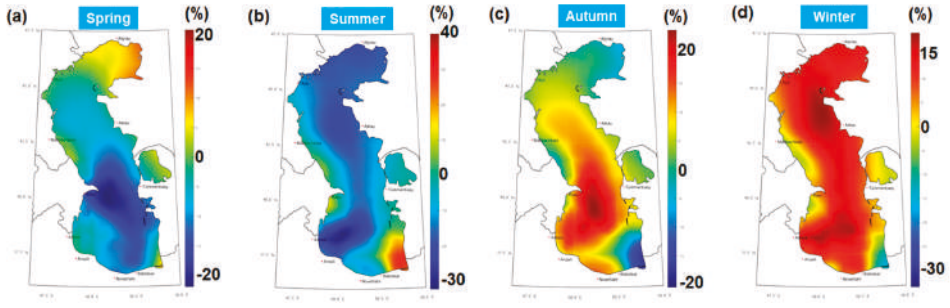

Figure 4. The spatial differences (in %) between the total time data and the four main seasons. The results are reported for the *U*80 parameter (average values) considering the 20-year time interval of ERA-Interim data, where: (**a**) spring; (**b**) summer; (**c**) autumn and (**d**) winter.

In Figure 5a, the evolution of the *U*80 parameter is presented for the reference sites indicated in Table 1. The average values (dotted line) reported to all the sites were approximately 5.2 m/s, and above this threshold, this study found: Atyrau (7.12 m/s), Olya (6.96 m/s), Aktau (6.68 m/s), Turkmenbasy (6.36 m/s) and Baku (5.87 m/s). A minimum wind speed value of 3.12 m/s corresponded to the site Anzali (south-west).

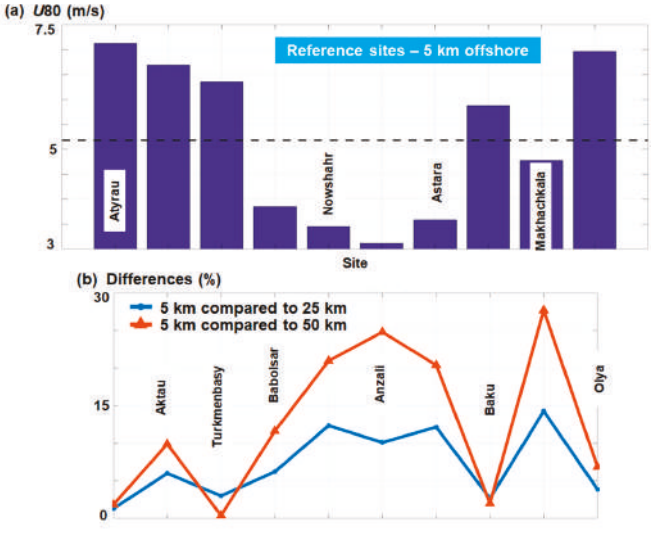

Figure 5. The distribution of the *U*80 parameter (average values) per reference sites considering the 20-year time interval of ERA-Interim data, where: (**a**) *U*80 values reported by the sites located at 5 km nearshore; (**b**) differences (in %) between the sites located at 5 km and the ones located at 25 km and 50 km, respectively.

The variation of the wind speed between various distances from the shoreline (5 km-25 km-50 km) is presented in Figure 5b. In general, the sites defined by important wind resources have not indicated important variations, this being the case of Atyrau, Baku or Olya. This suggests that a wind project located close to the shoreline will be a suitable solution. For the Turkmenbasy site, it was observed that the wind speed at 50 km offshore was lower than the one at 25 km, the differences being approximately 2.61%. It is clear that, in general, the wind speed increased heading towards offshore, this being the situation of Babolsar (25 km—6.2%; 50 km—11.62%), Anzali (10.1%; 24.79%) or Makhachkala (14.27%; 27.67%). In this case, the site Makhachkala (50 km) with 6.1 m/s exceeded the value of 6 m/s, which corresponded to the Baku site.

Figure 6 presents the monthly evolution of the *U*80 parameter taking into account all the available wind data. As expected, the northern part was dominated by more important conditions for the entire time interval considered., In July, it was observed that some wind energy hot-spots close to Olya site (in the south) or nearby Balbosar (in the north), reached a maximum value of 7 m/s. During the interval January–April, the consistency of the wind resources was more present in the entire northern region, with wind speed values observed at 9 m/s. In general, the sites located close to Olya (in the south) constantly indicated a higher wind resource, which makes them suitable candidates for the development of a wind project, if there is any energy demand in this region.

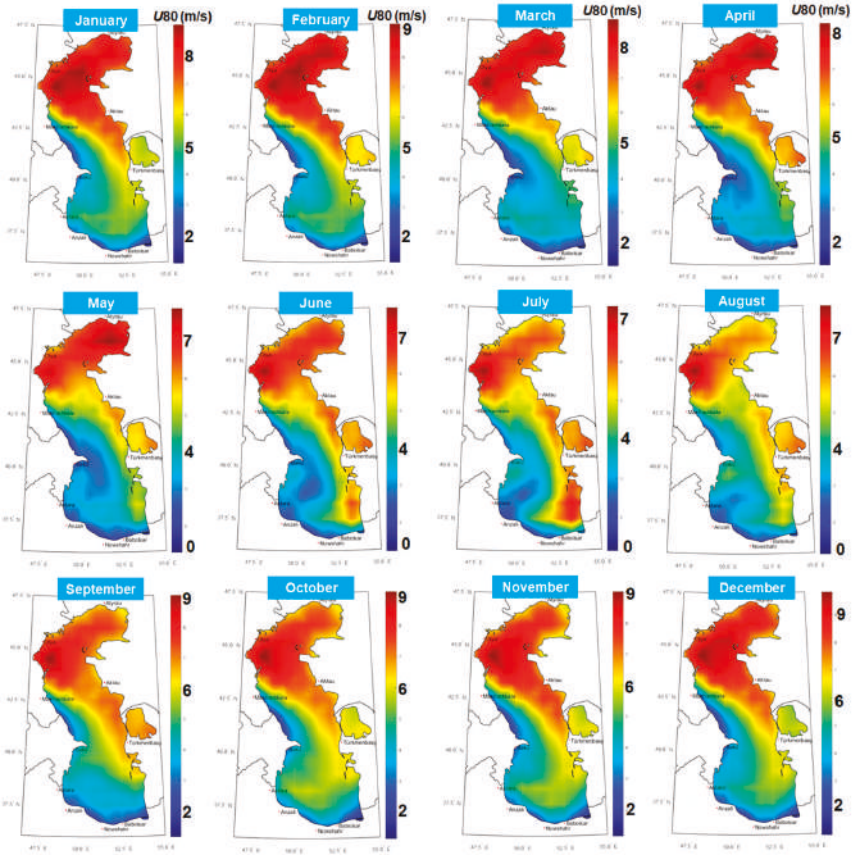

Figure 6. Monthly distribution of the *U*80 parameter (average values) reported by the ERA-Interim wind data for the 20-year time interval from January 1999 to December 2018.

3.3. Evaluation of the Wind Turbines

The downtime interval represents the inactivity period, during which the turbine will be shut down since the wind conditions are not suitable for the electricity production. In Figure 7, some case studies are presented. As the wind distribution located below the cut-in value and a dotted line that marks a distance of 50 km from the shore, a wind project can be usually implemented. In the case of the value 3 m/s, a minimum of 20% may be expected for the northern region, this value gradually increasing to 50% for the sites located in the central part of the target area, while a maximum of 70% may be expected in some isolated regions from the west and south. Small differences were noticed between the values 3 m/s and 3.5 m/s, the more notable values corresponded to the 5 m/s scenario (close to 90%). This indicates that a system as Siemens SWT-4.0 is not a suitable option for this enclosed basin.

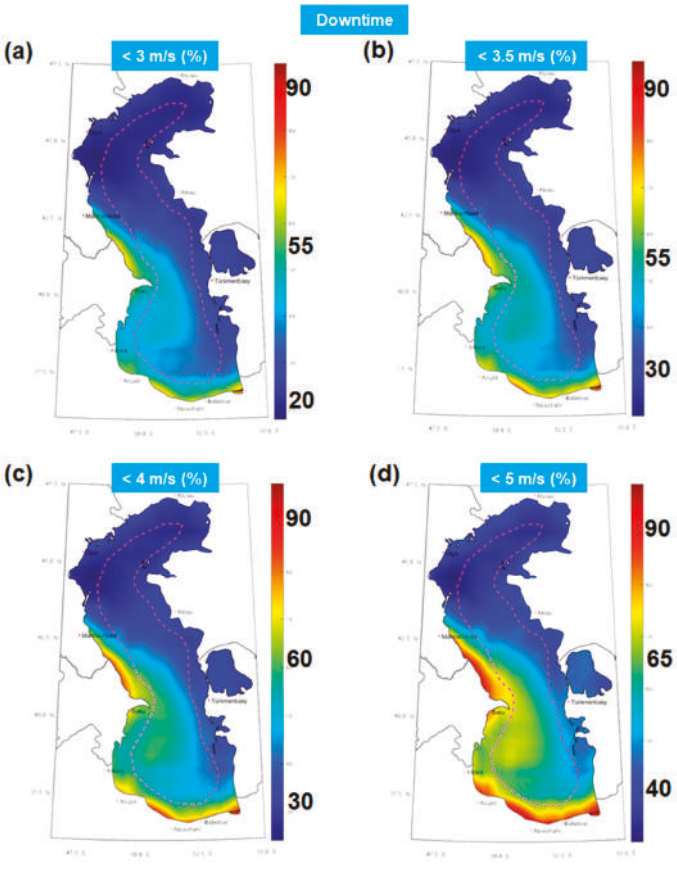

Figure 7. The downtime interval (%) corresponding to different cut-in values, where: (**a**) 3 m/s; (**b**) 3.5 m/s; (**c**) 4 m/s; (**d**) 5 m/s. The dotted line is located at approximately 50 km from the shoreline.

A top five downtime is presented in Table 3, taking into account as a reference the 3 m/s value. The lowest values were accounted by the same sites that include Atyrau, Olya, Aktau, Türkmenbasy and Makhachkala, regardless of the distance to the shore considered for evaluation. For the 5 km limit, a minimum of 20.76% was expected close to Atyrau and a maximum of 36.01% near Makhachkala. The same pattern was repeated for the 25 km, with a minimum of 20.31%, while in the case of 50 km,

there was a change of places between the fourth and fifth positions, for which a maximum of 34.4% was noticed.

Table 3. The top five downtimes sorted in an ascending order (corresponding to a 3 m/s cut-in value).

Distance to Shore	Site (%)				
5 km	Atyrau (20.76)	Olya (21.28)	Aktau (25.97)	Türkmenbasy (29.47)	Makhachkala (36.01)
25 km	Atyrau (20.31)	Olya (20.49)	Aktau (24.92)	Türkmenbasy (30.62)	Makhachkala (30.75)
50 km	Olya (19.89)	Atyrau (20.11)	Aktau (24.56)	Makhachkala (27.32)	Türkmenbasy (34.40)

Through the rated capacity, the percentage of time during which a particular turbine will operate at a full capacity can be identified. This is done by taking into account the wind speed located between the rated wind speed and the cut-out values. More details are presented in Figure 8. Only one spatial map was represented, since the colour distribution remained the same, and only the scale of the map was represented for different wind speed values. As expected, the values significantly decreased from 10.5 m/s to 15 m/s, It was observed that the energy hot spot located close to the Olya site did not exceed the 50 km limit (dotted line), where the best results were reported. The maximum values, oscillated between 15% and 30%, depending on the considered rated speed. This distribution closely followed the evolution of the wind speed with better results expected in north. In the southern region, it is possible that the considered wind turbines from Table 2 reported a negative performance (0%).

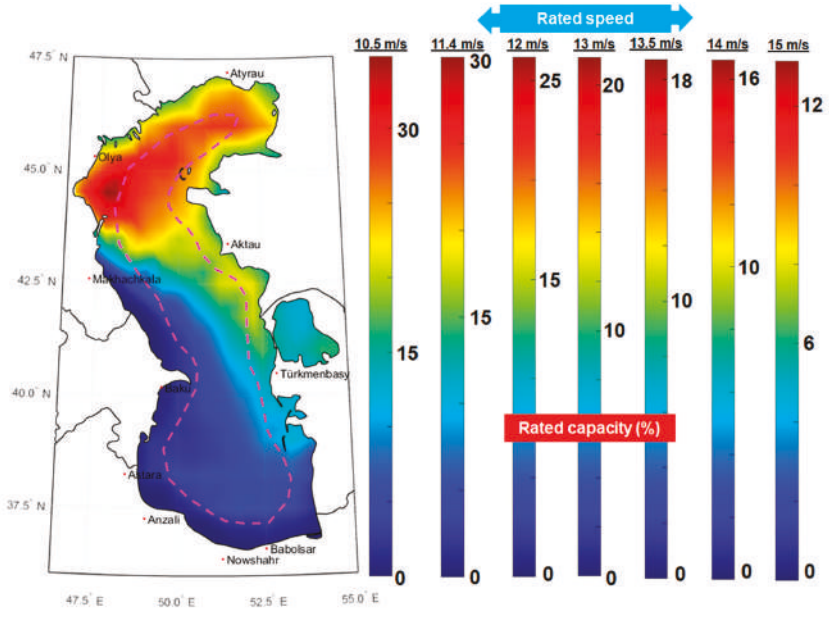

Figure 8. The rated capacity (%) reported for different rated wind speeds.

A more concise evaluation of the rated capacity is presented in Table 4, with the rated speed of 13 m/s as a reference. From the selected sites, Olya presented the best performances that varied between 14.7% (5 km) to 17.81% (50 km), compared to a minimum value of 3.96% (50 km) reported by Türkmenbasy, that was included in this classification.

Table 4. The top five rated capacities sorted in a descending order (reported to a 13 m/s rated speed).

Distance to Shore	Site (%)				
5 km	Olya (14.70)	Atyrau (13.17)	Aktau (7.61)	Türkmenbasy (5.30)	Makhachkala (1.34)
25 km	Olya (16.65)	Atyrau (14.09)	Aktau (9.59)	Türkmenbasy (5.30)	Makhachkala (3.77)
50 km	Olya (17.81)	Atyrau (14.50)	Aktau (10.38)	Makhachkala (6.25)	Türkmenbasy (3.96)

As a next step, the annual electricity production (AEP) was assessed by considering two reference sites, namely Atyrau and Baku. The selection of the Baku site was made by taking into account the interest for development of an offshore project in this region, the large population that lives in this region, and that it has some wind resources considering the results presented in Figure 5a. Figure 9 is focused on this evaluation which includes all the selected wind turbines. In the case of the systems where the hub height was indicated as site specific, different values were considered for assessment.

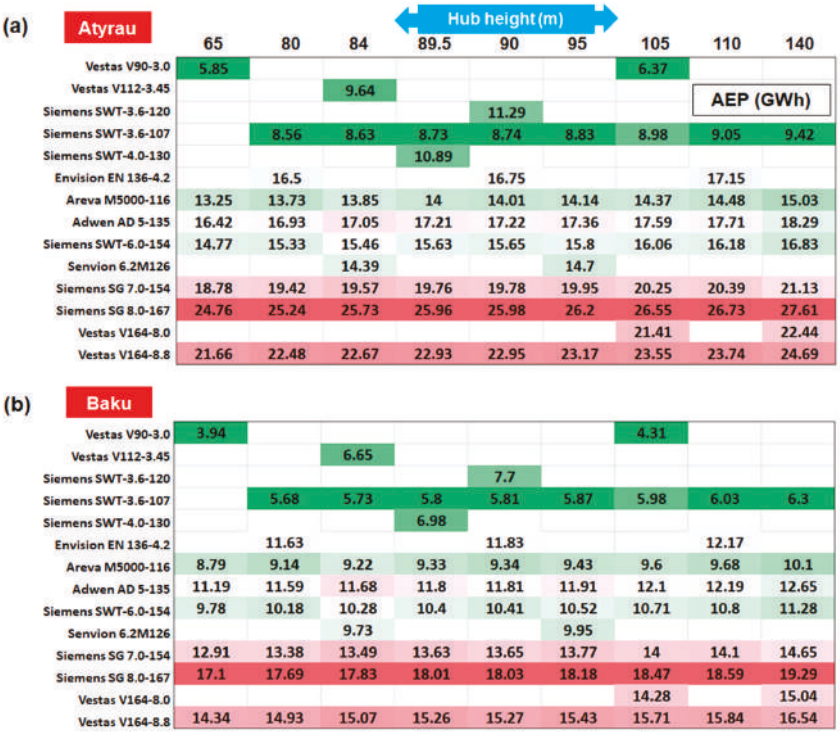

Figure 9. Annual electricity production (GWh) reported for the full time distribution, considering the sites: (**a**) Atyrau; (**b**) Baku. The points are located at a distance of 5 km from the shoreline.

It is clear that the site Atyrau (5 km from shore) indicated better performances than Baku (5 km from shore), regardless of the selected wind turbine, the lower and higher values being highlighted as a reference to the individual hub heights. As expected, the electricity production was related to the rated capacity and at the bottom, the systems rated below 4 MW were found. In addition, it is important to mention that the system, Siemens SG 8.0 MW, presented better results than the other two Vestas systems rated at 8 MW and 8.8 MW, making it a suitable candidate for this region. For the Atyrau

site, the authors expected a maximum value of 5.85 GWH in the case of Vestas V90-3.0 MW. These systems operate at a hub height of 65 m, while a maximum of 27.761 GWh is indicated by the Siemens SG 8.0 MW, if the rotor of this system works at a height of 140 m. In the case of the Baku site, a similar pattern was noticed, with the values oscillating between 3.94 GWh and 19.29 GWh. Also, it seems that some wind turbines presented lower performances compared to others, although they were defined by a higher rated capacity. This was the case of Vestas V112-3.45 MW compared to Siemens SWT-3.6-107, or for the generator, Adwen AD5-135, compared to Siemens SWT-6.0-154 and Senvion 6.2M126.

A similar analysis was performed in Figure 10, taking into account the capacity factor index. According to these values, Envision 4.2 MW stood out with more important values, being followed by Adwen AD5-135 and Siemens SG 8.0 MW. Regarding the Atyrau site, by observing the 80 m hub height, the values in the range of 27.13–44.86%, which were specific to some turbines rated at 3.6 MW and 4.2 MW, respectively, were noticed. Compared to these, the turbine rated at 8.8 MW indicated a value of approximately 29.16%. This is close to the lower value and similar to the one reported by Siemens SWT-6.0-154. In the case of the turbines, where the hub height was indicated as site specific, the authors obtained the following differences from 65 m to 140 m: Areva Multibrid M5000—4.07%; Adwen AD 5-135—4.23%; Siemens SWT-6.0-154—3.93%; Siemens Gamesa 7 MW—3.82% or Vestas V164-8.8 MW—3.93%. For the Baku site, lower values were expected from the turbines Vestas V90-3.0, Siemens SWT-3.6-107 and Senvion 6.2M126, while the turbine Envision 4.2MW seemed to be a suitable solution for this site. The turbines rated above 4.2 MW exceeded, in general, by 20%, and reached a maximum of 33.07% in the case of Envison 4.2 MW (110 m height), this turbine exceeded, in general, by 30%.

(a) Atyrau

Hub height (m)	65	80	84	89.5	90	95	105	110	140
Vestas V90-3.0	22.24						24.24		
Vestas V112-3.45			31.91						
Siemens SWT-3.6-120					35.8				
Siemens SWT-3.6-107		27.13	27.38	27.69	27.72	28	28.47	28.7	29.89
Siemens SWT-4.0-130				31.09					
Envision EN 136-4.2		44.86			45.52			46.6	
Areva M5000-116	30.25	31.36	31.62	31.96	31.98	32.29	32.8	33.05	34.32
Adwen AD 5-135	37.11	38.27	38.54	38.9	38.93	39.24	39.77	40.03	41.34
Siemens SWT-6.0-154	28.1	29.16	29.41	29.74	29.77	30.06	30.55	30.79	32.03
Senvion 6.2M126			26.71			27.29			
Siemens SG 7.0-154	30.63	31.66	31.91	32.23	32.26	32.54	33.02	33.25	34.45
Siemens SG 8.0-167	35.34	36.45	36.71	37.05	37.08	37.38	37.89	38.14	39.4
Vestas V164-8.0							30.55		32.03
Vestas V164-8.8	28.1	29.16	29.41	29.74	29.77	30.06	30.55	30.79	32.03

Cf (%)

(b) Baku

Vestas V90-3.0	14.98						16.41		
Vestas V112-3.45			22						
Siemens SWT-3.6-120					24.42				
Siemens SWT-3.6-107		18.01	18.18	18.4	18.42	18.61	18.96	19.12	19.99
Siemens SWT-4.0-130				19.93					
Envision EN 136-4.2		31.62			32.16			33.07	
Areva M5000-116	20.06	20.87	21.06	21.31	21.33	21.54	21.93	22.1	23.06
Adwen AD 5-135	25.29	26.19	26.4	26.67	26.7	26.93	27.36	27.55	28.6
Siemens SWT-6.0-154	18.61	19.37	19.55	19.79	19.81	20.01	20.38	20.55	21.46
Senvion 6.2M126			18.06			18.47			
Siemens SG 7.0-154	21.06	21.82	22	22.23	22.26	22.45	22.82	22.99	23.89
Siemens SG 8.0-167	24.4	25.25	25.44	25.7	25.73	25.95	26.35	26.53	27.52
Vestas V164-8.0							20.38		21.46
Vestas V164-8.8	18.61	19.37	19.55	19.79	19.81	20.01	20.38	20.55	21.46

Cf (%)

Figure 10. The capacity factor (%) reported for the full time distribution, considering the sites: (**a**) Atyrau; (**b**) Baku. The points are located at a distance of 5 km from the shoreline.

4. Discussions and Conclusions

One objective of the present work is to identify some suitable areas for the development of a wind project. From the literature review, it seems that the offshore sites that exceeded an average wind speed of 6 m/s (reported at 10 m height) are recommended [34]. Figure 11 presents this analysis, where the total time interval can be noticed, with the more promising areas being located in the northern sector. As expected, the region located south of the Olya site concentrated most of the wind energy. Some acceptable areas were noticed heading towards the north-east. During the winter time (December-January-February), the suitable areas were significantly extended, reaching the northern and eastern coast of the Caspian Sea. During this season, some promising results are expected from the sites located in the central part of this sea, more precisely, close to the Aktau site (east). Per total, according to this criterion ($U10 < 6$ m/s), a significant part of the Caspian Sea is not suitable for the development of an offshore wind project, this being also the case of the Baku location, where some offshore wind farms may occur in the near future.

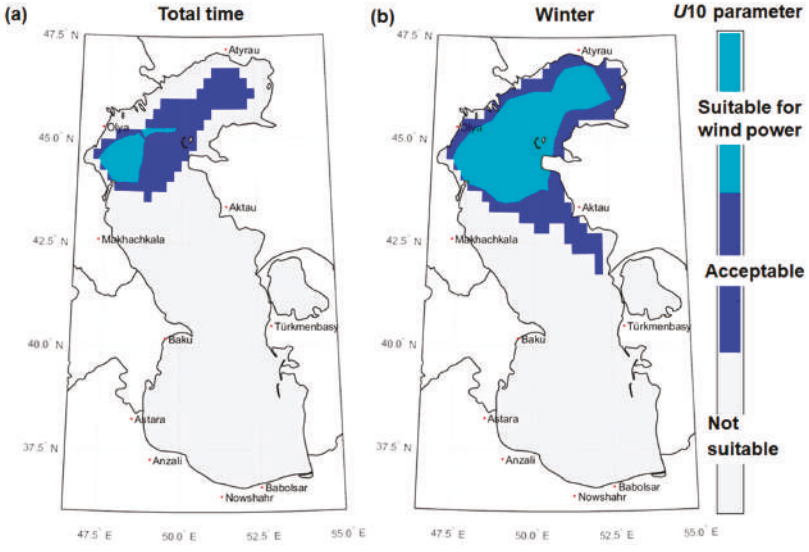

Figure 11. The suitability map for wind power with an average wind speed of 6 m/s as a reference. The results are indicated for: (**a**) full time distribution; (**b**) winter time.

Until now, the performances of the wind turbines were discussed in terms of their rated power. Another important parameter that needs to be taken into account is the turbine diameter, and this analysis is provided in Figure 12. The wind turbines presented in Table 2 were grouped in three main categories (small-medium-large), and the results were presented only for the sites Atyrau and Baku. These results showed a similar distribution for both sites, with the Atyrau site presenting slightly higher values.

From the analysis of the wind turbines included in the first category (small), the system, Envision EN 136-4.2 (hub height 80-90-110 m), seems to be more suitable for this location compared to Siemens SWT-4.0-130 that has a comparable rated capacity and operates at a height of 89.5 m. As for the second group (medium), significant results were noticed between Areva M500-116 and Siemens SWT-6.0-154, although similar hub heights were taken into account. From the systems rated above 7 MW, the better performances were expected from the Siemens SG 8.0-167, compared to Vestas V164-8.0 and Siemens SG 7.0-154, which were defined by a much lower rated capacity.

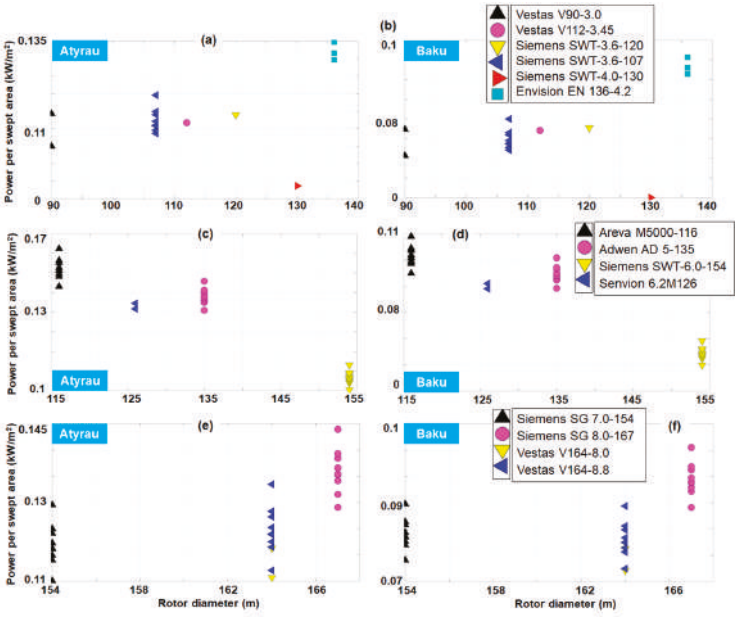

Figure 12. The classification of the wind turbines selected for the sites Atyrau and Baku, taking into account the power output per swept area. The results are grouped as follows: (**a**,**b**) small (3–4.2 MW); (**c**,**d**) medium (5–6.2 MW); (**e**,**f**) large (7–8.8 MW).

In the present work, a more complete description of the wind conditions corresponding to the Caspian Sea was provided by considering spatial maps and specific sites located near the major harbour cities of this region. According to the bathymetric data, significantly lower water depths are noticed in the northern part of this region. This means that they are suitable for the development of mono pile wind projects, taking into account that this solution can be used for water depths of 50 m [35]. For the rest of the regions, a floating wind farm has been indicated [36]. According to the wind data coming from the ERA-Interim project, the northern part of this sea was also defined by important wind resources, that seemed to be very suitable for a wind project. For this region, an average wind speed of 8–8.5 m/s (at 80 m height) were noticed, with a significant increase in the wind power which corresponded to autumn and winter. This environment was defined by important seasonal variations, which can reach a maximum of 40% in the southeast (in summer) or an increase with 15% of the wind speed for the entire basin (in winter).

When discussing the viability of an offshore wind project, an important issue to take into account are the financial aspects, especially in the case of the Caspian Sea. A common way to do this is to consider the levelized cost of energy (LCOE) that can be defined as [24]:

$$LCOE = \frac{CAPEX + \sum_{t=1}^{\eta} \frac{OPEX_t}{(1+r)^t}}{\sum_{t=1}^{\eta} \frac{AEP_t}{(1+r)^t}} \quad (4)$$

where: CAPEX—represents Capital Expenditure; $OPEX_t$—Operational expenditures reported for year t; AEP_t—Annual Energy Production corresponding to year t; r—the discount rate; η—lifetime of the project; t—year from the start of project.

Considering the methodology presented in Rusu and Onea [24], the following set-up was used: (a) Discount rate = 10%; (b) inflation = 2%; (c) ageing of the turbines = 1.6%; (d) CAPEX cost = 4500 USD/kW; (e) OPEX = 0.048 USD/kW; (f) project lifetime = 20 years (1999–2018). For simplicity, the hub height of the turbines was fixed to 80 m height and all the reference sites located at 5 km were taken into account. However from the results presented in Figure 2a, it is possible that some of them need to be defined by a lower quality of the wind data.

Figure 13 presents such an analysis, where a similar spatial pattern of the LCOE is indicated by the three groups of wind turbines. The better results corresponded to the sites Atyrau, Aktau, Turkmenbasy, Baku and Olya, where the values gradually decreased below 0.5 USD/kWh. A maximum LCOE value of 10 USD/kWh was reported by the site Anzali, this value gradually decreasing to 4.5 USD/kWh and 3 USD/kWh for turbines defined by higher rated capacity. Taking into account that the target of the European Union for the year 2025 is to obtain an LCOE of 0.11 USD/kWh [24], this study can conclude that the sites that exceed at this moment 0.5 USD/kWh cannot be taken into account for an offshore project. In Figure 13 (subplots b1 and c1), the turbines rated between 7 and 8.8 MW indicate better performances, reporting in some cases LCOE values below 0.25 USD/kWh. There is room for improvement and better performances can be obtained.

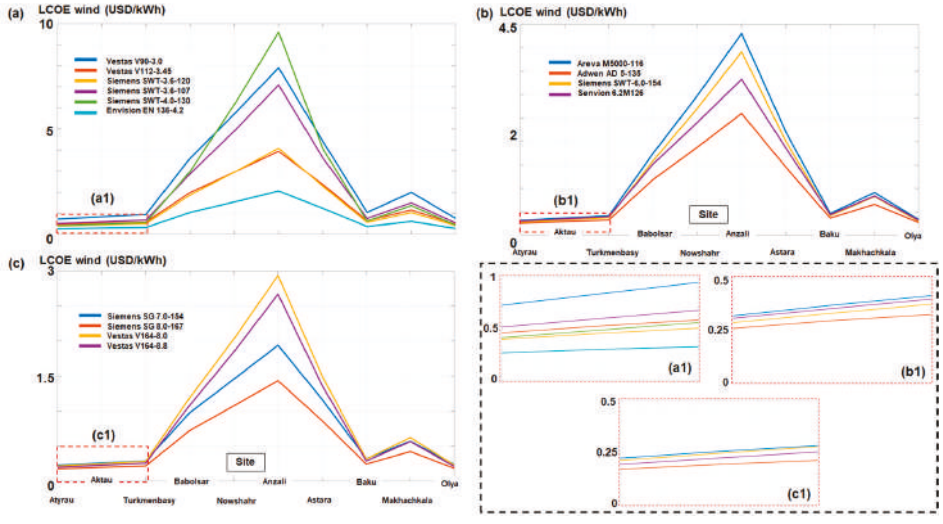

Figure 13. LCOE assessment considering the reference sites located at 5 km from the shore. The results were grouped in small, medium and large systems (**a**–**c**) including a detailed view of the values reported by the sites Atyrau, Aktau and Turkmenbasy (**a1**–**c1**). All the turbines were evaluated for an 80 m hub height.

The best sites to develop wind projects are close to Atyrau (north) and Olya (northwest), with the mention that the spatial maps indicate a hot-spot south of Olya (close to 44° latitude north) that presents more important wind resources. At this moment, there are plans to develop offshore wind projects in the vicinity of the Baku region (Absheron peninsula). By looking at the wind map, it can be noticed that this region is located in an area with moderate wind resources, where the wind speed conditions do not increase heading towards the offshore region. This means that a wind project located close to the shore will be preferable as the energy output will not significantly increase. Also to be considered is the development of a project along the shoreline in order to avoid the problems associated with marine areas, such as weather windows [37].

As in most of the regions located in the northern hemisphere, the wintertime presents more energetic wind resources [38,39], this being also the case for the Caspian Sea. During December, January and February, the entire northern area has been defined by important wind resources, which constantly indicated average wind speed values of 8.5–9 m/s. During the summer time, the areas suitable for a renewable project are significantly reduced, being possible to register a maximum of 7 m/s only in the southern part of Olya site.

As for the wind turbine performances, different generators were considered for assessment using as a reference the sites of Atyrau and Baku. The annual electricity production is directly related to the rated capacity of the turbines, but even so, an 8 MW system will perform much better than an 8.8 MW generator. By considering different hub heights, the electricity output for different configurations was established, being reported a maximum production of 27.61 GWh and 19.29 GWh for the Atyrau and Baku site, respectively. To obtain a higher capacity factor, probably a system rated at 4.2 MW or 5 MW will be more indicated, having reported values close to 50% for the Atyrau sites, and between 25% and 33% for the Baku location.

Finally, the Caspian Sea is an important area in terms of energy resources, being well known for the hydrocarbon extractions [40]. Nevertheless, there is interest for natural resources, and the development of a wind farm which will represent one-step forward for the development of a renewable portfolio, as it can be designed according to the electricity demand of the coastal communities from this region.

Author Contributions: F.O. performed the literature review, processed the wind data, carried out the statistical analysis and interpreted the results. E.R. guided this research, wrote the manuscript and drawn the conclusions. The final manuscript has been approved by all authors.

Funding: This work was carried out in the framework of the research project REMARC (Renewable Energy extraction in MARine environment and its Coastal impact), supported by the Romanian Executive Agency for Higher Education, Research, Development and Innovation Funding—UEFISCDI, grant number PN–III–P4–IDPCE–2016–0017.

Acknowledgments: ECMWF ERA-Interim data used in this study have been obtained from the ECMWF data server. The altimeter products were generated and distributed by Aviso (http://www.aviso.altimetry.fr/) as part of the SSALTO ground processing segment.

Conflicts of Interest: The authors declare no conflicts of interest.

Nomenclature

T	Avera–year (8760 hr/year)
r	discount rate
$U10$	wind speed reported for a 10 m height above sea level
$P(u)$	power curve of a wind turbine
P_E	electric power expected to be generated
R_P	rated power of the system
OPEXt	Operational expenditures reported for year t
CAPEX	Capital Expenditure
LCOE	Levelized Cost of Energy
AEP	Annual Electricity Production
NaN	Not A Number
$f(u)$	Weibull probability density function
ECMWF	European Centre for Medium-Range Weather Forecasts
Cf	Capacity factor
AVISO	Archiving, Validation and Interpretation of Satellite Oceanographic Data
z_{10}; z_{80}	reference heights
z_0	roughness of the sea surface

References

1. Yang, W.; Tian, W.; Hvalbye, O.; Peng, Z.; Wei, K.; Tian, X. Experimental research for stabilizing offshore floating wind turbines. *Energies* **2019**, *12*, 1947. [CrossRef]
2. Ishie, J.; Wang, K.; Ong, M. Structural dynamic analysis of semi-submersible floating vertical axis wind turbines. *Energies* **2016**, *9*, 1047. [CrossRef]
3. Offshore Wind in Europe—Key Trends and Statistics 2018. Available online: https://windeurope.org/about-wind/statistics/offshore/european-offshore-wind-industry-key-trends-statistics-2018/ (accessed on 8 March 2019).
4. Klinge Jacobsen, H.; Hevia-Koch, P.; Wolter, C. Nearshore and offshore wind development: Costs and competitive advantage exemplified by nearshore wind in Denmark. *Energy Sustain. Dev.* **2019**, *50*, 91–100. [CrossRef]
5. Vieira, M.; Henriques, E.; Amaral, M.; Arantes-Oliveira, N.; Reis, L. Path discussion for offshore wind in Portugal up to 2030. *Mar. Policy* **2019**, *100*, 122–131. [CrossRef]
6. Rusu, E.; Onea, F. Joint evaluation of the wave and offshore wind energy resources in the developing countries. *Energies* **2017**, *10*, 1866. [CrossRef]
7. Ganea, D.; Mereuta, E.; Rusu, E. An evaluation of the wind and wave dynamics along the european coasts. *JMSE* **2019**, *7*, 43. [CrossRef]
8. Rusu, E.; Onea, F. Evaluation of the wind and wave energy along the Caspian Sea. *Energy* **2013**, *50*, 1–14. [CrossRef]
9. Zountouridou, E.I.; Kiokes, G.C.; Chakalis, S.; Georgilakis, P.S.; Hatziargyriou, N.D. Offshore floating wind parks in the deep waters of Mediterranean Sea. *Renew. Sustain. Energy Rev.* **2015**, *51*, 433–448. [CrossRef]
10. EolMed—The First Offshore Wind Farm in the Mediterranean Sea. Available online: http://www.eolmed.fr/en/ (accessed on 29 May 2019).
11. Italy on Pole in Race for First Mediterranean Offshore Wind | Recharge. Available online: https://www.rechargenews.com/wind/1712851/italy-on-pole-in-race-for-first-mediterranean-offshore-wind (accessed on 29 May 2019).
12. Onea, F.; Deleanu, L.; Rusu, L.; Georgescu, C. Evaluation of the wind energy potential along the Mediterranean Sea coasts. *Energy Explor. Exploit.* **2016**, *34*, 766–792. [CrossRef]
13. Amirinia, G.; Kamranzad, B.; Mafi, S. Wind and wave energy potential in southern Caspian Sea using uncertainty analysis. *Energy* **2017**, *120*, 332–345. [CrossRef]
14. Onea, F.; Rusu, E. Efficiency assessments for some state of the art wind turbines in the coastal environments of the Black and the Caspian seas. *Energy Explor. Exploit.* **2016**, *34*, 217–234. [CrossRef]
15. Kerimov, R.; Ismailova, Z.; Rahmanov, N.R. Modeling of wind power producing in Caspian Sea conditions. *Int. J. Tech. Phys. Problems Eng.* **2013**, *15*, 136–142.
16. Alamian, R.; Shafaghat, R.; Miri, S.J.; Yazdanshenas, N.; Shakeri, M. Evaluation of technologies for harvesting wave energy in Caspian Sea. *Renew. Sustain. Energy Rev.* **2014**, *32*, 468–476. [CrossRef]
17. Kamranzad, B.; Etemad-Shahidi, A.; Chegini, V. Sustainability of wave energy resources in southern Caspian Sea. *Energy* **2016**, *97*, 549–559. [CrossRef]
18. Alamian, R.; Shafaghat, R.; Safaei, M.R. Multi-objective optimization of a pitch point absorber wave energy converter. *Water* **2019**, *11*, 969. [CrossRef]
19. Tavana, M.; Behzadian, M.; Pirdashti, M.; Pirdashti, H. A PROMETHEE-GDSS for oil and gas pipeline planning in the Caspian Sea basin. *Energy Econ.* **2013**, *36*, 716–728. [CrossRef]
20. Mityagina, M.; Lavrova, O. Satellite survey of Inner Seas: Oil pollution in the Black and Caspian Seas. *Remote Sens.* **2016**, *8*, 875. [CrossRef]
21. Efendiyeva, I.M. Ecological problems of oil exploitation in the Caspian Sea area. *J. Pet. Sci. Eng.* **2000**, *28*, 227–231. [CrossRef]
22. INTERVIEW—Azerbaijan's 200MW Offshore Wind Plan May be Tweaked After Feasibility Study. Available online: /news/interview-azerbaijans-200mw-offshore-wind-plan-may-be-tweaked-after-feasibility-study-503906/ (accessed on 30 May 2019).
23. Wind Power in Azerbaijan. REVE, Archives: Wind energy in Azerbaijan. Available online: https://www.evwind.es/tags/wind-energy-in-azerbaijan (accessed on 30 May 2019).

24. Rusu, E.; Onea, F. An assessment of the wind and wave power potential in the island environment. *Energy* **2019**, *175*, 830–846. [CrossRef]
25. Bathymetric Data Viewer. Available online: https://maps.ngdc.noaa.gov/viewers/bathymetry/ (accessed on 31 May 2019).
26. Home. United Nations. Available online: https://www.un.org/en/ (accessed on 31 May 2019).
27. Poli, P. Browse Reanalysis Datasets. Available online: https://www.ecmwf.int/en/forecasts/datasets/browse-reanalysis-datasets (accessed on 31 May 2019).
28. Wan, Y.; Fan, C.; Dai, Y.; Li, L.; Sun, W.; Zhou, P.; Qu, X. Assessment of the joint development potential of wave and wind energy in the South China Sea. *Energies* **2018**, *11*, 398. [CrossRef]
29. Onea, F.; Rusu, L. Evaluation of some state-of-the-art wind technologies in the nearshore of the Black Sea. *Energies* **2018**, *11*, 2452. [CrossRef]
30. Onea, F.; Rusu, L. A Study on the wind energy potential in the Romanian coastal environment. *J. Mar. Sci. Eng.* **2019**, *7*, 142. [CrossRef]
31. Welcome to Wind-Turbine-Models.com. Available online: https://en.wind-turbine-models.com/ (accessed on 20 May 2018).
32. Rusu, E.; Onea, F. A parallel evaluation of the wind and wave energy resources along the Latin American and European coastal environments. *Renew. Energy* **2019**, *143*, 1594–1607. [CrossRef]
33. MSWH/MWind: Aviso+. Available online: https://www.aviso.altimetry.fr/en/data/products/windwave-products/mswhmwind.html (accessed on 18 August 2018).
34. Vagiona, D.G.; Kamilakis, M. Sustainable site selection for offshore wind farms in the South Aegean—Greece. *Sustainability* **2018**, *10*, 749. [CrossRef]
35. Njomo-Wandji, W.; Natarajan, A.; Dimitrov, N. Influence of model parameters on the design of large diameter monopiles for multi-megawatt offshore wind turbines at 50-m water depths. *Wind Energy* **2019**, *22*, 794–812. [CrossRef]
36. Lerch, M.; De-Prada-Gil, M.; Molins, C. The influence of different wind and wave conditions on the energy yield and downtime of a Spar-buoy floating wind turbine. *Renew. Energy* **2019**, *136*, 1–14. [CrossRef]
37. O'Connor, M.; Lewis, T.; Dalton, G. Weather window analysis of Irish west coast wave data with relevance to operations 82 maintenance of marine renewables. *Renew. Energy* **2013**, *52*, 57–66. [CrossRef]
38. Onea, F.; Rusu, E. Wind energy assessments along the Black Sea basin. *Meteorol. Appl.* **2014**, *21*, 316–329. [CrossRef]
39. Onea, F.; Raileanu, A.; Rusu, E. Evaluation of the wind energy potential in the coastal environment of two enclosed seas. *Adv. Meteorol.* **2015**. [CrossRef]
40. Clem, R.S. Energy in the Caspian region: Present and future. *Eurasian Geogr. Econ.* **2002**, *43*, 661–662. [CrossRef]

energies

MDPI

Article

Volume-Based Assessment of Erosion Patterns around a Hydrodynamic Transparent Offshore Structure

Mario Welzel *, Alexander Schendel, Torsten Schlurmann and Arndt Hildebrandt

Ludwig-Franzius-Institute for Hydraulic, Estuarine and Coastal Engineering, Leibniz Universität Hannover, 30167 Hannover, Germany

* Correspondence: welzel@lufi.uni-hannover.de

Received: 1 July 2019; Accepted: 6 August 2019; Published: 10 August 2019

Abstract: The present article presents results of a laboratory study on the assessment of erosion patterns around a hydrodynamic transparent offshore foundation exposed to combined waves and currents. The model tests were conducted under irregular, long-crested waves in a scale of 1:30 in a wave-current basin. A terrestrial 3D laser scanner was used to acquire data of the sediment surface around the foundation structure. Tests have been conducted systematically varying from wave- to current-dominated conditions. Different volume analyzing methods are introduced, which can be related for any offshore or coastal structure to disclose physical processes in complex erosion patterns. Empirical formulations are proposed for the quantification of spatially eroded sediment volumes and scour depths in the near-field and vicinity of the structure. Findings from the present study agree well with in-situ data stemming from the field. Contrasting spatial erosion development between experimental and in-situ data determines a stable maximum of erosion intensity at a distance of 1.25 A, 1.25 times the structure's footprint A, as well as a global scour extent of 2.1–2.7 A within the present study and about 2.7–2.8 A from the field. By this means, a structure-induced environmental footprint as a measure for erosion of sediment affecting marine habitat is quantified.

Keywords: offshore wind farm; jacket; scour; wave-current interaction; spatial resolution; erosion patterns; sediment transport; laboratory tests

1. Introduction

To meet the rising demand for renewable energy, the expansion of offshore wind energy converters (OWECs) in coastal waters is progressing steadily. Due to continuing technological development, upcoming offshore wind parks will not only utilize larger turbines with a capacity of 10 MW and beyond [1], but also create opportunities to open new available space in larger water depths. As the average water depth increases in projected wind parks globally, different construction types are adopted that are more complex and have a larger footprint than commonly used monopiles. However, the installation and operation of those structures, especially if several are closely aligned next to each other, may lead to impacts on the formerly unaffected marine environment in the near- but also in the far-field. Potential impacts [2–4] include large scale morphological changes and entrainment of large quantities of sediment in the water body due to interaction of the structure with ocean currents and waves [5–7]. Of course, the scouring processes might also affect the sustainability of the structure itself over time. Unfortunately, only a limited understanding of environmental impacts and the impairment of the structure's stability over its lifetime due to scouring processes around complex foundation structures exist. This is why for some structures that are affected by scouring, e.g., gravity-based foundations (GBF), the installation of a scour protection system became mandatory. The protection of those structures against the degradation due to scour is often designed following a conservative, and thus, inefficient approach that is based on monopiles. Yet, this evident mismatch may also lead to

incorrect prediction of scour depths and unreliable design of scour protection (see Rudolph et al. [8]). This in turn might also impose an effect of superimposing global scouring processes, that possibly contribute to the subsidence of the seabed, in particular around complex structures see, e.g., Rudolph et al. [8] and Baelus et al. [9]. While the equilibrium scour depth around monopile foundations has been investigated and published extensively over the last decades, limited understanding exists for jacket-type foundations, see [8–11]. Even though the bed topography was measured, these studies were more focused on the local scour development for specific conditions rather than on the spatial scour development on a global extent. A literature study on model tests and field studies related to jacket-type foundations can be found in Welzel et al. [12].

Research conducted for groups of circular cylinders represents the basis of knowledge to understand the initiation and development of local and global scour around a hydrodynamic transparent structure like a jacket. For groups of circular cylinders, several studies outlined a dependency between the distance of piles (gap ratio) and the local as well as global scour development [13–15]. Furthermore, it is reported that hydrodynamic interactions between individual circular piles are small if the distance between them exceeds six times the piles' diameter (see e.g. [16–18]). Bolle et al. [10] transferred this knowledge to jacket structures, arguing that the distance was clearly above 6 D in their study and thus global scour does not have to be considered. To gain insights into potential effects of global scouring processes on the marine environment and the structures' stability, spatial seabed changes in the vicinity of the structure need to be measured. Although different measurement techniques and analysis methods were already applied in previous studies, they are rarely used to provide information beyond the calculation of volumes of displaced sediment. Porter [19] used a photogrammetric-based measurement system to analyze the scour hole, depth and shape in tidal currents around a monopile. Margheritini et al. [20] conducted physical model tests for the scour development around monopile foundations in unidirectional and tidal currents. They analyzed the scour volume by means of a laser probe bottom profiler. Stahlmann and Schlurmann [21] conducted small scale, 1:40, as well as large scale, 1:12, physical model tests for a tripod foundation in regular and irregular wave conditions and evaluated the scour development by using either a laser distance bottom profiler (for 1:40) or a multi-beam echo sounder (for 1:12). Hartvig et al. [22] investigated the scour and backfilling processes around a monopile foundation due to steady currents and combined wave-current load. A laser probe bottom profiler was used to obtain bed topography measurements for several time steps. Insights about scour processes and results on scour depth, scour volume and a scour shape factor are derived as a function of time and space. As the spatial investigation of erosion volumes around offshore structures so far has attracted little research interest (also for technical reasons of measurement instruments), few studies exist which may provide a systematic analysis. Studies of Margheritini et al. [20] and Hartvig et al. [22] systematically analyzed erosion processes and introduced a dimensionless erosion volume (normalized with a structural volume). Nevertheless, the lack of a spatial reference (e.g., the related interrogation area of the erosion volume) to the information of eroded sediment volume seems to be an important point missing for a further normalization.

However, several aspects regarding scouring processes around complex offshore structures remain (so far) disregarded and demand a more systematic investigation of erosion patterns. Consequently, the objective of the present paper addresses a systematic volume-based analysis of erosion processes to evaluate the degree and extent of the local and global scour development around a jacket structure. This enables the sediment redistribution footprint of the offshore structure to be deduced in the transition between the near- and the far-field. Therefore, hydraulic model tests have been carried out in the wave and current basin of the Ludwig-Franzius-Institute to conduct a systematic study of erosion processes around a jacket-type offshore foundation under waves, combined waves and current as well as steady current conditions. Different volume-analyzing concepts and calculation methods are introduced, which can be adapted, generally, for any offshore structure or coastal structure to reveal physical processes in complex erosion patterns.

The objectives of this paper are:

(1) The systematic study of global scour patterns in combined waves and current conditions around a jacket foundation.
(2) Gaining further insights into the spatial scouring process around jacket structures with detailed 3D laser scan measurements.
(3) The introduction and application of a novel method to analyze volume-based erosion processes with a spatial reference.
(4) The improvement of prediction methods to account for local and global erosion volumes/scour depths and the extent of global and local scour around jacket type offshore structures.
(5) The quantification of eroded sediment volume, and the determination of areas, which exhibit an increased erosion rate, and therefore, have an impact on the natural dynamics of the ocean floor.

It should be noted that the present physical model tests were part of a fundamental study previously described in [12]. While Welzel et al. [12] focused on local scour depths, measured for a wide range of wave, wave-current and steady current conditions, the present study concentrates on the volume-based assessment of spatial erosion processes in the near-field and vicinity of the structure.

2. Experimental Setup

The physical model tests have been conducted using a jacket-type model in the 3D wave and current basin of the Ludwig-Franzius-Institute, Leibniz Universität Hannover, Germany. The wave basin has a maximum water depth of 1 m, a total length of 40 m and a width of 24 m (see Figure 1). Passive wave absorbers are installed at three sides of the wave basin, resulting in an effective usable length of 30 to 15 m (see Figure 1). An integrated active wave absorption system further reduces reflections. The snake type wave machine consists of 72 wave paddles, allowing generation of regular and irregular waves at angles of 45° between 135° degrees. For the present study a perpendicular wave direction was set to 90° to the current coming from 0° (see Figure 1).

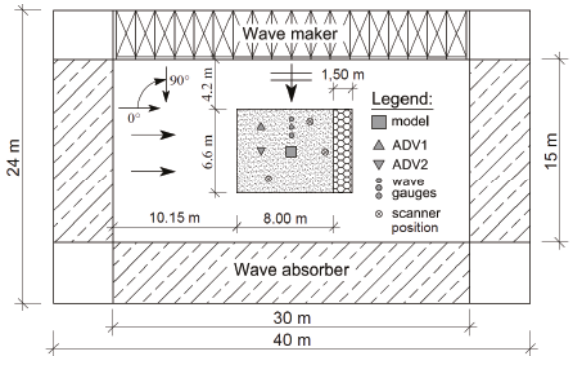

Figure 1. Sketch of the wave basin, plan view including the test setup, unidirectional current is coming from left to right with 0°, waves are propagating perpendicular in 90°.

This superposition angle was chosen to enable a better comparability to other studies as well as to investigate the influence of waves approaching perpendicular to a current on the global scour development. As shown in Figure 2b, the water depth of 0.67 m, representing a water level of 20 m in prototype scale according to the model scale of 1:30, was kept constant during the study. The sediment pit is located in the center of the basin, providing an additional depth of 1.2 m, a length of 8 m and a width of 6.6 m. A sediment trap with a length of 1.5 m at the downstream side of the pit was installed to prevent large amounts of sediment from being transported as bed load into the pump sump. A jacket structure was assembled to physically mimic a generic structure of a jacket-type foundation without

considering the influence of post piles or mud-mats. The physical model was constructed using 3D printed parts, which were glued together, sanded down and painted with filler and lacquer in multiple layers to achieve a smooth coating of the surface. The jacket structure has been built in a quadratic cross section consisting of four main piles with a diameter of 4 cm each and with a distance of 0.55 m between them. The piles below the lowest nodes were made out of aluminum and were connected to the bottom of the wave basin. The model was installed in the middle of the sediment pit. As the jacket structure was not rotated during the laboratory experiments, only one orientation of the model with respect to the current and wave direction was investigated in the present study. The model was installed and constructed in a way that the lowest node of the structure was positioned in a distance of one pile diameter D (with D = 4 cm) above the sediment bed, as shown in Figure 2. Consequently, a substantial influence of the jacket structure on the flow and thus on the sediment bed was intended. The sediment pit was filled with sand with a median diameter of $d_{50} = 0.19$ mm. To achieve a good compaction, without entrapped air, the sand was installed in wet condition and levelled with aluminum bars.

Two Acoustic Doppler Velocimeters (ADVs, Vectrino+, Nortek AS, Rud, Norway) measured wave and current induced flow velocities. One was placed 2.5 m upstream (in current direction) from the model (ADV2), and the other one (ADV1) was positioned in line with the wave gauge array.

Both ADVs were installed in a distance of 2.5 D (10 cm) over the sediment surface, vertically (looking down). Additional preliminary tests were carried out to measure the undisturbed current velocity U_c. Furthermore, vertical velocity profiles of horizontal flow components were measured at the location of ADV2 to calculate the undisturbed and depth-averaged current velocity $\overline{U}$. The undisturbed orbital velocity U was measured during previously conducted tests with ADV1 at a distance of 10 cm above the sand level. A terrestrial 3D laser scanner (Focus 3D, FARO, Lake Mary, FL, USA) was used to measure the surface elevation around the model. The FARO Focus 3D laser scanner offers the advantage of high-resolution measurements of up to 70 million data points per scan. In comparison to photogrammetric [20], echo sounder based measurement techniques [23] as well as measurements with laser probe bottom profiler [22], the 3D laser scanning method provides higher resolution and therefore a better accuracy to measure the scour patterns around the structure. The high accuracy of up to ±1 mm is especially important for volume analyzes around small/thin objects (e.g., the present structure with diameters D = 4 cm).

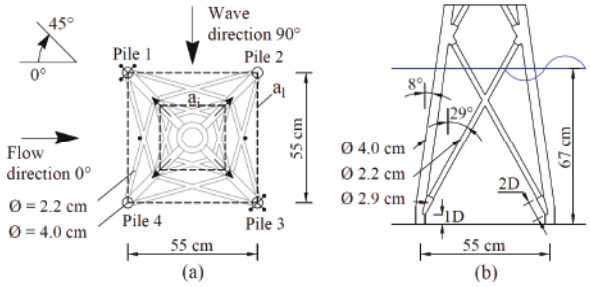

Figure 2. Schematic view of the jacket model (**a**) plan view on the model, including dimensions, the mounted echo sounding transducer, the reference structure footprint a_1 and the increasing interrogation area a_i to compute the erosion volume (**b**) side view of the model with dimensions, angles and water level, D = 4 cm.

As mentioned previously, the present tests were part of a larger investigation, in which the time dependent development of the scour around the jacket at different locations was measured and analyzed (cp. [12]). For this, measurements were carried out by means of echo sounding transducers with a diameter of ~1cm around pile 1 and pile 3 as well as in between the piles. These echo sounders are additionally illustrated in Figure 2. For more detailed information about the experimental setup and procedure refer to Welzel et al. [12].

Experimental Procedure and Test Conditions

Before each test, the sediment bed was smoothed under wet conditions (water depth kept at the level of sediment bed) by making use of aluminum bars. Subsequently the wave basin was carefully filled overnight. No general starvation of the bed (general seabed lowering) has been observed in the present study. Therefore, the measured erosion patterns can be attributed to the presence of the structure. JONSWAP wave spectra were generated until a maximum amount of 6500 waves (or 7 h for test 5) were reached in one test. Studies related on scour around OWECs in combined waves and current exhibit test durations in ranges of 1 to 3 hours (see, e.g., [11,24–26]). Some of those studies did not reach an equilibrium stage of the related scour depth. Therefore, a maximum amount of 6500 waves was chosen in the present study (test durations of 3.7 between 8.3 hours) to ensure the erosion process to reach its equilibrium stage. The test procedure can be summarized as follows:

(1) Smoothing the sand level and carefully filling the basin to avoid disturbances of the adjusted sand level.
(2) Running the desired test until the scour process has attained an (almost) equilibrium stage.
(3) Emptying the wave basin and carefully draining the sand pit to avoid further influence on the scour pattern.
(4) 3D scans of the global sediment surface around the structure.

The maximum value of the undisturbed orbital velocity U_m (see Equation (1)) is calculated with U_{rms}, the root-mean-square value (RMS) of the orbital velocity U at the bottom in the direction of the waves defined as ${U_{rms}}^2 = \int_0^\infty S(f)df$, with $S(f)$ = power spectrum of U which corresponds to the wave component, with f = frequency. As investigated in [27], the Keulegan-Carpenter number is defined as KC $= U_m T_p / D$, in which T_p = peak wave period and D = pile diameter. The parameter U_{cw} (see Equation (2)) represents a wave current velocity ratio introduced by Sumer and Fredsøe [27] to assess the ratio of undisturbed current U_c to undisturbed wave generated flow velocity U_m:

$$U_m = \sqrt{2} U_{rms} \tag{1}$$

$$U_{cw} = \frac{U_c}{(U_c + U_m)} \tag{2}$$

The Shields parameter, which is based on the current velocity U_c and the orbital velocity U_m, was determined by the approach of Soulsby [28]. The test program consisted of a wave only test, three tests in which different wave and current loads were combined, and a final test with current-only conditions. Current velocities and wave parameters were selected to cover a wide range of U_{cw} and KC numbers. A critical Shields parameter of $\theta_{cr} = 0.049$ was calculated for the sediment of the present study. Considering the Shields parameters given in Table 1, all tests have thus been conducted under live bed conditions.

Table 1. Test conditions/Measured values (waves are propagating in 90° to the current).

Test	H_s [m]	T_p [s]	Bed Orbital Velocity U_m [cm/s]	Depth Averaged Current Velocity $\bar{U}$ [cm/s]	Current Velocity 10 cm Above Bed U_c [cm/s]	KC [-]	U_{cw} [-]	Shields Parameter θ [-]	Global Eroded Volume: for an Area of 1.25 A V_D [-]	Local Eroded Volume: Diameter of 6 D V_D [-]
1	0.165	4.5	20.8	-	-	23.4	0.00	0.080	−0.49	−0.49
2	0.165	4.5	20.8	11.4	10.1	23.4	0.33	0.085	−14.14	−10.62
3	0.158	3.4	17.5	24.3	22.5	14.9	0.56	0.087	−27.26	−18.50
4	0.147	2.0	13.3	41.7	38.8	6.7	0.75	0.123	−43.61	−23.82
5	-	-	-	41.7	38.8	-	1.00	0.084	−55.52	−27.19

* Test 1–5 are related (in the same order) to test 3, 10, 8, 6 and 13 in Welzel et al. [12].

3. Calculation of Erosion Volumes

The determination of dimensionless erosion volumes analyzed over increasing interrogation areas (a_i), enables the spatial assessment of eroded sediment quantities (eroded sediment per surface area) around offshore structures. To enable an improved analysis of erosion processes, in particular of the related erosion patterns, only erosion volumes of sediment are considered within each interrogation area without the additional influence of deposited sediment volume as the deposited sediment patterns would affect the analysis of the considered erosion. Different techniques for the analysis of these volumes are introduced in the following. The application of those techniques is not limited to jacket-type structures as used in this study but can also be adapted for other complex structures to reveal physical processes behind complex erosion patterns. To avoid optically shadowed interrogation areas in close proximity of the structure, scans were taken from three different angles and subsequently merged into a single 3D point cloud, providing a high-resolution bed topography in a point density of 100 data points per cm^2 in the carefully drained wave basin around and beneath the structure. No changes in the sediment bed have been observed while slowly draining the sediment pit. To ensure the same spatial reference for every laser scan taken, 6 reference spheres were set in preparation of every measurement. Each merged measurement was pre-processed to reduce the number of outliers as well as to cut unnecessary data points. The pre-processed point cloud data were exported and further processed with MATLAB®. The irregular spaced point cloud data were interpolated by a cubic Delaunay triangulation to calculate the Z value of each data point and converted into a regular 3D mesh grid in a 2 mm resolution. Similar as proposed by Vosselman [29] a slope-based filtering method was implemented to reduce remaining outliers. The x- and y- coordinate system was centered to the middle of the structure. Erosion volumes $V_{erosion}(a_i)$ located in a considered interrogation area a_i, were calculated by subtracting the digital elevation model (DEM) from the reference level at the beginning of a test. As stated by Raudkivi and Ettema [30] for the case of monopiles, the extent and shape of a scour hole is related to the pile diameter, but can also be expressed by a dimensionless volume (see Margheritini et al. [20], Hartvig et al. [22]). Accordingly, the dimensionless eroded volume within a certain area a_i is defined in this study as:

$$V_{D,i} = \frac{V_{erosion}(a_i)}{n\,D^3} \tag{3}$$

in which n is the number of piles, a_i a rectangular area (see Figure 3) and D the pile diameter. The investigated erosion patterns are a result of the complex flow and scouring mechanism, which are briefly described in Section 4.1. In the present study the global erosion volume is related with the four main piles of the jacket ($n = 4$) for global erosion calculations and $n = 1$ for local erosion analyses in the near-field of an individual single pile.

In contrast to the erosion volume $V_{D,i}$, the cumulative erosion volume $V_{A,i}$ represents a volume which is related to a normalized ratio of the area a_i/a_1, with a_1 being the area of the structure's footprint. By considering monotonously increasing areas around the structure, the development of the erosion volume with increasing distance from the center of the structure can be evaluated. This approach enables both an insight into the spatial extent and a quantitative measure how the erosion process translates from local to global patterns. By this means also the distance to which the structure has a quantifiable influence on the mobile seabed can be projected. The cumulative erosion volume is defined as:

$$V_{A,i} = \frac{V_{D,i}}{a_i/a_1} \tag{4}$$

$V_{A,i}$ and $V_{I,i}$ both provide a quantity of an erosion volume in reference to a specific area (see Figure 3). The incremental erosion volume $V_{I,i}$ is representing the net gradient volume $(V_{D,i} - V_{D,i-1})$ related to a corresponding ratio of areas $a_i/a_1 - a_{i-1}/a_1$. In addition to $V_{A,i}$, the incremental erosion volume $V_{I,i}$ provides information on the variation of erosion volumes between two individual areas a_i and a_{i-1}. Thereby, it is possible to assess and analyse the volumetric change of sediment with the

erosion intensity as eroded volume per area with an increasing distance from the center of the structure. The incremental erosion volume is given by:

$$V_{I,i} = \frac{V_{D,i} - V_{D,i-1}}{a_i/a_1 - a_{i-1}/a_1} \tag{5}$$

The incremental erosion volume $V_{I,i}$ and the incremental erosion depth $D_{V,i}$ are representing both a net gradient volume, relating to an area between two adjacent interrogation areas a_i and a_{i-1}. The incremental erosion volume $V_{I,i}$ Equation (5) is directly related to Equations (3) and (4) and represents an erosion volume in relation to an area. On the other hand, the incremental parameter $D_{V,i}$ depicts an erosion depth for an interrogation area, calculated by normalisation with the pile diameter. This enables a comparison between scour depths and bathymetric surface data as well as a quantification of local and global scour extends for the design and prediction of the foundation structure:

$$D_{V,i} = \left(\frac{V_i - V_{i-1}}{a_i - a_{i-1}}\right)/D \tag{6}$$

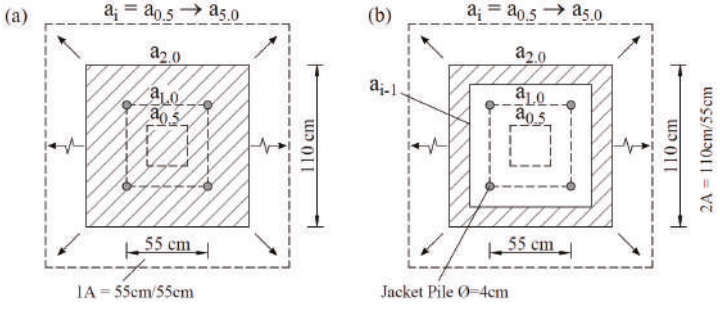

Figure 3. Schematic sketch of increasing rectangular interrogation areas a_i around the present model, (**a**) illustrated exemplarily for an area $a_i = a_2$, related to Equation (4) (a_2 = 1.1 × 1.1 m, shaded area); (**b**) as well as increasing incremental areas, related to Equation (5). Interrogation areas a_i are centered to the structure, starting at $a_{0.5}$ up to a_5.

4. Results

4.1. Changes in Bed Topography

It is reasonable to assume from current understanding of scouring and scour extent, that the near bed flow acceleration around a jacket structure is focused along the individual piles. This in turn leads to a mobilization and transport of the sediment bed. Furthermore, it can be assumed that structural elements as braces which are close to the seabed are generally causing additional vortex shedding and streamline contraction, also leading to a potential increase of bed shear stresses, and thus, sediment mobilization. The interaction of structural elements, flow and sediment bed is particularly pronounced if the structural elements are located close to the seabed, as shown in Welzel et al. [31]. To visualize the impact of the structure on the spatial erosion and deposition of sediment, Figure 4 presents an exemplary photo of the model setup and the final scour pattern after test 4 (additional photos of tests 2–5 are provided and described in Welzel et al. [12]).

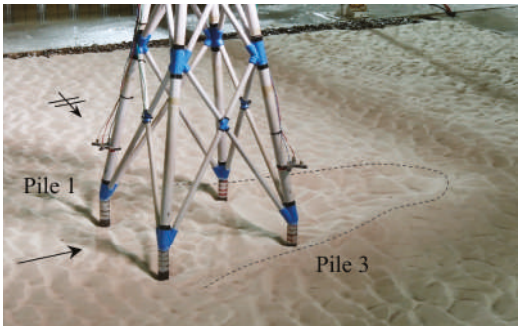

Figure 4. Exemplary photo of the model setup and scour pattern after test 4; the dashed line illustrates the extent of the global scour, current is coming from left to right with 0°, waves are propagating perpendicular in 90°.

In the following, the measured bed topography of tests 1–5 are described and graphically illustrated. Figure 5 is divided in to two color representations, color-coding on the left is optimized to differentiate between global (green) and local erosion (blue) as well as deposition (red). Whereas the colorbar on the right side is optimized regarding different elevations, using an HSV colourmap with an additional computed light source. Distances along the x and y axis are given as a dimensionless value times the structure footprint spacing (see Figure 5), defined in the following as A (A = x or y distance/structure footprint reference distance; e.g., 0.5 A = 0.275 m/0.55 m). Test 1 was conducted under wave only conditions ($U_{cw} = 0$), with waves approaching from 90°. For this condition, an overall deposition of sediment around and beneath the structure was observed (Figure 5a). However, reasonable magnitudes of local scour depths were measured around the piles. Similar to those observed in the local scour development (cp. Welzel et al. [12]), measurements of the present study in general confirm a low erosion, in particular for globally affected areas.

Figure 5b illustrates results stemming from test 2, which is conducted under wave dominated flow conditions (U_m = 20.8 cm/s, KC = 23.4, U_{cw} = 0.33) with a superimposed current of U_c = 10.1 cm/s. The 3D scan reveals short-crested sand ripple migration in the wave direction with slightly longer crests compared to test 1. As the same wave spectra were used as in test 1, the change in bed topography indicates that the superimposed steady current of U_c = 10.1 cm/s has a significant impact on the erosion of sediment around the structure. In contrast to test 1, full coverage of the spatial erosion processes is now visible, which is confined to the area beneath the structure. On the other hand, a large deposition of sediment formed at the lee side of the structure (in terms of current flow direction). The extent of the sediment deposition might be a result of the waves, which prevent the sediment from settling down and instead re-distribute the sediment over a relatively large area. It is assumed that this erosion and deposition pattern is a direct consequence of the sediment being picked-up and entrained by the waves and then being transported downstream by the current. These processes cumulate in an increase in the global scour, which reached a maximum global scour depth of about D_V = −0.3 D in a distance of 1.2–1.25 A.

The 3D scan of test 3 (Figure 5c) reveals a long-crested sand ripple migration into the direction of the progressing wave. The test was conducted with a slightly smaller orbital velocity (U_m = 17.5 cm/s, KC = 14.9) and an increased current velocity (U_c = 22.5 cm/s) compared to the tests before. This led to a wave current velocity ratio of U_{cw} = 0.56. This particular pattern reveals that erosion of sediment was taking place mainly in the direction of wave propagation. This might be a result of the combination of flow contraction stemming from the current component and vortices induced by waves that dominate the local sediment transport process. Nevertheless, in relation to the current direction, deposition of sediment was found on the lee side and at a small distance from the structure, confined to a long-crested

dune-like sediment accumulation. For this test, an erosion depth up to D_V = −0.54 D was measured for a distance of approx. 1.2–1.25 A.

Test 4 (Figure 5d) was conducted under current-dominated conditions ($U_{cw} = 0.75$). Here, sand ripples with comparable long crests and smaller heights (as compared to steady current conditions) migrated in the current direction. Measurements for test 4 indicate a more globally affected erosion process in particular in between the structure's footprint area. Laterally distributed erosion areas, emerging from the upstream located piles (pile 1 and 4), indicate that the bed topography is influenced by structure-induced near-bed vortices that arise from the front piles and might be influenced by perpendicular approaching orbital wave motion. Sediment is deposited behind the structure, elongated in the current direction. The global scour in between the structure footprint (areas ≤ 1 A) is increased significantly (D_V = −0.6 D) in comparison to tests 1–3. The incremental erosion depth value increases on up to D_V = −0.71 D over a distance of approximately 1.2–1.25 A.

Figure 5e illustrates test 5, conducted under steady current conditions without the presence of waves for a flow velocity of $U_C = 38.8$ cm/s ($U_{cw} = 1.0$). The absence of the superposed orbital wave motion led to shorter crested sand ripples migrating in the current direction. Ripples are generally higher and longer than those under combined wave-current load (see Figure 5d). A comparison with studies of [32] and [33] shows a similar bedform of ripples under current only conditions, indicating a fully developed ripple length and height. The 3D scan, depicted in Figure 5d reveals a globally affected erosion pattern with comparable high scour depths (D_V = −0.75 D) in between the structure footprint (areas ≤ 1 A) and a maximum global scour depth of −0.84 D (for 1.2–1.25 A), which is further increased in comparison to test 4. The eroded sediment is deposited behind the structure elongated over a longer distance than shown in test 4.

Present results show that the extent and distribution of the spatial scouring process depends on the hydraulic conditions, i.e., whether the flow is current, or wave dominated. For wave dominated conditions the oscillating flow induced by irregular waves is leading to backfilling of once eroded areas, and thus also to a considerably lower erosion rate, while a more current dominated flow is leading to a more constant bed load and suspended load transport in downstream direction. Therefore, wave dominated conditions of the present study lead to smaller global scour depths, whose pattern seems to align with the direction of wave propagation. Current dominated conditions cause a deeper global scour, whose largest intensity can be found between the individual piles of the jacket structure.

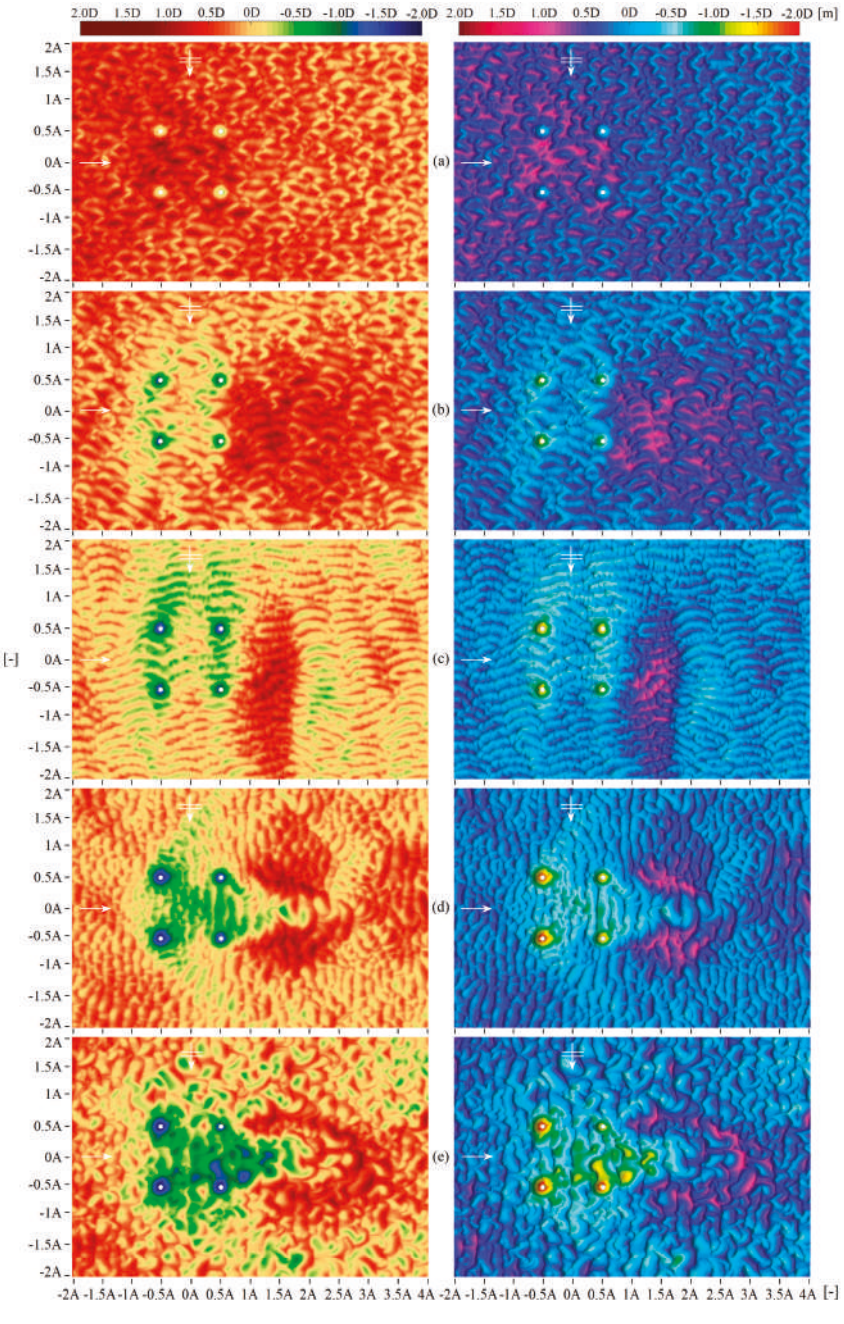

Figure 5. Bed topography measured after test 1–5 (**a**–**e**), top view on erosion and deposition around the jacket structure, current is coming from left to right, waves are propagating in 90° to the current, x and y distances given times the structure footprint length of 0.55 m, 1 A = 0.55 m/0.55 m [-]; (**left**) optimized illustration to differ between global (green) and local (blue) erosion depths as well as deposition (red); (**right**) HSV colourmap to differentiate between different elevations.

4.2. Analysis of Global Erosion Volumes

Figure 6a illustrates the dimensionless eroded sediment volume $V_{D,i}$ with increasing distance from the center of the structure. A general trend of increasing erosion volumes depending on the wave current velocity ratio U_{cw} of each test is depicted. This correlation is in agreement with the observations on the bed topography around the structure as illustrated in Figure 5. The volume of eroded sediment is increased (independently of U_{cw}) with increasing distance from the structure as expected. However, the rate of volume growth with increasing distance is not constant see Figure 6a. Instead, the volume of eroded sediment is increased rapidly in areas in close proximity to the structure and loses its influence with distance from the jacket. Again, this might be expected, as the amount of eroded volume near the structure is mainly controlled by the local scouring process around the piles. With growing distance from the structure, the influence of the global scouring process on the erosion volume diminishes. Thus, the inconsistent development of $V_{D,i}$ is an indication for different erosion processes taking place, the change in the dominance between those processes and thus also an indication for different erosion intensities (eroded sediment volume per area) around the structure.

In addition, to elucidate the dependency of the erosion process on the distance from the structure, Figure 6b illustrates the cumulative erosion volume $V_{A,i}$ as a function of A. Test 1–3 have been conducted under wave current velocity ratios of $U_{cw} = 0$–0.56. In tests 1–3, wave spectra with higher orbital velocities were studied, leading to a more wave dominated erosion pattern with lower values of $V_{A,i}$. In comparison, test 4–5 have been conducted under current dominated conditions, leading to higher magnitudes of $V_{A,i}$. To allow a comparison between each test, whether a more global or more local erosion process dominated the morphodynamic regime, values around the main piles for approx. 1–1.25 A are compared with magnitudes in between the structure footprint 0.5–1 A, which is more affected by global erosion processes. Therefore, the representation of the cumulative erosion volume $V_{A,i}$ reveals a more locally pronounced erosion of sediment around the main piles for test 1–3, as values in between the structure 0.5–1 A are significantly smaller than the maximum value observed in a distance of 1.25 A around the main piles. While measurements for tests 4 and 5 are indicating a more globally affected erosion process as values in between the structure footprint (0.5–1 A) are exhibiting magnitudes of a similar values than the maximum erosion value (1.25 A). However, Figure 6b shows a stable peak at about ~1.25A for each test. Here, the local scour around each pile is superimposed with the global erosion pattern around the foundation structure. Areas in between the structure footprint (A < 1) show larger fluctuations as they are further away from the more stable local scour and normalized over smaller areas. Subsequently, Figure 6b indicates a similar decrease of the cumulative erosion volume $V_{A,i}$ for gradients beyond 1.25 A.

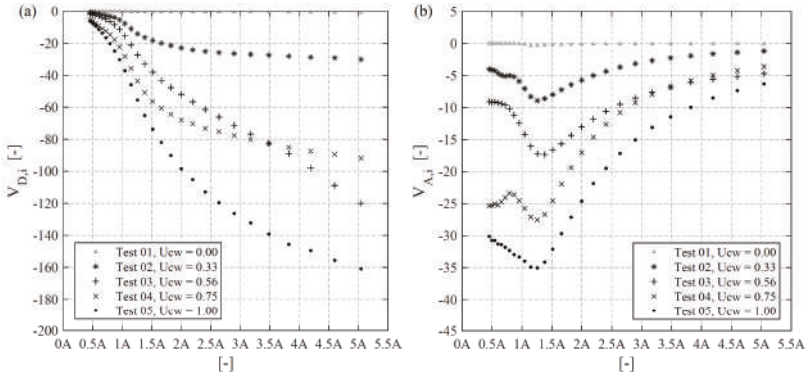

Figure 6. (**a**) Dimensionless eroded sediment volume $V_{D,i}$ (see Equation (3)) as function of the distance from the center of the structure A; (**b**) cumulative eroded volume $V_{A,i}$ (see Equation (4)) in dependency to the dimensionless distance A given times the structure footprint of 0.55 m, 1 A = 0.55 m/0.55 m [-].

As deposition of sediment is not considered, the decrease of eroded volume per area might be explained with a general decrease of flow contraction and disturbances due to vortices. The aforementioned peak of the cumulative eroded volume $V_{A,i}$ at around 1.25 A is compared to U_{cw} in Figure 7. Obviously, a slight current superimposed on waves causes the erosion volume to increase significantly. With further increasing values of U_{cw} the maximum eroded sediment volume increased as well. Furthermore, the comparison of values measured in test 4 and 5 shows the addition of irregular waves reduce the amount of eroded sediment. Overall, Figure 7 reveals a rather strong dependency of the maximum eroded volume on U_{cw}. The maximum of eroded sediment $V_{A,max}$ can be described as a function of the wave current velocity ratio as follows:

$$V_{A,max} = -1.3(0.1 + \exp(-4.6\, U_{cw}))^{-1.5} \tag{7}$$

Equation (7) enables the calculation and prediction of the maximum cumulative erosion volume $V_{A,max}$, which appears to be found in a distance of about 1.25 times the structure footprint. Thus, $V_{A,max}$ quantifies the maximum erosion volume depending on U_{cw} and is convertible into the parameters introduced in Section 3 (Equations (3)–(6)). The knowledge of this distance, as well as of the values of the eroded sediment at this point, might be of practical use for the prediction of scour and the design of a scour protection system in a graduated intensity starting at $V_{A,max}$. By this means, it might be possible to adapt areas with different erosion intensities to different scour protection areas (e.g., different stone sizes) with a reference on the maximum erosion intensity at $V_{A,max}$. Due to the limited number of tests, the influence of different KC numbers on the transition between wave and current dominated hydrodynamic conditions could not be studied as of now. However, it is expected, that a wide range of U_{cw} and KC values would lead to an array of non-dimensional erosion volume curves comparable to the transition of wave and current dominated scour depth at a jacket structure, see Welzel et al. [12] as well as originally developed for cylindrical piles (see e.g., [14,26,27,34–36]).

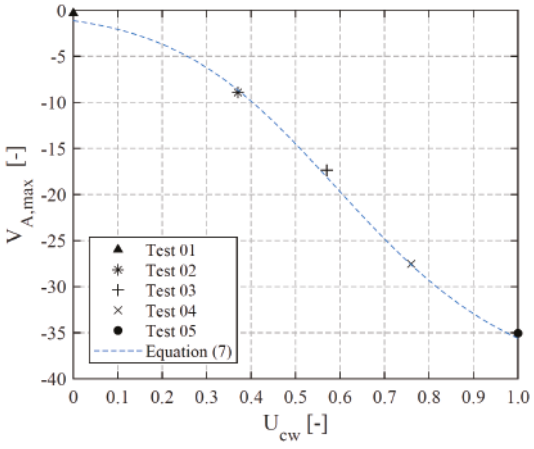

Figure 7. Maximum cumulative erosion volume $V_{A,max}$ (see Equation (4)) of test 1–5, depicted over the wave current velocity ratio U_{cw} (see Equation (2)) in comparison to Equation (7) (see also Figure 6b; ~1.25 A).

Figure 8 illustrates the cumulative erosion volume $V_{A,i}$ (see also Figure 6b) normalized with the maximum value $V_{A,max}$ for each test to further elaborate the differences in the development of erosion volumes over the distance from the center of the structure. Starting from a distance of 1.25 A, this representation reveals a rapidly increasing dependency on hydraulic conditions with decreasing distance. Therefore, values corresponding to test 1–3 reveal lower magnitudes in between the structure footprint (0.5–1 A), while values of test 4–5 show magnitudes (0.5–1 A) similar to $V_{A,max}$ around the

main piles. On the other hand, for distances larger than 1.25 A, the dependency of erosion volumes on the hydraulic condition is much less pronounced. Values for distances > 1.25 A reveal a similar decreasing trend for gradients of eroded sediment. Figure 8 also indicates that the global scouring process is more affected by a change of hydraulic conditions and the interaction of the structure than by the local erosion process, which is limited to approximately 1–1.25 A. An exception is test 1, where large amounts of sediment were deposited near the structure. Test 1 was considered as an outlier for the derivation of Equations (9) and (10) as the test was influenced due to sediment deposition around the structure (see Section 4.1). A combination of Equation (7) and additional terms, that relate to the increase and decrease of erosion volume with change in U_{cw} and distance to structure, leads to a general description of non-dimensional areal erosion volumes for the present study:

$$V_{A,i} = V_{area} - 1.3(0.1 + \exp(-4.6\ U_{cw}))^{-1.5} \tag{8}$$

with:

$$V_{area\ A\ <\ 1.25A} = (0.1 + \exp(-10\ A + 8))^{-0.9} B - C \tag{9}$$

$$V_{area\ A\ >\ 1.25A} = -2.2\ \exp(-0.7\ A) - 0.11 \tag{10}$$

In which $V_{A,i}$ is calculated for the development over the wave current velocity ratio U_{cw}, multiplicated with a factor V_{area} in relation to the size of the area to consider for areal volume differences. Equation (9) accounts for the development of distances < 1.25 A, with $B = (-5.2\ U_{cw} + 6.9)10^{-2}$ and $C = (3.8\ U_{cw} + 4.9)10^{-1}$ to account for different wave current velocity ratios (U_{cw}), while Equation (10) describes the decreasing trend of dimensionless erosion volumes for areas > 1.25 A in dependency to the size of the considered area, which is given with the dimensionless distance A (structure footprint = 1 A).

Equation (8) (approx. R^2 = 0.87) allows the calculation of cumulative erosion volumes $V_{A,i}$ which makes it possible to quantify the intensity of erosion in reference to the spatial extent. Values calculated with Equation (8) can be converted into parameters introduced in Section 3, Equations (3)–(6). In consequence, it is possible to estimate sediment volumes or scour depths in relation to the hydraulic condition or distance from the center of the structure. The calculated erosion volumes can give important information about a possible impact of a structure or a wind park on the natural dynamics of the ocean floor environment. The knowledge of the value of eroded sediment around and within the foundation structure, thus is also of practical use for the prediction of scour depths or eroded sediment volumes, in example for the design of a structure or a scour protection system around such complex foundation structures.

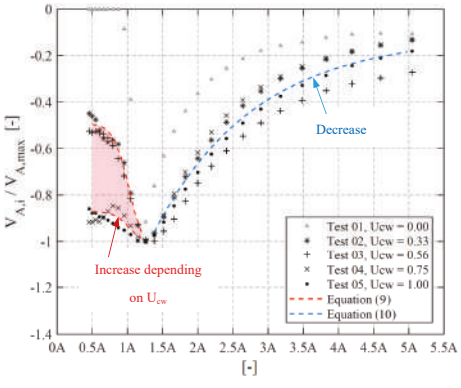

Figure 8. Cumulative erosion volume $V_{A,i}$ (see Equation (4)), normalized with the maximum value $V_{A,max}$ as a function of the distance A to the center of the structure, compared with predicted erosion volumes relating to Equation (9), A < 1.25 A and Equation (10) for A > 1.25 A, R^2 = 0.87 for Equation (8) including Equations (9) and (10).

Figure 9 is illustrating cumulative erosion volumes $V_{A,i}$, compared with calculated values of Equation (8) in relation to the distance of each interrogation area to the center of the structure. Measured areal erosion volumes generally agree with the calculated values relating to Equation (8). Nevertheless, some minor differences can be recognized for the areal development (regarding the representation of Equations (9) and (10)) of test 3 and 4.

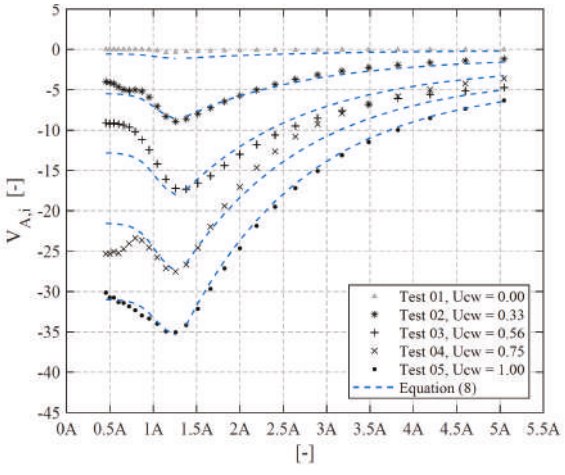

Figure 9. Cumulative erosion volume $V_{A,i}$ (see Equation (4)) as a function of the distance A to the center of the structure, compared with calculated values after Equation (8).

A comparison of erosion volumes for test 3 (see Figure 9) shows lower eroded sediment volumes within areas of 0.5 A up to 1.25 A as well as slightly higher erosion volumes for areas > 1.25 A. In contrast, test 4 reveals a slightly higher erosion intensity (erosion per area) for the areal development within 0.5–1.25 A as well as a lower intensity for areas > 1.25 A for measured compared to predicted values, see Figure 9. Additionally, Figure 10 illustrates the non-dimensional incremental erosion volumes around the jacket structure and compares them with predicted values obtained with Equation (8). The comparison with Equation (8) shows that predicted values (calculated with Equation (8) and converted from $V_{A,i}$ in to $V_{I,i}$) can correctly describe measured values of $V_{I,i}$ of the present study. In contrast to $V_{A,i}$, the incremental erosion volumes $V_{I,i}$ exhibit an enhanced fluctuation near the pile which can be explained with the calculation method related to Equation (5). For a distance from the center of the structure > 1.2 A, erosion rates decrease significantly towards an equilibrium stage at a distance of about 3.5 A. The convergence of erosion volume within all tests might thus be used to define the maximum extent of the global scour around the structure. Due to a natural ripple migration under live bed conditions, a certain erosion rate still remained for areas which were unaffected by the immediate structure's influence on the flow. Therefore, the global scour extent is defined with a threshold of less than 10% of the peak value (at 1.2 A), in reference to the value of an interrogation area, located in a distance of 5 A. For all tests this was the case at a distance between 2.1–2.7 A. As a consequence, the maximum erosion intensity (erosion per area) is reduced by about 90% in this distance. Contrary to approaches which were partly applied to predict global scour development in the past (see e.g. Bolle et al. [10] and Sumer and Fredsøe, [14]), the present study reveals a significant impact of the complex structure on the morphodynamic regime, which extends up to a distance of 2.7 A from the structure.

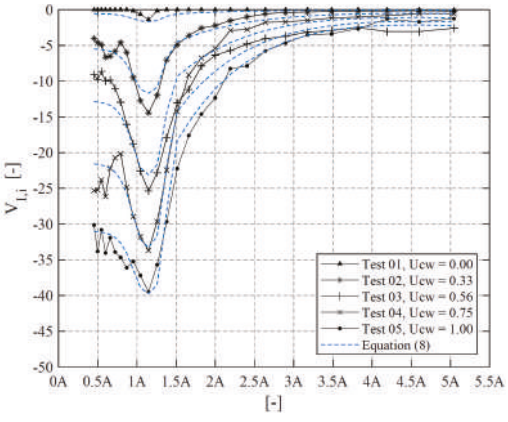

Figure 10. Incremental erosion volume $V_{I,i}$ (see Equation (5)) depicted over the structure footprint length A and compared with calculated values stemming from Equation (8).

To provide a comparison to data obtained in the field, Figure 11 juxtaposes data measured in this study with in-situ field data from Rudolph et al. [8], Baelus et al. [9] and Bolle et al. [10]. As erosion volumes are not available for the field datasets, the data is given in terms of the incremental erosion depth $D_{V,i}$ in Figure 11. Bolle et al. [10] and Baelus et al. [9] presented field data around the same jacket structure (with D_{pile} approx. = 2 m) in the Thornton Bank offshore wind farm located in the southern North Sea. The authors analyzed several scans of the bed topography at various points in time over a period of three years. Rudolph et al. [8] analyzed bathymetric surveys after three years around a wellhead jacket production platform which was founded by additional post piles and near bed braces. A comparison between common prediction approaches for single piles and the scour development observed in [8] led to a factor of 3–4 times the predicted local scour depths, which might be explained by the disturbing effect of additional structural elements close to the seabed. In consequence, the disturbance impact of the foundation structure on the scour development could not be represented by the pile diameter $D_{pile} = 1.2$ m alone. Instead, the influence of additional post piles as well as the horizontal and diagonal braces have to be considered since additional effects increase the local contraction of the flow and influence the vortex system. Therefore, data of Rudolph et al. [8] are compared in Figure 11 with the post pile diameter = 1.2 m, as well as with an artificially increased diameter = 2 m, similar to the one in [9] and [10]. Furthermore, the data shown in Figure 11 are calculated in reference to the post dredging survey given in [9] and [10] as well as a reference value given in [8]. Whereas a direct comparison of magnitudes of erosion depths between the present study and the field measurements is hindered by missing information on hydraulic conditions, the development of erosion depth with changing distance from the center of the structure can be compared. Therefore, it is revealed that the in-situ field data are generally in agreement with the areal distribution of the incremental erosion depth measured in the present study, given in Figure 11 with the dependence to the dimensionless distance A. The comparison shows in particular that the bathymetric surveys, similarly, yield a peak of erosion depth at a distance of around 1.2–1.25 A. In addition, all datasets exhibit a similar development of erosion depths before and after this distance, i.e., a rapid increase of depths towards the structure and a slower decrease with increasing distance.

As the bed topography, especially shown in Baelus et al. [9] was illustrated over an area of A > 3, the global scour extent is analyzed related to the previously introduced definition. The bathymetric surveys of [8] and [9] indicate a reduction of the maximum erosion rate by 90% in a distance of 2.7–2.8 times the structure footprint length (2.7–2.8 A), which is in line with the distance obtained for the data in this study. In this respect, the bathymetric surveys of Bolle et al. [10] show a time dependent context of the global scour development around the jacket foundation as those surveys

were conducted 3 and 5 months after the installation. On the other hand, the bathymetric surveys of Rudolph et al. [8] and Baelus et al. [9] were measured three years after the installation of the jacket structure. In addition to the varying and unknown hydraulic conditions, differences between the field data and the test results might stem from a difference in the time dependent stage of the global scour development as well as differences in the structural design.

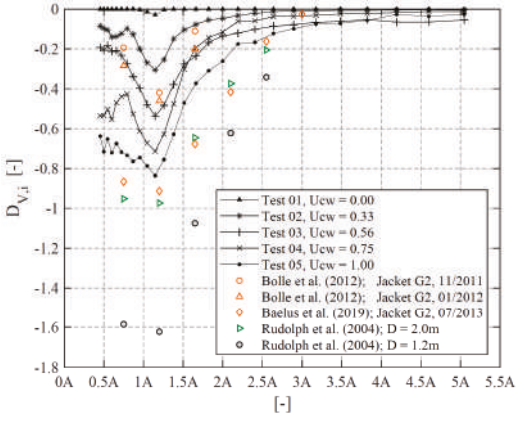

Figure 11. Global erosion of the dimensionless incremental erosion depth $D_{V,i}$ (see Equation (6)) around the jacket structure plotted over the structure footprint A, compared with in-situ field measurements of Rudolph et al. [8], Baelus et al. [9] and Bolle et al. [10].

The previously described comparison illustrates that findings stemming from the present laboratory study, generally agree with data from field studies (surveys of Rudolph et al. [8]; Baelus et al., [9] and Bolle et al. [10]). Furthermore, it is shown that predicted values (calculated with Equation (8)) generally agree with measurements from the present study. It is shown that the introduced equations and methods generally account for the spatial extent of global erosion volumes and scour depths around the compared jacket structures, also for jacket structures which have a non-symmetric footprint as shown with the compared field data of Rudolph et al. [8]. Additionally, it is revealed that it is possible to determine areas which exhibit or exceed a certain erosion rate. A similar areal distribution of eroded sediment volume as well as a global scour extent in a range of the present study (2.1–2.7 A) is found with a comparison of in-situ data (2.7–2.8 A). The comparison between the present study and in-situ field measurements reveals a significant impact on the near field ($A < 1$) but also on the morphodynamic regime close to the structure ($2.7 > A > 1$). Furthermore, the analysis proves, that jacket structures, known as "hydrodynamic transparent" can also cause global scouring under certain hydrodynamic conditions.

4.3. Local Scour around Individual Piles

In this section the local scour around each pile is analyzed thoroughly and compared with the global erosion on the near-field bed topography around the structure. For this, local and global erosion volumes are analyzed and defined. In contrast to definitions given in previous paragraphs, related interrogation areas a_i are arranged in a circular pattern and are related to a distance times the pile diameter (see Figure 12).

Figure 13 shows a top view of the measured bed topography over an area of 7 D around each pile. X and Y coordinates refer to the center of each individual pile and are given in multiples of the diameter. This allows a direct comparison between the bed topography and the analyzed erosion depths $D_{V,i}$. A shadowing effect of the jacket piles, which could not be eliminated with the present filtering method, seemed to have only marginal influence on the computed surface elevation near

the piles. This is observed for example in Figure 13e around pile 1. The influences were found to be negligible for the calculated erosion volumes.

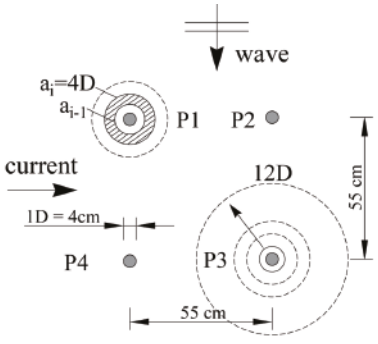

Figure 12. Schematic showing the increasing circle interrogation areas a_i around pile (P1–P4), illustrated exemplarily for a circle area a_i with a diameter of 4 D for pile 1, related to Equation (6).

Similar to what was found in the global erosion analysis, the local bed topography generally confirms the trend of deeper scour with an increasing wave current velocity ratio. The bed topography of test 1 (Figure 13b), on the one hand, illustrates the deposited sediment volume as an influence on the measurement, but on the other hand, also shows a reasonable local erosion depth around each pile. Furthermore, the bed topography for tests 2–5 (Figure 13c–f) shows an increase in scouring on the upstream side of each pile, relative to the current direction, as well as higher erosion rates for pile 1 and 4 (upstream located, in current direction) in comparison to pile 2 and 3 (downstream located). The bed topography measured for tests 4 and 5 around pile 1 and 4 (Figure 13e,f) shows a similar magnitude of erosion. As shown by Welzel et al. [12], for current dominated flow conditions with values of $U_{cw} >$ 0.7 the local scour depth approach values similar to that in current only conditions, whereas the bed topography measured after test 5 (Figure 13f) shows a significant deeper scour around pile 3 and a less pronounced scour depth around pile 2 than around the equivalent piles after test 4. Nevertheless, a clear explanation despite the fluctuations due to erosion and backfilling is not found yet for the difference between pile 2 and 3 at the end of test 5. Furthermore, especially test 4 and 5 reveal a slightly higher erosion of sediment in an area under the diagonal braces (crossing the current direction), which is an indicator for increased bed shear stresses below these diagonal braces. A similar erosion pattern with increased scour depths below the braces was found by Welzel et al. [31], who conducted tests for the same hydraulic conditions and the same jacket structure, only with the difference that the lowest nodes were closer to the seabed.

Figure 14 compares the development of the erosion depth $D_{v,i}$ for each pile over increasing circle areas. Independent of the hydraulic condition and the position of each pile, the maximum erosion depth was always found at a distance from the pile of around 2 D. At the inner most points measurements show that the bed elevation appears to decrease again. As shown in Figure 14 measurements, related to areas > 2 D reveal a similar decreasing trend of erosion, in relation to the slope of the scour hole. As sand is being re-distributed, the local slope angle exceeds the internal friction angle, hence the inner frictional forces of sediment grains are not able to withstand the gravity acting on the grains and thus sediment sliding occurs. Sediment slides from higher to lower locations of the bed and erodes again. A comparison of the incremental erosion depth $D_{V,i}$ of global areas (cp. Figure 11) with local erosion depth values (Figure 14) illustrates a significantly higher erosion per surface area for eroded sediment close around each pile. With distance from the pile, the erosion depth resembles that of the global erosion value. However, it remains strongly dependent on U_{cw} even for larger distances to the pile. The global scour depths for different values of U_{cw} clearly converged with increasing distance from the structure, indicating a boundary of influence of the structure's interaction with the flow. The influence

is not as clear for the local scouring processes around the main piles, illustrated in Figure 14. The global erosion causes a subsidence of the seabed simultaneously to the deepening of the local scour hole. However, Figure 14 reveals a boundary of influence at a distance from the pile at which the gradient of the erosion depth clearly decreases. Based on this definition, the size of the local scour hole is found to be about 5–6 D for the present study and 3 D as an outlier for test 1. Thus, the maximum extent of the local scour hole is defined as six times the pile diameter. The distance of about 6 D, at which the gradient of erosion clearly decreases, thus might be interpreted as the boundary of influence of the local scour processes on the global ones. The knowledge of this distance, as well as of the values of eroded sediment, is of practical use for the design of a scour protection system and the required spatial extent.

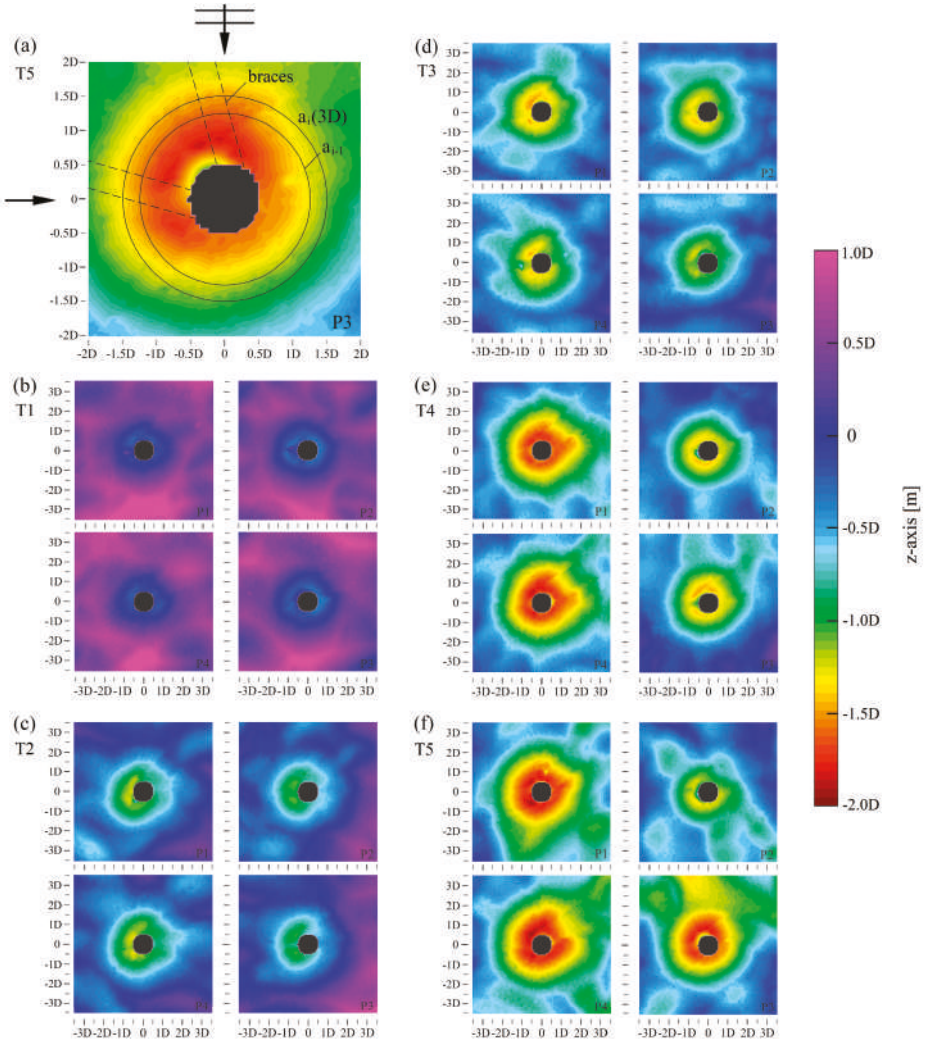

Figure 13. (**a**) Local bed topography, illustrated as an example for test 5, pile 3 with a sketch of the diagonal braces, including the direction of the incoming current, which is coming from left to right, waves are perpendicular to the current as well as exemplary circles related to an incremental interrogation area of 3 D and the directions of the diagonal braces; (**b–f**) local bed topography related to test 1–5; (**b–f**) in an area of 7 D around each main pile of the jacket structure.

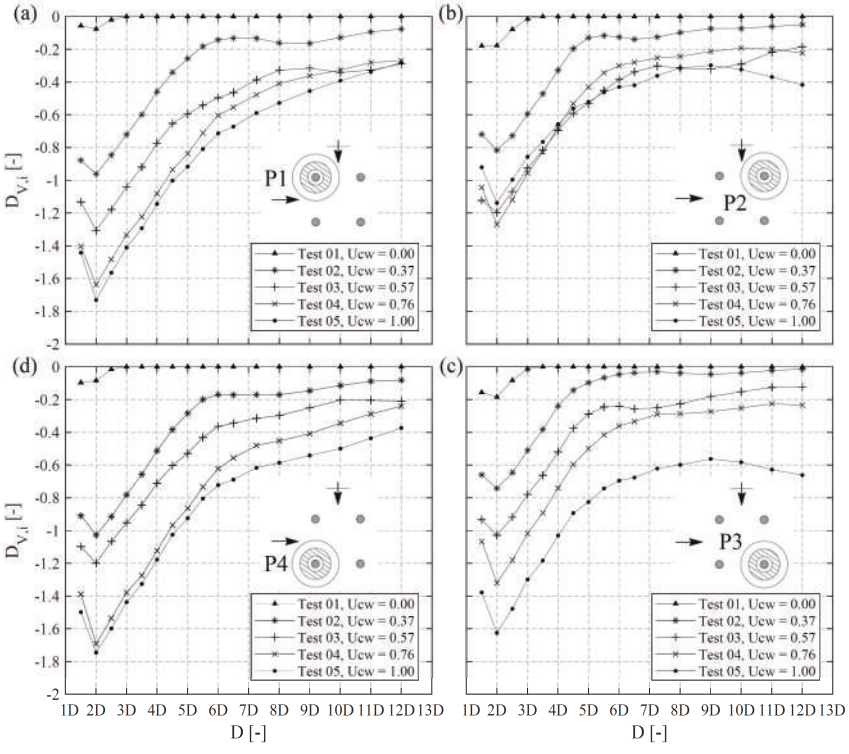

Figure 14. Local, nondimensional erosion depth D_V (see Equation (6)) plotted over increasing diameters D around pile 1–4 (**a**–**d**), inner graphical subset of figure a–d is showing the related pile location, current (0° from left to right) and wave (90° perpendicular to the current) direction.

The literature reports that hydrodynamic interactions are relatively small for distances > 6 D around circular cylinders [16–18], which is partly transferred as a border of influence for global scouring processes [10]. The present jacket model has a spacing of ~14 D between the pile centers, which is far above a previously described critical distance of 6 D. The volume analysis presented in paragraph 3 proves that there is a significant influence on the global erosion for areas > 6 D for the present structure. Nevertheless, the illustrated erosion depth shown in Figure 14 also confirms that hydrodynamic interactions are significantly smaller for distances > 6 D.

To quantify and compare local and global erosion processes on the overall eroded sediment volume, global erosion volumes are calculated for a threshold of 1.25 A as this distance was found to mark the maximum erosion intensity around the structure. The local eroded sediment volume is considered to be limited to an area of approximately 6 D, as discussed previously, and is summed up for all four piles. Figure 15 illustrates the difference between local and global dimensionless erosion volumes V_D as a function of U_{cw}. For values smaller than U_{cw} = 0.56 large amounts of the global erosion volume can be attributed to local scouring processes around the individual piles. In particular, for U_{cw} = 0.56, 68% of the erosion volumes can be referred to locally eroded sediment and 32% to globally eroded sediment volumes. However, Figure 15 also reveals that the share of global erosion processes is significantly increased in current dominated hydrodynamic conditions. Measurements of the present study show an increase to about twice the amount of locally eroded sediment volume under current dominated conditions, see Figure 15.

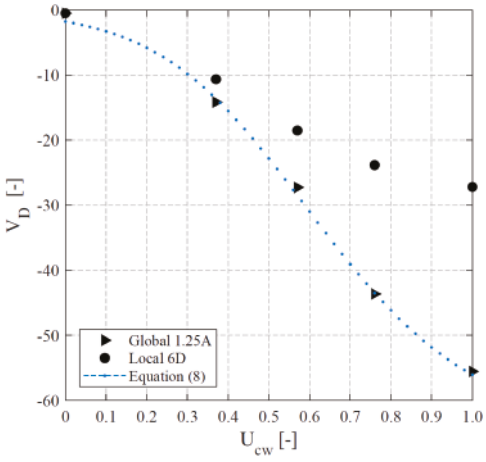

Figure 15. Comparison between non-dimensional local erosion volumes V_D (see Equation (3)) of pile 1–4, depicted over the wave current velocity ratio U_{cw} (see Equation (2)) for circular areas of 6 D and global erosion volumes for rectangular areas of 1.25 times the structure footprint length (1.25 A).

5. Remarks Regarding Practical Application and Scale Effects

Remark 1: Uncertainties regarding various scale effects may exist and must be considered when results of small-scale experiments are extrapolated to prototype conditions. Scale effects in laboratory experiments with a movable bed, e.g., the erosion of sediment, are attributed to the well-known difficulties in geometrically scaling sediment [37,38]. To avoid cohesive behaviour, the sediment was not geometrically scaled in accordance with the model length scale. Instead, to ensure some form of similitude of sediment mobility, the flow velocities were scaled related to the desired flow intensities, i.e. to reach shields parameters (calculated after Soulsby and Clarke [39]) close to the critical Shields parameter. In addition, wave parameters were selected to achieve a certain range of Keulegan-Carpenter numbers and wave current velocity ratios U_{cw}. As a result of the disproportional scaled sediment, i.e., relatively large grain sizes compared to field conditions with comparable small velocities in the present tests, it is expected that bedload transport is thus overrepresented in relation to suspended sediment transport. In consequence, a complete similitude in sediment transport and sediment pick-up rate is not reached. A possible scale effect in consequence of the underestimated ration of suspended load might be that sediment is transported over shorter distances as in prototype scale, presumably leading to different deposition patterns of sediment.

Remark 2: As a consequence of the disproportionally scaled sediment, the bed forms, e.g., ripples are also larger in the laboratory experiments than in the field. The dynamic flow field over ripples causes form drag and turbulence associated with erosion on the stoss side (upstream side) and deposition of sediment on the lee side (downstream side) of the ripples. As an effect of the increased ripple size the boundary layer is also affected and might be increased in thickness, thus leading to a larger horseshoe vortex, influencing the scour development around the piles [14]. Furthermore, according to Sutherland and Whitehouse [40] there is an increased sediment transport due to ripple migration in a model with non-linear flows with proportional larger ripples than in a prototype scale with equally non-linear flows.

Remark 3: In order to compare the present results with field measurements, it is also important to know which temporal stage of the scouring process was reached during the tests, i.e., whether or not an equilibrium stage was achieved. As tests of the present study have been part of Welzel et al. [12], in which the development of scour around the jacket at different locations over time was analyzed, the test duration was generally chosen to enable the scour process to reach the equilibrium

stage. By an extrapolation of the expected equilibrium scour depths, Welzel et al. [12] concluded that around 90% of the equilibrium depths were reached for the local scouring processes at the end of the tests. In contrast, the study did not show a clear attainment of an equilibrium stage for measurements related to the global scour depth, particularly under higher current velocities. With a scale factor of 1:30, present test durations correspond to a storm duration of ~20–45 hours, depending on the wave period. This is in the range of typical storm durations in the North Sea [41], but presumably not enough to reach a global scour equilibrium stage (also under laboratory conditions). The local scour depth data and combined bed topography data of Baelus et al. [9] and Bolle et al. [10] indicate a similar trend of a faster developing local scour and a slower developing global scour. Results of [9,10] and [12] therefore indicate that local and global scouring rates are controlled by scouring processes on different time scales. However, the results also indicate that local and global scouring processes are affected by a characteristic depth ratio but are correlated to each other by means of entwined feedback mechanisms, presumably leading to an influence of the global scour on the local scour development and vice versa (see [12]). In particular, the timescale of the global scour development as well as the impact on the local scour development seems to be an important research question in this context, which remains unsolved.

Remark 4: Furthermore, it should be noted that prediction approaches as Equation (8) and Equation (7) are derived for tests based on the present study. Therefore, caution must be exercised when these equations are applied and extrapolated to prototype conditions. To better estimate differences to prototype conditions, scale effects have been discussed and measurements of the present study were compared to available field studies on the scour development around jacket structures (see Figure 11).

6. Summary and Conclusions

Only a few studies exist which provide an approach to analyze complex erosion patterns around offshore foundations. Therefore, hydraulic model tests were carried out, investigating the spatial erosion process in the near-field and vicinity of the hydrodynamic transparent jacket-structure in combined wave and current conditions. The main conclusions can be summarized as follows:

- Different volume analyzing methods and dimensionless parameters are introduced which can be generally adapted for any other offshore structure or coastal structure to reveal physical processes in complex erosion patterns. Therefore, eroded sediment volumes are normalized in relation to a structural volume $V_{D,i}$ as well as in relation to the considered erosion area, $V_{A,i}$, $V_{I,i}$ and the structural diameter $D_{V,i}$, given in Equations (3)–(6).
- A comparison between locally (circle area of 6 D around each pile) and globally (area of 1.25 times the structure footprint) attributed erosion volumes revealed that wave dominated hydrodynamic conditions with $U_{cw} \leq 0.57$ led to scour patterns which were dominated by local erosion around the piles (68% locally, 32% globally, for $U_{cw} = 0.57$). Furthermore, it is shown that the share of globally eroded sediment volume is significantly increased in current dominated conditions $U_{cw} \geq 0.75$ (33% locally, 67% globally, for $U_{cw} = 1.0$).
- The literature reports that hydrodynamic interactions between groups of circular piles are small if the distance between them is larger than six times the piles' diameter [14–16]. In the past, this was partly interpreted as a border beyond which global scour around jacket-type foundations may not occur [10]. In contrast to this, insights from the present study illustrate that the area of the seafloor affected by a supposedly transparent hydraulic structure is considerably larger than expected and is estimated to be 2.1–2.7 times the structure's footprint for the present study.
- A comparison reveals that findings stemming from the present study generally agree well with in-situ data from field studies [8–10]. Similar areal distributions of eroded sediment volume with a stable maximum of the erosion intensity at 1.25 A (1.25 times the structure's footprint) as well as a global scour extent in a similar range to the present study (2.1–2.7 A) is found from a comparison of in-situ data (2.7–2.8 A).

- To improve the prediction of global scour around jacket-type offshore foundations, empirical expressions (Equations (7) and (8)) are proposed to account for the areal development and extent of global erosion volumes and scour depths in the near-field and vicinity of the foundation structure. The analysis and derivation is explained stepwise and is based on insights of the introduced methods. Furthermore, the knowledge of the extent of erosion patterns in relation to the erosion intensity, as well as of the value of the eroded sediment at different points, is useful for the design of a scour protection system around such complex foundation structures. While the former might be used to determine the required spatial extent of a scour protection, the latter helps determining the volume, which has to be refilled by a subsequently installed scour protection.
- Results allow a prediction of areas which exceed a certain erosion rate as well as a quantification of spatially eroded sediment in the near-field and vicinity of the foundation structure. By this means a structure-induced environmental footprint as a measure of eroded sediments partially affecting marine habitat can be exposed. Once eroded sediment is entrained into the water column it deposes behind the structure with the effect of burying marine habitats and can be transported over long distances due to long lasting vortices and an increased turbulence and mixing [5–7]. As a consequence, not only areas in the vicinity but also in the far-field of the structure can be affected, with potential impacts [2–4] on the marine wildlife and the ocean seabed environment in general. These potential impacts to the marine environment might represent an important hurdle for the future of wind technology in general.

Author Contributions: For this research article the specifying of the individual contributions of the authors is as follows: idea and concept of the article, M.W.; methodology, M.W.; investigation and volume calculations, M.W.; resources, T.S.; writing—original draft preparation, M.W.; writing—review and editing, M.W., A.S., T.S. and A.H.; supervision, T.S. and A.H.; project administration, T.S. and A.H.; funding acquisition, T.S.

Funding: The present study is part of the research project "HyConCast—Hybrid substructure of high strength concrete and ductile iron castings for offshore wind turbines" (BMWI: 0325651A). The authors gratefully acknowledge the support of the German Federal Ministry for Economic Affairs and Energy within the funded project. The publication of this article was funded by the Open Access fund of Leibniz Universität Hannover.

Acknowledgments: The authors gratefully acknowledge the support of T. Kreklow, and F. Faltin for their support in conducting the laboratory experiments and pre-processing of the 3D scan data. The authors thank also the FZK and in particular M. Miranda-Lange for support related to the 3D scanner.

Conflicts of Interest: The authors declare no conflict of interest.

Notations

	Reference distance times the structure footprint length;
A	A given times the structure footprint distance, for this structure 0.55 m in both directions, 1 A = 0.55 m/0.55 m, A = x or y distance / structure footprint distance in x or y direction
a_1	Structure footprint area; for the present study $a_1 = 0.55\ m \times 0.55\ m$
a_i	Interrogation area a_i in dependence to i
B	Additional term of equation (9); $B = 10^{-2}(-5.2\ U_{cw} + 6.9)$
C	Additional term of equation (9); $C = 10^{-1}(3.8\ U_{cw} + 4.9)$
D	Pile Diameter of the main struts of the jacket structure D or D_{pile}
D_{sleeve}	Diameter of the pile sleeve of the jacket structure
D_{leg}	Diameter of the legs of the jacket structure
$D_{V,i}$	Incremental erosion depth; representing an erosion depth of the related interrogation area times the pile diameter
d_{50}	Grain size for which 50% of the material by weight is finer
f	Frequency
g	Gravitational acceleration
H_s	Significant wave height
KC	Keulegan-Carpenter number
n	Number of piles

$S(f)$	Velocity frequency spectrum
U	Orbital velocity at the bed in direction of the waves
U_c	Undisturbed current velocity at 2.5 D from bed
$\overline{U}$	Mean current velocity of the vertical profile
U_{cw}	Wave-current velocity ratio $U_{cw} = U_c/(U_c + U_m)$
U_m	Undisturbed maximum orbital velocity at 2.5 D from bed
U_{rms}	Root-mean-square (RMS) value U of at the seabed
$V_{A,i}$	Cumulative erosion volume; $V_{D,i}$ in relation to each normalized area a_i/a_1
V_{area}	Additional term in equation (8) to account for the areal development of volumes
$V_{D,i}$	Dimensionless erosion volume; $V_{erosion}$ of an interrogation area a_i in relation to the structural reference volume
$V_{I,i}$	Incremental erosion volume; the net gradient volume $\left(V_{D,i} - V_{D,i-1}\right)$ in relation to each corresponding area $a_i/a_1 - a_{i-1}/a_1$.
$V_{erosion}$	Eroded sediment volume in m^3 below a reference value based on the pre-scans
θ	Shields parameter
θ_{cr}	Critical value of the Shields parameter

References

1. International Renewable Energy Agency (IRENA). *Offshore Innovation Widens Renewable Energy Options: Opportunities, Challenges and the Vital Role of International Co-Operation to Spur the Global Energy Transformation (Brief to G7 Policy Makers)*; IRENA: Abu Dhabi, UAE, 2018.
2. Carpenter, J.R.; Merckelbach, L.; Callies, U.; Clark, S.; Gaslikova, L.; Baschek, B. Potential Impacts of Offshore Wind Farms on North Sea Stratification. *PLoS ONE* **2016**, *11*, e0160830. [CrossRef] [PubMed]
3. Shields, M.A.; Woolf, D.K.; Grist, E.P.M.; Kerr, S.A.; Jackson, A.C.; Harris, R.E.; Bell, M.C.; Beharie, R.; Want, A.; Osalusi, E.; et al. Marine renewable energy: The ecological implications of altering the hydrodynamics of the marine environment. *Ocean Coast. Manag.* **2011**, *54*, 2–9. [CrossRef]
4. Miller, R.G.; Hutchison, Z.L.; Macleod, A.K.; Burrows, M.T.; Cook, E.J.; Last, K.S.; Wilson, B. Marine renewable energy development: Assessing the Benthic Footprint at multiple scales. *Front. Ecol. Environ.* **2013**, *11*, 433–440. [CrossRef]
5. Grashorn, S.; Stanev, E.V. Kármán vortex and turbulent wake generation by wind park piles. *Ocean Dyn.* **2016**, *66*, 1543–1557. [CrossRef]
6. Vanhellemont, Q.; Ruddick, K. Turbid wakes associated with offshore wind turbines observed with Landsat 8. *Remote Sens. Environ.* **2014**, *145*, 105–115. [CrossRef]
7. Vanhellemont, Q.; Ruddick, K. Landsat-8 as a Precursor to Sentinel-2: Observations of Human Impacts in Coastal Waters. Presented at the 2014 European Space Agency Sentinel-2 for Science Workshop, Frascati, Italy, 20–23 May 2014. ESA Special Publication SP-726.
8. Rudolph, D.; Bos, K.J.; Luijendijk, A.P.; Rietema, K.; Out, J.M.M. Scour Around Offshore structures—Analysis of Field Measurements. In Proceedings of the Second International Conference on Scour and Erosion, ICSE 2, Singapore, Singapore, 14–17 November 2004.
9. Baelus, L.; Bolle, A.; Szengel, V. Long term scour monitoring around offshore jacket foundations on a sandy seabed. In Proceedings of the Ninth International Conference on Scour and Erosion, ICSE 9, Taipei, Taiwan, 5–8 November 2018.
10. Bolle, A.; de Winter, J.; Goossens, W.; Haerens, P.; Dewaele, G. Scour monitoring around offshore jackets and gravity based foundations. In Proceedings of the Sixth International Conference on Scour and Erosion, ICSE 6, Paris, France, 27–31 August 2012.
11. Chen, H.H.; Yang, R.Y.; Hwung, H.H. Study of Hard and Soft Countermeasures for Protection of the Jacket-Type Offshore Wind Turbine Foundation. *J. Mar. Sci. Eng.* **2014**, *2*, 551–567. [CrossRef]
12. Welzel, M.; Schendel, A.; Hildebrandt, A.; Schlurmann, T. Scour development around a jacket structure in combined waves and current conditions compared to monopile foundations. *Coast. Eng.* **2019**, *152*, 103515. [CrossRef]
13. Sumer, B.M.; Fredsøe, J. Wave scour around group of vertical piles. *J. Waterw. Port Coast. Ocean Eng.* **1998**, *124*, 248–256. [CrossRef]

14. Sumer, B.M.; Fredsøe, J. *The Mechanics of Scour in the Marine Environment*; World Scientific: Hackensack, NJ, USA; Singapore; London, UK; Hong Kong, China, 2002.
15. Yagci, O.; Yildirim, I.; Celik, M.F.; Kitsikoudis, V.; Duran, Z.; Kirca, V.S.O. Clear water scour around a finite array of cylinders. *Appl. Ocean Res.* **2017**, *68*, 114–129. [CrossRef]
16. Breuers, H.N.C. *Local Scour Near Offshore Structures*; Delft Hydraulics Publication: Delft, The Netherlands, 1972.
17. Hirai, S.; Kuruta, K. *Scour around multiple- and submerged circular cylinders. Memoirs Faculty of Engineering*; Osaka City University: Osaka, Japan, 1982; Volume 23, pp. 183–190.
18. Hildebrandt, A.; Sparboom, U.; Oumeraci, H. Wave forces on groups of slender cylinders in comparison to an isolated cylinder due to non-breaking waves. In Proceedings of the International Conference on Coastal Engineering, NO. 31, Hamburg, Germany, 31 August 2008.
19. Porter, K.E. Seabed Scour Around Marine Structures in Mixed and Layered Sediments. Ph.D. Thesis, University College London (UCL), London, UK, 2016.
20. Margheritini, L.; Frigaard, P.; Martinelli, L.; Lamberti, A. Scour around monopile foundations for offshore wind turbines. In Proceedings of the First International Conference on the Application of Physical Modelling to Port and Coastal Protection (CoastLab06), Porto, Portugal, 8–10 May 2006. Faculty of Engineering, University of Porto.
21. Stahlmann, A.; Schlurmann, T. Kolkbildung an komplexen Gründungsstrukturen für Offshore-Windenergieanlagen—Untersuchungen zu Tripod-Gründungen in der Nordsee. *Bautechnik* **2012**, *89*, 293–300. [CrossRef]
22. Hartvig, P.A.; Thomsen, J.M.; Frigaard, P.; Andersen, T.L. Experimental Study of the development of scour and backfilling. *Coast. Eng.* **2010**, *52*, 157–194. [CrossRef]
23. Porter, K.; Simons, R.; Harris, J. Comparison of three techniques for scour depth measurement: Photogrammetry, Echosounder profiling and a calibrated pile. In Proceedings of the International Conference on Coastal Engineering, No. 34, Seoul, Korea, 15–20 June 2014.
24. Raaijmakers, T.; Rudolph, D. Time-dependent scour development under combined current and waves conditions—laboratory experiments with online monitoring technique. In Proceedings of the Fourth International Conference on Scour and Erosion, ICSE 4, Tokyo, Japan, 5–7 November 2008.
25. Petersen, T.U.; Sumer, B.M.; Fredsøe, J. Time scale of scour around pile in combined waves and current. In Proceedings of the Sixth International Conference on Scour and Erosion, ICSE 6, Paris, France, 27–31 August 2012.
26. Qi, W.G.; Gao, F.P. Physical modeling of local scour development around a large-diameter monopile in combined waves and current. *Coast. Eng.* **2014**, *83*, 72–81. [CrossRef]
27. Sumer, B.M.; Fredsøe, J. Scour around pile in combined waves and current. *J. Hydraul. Eng.* **2001**, *127*, 403–411. [CrossRef]
28. Soulsby, R. *Dynamics of Marine Sands: A Manual for Practical Applications*; Thomas Telford: London, UK, 1997.
29. Vosselman, G. Slope Based Filtering of Laser Altimetry Data. *Int. Soc. Photogramm. Remote Sens. Congr. Amst.* **2000**, *33*, 935–942.
30. Raudkivi, A.J.; Ettema, R. Clear-water scour at cylindrical piers. *J. Hydraul. Eng.* **1983**, *109*, 338–350. [CrossRef]
31. Welzel, M.; Schlurmann, T.; Hildebrandt, A. Local scour development and global sediment redistribution around a jacket-structure in combined waves and current. In Proceedings of the Ninth International Conference on Scour and Erosion, ICSE 9, Taipei, Taiwan, 5–8 November 2018.
32. Coleman, S.E.; Melville, B.W. Bed-Form Development. *J. Hydraul. Eng.* **1994**, *120*, 544–560. [CrossRef]
33. Flemming, B.W. Zur Klassifikation subaquatischer, strömungstransversaler Transportkörper. *Boch. Geol. Geotech. Arb.* **1988**, *29*, 93–97.
34. Rudolph, D.; Bos, K.J. Scour around a monopile under combined wave current conditions and low KC-numbers. In Proceedings of the Third International Conference on Scour and Erosion, ICSE 3, Amsterdam, The Netherlands, 1–3 November 2006.
35. Zanke, U.C.E.; Hsu, T.W.; Roland, A.; Oscar, L.; Reda, D. Equilibrium scour depths around piles in noncohesive sediments under currents and waves. *Coast. Eng.* **2011**, *58*, 986–991. [CrossRef]
36. Sumer, B.M.; Petersen, T.U.; Locatelli, L.; Fredsøe, J.; Musumeci, R.E.; Foti, E. Backfilling of a Scour Hole around a Pile in Waves and Current. *J. Waterw. Port Coast. Ocean Eng.* **2013**, *139*, 9–23. [CrossRef]

37. Ettema, R.; Melville, B.W.; Barkdoll, B. Scale effects in pier-scour experiments. *J. Hydraul. Eng.* **1998**, *124*, 639–642. [CrossRef]
38. Hughes, S.A. *Physical Models and Laboratory Techniques in Coastal Engineering*; World Scientific Publishing Co. Pte. Ltd: Singapore; London, UK, 1993.
39. Soulsby, R.; Clarke, S. *Bed Shear-Stresses under Combined Waves and Currents on Smooth and Rough Beds*; Report TR 137 Rev 1.0; HR Wallingford: Wallingford, UK, 2005.
40. Sutherland, J.; Whitehouse, R.J.S. *Scale Effects in the Physical Modelling of Seabed Scour*; Report TR 64; HR Wallingford: Wallingford, UK, 1998.
41. Hildebrandt, A.; Schmidt, B.; Marx, S. Wind-wave misalignment and a combination method for direction-dependent extreme incidents. *Ocean Eng.* **2019**, *180*, 10–22. [CrossRef]

energies

MDPI

Review

Control Strategies Applied to Wave Energy Converters: State of the Art

Aleix Maria-Arenas [1,*], Aitor J. Garrido [2], Eugen Rusu [3] and Izaskun Garrido [2]

[1] Department of Engineering, Wedge Global S.L., 35017 Las palmas de Gran Canaria, Spain
[2] Automatic Control Group—ACG, Department of Automatic Control and Systems Engineering, Engineering School of Bilbao, University of the Basque Country (UPV/EHU), 48012 Bilbao, Spain
[3] Department of Applied Mechanics, University Dunarea de Jos of Galati, Galati 800008, Romania
* Correspondence: aarenas@wedgeglobal.com

Received: 29 June 2019; Accepted: 6 August 2019; Published: 14 August 2019

Abstract: Wave energy's path towards commercialization requires maximizing reliability, survivability, an improvement in energy harvested from the wave and efficiency of the wave to wire conversion. In this sense, control strategies directly impact the survivability and safe operation of the device, as well as the ability to harness the energy from the wave. For example, tuning the device's natural frequency to the incoming wave allows resonance mode operation and amplifies the velocity, which has a quadratic proportionality to the extracted energy. In this article, a review of the main control strategies applied in wave energy conversion is presented along their corresponding power take-off (PTO) systems.

Keywords: ocean energy; marine energy; wave energy; renewable energy; wave energy converter; control system

1. Introduction

Marine Renewable Energy (MRE) is one of the least tapped renewable energy resources. Despite decades of development efforts, more than 90% of the 529 MW of the MRE operating capacity at the end of 2017 was represented mainly by two tidal barrage facilities: 254 MW from Sihwa plant in the Republic of Korea (completed in 2011) and the 240 MW La Rance tidal power station in France (built in 1966) [1]. Main barriers for MRE causing this slow development are analyzed in [2] with special interest in the Mediterranean Sea (MS), although the results can be applied to a great extent for any other geographical areas. Remarkable conclusions about MRE barriers include:

- Bathymetry and distance to shore: Near-shore facilities can have a direct affection on nearby coastal areas, maritime routes, fishing areas or visual impacts. Narrow and step near-shore continental shelfs can also have a negative impact for economic reasons, mainly installation (including grid connectivity) and maintenance.
- Electricity infrastructure: On the contrary, if we move large distances from the shore to minimize the previously cited negative impacts over coastal areas, it can significantly increase the relevant cost of cabling and substations, especially for areas with large depths.
- Potential environmental impacts: Underwater noise, sediment dispersal, increased turbidity, electromagnetic field effects (EMF), wave radiation and diffraction alteration can lead to significant changes to coastal morphology; fixed structures can also generate artificial reef effect. It is concluded that environmental impacts for MRE are hardly clear and not sufficiently quantified, hence, more research is necessary about this topic.
- Economics: The great diversity of MRE technologies and the early development status result in a wide range of levelized cost of energy (LCOE) [3], in the particular case of wave energy

ranging from 108 €/MWh to 530 €/MWh. This level of economic uncertainty creates a less favorable environment for investments.

- Legal and regulatory framework: There is a lot of uncertainty in this regard for MRE, and it is not adequately addressed by the relevant national/international entities. Many key parameters affecting directly any MRE installation are interrelated with several other aspects such as the environmental impact assessment, rights and ownership, international law, management of ocean space, etc.

Geographical or energy islands remain as the most interesting technological enablers for MRE research and deployment, as highlighted in [4]. For remote areas or small islands, the electrical energy production is still based on outdated, polluting and expensive technologies, powered by fossil fuels. Many islands around the world are working on important projects in order to achieve energetic independence based on MRE. Hybrid solutions such as solar-wave [5] or wind-wave [6] can also favor the development of MRE, combining more stablished technologies such as offshore wind and PV in the same offshore device (e.g., spar sharing) or energy farm.

MRE technologies have seen new capacity come online over the recent years; in particular, wave energy development in Spain [7] holds some notorious projects, such as the so called MARMOK-A-5 being the first operational point absorber connected to the grid in Spain, developed by OCEANTEC (acquired by IDOM in September 2018), installed at BIMEP test site in 2016. Mutriku Wave Power Plant, operates since July 2011 connected to the grid, being the first oscillating water column (OWC) multi-turbine facility acting as a test rig for different technology developers; the Portuguese company Kymaner finished testing of its bi-radial air turbine last August 2018. WEP+ demonstration project, based on the industrial scale W1 point absorber developed by Wedge Global, accumulated roughly 5 years of testing at PLOCAN test site on the Canary Islands. LifeDemoWave demonstration project deployed a 25-kW prototype in June 2018 in the Galician coast for a no grid connected test. European highlights from 2018 resulted from H2020 funded projects, including the fabrication of the second Penguin Wave Energy Converter (WEC) at EMEC as part of the CEFOW project, the deployment of the Corpower WEC at EMEC, the installation of the new turbine on the Marmok wave device and the deployment of Minesto's Deepgreen500 device.

The wave energy sector is still in a very early development stage when compared to other renewable energies, especially wind or solar PV. There is a low level of consensus among the WEC technology developers that are still, at best, in a prototype demonstration phase, and there is a lot of discussion among said developers about the best WEC topology and/or PTO configurations. It is not so common to discuss at this level about control strategies given the difficulties in effectively implementing most of the control strategies listed in Section 3 of this review. Most of the existing industry scale prototypes in the water have the simplest control strategy resulting in low energy absorption.

The main purpose of this article is to establish a framework for the control strategies being discussed over the recent years (2017–2019) for WECs. References older than 2017 will not be discussed (unless for introductory purposes) to avoid redundancies with older reviews with a similar approach. A brief review will be provided about the analytical formulation of the mean power absorption and optimal control [8] particularized for heaving WECs, which is the most extended WEC technology in the form of floating point absorbers [9]; however, the same approach is extensible to any other oscillatory mode (sway, surge, pitch, roll or yaw). A point absorber is a floating buoy moored (2 bodies) or fixed (1 body) to the seabed. The incoming waves induce into the floating body a synchronous oscillation mainly in heave motion. It is this movement that is converted into an energy vector (e.g., hydrogen [10], desalination [11] or electricity) through a power take-off located inside the buoy.

Great effort has been made in the last decades about control strategies for WEC, as we can see from older state-of-the-art reviews such as [12–14]. The main objective in wave energy conversion for control is the maximization of power absorption, aiming for resonance operation. The best control approach to achieve said resonance is known as complex-conjugate control, based on solving the impedance matching problem. As we will explain later, this control always achieves optimal power absorption

since it regulates the system reactance and resistance simultaneously. However, this control strategy is not practical for real world applications because of large motions and loads. Hence, under-optimal control solutions, it needs to be analyzed and implemented considering physical constrains in motion, force and power rating of the WEC.

In Section 2 a brief introduction about wave energy technology is presented with the purpose of helping the uninitiated reader understand the different technologies and parts (oscillator body, PTO) of WECs. In Section 3, we will start with a comprehensive introduction for WEC modelling and optimal control, as originally introduced in [15], to establish a reference framework, continuing with classification, introduction and discussion for each control strategy found in recent WEC control publications. Finally, conclusion and further research end the article in Section 4.

2. Wave Energy Technology

In the same way that a wind turbine transforms the kinetic energy of the wind into mechanical energy of rotation through the blades, and this one into electrical energy through the electrical generator, a WEC transforms the energy from the waves into mechanical energy through the oscillating body and this one into an energy vector through the PTO.

In the wind energy sector, there is a predominant type over the rest, the three-bladed horizontal axis turbine; it is not so for wave energy, where there is a wide spectrum of options for both oscillator body and PTO without a clear predominant type. Over 1000 different wave energy conversion techniques were patented in Japan, North America and Europe [16] just in 2004, and it is expected this number has greatly increased since 2004 based on the general renewables energies patent numbers shared recently by EMW Law [17].

2.1. Wave Energy Converters

Despite the great number of different technologies for harvesting wave energy, all of them can generally be categorized on the basis of three criteria [18–21].

2.1.1. Location

This classification is according to the relative distance between the device, coast and seabed depth. This classification is somehow qualitative because of the many differences between continental shelfs around the world. Nevertheless, this classification is not used in practical discussions and remains as a first qualitative approach to WEC technologies.

- Onshore: Located in coast proximity, commonly affected by swallow waters ($h/\lambda < 1/25$), where h is the water depth and λ is the wavelength. These converters are usually integrated in a breakwater, dam, fixed to a cliff or rest on the seabed. The distinctive characteristics for these converters are easy maintenance and installation. The drawbacks are that coastline waves have less energy than deep-water waves along with a potential coastline reshape.
- Nearshore: They are installed close to the shore, commonly affected by swallow or intermediate waters ($1/25 < h/\lambda < 1/2$). Their deployment and maintenance expenses are limited since they do not need mooring systems as they are usually fixed or rest on the seabed.
- Offshore: They are placed in deep waters ($h/\lambda > 1/2$), far from the shore. They are able to harvest energy from the most energetic places, but installation and maintenance can be much more expensive because of the required mooring systems (high depth), long underwater cabling, underwater substations and offshore maintenance.

2.1.2. Dimensions of the Prime Mover and Orientation with Respect to the Wave

This classification is according to the orientation of the wave energy device with respect to the wave propagation front (Figure 1). This classification along with the working principle are used to clearly differentiate any WEC.

- Attenuators: The length of the device is of the same order of magnitude (or larger) than the wavelength; these devices are oriented in such a way that they are parallel to the incident wave.
- Terminators: Similar in dimensions to attenuators but placed perpendicular to the incident wave.
- Point Absorbers: Axisymmetric devices capable of harvesting waves from any direction, known as antenna effect, their dimensions are usually an order of magnitude lower than the wavelength.

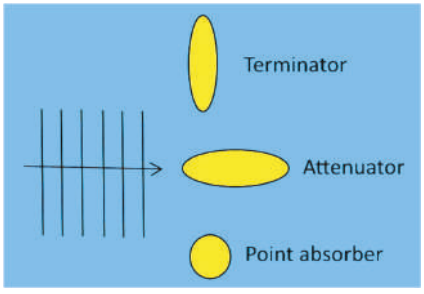

Figure 1. Classification according to device dimensions and orientation.

2.1.3. Working Principle

Oscillating water column: This type of technology builds, among its main elements, an air chamber. It is this air, subjected to oscillating pressure by the action of the waves, which ascends or descends moving a conventional air turbine linked to an electrical generator (Figure 2). Hence, the air turbine can take advantage of the complete oscillation cycle of the wave. It is generally installed in a breakwater, but there are shore-based and floating models. The main benefits for oscillating water column concept commonly accepted are its simplicity and robustness [22]. Common examples are Oceanlinx device deployed in 2005 designed to sit in shallow water, approximately 21 m wide and 24 m long, and Mutriku wave energy plant, located in the Bay of Biscay and commissioned in July 2011, which is one of the few wave energy plants still in operation.

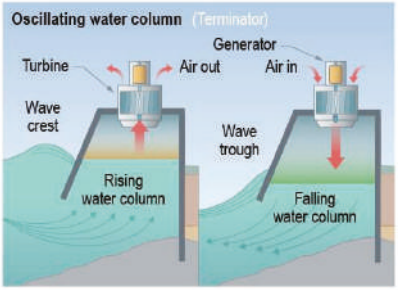

Figure 2. Oscillating water column working mode of operation [22].

Floating structures: Unibody or multibody structures moving in heave, pitch, roll or in any combination of the three (Figure 3) when affected by a wave. The relative movement between different parts of the device allows converting it into electricity. These kinds of devices are rarely named as floating structures but using the dimensions with respect to the wave: attenuators or floating-point absorbers. Multiple examples can be found for this kind of technology. Pelamis was an attenuator floating structure deployed during 2007. The machine is composed by a number of semi-submerged, linked sections. These sections move relatively when the waves pass along the length of the machine. W1 is a point absorber floating technology deployed in 2014. The machine has two main bodies linked without restrictions in heave motion, which allows the relative movement between them.

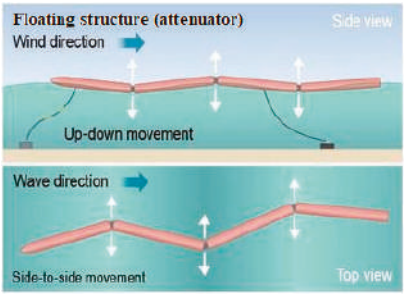

Figure 3. Floating structure with multiples bodies mode of operation. Reprinted from [22].

Pressure differential: Typically located nearshore, this kind of technology can be explained as a combination of two technologies working together—oscillating water column and floating point-absorbers. This is because it uses the working principle for both: difference of pressure and relative heave/pitch/roll displacement between parts, the fixed air chamber in the seabed and the moveable upper body (Figure 4). When a wave crest passes over the device, the water pressure above the device compresses the air within the cylinder, moving the upper cylinder down creating a relative movement in the same way as in punctual absorbers, this happens in the opposite way when a trough passes over. Potential advantages of these devices include: Better survivability, they are not exposed to splash zone corrosion nor the various hazards that could take effect when floating on surface and reduced/negligible visual impact. A major drawback for pressure differential technology is the required underwater maintenance. A good example of evolution with pressure differential technology is Carnegie Clean Energy device (CETO). Deployed in 2015, CETO 5 served the purpose of delivering pressured water for reverse osmosis membranes in the desalination plant, but CETO 6 (still in development) will include electrical generation onboard.

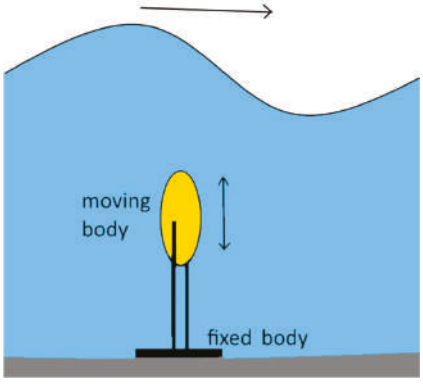

Figure 4. Pressure differential mode of operation.

Overtopping devices: These devices collect the water from the incident waves into a reservoir in order to move one or more reduced jump hydraulic turbines, usually Kaplan turbines. They take advantage of the potential energy of the waves to convert it, through synchronous generators, into electrical energy (Figure 5). Within this type of device, we can distinguish between converters with a fixed structure located on the coast (onshore) and those with a floating structure far away from it (nearshore–offshore). A common example of these kind of devices is the Wave Dragon [23], which is characterized by having a reflector that directs the incident waves towards a ramp to the reservoir above sea level.

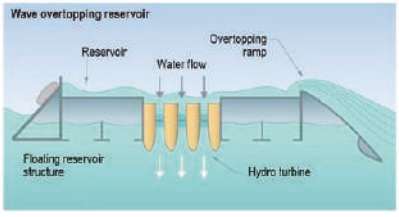

Figure 5. Overtopping mode of operation [22].

Oscillating wave surge: These devices typically have one end attached to a fixed structure or the bottom of the sea while the other end is free to move. A hinged deflector, this part is positioned perpendicular to the wave direction, terminator (Figure 6). The axis of the deflector (or paddle) oscillates like a pendulum mounted on a pivoting joint in response to the impact of the horizontal movement of the wave particle. They often come in the form of floats, fins or membranes. This working principle could be associated to the unique Japanese 'Pendulor' system [24]; but these devices do not take advantage of any harbor resonance. An example for this kind of technology is the Aquamarine Power Oyster, a nearshore device, where the top of the deflector is above the water surface and is hinged from the sea bed.

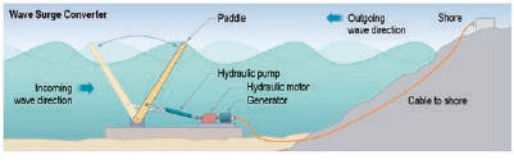

Figure 6. Oscillating wave surge mode of operation [22].

2.2. Power Take-Off Systems

In this section, a brief introduction for each of the different PTO technologies, as presented in [18,25–27], is given. Three main technology paths can be applied to obtain electricity from the wave power conversion chain (PCC), converting the energy being carried by the wave into fluid capture, linear motion or rotary motion. Many different rotary electrical solutions can be applied, but these technologies imply a lot of intermediate steps: Pistons, accumulators, air chambers or mechanical gear systems [25]. The number of intermediate steps is critical for the wave energy conversion efficiency and reliability:

- Efficiency: The larger the number of intermediate steps, the greater are the mechanical and transformation losses that we obtain as a result of the PCC. This causes a reduction in the annual energy production (AEP), which in turn affects the levelized cost of the electricity (LCOE), increasing it.
- Reliability: The offshore equipment undergoes an accelerated degradation in comparison with the same equipment implemented within a ground installation due to the high salinity of the maritime environment where it is implemented. This fact makes it desirable to minimize the amount of equipment to monitor and maintain while the equipment is in operation.

2.2.1. Air Turbines

Commonly used in OWC devices, air turbines require an air chamber to convert wave energy into mechanical power (Section 2.1.3). The basic principle is to drive the air turbine with the oscillating air pressure in the air chamber as a consequence of the oscillating water level. As a result, this PTO solution presents a challenge coming from the bidirectional nature of the flow. A possible solution

for this challenge includes non-returning valves combined with a conventional turbine. However, due to complexity, size and high maintenance costs, this configuration is not considered as a viable option [25]. A better solution involves a self-rectifying air turbine that converts an alternating air flow into a unidirectional rotation.

2.2.2. Hydraulic Systems

These are typically used in attenuators, point absorbers and wave surge devices (Section 2.1.3), in which the energy conversion system is based on taking advantage of the linear movement generated by the interaction of the body (or bodies) with the waves. Conventional rotary electrical solutions may not be directly compatible [25]. Therefore, a suitable conversion interface is required between the linear energy capture and the electrical generator, capable of operating with high forces at low frequencies, such as hydraulic systems that operate reversed with respect to their traditional counterpart, that is, the movement of the body feeds the energy of the hydraulic motor which in turn feeds an electric generator.

2.2.3. Hydro Turbines

Used for overtopping devices [25], hydraulic turbines [28] take advantage of the potential energy of the water stored in the accumulation chamber of the device, which is converted to mechanical power using low-head turbines and rotary electrical generators.

2.2.4. Direct Mechanical Drive Systems

This form of PTO solution requires additional mechanical systems driving a rotary electrical generator [25]. It can comprise pulleys, cables, gear boxes or energy storage systems, such as Flywheels (for rotation-based systems) in order to accumulate and release energy, if needed, for reactive operation or to smooth any power variation.

2.2.5. Direct Electrical Drive Systems

Direct electrical drive PTO directly couples the moving part of the electrical generator with the moving body of the WEC [25]. A direct electrical drive PTO system presents two main parts: (i) a translator coupled to the moving body of the WEC, which can be equipped with permanent magnets (conventional solution) or magnetic steel (switched reluctance) and (ii) the stator equipped with coils. The waves induce a heave motion in the moving body coupled with the translator, generating a relative displacement of the translator within the stator, inducing electrical current.

Critical added value of direct linear drive systems is the ability to move instantly in any of the 4-quadrant modes of operation, commonly called 4-quadrant control, allowing instant swap from motor to generator mode at any given moment of the wave oscillation cycle (upwards or downwards) to handle the required reactive power for some of the control strategies we will list in Section 3.

In the first (I) and third (III) quadrants, the electric machine delivers positive power, clockwise or counterclockwise, supplying mechanical energy (motor). On the other hand, in the second (II) and fourth (IV) quadrants, the electric machine delivers negative power, supplying electrical power (generator). Applying a single cycle of regular waves to a WEC, for example, the period between two consecutive wave peaks, the required operation for each quadrant will be as follows: During the downward movement the electric machine will work in downward generator mode (quadrant II) once it reaches the valley, and the consequent upward movement the electric machine will start working in upward generator mode (quadrant IV). If the WEC is operating with a control strategy that requires to brake or accelerate the machine within the same cycle to achieve resonance, as we will see in the next section, the instantaneous swap between the quadrants II-I-III or IV-I-III will be required.

Additionally, direct drive electrical systems have less components to maintain, avoiding intermediate steps while providing simpler/cheaper construction and better reliability. Thus, direct

drive is the preferable technology for WECs and offshore facilities where reliability and efficiency are key parameters.

3. Control Strategies

The control problem for the wave energy sector does not fit the classic description of control for other industries where control strategies involve the use of feedback (open loop, closed loop and set-point tracking) and forcing the system variables to a constant value. Instead, WEC control aims for maximization of captured energy while relying on feedforward control to generate optimal device velocity or PTO force setpoints (Figure 7).

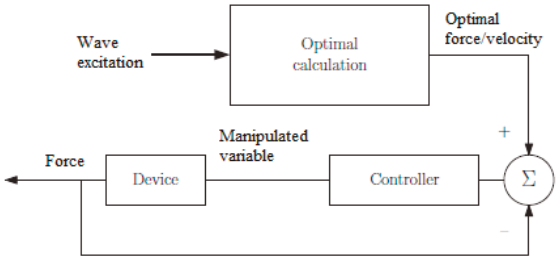

Figure 7. Hierarchical control structure. Manipulated variable depends on the PTO: Bypass valves, swashplate angle, excitation current or conduction angle. Optimal force/velocity calculated as setpoint for the feedforward control.

Optimal calculation involves the performance function of the form:

$$J = \int_0^T v(t) f_{PTO}(t) dt \tag{1}$$

where $v(t)$ is the device velocity, and $f_{PTO}(t)$ is the exerted PTO force. To ease the understanding of how control maximizes this captured energy, we will start in Section 3.1 with a simple analytical revision of the mean absorbed power and optimal control as originally defined in [15] and further discussed in [8], concluding with a discussion of why suboptimal control approaches are required before starting with the main topic for this paper, recent studies about different control strategies for wave energy converters.

A good qualitative first approach to understand how to maximize the absorbed power is the concept of resonance. A system being excited at its natural frequency is described as resonant. When operating in resonance, the response amplitude is highest. Resonance does not usually occur naturally for wave energy converters that have a natural frequency higher (Figure 8) than the power-rich frequency components of a typical wave spectrum, so we have to trick the system into resonance tuning the PTO damping and stiffness as needed, solving the impedance matching problem as we will explain later.

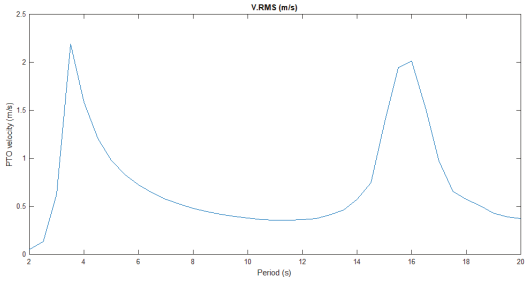

Figure 8. Variation of WEC oscillator velocity (no PTO) for a set of regular wave frequencies with Reference Model 3 [29] geometry with minor variations; simulations performed in WECSIM [30]. Natural resonance operation found for periods of 3.8 s and 16.4 s.

3.1. Numerical Modeling

For any WEC, the inertial force is balanced by the whole forces acting on the WEC. These forces are usually split into external loads, WEC-wave interaction (hydrostatic force, excitation load and radiation force) and reaction forces (caused by PTO, mooring or end-stop mechanism). Interaction between WECs (i.e., floater) and ocean waves is a high-order nonlinear process that can be simplified to linear equations for waves and small-amplitude device oscillation motions, which is acceptable throughout the device's operational regime. This means that the superposition principle applies [31].

The PTO system results in a complex nonlinear dynamic behavior. To keep the superposition principle valid, the PTO forces must be linearized. In this linear form, the PTO force is composed of two contributions [32]: A force proportional to velocity (damper) and a force proportional to the displacement (spring). Mooring systems are often represented by a linear function of the captor displacement and the mooring spring stiffness. End-stop mechanism and other constrains (velocity or PTO force operational limits) are abrupt nonlinear forces which are usually not considered, given the complexity of a nonlinear approach for wave energy conversion. Instead, the optimum method of achieving an acceptable displacement amplitude is to increase the PTO damping until the body has the maximum allowance displacement [33].

In [8], M. Alves obtains the mean absorbed power assuming linearity and sinusoidal waves for a heave motion wave energy converter as:

$$P_a = \frac{1}{2}\frac{B_{pto}\omega^2\left|\hat{F}_e\right|^2}{\left[-\omega^2(m+A)+G+K_{pto}+K_m\right]^2-\omega^2\left(R+B_{pto}\right)^2} = \frac{1}{2}\frac{B_{pto}\omega^2\left|\hat{F}_e\right|^2}{\left|Z_i+Z_{pto}\right|^2} \tag{2}$$

where ω is the wave frequency, $\hat{F}_e$ is the excitation force, m is the total inertia of the captor, A is the added mass, G is the hydrostatic spring stiffness, K_{pto} is the PTO mechanical spring, K_m is the mooring spring stiffness, R is the radiation damping, B_{pto} is the PTO damping, Z_i is the intrinsic impedance and Z_{pto} is the PTO impedance.

An alternative, yet equivalent, formulation considers the force-to-velocity model of a WEC in the frequency domain [15] as,

$$\frac{V(\omega)}{F_{ex}(\omega)+F_u(\omega)} = \frac{1}{Z_i(\omega)} \tag{3}$$

where $V(\omega)$, $F_{ex}(\omega)$, and $F_u(\omega)$ represent the Fourier transform of the velocity v(t), excitation force $f_{ex}(t)$ and control force $f_{pto}(t)$, respectively. $Z_i(\omega)$ is the intrinsic impedance in the frequency domain of the system as

$$Z_i(\omega) = B_r(\omega) + \omega[M + M_a(\omega) - \frac{K_b}{\omega^2}] \tag{4}$$

where $B_r(\omega)$ is the radiation damping (real and even) and $M_a(\omega)$ is the frequency-dependent added mass, often replaced by its high-frequency asymptote m∞.

The model in (4) allows the derivation of conditions for optimal energy absorption assuming a linear approach, and the intuitive design of the energy-maximizing controller in the frequency domain [15] as

$$Z_{PTO}(\omega) = Z_i^*(\omega) \tag{5}$$

The choice of Z_{PTO} as in (5) is referred to as optimal, reactive or complex conjugate control which is the solution to the so-called impedance-matching problem. Technically, reactive control refers only to the fact that the PTO reactance must cancel the inherent reactance. However, the PTO resistance and the hydrodynamic resistance must also be equal. Thus, complex-conjugate control is a more accurate description since it refers to the fact that the optimum PTO impedance equals the complex conjugate of the intrinsic impedance.

The result in (5) has a number of relevant implications [34]:

- The result is frequency dependent, implying a great optimization difficulty for irregular seas containing a mixture of frequencies.
- Future knowledge of the excitation force may be required. While this knowledge is straightforward for regular waves, it is more complex for irregular seas.
- Since force and velocity can have opposite signs, the PTO may need to supply power for some parts of the sinusoidal cycle.
- The optimal control takes no constrains into consideration; it is more than likely a real system will have velocity and displacement constrains.

Nevertheless, delivering optimal control may be infeasible due to the associated excessive motions and loads in extreme waves. Hence, alternative suboptimal control schemes have been implemented, which include physical constraints on the motions, forces and power rating of the device. While a lot of discussion and different approaches can be found over the recent years for sub-optimal control solutions, we have classified most of them according to the nomenclature that most commonly appears—damping, reactive, latching and model predictive control.

3.2. Damping Control

A widely studied approach to avoid the difficulties in the implementation of the feedback control of the WECs is known in the literature as linear damping of the PTO, also called passive loading [35] or resistive [36], a suboptimal approach where the instantaneous value of the PTO force is linearly proportional to the oscillating body speed, that is to say

$$f_{pto}(t) = -B_{pto}v(t) \tag{6}$$

where $B_{pto} > 0$ is the PTO damping coefficient. This methodology does not require a prediction of the excitation force, thus making it a simple strategy to implement. In fact, it is the one we can usually find in the demonstrators or pre-commercial devices currently deployed around the world. Conventionally, it only requires knowing the instantaneous value of the PTO velocity, for which measurement instruments are usually available in the market.

Figure 9 shows a simulation example in WECSIM [30] for Reference Model 3 using damping control; the electric power (Pe) is always negative, Pe < 0, so the machine does not need to return energy at any point of the oscillating cycle to maximize the energy output in resonance operation.

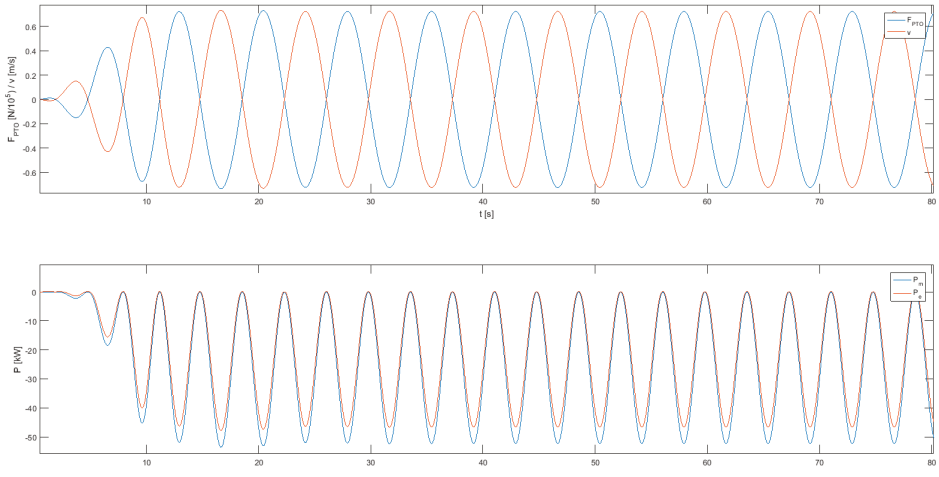

Figure 9. Linear damping–WEC simulation for regular waves. In the upper graphic PTO force (blue) is compared with PTO velocity (red). The lower graphic represents ideal power output (blue) and power output considering electrical losses (red); negative values for power means the WEC is delivering energy to the grid.

Damping control, however, provides a much smaller amount of power absorbed when compared to other strategies such as reactive control [37], as we will see in the next section, and the linear relationship between the speed and the force of the PTO, when it is a straightforward relation, may not be easy to implement without using any feedback control. In addition, the optimal value of the PTO damping, which is the value of B_{pto} that maximizes the instantaneous power absorbed, can be easily calculated for regular waves. However, in practice, where the incident wave is irregular (defined by the wave spectrum), B_{pto} is more difficult to calculate because of the changes in the spectral components of the incident wave which are not constant over time, so a real time feedback control for a time-varying damping value is required.

Therefore, we can distinguish between a real time-varying damping control and a constant (or passive) damping control. First generation WEC control is based on damping strategies with constant values for B_{pto}. This particular strategy is still very common in recent WEC prototypes by technology developers (given the simplicity of implementation).

3.2.1. Constant Damping Control

The work [38] presents a PTO force via constant damping coefficient applied to compare the power conversion performances of three WEC devices modelled in a computational fluid dynamic software (CFD) model based on a 1/50 scale heaving point absorber WEC. Results from this article quantify crucial hydrodynamic parameters for the three devices, revealing a prominent affection of the device amplitude response in free motion without PTO. When PTO is included under effect of regular and irregular waves, the joint effects of geometry and PTO damping on the power absorption are very significant.

Experimental evidence with CECO device (a floating point absorber) with different linear damping coefficients is shown in [39] with the following conclusions: (a) optimal PTO damping coefficients for low-energy irregular waves are higher than for high-energy regular waves, and (b) wave conditions affect significantly the optimal damping coefficients.

3.2.2. Time-Varying Damping Control

Passive damping control is analyzed and compared in [35] with a real-time passive control (PC) based on the Hilbert–Huang transform (HHT). For this solution the damping coefficient is time-varying and tuned instantaneously, based on the frequency of the excitation force. This solution adds a grade of complexity to damping control, since it is required that excitation force be known. The results of this study prove that the proposed solution with real-time calibration of the damping coefficient improves from 21% to 65% the results that a conventional damping control strategy can obtain.

An experimental solution to calibrate the optimum damping coefficients has been presented in [40], based on tank testing experiments on the power performance of a bottom hinged oscillating wave surge converter (OWSC) for regular and irregular waves with damping control, testing different damping coefficients for different wave conditions. The best damping coefficient based on performance was obtained. In this study it is concluded that there are no differences between linear or non-linear strategies in relation to the amount of energy absorbed, but nonlinear strategies have better stability and a broader damping range.

Damping control is electronically implemented in a solid-state relay (SSR) with pulse-width modulation (PWM) in [38]. The objective for this analysis is to mimic analog current flow and compare it with a nonlinear model predictive control (NMPC). It is concluded that peak values of absorbed power and the capture width greatly improve, compared with passive damping strategy.

3.3. Reactive Control

Reactive control is often misleading in the literature and can be confused with complex conjugate control. As the differences between these definitions were already explained in Section 3.1, for clarity reasons, we will keep "reactive control" as it can be usually found in the literature, but a new term such as "sub-optimal reactive control" should be used, as it is done in [41]. These control strategies usually involve the tuning of both PTO resistance and reactance (B_{pto} and K_{pto}), taking into account constrains such as PTO power rating or displacement limits, adjusting the resistance of the PTO to avoid non-linear approaches [33]. Therefore, we will need to consider the generic approach to a PTO characterization as explained in Section 3.1.

$$f_{pto}(t) = -B_{pto}v(t) - K_{pto}x(t) \tag{7}$$

where K_{pto} is the stiffness coefficient, and $x(t)$ is the displacement in the PTO. This kind of control when implemented in demo prototypes usually employs a tabular approach to alleviate the computational constrains required to calculate optimum values in real time. Hence, sub-optimal values for damping and stiffness coefficients are pre-calculated with an optimization algorithm to be stored in tables. For this reason, this particular technique is prone to modelling errors requiring a reanalysis of the constant values after a certain testing period.

Figure 10 shows a simulation in WECSIM for Reference Model 3 [29] using reactive control. The electric power (Pe) varies between positive and negative values, so the PTO needs to switch from motor to generator mode and vice versa at least two times for every oscillation cycle. This kind of mode switching is commonly called "4-quadrant control" and is not obtainable within the time constrains for all of the available typologies of PTOs in the market. Reactive power is a back and forth exchange between the PTO and the oscillating body and does not contribute to the facility energy production. This energy may be supplied by any hydraulic, compressed-air, thermal, chemical, kinetic, electrostatic, electromagnetic storage source [42] or the electrical grid. The biggest disadvantage of reactive strategies comes from the reactive energy exchange process. This process does not suppose an electrical energy gain, but it is subject to dissipative energy loss processes. The magnitude of these losses can negatively affect the overall efficiency of the device.

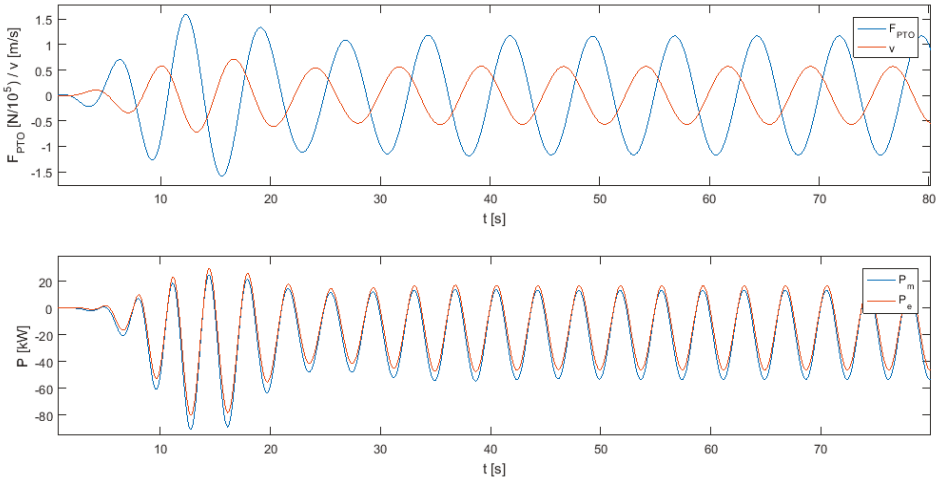

Figure 10. Reactive control–WEC simulation for regular waves.

Energy storage requirements for the reactive power are analyzed in [41] based on a time-domain approach. These storage systems facilitate the exchange of reactive energy and can help to decrease the associated losses, so they are a critical element of the system to maximize the power absorption.

The performance of a floating heaving-only point absorber is analyzed in [43]. The objective is to maximize the wave energy absorption by actively controlling damping and stiffness parameters on the basis of a linear model in the frequency domain. The study concludes with a comparison of the results with similarly validated studies.

Reinforcement learning methodologies are studied in [44]. Calculating the optimum reactive control variables by means of a Q-learning algorithm, the model is able to maximize the energy absorbed for each sea state.

3.4. Latching/Unlatching

Firstly suggested in [45], the latching control is based on achieving the resonance of the WEC through a clamping system, fixing the device during a certain part of the wave oscillation cycle [46]. When the device is released, the control of the device is usually governed by a linear damping as in Section 3.2. This way, the device presents resonance operation without need of reactive power control. However, some energy needs to be drawn from an external source in order to activate the clamping system when the device velocity is null. The critical point for this control strategy is the calculation of the latching-unlatching time periods. Latching control avoids the two-way energy transfer and the associated energy dissipation that characterize reactive control, so a wider spectrum of PTO systems operating only in generator mode can be used under this control strategy.

Setting as base case scenario the passive damping control strategy in [47], the performance improvement when latching control strategy is applied was quantified. The results show that the capture width increases by 70% and the optimal damping coefficient decreases by 60%.

An economic approach was made with different latching control strategies assessed for the WEC in [48], including an interesting comparison with passive damping control. Results are based on the simulated performance of the WEC using regular monochromatic waves, revealing similar annual energy production for constant damping when compared with suboptimal latching, 201 and 197 MWh/yr, respectively. Optimal latching shows the best results with a 45% increase over the annual energy production, 286 MWh/yr.

3.5. Model Predictive Control

Due to its ability to deal with linear and non-linear models, together with the system constrains and real time evaluation of future behavior, model predictive control (MPC) is a widely used and analyzed strategy in the industry [49], and it should not be different for WECs. MPC solutions can handle the physical constraints present for any WEC technology and the non-causal optimal control solution.

However, the problem of maximizing WEC energy requires an important modification over the regular approach in the objective function of the MPC, resulting in a potentially non-convex optimization problem. Given the benefits and growing understanding of these algorithms, this strategy has become the most common control research topic in recent years. MPC maximizes the energy absorption, applying at each time step the optimum force to achieve resonance over a future time horizon, as firstly defined in [50].

As a starting point, [51] presents results of a comparison between MPC control and classical (complex-conjugate control) methods for a Linear Permanent Magnet (LPMG) PTO controlled by a machine side back-to-back actuator. It is concluded that complex-conjugate control when applied to real world solutions shows to be inefficient in maximizing the power absorption from the ocean waves.

Presented as an improvement to reactive control, a predictive strategy is analyzed in [52] where a neural network trained with machine learning is used to predict future waves (height and period), affecting the WEC and optimizing in real time the relevant parameters for the wave energy absorption (PTO stiffness coefficient and PTO damping coefficient). The algorithm does not present any improvements over similar state-of-the-art reactive control solutions in relation with the absorbed power, but it solves associated control inaccuracies from laboratory calibration and enables the controller to be adaptative to variations in the machine response caused by ageing.

In a similar way for a heaving point-absorber, a neural network is employed to forecast the short-term wave height and period in [53] to implement real-time adaptative latching control. This work presents some results comparing the differences of absorbed power for a particular wave scenario with and without control.

An innovative MPC solution is proposed in [54]. Named as robust model predictive control (R-MPC), it combines a predictive controller considering PTO constrains, ensuring maximum power absorption while being realistic, and an innovative model to solve some parametric uncertainties and model mismatches.

An interesting approach to control strategies for 3-degree of freedom WECs is presented in [55] and compared with classical heave-only WECs. Presenting a parametric MPC, it optimizes independently the pitch-surge and heave motion. Numerical algorithms are employed to find the optimal conditions and results. In this work, several numerical tests are conducted for regular and irregular waves. The presented results reveal a great improvement in absorbed power over heavy-only WECs. Contrary to these results, in [56] A. Korde states that near-optimal control for pitch-surge motions are not significant for wave energy absorption when compared to heave motion which is presented as the dominant contributor to power absorption.

A hybrid MPC strategy is presented in [57], constrains are applied to PTO damping and damping force for a two-body WEC. A Mixed-integer Quadratic Programming (MIQP) problem is proposed to obtain the maximum power absorption. Results from this problem are compared with other MPC solutions and classical models for an irregular wave scenario.

Future wave frequency prediction is used in [58] using a Fuzzy Logic controller to determine the optimum PTO damping and stiffness coefficients in real time. The proposed solution combines some regular tuning techniques with an innovative slow tuning methodology.

Fatigue, reliability and survivability controlled by MPC are analyzed in [36]. The results show a trade-off between maximized electrical power and the necessary dimensions for the WEC to resist large loads and fatigue periods. These results are also compared with conventional reactive control, where MPC improves the average annual energy production by 29%.

3.6. Others

This category includes any mixed or innovative control strategies that do not clearly fit into any of the categories presented above.

A genetic algorithm is used to optimize truncated power series along with the geometry for nonlinear WECs in [59]. It enables higher energy harvesting without large motions and less dependence of reactive power as a result.

A so-called Adaptive Parameter Estimation (APE) is proposed in [60]. The algorithm updates in real time several WEC model parameters such as the radiation and excitation force coefficients, combining the benefits associated with optimal control (maximum energy output) and APE dealing with any of the model parameter variation.

In [61] a new power take-off technique is proposed for oscillating wave surge WECs. The main innovation is to avoid any kind of braking system while keeping the amplitude within the specified range. Then, the results are compared with constant damping control, showing the benefits of the new proposed control system.

A new controller which is a variation for the complex conjugate through impedance matching in the time-domain is proposed in [62,63]. The main benefit for the proposed control lies in that it does not need a wave prediction or measurement. It is novel in that it is a feedback strategy with a multi-resonant generator strategy, decomposing the control problem into multiple sub-problems with independent single-frequency controllers. The solution is based on the spectral decomposition of the measurement signal which is employed to construct the optimal solution.

Stochastic control derived from optimal control for heave-only point absorbers considering force constrains is analyzed in [64]. Results indicate performance close to optimal in terms of mean absorbed power.

A crosscutting solution can be found for a cabin-suspended catamaran with a motion control system in [65]. The main objective is to minimize the heave velocity in the cabin, but a secondary measured result of interest for this review is the power absorption from incoming waves which can then be used as an energy vector for different applications, such as feeding auxiliary systems or driving the main engines.

4. Conclusions and Further Research

Since the mean absorbed power for any WEC is frequency dependent, maximum power absorption is achieved in resonance operation when the natural frequency of the WEC matches the wave frequency, causing the excitation force. We can force the WEC into resonance with different control strategies tuning the PTO damping and stiffens constants (B_{pto} and K_{pto}). In this article, we have classified different wave energy technologies based on different criteria commonly used in the literature. Optimal control strategy (complex conjugate control) based on solving the impedance matching problem is impractical for implementation, given the need for future knowledge of the excitation force in irregular waves and the absence of constrains in force and speed for the PTO. Hence, suboptimal control techniques are required, such as damping, reactive (misleading definition which should be revised to suboptimal reactive), latching, MPC and other novelty control ideas.

Wave Energy Technologies are still far from the commercialization point. Only a few successful demonstration projects can be found all over the world and even less when we try to find grid connected projects. Several regulatory, social, economic, environmental and technological barriers need to be addressed from different stakeholders at the same time to perceive an effective pulling action. Control strategies is one of the main technological topics to be discussed. Great efforts have been made over the years in developing effective suboptimal solutions for WECs.

Damping control, usually constant damping control, has been (and still is) the best approach for technology developers willing to test an industrial scale WEC device, given the simplicity of implementation and the safety of operation. Safety is not a minor issue for industrial scale marine devices. Large forces and motions provided by optimal control and top suboptimal approaches could

exceed the operational limits of prototype devices fabricated by shipyards and/or associated industries still unfamiliar with WEC technology.

Reactive control is the natural evolution from damping control, presenting an affordable tabular approach for any WEC prototype being deployed for a demonstration phase. Calibration of PTO constants based on simulations or previous experiences do not represent a challenge to the current state of art, although this kind of control strategy requires a PTO capable of switching from motor to generator mode multiple times in a single wave oscillation.

Latching control solves the PTO limitation of reactive control, but it requires an additional clamping mechanism to be installed and energized in the WEC, generating extra costs while also lowering the reliability. Offshore equipment, especially mechanical pieces, are prone to failure because of the extreme salinity ambient. Even well protected (marinization) pieces require a yearly basis maintenance to avoid failures.

MPC solutions represent the best approach to optimal control. Enabling excitation force prediction applies at each time step the optimum PTO force for maximum energy absorption while still considering constrains (non-linear models). MPC has been found to be the most interesting topic among the scientific community (Figure 11) over the recent years, given the good results presented in different articles. This is due to the growing experience in simulated and tank-testing environments, the incremental available advances in computational capacity and the improved expertise with environments based on neural networks. Nevertheless, the complexity of implementation and absence of industry scale demonstration projects disfavored MPC solutions for WEC technology developers. MPC strategies can become a WEC technology enabler in the near future. Maximizing the energy reliability while maintaining equipment costs will result in overall reduction of LCOE, along with the support from different stakeholders. Caring about the other WEC barriers previously presented will result in a market competitive renewable energy technology.

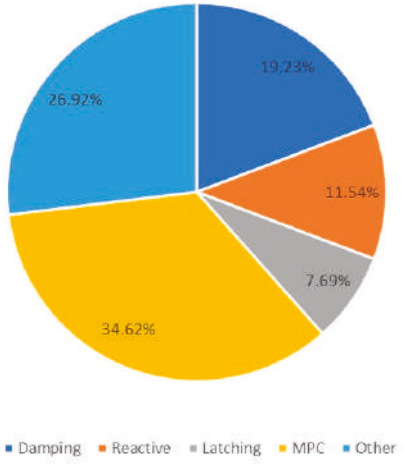

Figure 11. Recent studies for different WEC control strategies, 2017–2019.

Author Contributions: A.M.-A. conceived of the presented idea and took the lead in writing the manuscript. A.J.G., E.R. and I.G. reviewed and supervised the manuscript. All authors discussed the results and contributed to the final manuscript.

Funding: This work was supported in part by the Basque Government through project IT1207-19 and by the MCIU through the Research Project RTI2018-094902-B-C22 (MCIU/AEI/FEDER, UE).

Acknowledgments: The authors gratefully acknowledge Wedge Global for the helpful discussion and support.

Conflicts of Interest: The authors declare no conflict of interest.

References

1. REN21. *Renewables 2018 Global Status Report*; REN21: Paris, France, 2018.
2. Soukissian, T.H.; Denaxa, D.; Karathanasi, F.; Prospathopoulos, A.; Sarantakos, K.; Iona, A.; Georgantas, K.; Mavrakos, S. Marine Renewable Energy in the Mediterranean Sea: Status and Perspectives. *Energies* **2017**, *10*, 1512. [CrossRef]
3. Doe Office of Indian Energy. US Department of Energy. Available online: https://www.energy.gov/sites/prod/files/2015/08/f25/LCOE.pdf (accessed on 14 July 2019).
4. Franzitta, V.; Curto, D.; Rao, D. Energetic Sustainability Using Renewable Energies in the Mediterranean Sea. *Sustainability* **2016**, *8*, 1164. [CrossRef]
5. Franzitta, V.; Catrini, P.; Curto, D. Wave Energy Assessment along Sicilian Coastline, Based on DEIM Point Absorber. *Energies* **2017**, *10*, 376. [CrossRef]
6. Karimirad, M.; Koushan, K. WindWEC: Combining wind and wave energy inspired by hywind and wavestar. In Proceedings of the 2016 IEEE International Conference on Renewable Energy Research and Applications (ICRERA), Birmingham, UK, 20–23 November 2016.
7. OES. Ocean Energy Systems. IEA. Available online: https://www.ocean-energy-systems.org/ocean-energy-in-the-world/ (accessed on 12 July 2019).
8. Alves, M.; Causon, D.; Child, B.; Davidson, J.; Elsaßer, B.; Ferreira, C.; Fitzgerald, C.; Folley, M.; Forehand, D.; Giorgi, S.; et al. *Numerical Modelling of Wave Energy Converters*; Elsevier: London, UK, 2016.
9. Magagna, D.; Monfardini, R.; Uihlein, A. *JRC Ocean Energy Status Report*; European Commission: Brussels, Belgium, 2016.
10. Orecchini, F. The era of energy vectors. *Int. J. Hydrogen Energy* **2006**, *31*, 1951–1954. [CrossRef]
11. Franzitta, V.; Curto, D.; Milone, D.; Viola, A. The Desalination Process Driven by Wave Energy: A Challenge for the Future. *Energies* **2016**, *9*, 1032. [CrossRef]
12. Wilson, D.; Bacelli, G.; Coe, R.G.; Bull, D.L.; Abdelkhalik, O.; Korde, U.A.; Robinett, R.D., III. *A Comparison of WEC Control Strategies*; Sandia National Laboratories: Albuquerque, NM, USA, 2015.
13. Ozkop, E.; Altas, I.H. Control, power and electrical components in wave energy conversion systems: A review of the technologies. *Renew. Sustain. Energy Rev.* **2017**, *67*, 106–115. [CrossRef]
14. Wang, L.; Isberg, J.; Tedeschi, E. Review of control strategies for wave energy conversion systems and their validation: The wave-to-wire approach. *Renew. Sustain. Energy Rev.* **2018**, *81*, 366–379. [CrossRef]
15. Falnes, J. *Ocean Waves and Oscillating Systems*; Cambridge University Press: Trondheim, Norway, 2002.
16. Duckers, L. Wave energy. In *Renewable Energy*, 2nd ed.; Boyle, G., Ed.; Oxford University Press: Oxford, UK, 2004; p. 8.
17. Bioenergy International. Global Green Energy Patent Filings 2017 Jump 43% Compared to 2016. Available online: https://bioenergyinternational.com/research-development/global-green-energy-patent-filings-2017-jump-43-compared-to-2016 (accessed on 13 July 2019).
18. Ochs, M.E.; Bull, D.L.; Laird, D.L.; Jepsen, R.A.; Boren, B. *Technological Cost-Reduction Pathways for Point Absorber Wave Energy Converters in the Marine Hydrokinetic Environment*; Sandia Report 7204; Sandia National Laboratories: Albuquerque, NM, USA, 2013.
19. Drew, B.; Plummer, A.R.; Sahinkaya, M.N. A review of wave energy converter technology. *Proc. Inst. Mech. Eng. Part A J. Power Energy* **2009**, *223*, 887–902. [CrossRef]
20. Clément, A.; McCullen, P.; Falcão, A.; Fiorentino, A.; Gardner, F.; Hammarlund, K.; Lemonis, G.; Lewis, T.; Nielsen, K.; Petroncini, S.; et al. Wave energy in Europe: Current status and perspectives. *Renew. Sustain. Energy Rev.* **2002**, *6*, 405–431. [CrossRef]
21. O'Sullivan, D.; Blavette, A.; Mollaghan, D.; Alcorn, R. *Dynamic Characteristics of Wave and Tidal Energy Converters and a Recommended Structure for Development of a Generic Model for Grid Connection*; A Report Prepared by HMRC-UCC for OES-IA under ANNEX III, Document No. T0321. Cork, Ireland, 2010. Available online: https://hal.archives-ouvertes.fr/hal-01265981/document (accessed on 14 August 2019).
22. Laboratory, N.R.E. Marine and Hydrokinetic Technology Glossary. Available online: https://openei.org/wiki/Marine_and_Hydrokinetic_Technology_Glossary (accessed on 22 May 2019).
23. Wave Dragon. Available online: http://www.wavedragon.net/ (accessed on 22 May 2019).
24. Matt, F.; Trevor, W.; Max, O. The Oscillating Wave Surge Converter. In Proceedings of the International Offshore and Polar Engineering Conference, Toulon, France, 23–28 May 2004.

25. Pecher, A.; Kofoed, J.P. *Handbook of Ocean Wave Energy. Ocean Engineering & Oceanography*; No. Power Take-Off Systems for WECs; Springer: Berlin/Heidelberg, Germany, 2017; Volume 7.
26. Schwartz, D.; Mentzer, A. *Feasibility of Linear Induction Wave Power Generation*. Available online: https://linearinductionwavepower.weebly.com/ (accessed on 22 May 2019).
27. So, R.; Casey, S.; Kanner, S.; Simmons, T.K.A.B.A. PTO-Sim: Development of a Power Take Off Modeling Tool for Ocean Wave Energy Conversion. 06 2014. Available online: https://energy.sandia.gov/wp-content/uploads/2014/06/2015-IEEE-PES_PTO-Sim_Nak.pdf (accessed on 22 May 2019).
28. Basic Principles of Turbomachines. IIT 2016. Available online: http://nptel.ac.in/courses/112104117/chapter_7/ (accessed on 19 July 2019).
29. Sandia. Reference Model Project. Available online: https://energy.sandia.gov/energy/renewable-energy/water-power/technology-development/reference-model-project-rmp/ (accessed on 21 June 2019).
30. NREL&Sandia. WECSIM. Available online: https://wec-sim.github.io/WEC-Sim/ (accessed on 22 May 2019).
31. Denis, M.S. Some Cautions on the Employment of the Spectral Technique to Describe the Waves of the Sea and the Response Thereto of Oceanic Systems. In Proceedings of the Offshore Technology Conference, Houston, TX, USA, 29 April–2 May 1973.
32. Xuereb, A.; Spiteri Staines, C.; Sant, T.; Mule Stagno, L. *Design of a Linear Electrical Machine for a Wave Generation System in the Maltese Waters*; Sayigh, A., Ed.; Renewable Energy in the Service of Mankind; Springer International Publishing: New York, NY, USA, 2015; Volume I.
33. Evans, D. Maximum wave-power absorption under motion constraints. *Appl. Ocean Res.* **1981**, *3*, 200–203. [CrossRef]
34. Ringwood, J.V.; Bacelli, G.; Fusco, F. Energy-Maximizing Control of Wave-Energy Converters. *IEEE Control Syst. Mag.* **2014**, *34*, 30–55.
35. Garcia-Rosa, P.B.; Kulia, G.; Ringwood, J.V.; Molinas, M. Real-Time Passive Control of Wave Energy Converters Using the Hilbert-Huang Transform. *IFAC-PapersOnLine* **2017**, *50*, 14705–14710. [CrossRef]
36. Nielsen, K.M.; Pedersen, T.S.; Andersen, P.; Ambühl, S. Optimizing Control of Wave Energy Converter with Losses and Fatigue in Power Take off. *IFAC-PapersOnLine* **2017**, *50*, 14680–14685. [CrossRef]
37. Son, D.; Yeung, R.W. Real-time implementation and validation of optimal damping control for a permanent-magnet linear generator in wave energy extraction. *Appl. Energy* **2017**, *208*, 571–579. [CrossRef]
38. Jin, S.; Patton, R.J.; Guo, B. Enhancement of wave energy absorption efficiency via geometry and power take-off damping tuning. *Energy* **2019**, *169*, 819–832. [CrossRef]
39. Rodríguez, C.A.; Rosa-Santos, P.; Taveira-Pinto, F. Assessment of damping coefficients of power take-off systems of wave energy converters: A hybrid approach. *Energy* **2019**, *169*, 1022–1038. [CrossRef]
40. Jiang, X.; Day, S.; Clelland, D. Hydrodynamic responses and power efficiency analyses of an oscillating wave surge converter under different simulated PTO strategies. *Ocean Eng.* **2018**, *170*, 286–297. [CrossRef]
41. Korde, U.A. Preliminary consideration of energy storage requirements for sub-optimal reactive control of axisymmetric wave energy devices. *Annu. Rev. Control* **2015**, *40*, 93–101. [CrossRef]
42. Robyns, B.; François, B.; Delille, G.; Saudemont, C. *Energy Storage in Electric Power Grids*; Wiley-ISTE: Lille, France, 2015.
43. Jin, P.; Zhou, B.; Göteman, M.; Chen, Z.; Zhang, L. Performance optimization of a coaxial-cylinder wave energy converter. *Energy* **2019**, *174*, 450–459. [CrossRef]
44. Anderlini, E.; Forehand, D.; Bannon, E.; Xiao, Q.; Abusara, M. Reactive control of a two-body point absorber using reinforcement learning. *Ocean Eng.* **2018**, *148*, 650–658. [CrossRef]
45. Budal, K.; Falnes, J. Optimum operation of wave power converter. *Mar. Sci. Commun.* **1977**, *3*, 133–150.
46. Babarit, A.; Duclos, G.; Clément, A. Comparison of latching control strategies for a heaving wave energy device in random sea. *Appl. Ocean Res.* **2004**, *26*, 227–238. [CrossRef]
47. Wu, J.; Yao, Y.; Zhou, L.; Göteman, M. Real-time latching control strategies for the solo Duck wave energy converter in irregular waves. *Appl. Energy* **2018**, *222*, 717–728. [CrossRef]
48. Temiz, I.; Leijon, J.; Ekergard, B.; Bostrom, C. Economic aspects of latching control for a wave energy converter with a direct drive linear generator power take-off. *Renew. Energy* **2018**, *128*, 57–67. [CrossRef]
49. Faedo, N.; Olaya, S.; Ringwood, J.V. Optimal control, MPC and MPC-like algorithms for wave energy systems: An overview. *IFAC J. Syst. Control* **2017**, *1*, 37–56. [CrossRef]
50. Hals, J.; Falnes, J.; Moan, T. Constrained Optimal Control of a Heaving Buoy Wave-Energy Converter. *J. Offshore Mech. Arct. Eng.* **2010**, *133*, 011401. [CrossRef]

51. O'Sullivan, A.C.; Lightbody, G. Co-design of a wave energy converter using constrained predictive control. *Renew. Energy* **2017**, *102*, 142–156. [CrossRef]
52. Anderlini, E.; Forehand, D.; Bannon, E.; Abusara, M. Reactive control of a wave energy converter using artificial neural networks. *Int. J. Mar. Energy* **2017**, *19*, 207–220. [CrossRef]
53. Li, L.; Yuan, Z.; Gao, Y. Maximization of energy absorption for a wave energy converter using the deep machine learning. *Energy* **2018**, *165*, 340–349. [CrossRef]
54. Jama, M.; Wahyudie, A.; Noura, H. Robust predictive control for heaving wave energy converters. *Control Eng. Pract.* **2018**, *77*, 138–149. [CrossRef]
55. Zou, S.; Abdelkhalik, O.; Robinett, R.; Korde, U.; Bacelli, G.; Wilson, D.; Coe, R. Model Predictive Control of parametric excited pitch-surge modes in wave energy converters. *Int. J. Mar. Energy* **2017**, *19*, 32–46. [CrossRef]
56. Korde, U.A.; Lyu, J.; Robinett, R.D.; Wilson, D.G.; Bacelli, G.; Abdelkhalik, O.O. Constrained near-optimal control of a wave energy converter in three oscillation modes. *Appl. Ocean Res.* **2017**, *69*, 126–137. [CrossRef]
57. Xiong, Q.; Li, X.; Martin, D.; Guo, S.; Zuo, L. Semi-Active Control for Two-Body Ocean Wave Energy Converter by Using Hybrid Model Predictive Control. In Proceedings of the ASME Dynamic Systems and Control Conference, Atlanta, GA, USA, 30 September–3 October 2018.
58. Burgaç, A.; Yavuz, H. Fuzzy Logic based hybrid type control implementation of a heaving wave energy converter. *Energy* **2019**, *170*, 1202–1214. [CrossRef]
59. Abdelkhalik, O.; Darani, S. Optimization of nonlinear wave energy converters. *Ocean Eng.* **2018**, *162*, 187–195. [CrossRef]
60. Zhan, S.; Wang, B.; Na, J.; Li, G. Adaptive Optimal Control of Wave Energy Converters. *IFAC-PapersOnLine* **2018**, *51*, 38–43. [CrossRef]
61. Senol, K.; Raessi, M. Enhancing power extraction in bottom-hinged flap-type wave energy converters through advanced power take-off techniques. *Ocean Eng.* **2019**, *182*, 248–258. [CrossRef]
62. Song, J.; Abdelkhalik, O.; Robinett, R.; Bacelli, G.; Wilson, D.; Korde, U. Multi-resonant feedback control of heave wave energy converters. *Ocean Eng.* **2016**, *127*, 269–278. [CrossRef]
63. Lekube, J.; Garrido, A.J.; Garrido, I. Rotational Speed Optimization in Oscillating Water Column Wave Power Plants Based on Maximum Power Point Tracking. *IEEE Trans. Autom. Sci. Eng.* **2017**, *14*, 681–691. [CrossRef]
64. Sun, T.; Nielsen, S.R. Stochastic control of wave energy converters for optimal power absorption with constrained control force. *Appl. Ocean Res.* **2019**, *87*, 130–141. [CrossRef]
65. Han, J.; Kitazawa, D.; Kinoshita, T.; Maeda, T.; Itakura, H. Experimental investigation on a cabin-suspended catamaran in terms of motion reduction and wave energy harvesting by means of a semi-active motion control system. *Appl. Ocean Res.* **2019**, *83*, 88–102. [CrossRef]

energies

MDPI

Article

Impact of Electrical Topology, Capacity Factor and Line Length on Economic Performance of Offshore Wind Investments

Sadik Kucuksari [1,*,†], Nuh Erdogan [2,*,†] and Umit Cali [3,*,†]

1 Department of Technology, University of Northern Iowa, Cedar Falls, IA 50614, USA
2 Marine and Renewable Energy Centre, University College Cork, P43 C573 Cork, Ireland
3 Department of Engineering Technology and Construction Management, University of North Carolina at Charlotte, Charlotte, NC 28223, USA
* Correspondence: sadik.kucuksari@uni.edu (S.K.); nuh.erdogan@ucc.ie (N.E.); ucali@uncc.edu (U.C.); Tel.: +1-319-273-2753 (S.K.)
† These authors contributed equally to this work.

Received: 10 July 2019; Accepted: 16 August 2019; Published: 20 August 2019

Abstract: In this study, an economic performance assessment of offshore wind investments is investigated through electrical topology, capacity factor and line length. First, annual energy yield production and electrical system losses for AC and DC offshore wind configurations are estimated by using Weibull probability distributions of wind speed. A cost model for calculating core energy economic metrics for offshore wind environment is developed by using a discount cash flow analysis. A case study is then conducted for a projected offshore wind farm (OWF) rated 100 MW and 300 MW sizes situated in the Aegean sea. Finally, a sensitivity analysis is performed for AC and DC OWFs with three different capacity factors (e.g., 45%, 55% and 60%) and various transmission line lengths ranging from 20 km to 120 km. The OWF is found to be economically viable for both AC and DC configurations with the estimated levelized cost of electricity (LCOE) ranging from 88.34 $/MWh to 113.76 $/MWh and from 97.61 $/MWh to 126.60 $/MWh, respectively. LCOEs for both options slightly change even though the wind farm size was increased three-fold. The sensitivity analysis reveals that, for further offshore locations with higher capacity factors, the superiority of AC configuration over the DC option in terms of LCOE reduces while the advantage of DC configuration over the AC option in terms of electrical losses is significant. Losses in the AC and DC configurations range from 3.75% to 5.86% and 3.75% to 5.34%, respectively, while LCOEs vary between 59.90 $/MWh and 113.76 $/MWh for the AC configuration and 66.21 $/MWh and 124.15 $/MWh for the DC configuration. Capacity factor was found to be more sensitive in LCOE estimation compared to transmission line length while line length is more sensitive in losses estimation compared to capacity factor.

Keywords: cost-benefit analysis; DC collection; energy economics; HVDC; HVAC; levelized cost of electricity (LCOE); offshore wind

1. Introduction

Technological developments and changes in lifestyles have driven significantly the increase in energy usage worldwide. Global energy consumption increased by 48.3% from 2002 to 2018 [1]. The use of energy is predicted to rise by 28% by 2040 [2]. Accordingly, global electrical energy use is expected to increase by 58% in the next two decades as well. The increase in electrical energy use contributes to CO_2 emissions and creates environmental concerns. Over the past two decades, renewable energy resources have provided alternatives for energy generation, specifically on electrical energy through solar and wind energy utilizations. The share of renewables for electrical energy generation reached

26% in 2018 [2]. Among the renewable energy resources, excluding conventional hydropower, wind energy has the highest share in terms of installed capacity [3]. Global installed wind power capacity has increased about 30 fold from 2000 to 2017, reaching a cumulative capacity of 591 GW at the end of 2018 [4]. Having higher wind energy potential due to less friction on water surfaces makes offshore wind farms more favorable over their onshore counterparts [5]. The global installed offshore wind power capacity has increased from 4177 MW to 23,140 MW from 2011 to 2018 [6]. The installed capacity of 4.5 GW in 2018 has broken the records on increase in a single year. The fast growth in the offshore wind sector deserves special attention with regard to technical, economical and efficient electric power delivery. From an economical point of view, the cost of offshore systems is higher [7] and varies from project to project since the cost of offshore installations is extremely dependent on their site conditions and location as opposed to their on-shore counterparts [8]. To maintain the offshore market growth given the expected increase in turbine sizes and efficiency, cost-effective solutions for the offshore wind energy sector need to be explored.

An offshore wind farm (OWF) configuration typically consists of collection and transmission systems at medium and high voltages, respectively, including an offshore and/or onshore substation. Most of the current offshore wind farms are all alternating current (AC) systems both at collection and transmission systems. Considering the 20% share of transmission system cost over the total cost figure, alternative solutions may reduce the overall cost [9]. One of the growing alternatives for delivering the generated wind power is using high voltage direct current (HVDC) instead of high voltage alternating current (HVAC) for the transmission system since situated further offshore distances started to become more common [10] and HVDC provides benefits over HVAC for longer distances. Even though less charging current occurs over the HVDC cables [11], the total system losses can be higher due to the additional losses associated with the power electronics components of OWFs [12]. Another alternative transmission that appeared is low frequency AC (LFAC) offshore wind systems, which are found to be more costly than their HVAC and HVDC counterparts for longer distances from the coast [13]. Among three alternatives of power transmission, HVDC becomes more attractive over LFAC and HVAC systems due to the higher transmission line losses and costs associated with the AC systems for far further situated offshore locations. While implementing the HVDC system to overcome these challenges, its economical performance assessment needs to be carefully studied [11]. Medium voltage collection system design starts with the micro sitting of wind turbines using optimization methods that consider many parameters such as wind direction and wake effect [14]. As for a high voltage transmission system, DC topology for collection system is being discussed to be an alternative to AC collection system as it may reduce cable losses and costs. The improvement in DC control and protection device technology also will make the DC collection system more attractive over AC collection in which the control and protection devices are well established and used [15]. Currently, there are no OWF with DC collection systems but a few prototypes are being investigated [15,16]. A detailed cost analysis is therefore needed for both complete AC and DC collection and transmission systems since the cost depends on various parameters such as rated power, wind capacity factor, losses, distance from the shore and so forth [5,12].

The cost of the above-mentioned alternative transmission systems is studied to better shape the future direction of OWF configurations. The economic benefits of various offshore network configurations, including HVAC and HVDC, for the coordinated development of interconnection energy flow are presented in Reference [10]. A comparison of incremental operational and investment costs is examined through a cost model using Monte Carlo approach. Results suggest that coordinated multi-terminal HVDC grid with H-grid configuration could offer operational benefits compared to radial connection. However, under certain circumstances the benefits may be reduced. The study is limited with considering only transmission system and focuses more on the interconnection of different configurations. A cost model for HVAC and HVDC cost comparison was redesigned in Reference [12] considering the losses. It is shown that OWFs installed in a larger size and situated further offshore result in reduced costs for HVDC transmission [17]. Xiangyu et. al in Reference [18]

presented a techno-economic analysis of voltage source converter (VSC) based HVDC and HVAC transmission systems for OWFs. They showed that the VSC based HVDC is superior in terms of both economic and technical benefits over the HVAC while the latter includes higher electrical losses. A detailed cost-benefit analysis and power loss calculations were performed for HVAC and several HVDC configurations in Reference [11]. It was found that a critical transmission distance of 85 km makes the VSC based HVDC more economical. A cost analysis for three transmission systems (i.e., HVAC. HVDC, LFAC) is presented in Reference [19]. Results indicated that LFAC may become the cost effective option for shorter distances while HVDC is the most cost effective for longer transmission distances. Similar results are presented in Reference [13] in which the LFAC is found to be more competitive at medium distances between 50–200 km from shore compared to its HVDC counterpart. Instead of delivering power from offshore through HVDC, it is even considered to energize offshore oil industry platforms from an onshore power grid [20]. It is proved that receiving electrical energy through a HVDC transmission to offshore platforms can be more economical comparing to local diesel-fired electricity generation. Techno-economic comparison of HVDC and HVAC is presented in Reference [21]. A wind farm rated 300 MW is used for comparison of different wind turbine topologies, power losses, grid requirements and black start capacity of the two topologies. Results show that the break-even distance of the two systems is found to be 80 km and depends upon the wind turbine technology used, the economic superiority of one over another may be different. An economic comparison of HVAC and HVDC topologies for OWFs at varying rated power from 250 MW to 1500 MW in Great Britain is presented in Reference [22]. Unlike the previous literature, the results show that the break-even cost of the two systems can be only achieved for higher wind farm scales with further offshore locations (i.e., a rated power of 500 MW and a transmission line of 160 km). However, the impact of the collection system on the cost calculations is not considered. Technical and economic comparison of HVAC and HVDC, along with the HVDC market size and high-level comparison of HVDC system components, are presented in Reference [23]. It is concluded that HVDC transmission is beginning to dominate the market and multi-terminal DC networks are expected to play a significant role in the future. The economic analysis in this study is not presented in detail and mainly considers the comparison of some existing or case studies.

While the above-mentioned studies focus on the transmission system, few studies have presented the DC collection system for OWF [15,24]. Possible designs, topologies, converter types and platform configurations are given to provide an inside for the possible usage of DC collection systems together with the HVDC transmission [15]. In Reference [24], a new converter topology was proposed to decrease losses within the DC collection system as an alternative to AC topology. The study in Reference [25] presents a cost assessment for the collection system of an OWF. Since the collection system voltage level is not as high as that of transmission system, the AC and DC configurations may have different relations in terms of cost. The length of the collection system considered is very short. The comparison for overall cost and losses shows that the DC collection system has higher costs and losses compared to the AC collection counterpart. However, as the difference is found to be much less, a detailed cost and loss analysis is still needed for different OWF electrical topologies with practical offshore distances. Reference [16] focuses on a collection system with traditional AC and various DC configurations that are both connected to a power system through a HVDC transmission line. Results concluded that DC configuration for larger scale OWFs may not be economically feasible compared to AC systems due to the DC/DC converters' size. Another study on optimizing OWF design and reducing cost is presented in Reference [26], in which different turbine foundations, AC collection and HVDC transmission for OWFs are considered in a sensitivity analysis. Results suggest that the cost factors mainly vary with the turbine size.

The feasibility of offshore wind investments requires a comprehensive analysis of possible electrical topologies in terms of loss and cost perspectives in a decision making process. HVDC transmission systems have been heavily investigated in search of a viable OWF for further offshore installations. However, the use of DC topology for a medium voltage collection system together with

HVDC can bring a new approach to future OWFs for economic viability. This paper, therefore, presents a detailed techno-economic analysis for conventional all AC and emerging all DC OWF configurations. Radial AC and DC OWF topologies are proposed. Considering the Weibull probability distribution function for wind speed, annual energy yield and the losses of OWF electrical system components are estimated in detail and included in cost calculations. Energy economics metrics such as LCOE, net present value (NPV) and discounted pay-back period (DPBP) are calculated using a discounted cash flow analysis. The proposed analysis is implemented for a possible offshore site in the Aegean Sea, which was found to have the highest capacity factor among the 55 possible offshore locations in Turkey in an earlier study [4]. Two OWF sizes of 100 MW and 300 MW are studied to investigate the impact of electrical topologies on OWF economics in terms of installed capacity. A sensitivity analysis is finally performed for three offshore locations with various capacity factors and distances to shore. The rest of this paper is organized as follows. Section 2 describes the electrical topologies considered. Loss estimation is expressed in Section 3 while economic analysis is evaluated for the selected OWF in Section 4. Results and discussion are presented in Section 5. Finally, Section 6 provides the concluding remarks.

2. Description of Electrical Topologies Considered

Several solutions in terms of electrical topology (i.e., AC, DC and hybrid) have been proposed for both collection and transmission systems [11]. Since the best techno-economic solution for a given application depends on total wind power generated and distance from shore, AC and DC topologies will be considered separately for the configuration of OWF collection and transmission systems.

This offshore site is selected as a result of earlier extensive study based on a multi-criteria site selection work that considers many decision criteria in terms of technical (e.g., wind speed and sea depth), social and civil restrictions, that is, territorial waters, military areas, civil aviation, shipping and pipeline routes and environmental concerns [4]. It was also found in another earlier study [8] that the selected site is less favorable in terms of economics compared to other offshore sites in the Aegean sea since it is far from the point of common coupling which makes its electrical system investment cost higher. The examined OWF is considered to be rated 100 MW and 300 MW. It consists of an inner collection system with 25 and 75 turbine system sets, respectively, connected to an onshore substation in the island and high voltage (HV) submarine transmission cables between the onshore substation and the point of common coupling busbar in the mainland.

2.1. AC Offshore Wind Energy System

The AC OWF configuration considered in this study is shown in Figure 1. The collection system consists of several radial branches that are connected to an onshore substation via submarine cables. Each turbine set rated at 4 MW includes AC–DC and DC–AC converters and a step-up transformer rated 0.69 kV/33 kV, 4.5 MVA. The bus voltage at the AC collection system is thus 33 kV. An onshore substation is considered in the island. It consists of 1 and 3 step-up transformers rated 33 kV/154 kV, 100 MVA including reactive power compensation and grid interface control units. The transmission system includes a three-phase HVAC submarine cable that connects the OWF to the power system in the mainland.

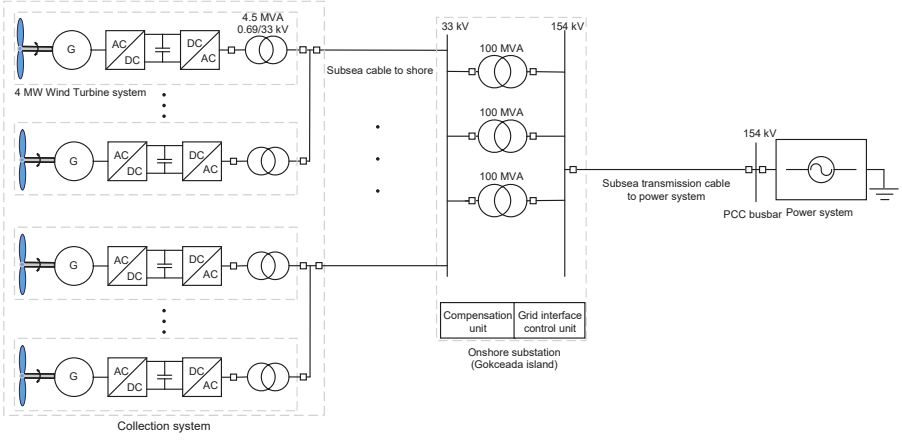

Figure 1. Configuration of proposed AC OWF.

2.2. DC Offshore Wind Energy System

The proposed DC OWF is shown in Figure 2. In this configuration, each turbine is coupled to AC-DC and DC-DC converters that creates a medium voltage (MV) DC bus in the collection system. The collection system is connected to another multi-level step-up DC–DC converter at an onshore platform through monopolar DC 30 kV submarine cables. The onshore platform DC converter is rated at 100 MW and 300 MW. The transmission system includes bipolar HVDC (e.g., 150 kV) submarine cables. Another onshore converter station is placed on the mainland to connect the OWF to the power system. This converter station consists of a multilevel cascaded DC-AC converter including DC capacitors, reactors and filters.

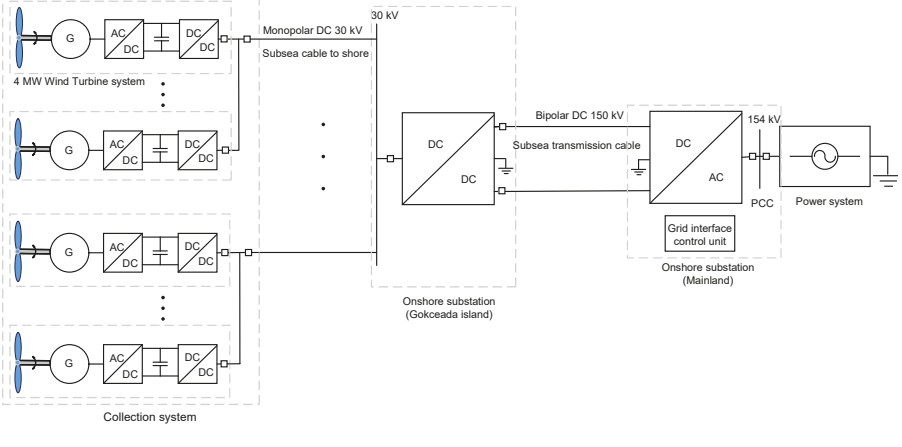

Figure 2. Configuration of proposed DC OWF.

2.3. Electrical Design for Offshore Wind Farm Collection System

The radial design for an OWF collection system was shown to be the most cost-effective option in an earlier study [8]. Herein, based on engineering judgments, radial designs are considered for both the OWFs rated 100 MW and 300 MW as shown in Figure 3. To maximize wind energy usage as well as reduce wake effects, turbines sit perpendicular to the main wind direction and in rows spacing 3.6 rotor diameters (D) within each row and 7 D between rows as recommended in [27].

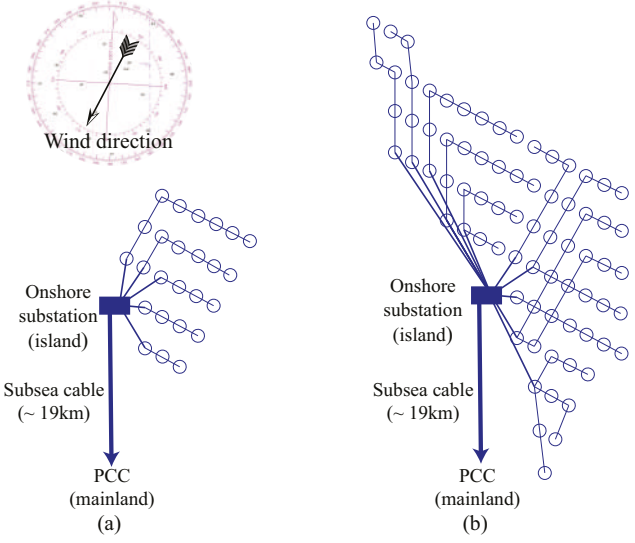

Figure 3. Proposed electrical layouts of the OWF collection system: (**a**) 100 MW. (**b**) 300 MW. Each circle represents the wind turbine system given in Figures 1 and 2.

3. Annual Energy Yield and Electrical Losses Estimation

Estimating wind power output is an integral element of energy business which can be categorized into two clusters—long-term and short-term energy forecasting, respectively. Short-term forecasting tools with hour ahead and day ahead forecast horizons are used for daily operations such as optimal scheduling of the utilities while estimation of annual energy production (AEP) is used for investment decisions for energy generation projects [28]. Within the scope of this article, AEP figures are estimated using an open source renewable energy resource assessment tool named Virtual Wind Farm (VWF) [29]. VMF is based on the weather data which originates from satellite observations and global reanalysis models such as NASA's MERRA (Modern-Era Retrospective Analysis for Research and Applications). The model generates the hourly wind power and wind speed values for the given location for the entire year [30]. The Siemens Wind Turbine SWT-4.0-130 is used in the model [31]. The cut in wind speed (v_{min}) is 5 m/s and the cut out wind speed (v_{max}) is 25 m/s while the rated wind speed is 12 m/s. As wind speed can greatly vary for the cycle of a year, power components (i.e., converters, transformers, etc.) of an OWF are not rated loaded for the most of the time of a year. Using Weibull distribution for power loss of a wind farm achieved more accurate results in Reference [32]. To have more accurate values in estimating losses of each system components, this study therefore considers the Weibull probability distribution function for wind speed. The steady state current values are used in the following calculations.

3.1. Power Electronics Losses

The power electronics (PE) losses for the AC offshore configuration include the losses in the turbine converters within the collection system while the PE losses for the DC counterpart include the losses in the turbine converters, the onshore DC-DC and DC-AC converters. The turbine converter losses are the sum of the switching and conduction losses in the IGBTs(P_{IGBT}) and the freewheeling diodes (P_{FWD}) that are given, respectively, as follows [25]:

$$P_{IGBT-turbine} = N_{sw}(V_{CEO} \cdot I_{c-ave} + R_C \cdot I_{c-rms}^2 + (E_{onT} + E_{offT}) \cdot f_{sw}), \quad (1)$$

$$P_{FWD-turbine} = N_{sw}(V_{DO} \cdot I_{d-ave} + R_D \cdot I_{d-rms}^2 + E_{onD} \cdot f_{sw}), \quad (2)$$

where V_{CEO} and V_{DO} are the on-state voltages (V), I_{c-ave} and I_{d-ave} are the average currents (A), R_C and R_D are the on-state resistances (Ω), I_{c-rms} and I_{d-rms} are the rms currents, for the IGBT and diode, respectively. E_{onT} and E_{offT} are the IGBT's turn-on and off energy losses (W), respectively and E_{onD} is the diode reverse recovery energy loss (W). f_{sw} is the switching frequency which is selected as 1260 Hz. N_{sw} is the number of switches (IGBT or diode). The ABB IGBT modules of type 5SNA 3600E170300 is considered in the turbine converters [33].

To get a high conversion ratio (e.g., 1:5) at MW level, the multilevel step-up DC-DC converter topology proposed in Reference [34] is used for the onshore DC-DC converter. Based on the conventional boost converter configuration, the topology consists of two half-bridges (clamped IGBTs) in the lower position and four chopper (clamped diodes) in the upper position. The ABB IGBT modules of type 5SNA 1200G450300 is used in the onshore DC-DC converter [33]. The switching losses are comprised of the upper and lower stacks IGBT switching losses and upper stack diode reverse recovery losses while the conduction losses comprise the upper and lower stacks IGBT conduction losses and upper and lower stacks diode conduction losses. The total losses are the sum of switching and conduction losses which can be expressed for the IGBT and diode, respectively, as follows [34]:

$$P_{IGBT-HVDC} = 2Nf_{sw}E_{offT} + 4Mf_{sw}E_{onT} + 4Mf_{sw}E_{offT} + 2NV_{CEO}I_N\lambda_{N1} + 2MV_{CEO}I_M\lambda_{M1}, \quad (3)$$

$$P_{FWD-HVDC} = 4M \cdot f_{sw} \cdot E_{onD} + 2NV_{DO}I_N\lambda_{N2} + 2MV_{DO}I_M\lambda_{M2}, \quad (4)$$

where $N = 4$ is the number of upper sub modules, M = 2 is the number of lower sub modules. I_N and I_M are the average currents in the upper and lower stacks, respectively. λ refers to the ratio of the conduction time to the switching period. The switching frequency of 1 kHz is taken in the calculation.

For the onshore DC-AC converter, the cascaded multilevel converter topology [35] is considered. The topology uses five series connected H-bridges in each phase which creates 11-level line-to-neutral voltage and hence 21-level line-to-line voltages. The ABB IGBT modules of type 5SNA 0750G650300 rated 6500 V is used in the onshore DC-AC converter [33]. The switching frequency of 1 kHz is taken. The associated PE losses in the IGBT modules ($P_{IGBT-HVAC}$) and ($P_{FWD-HVAC}$) can be calculated as given by (1) and (2), respectively. Thus, total PE losses for AC and DC offshore configurations are obtained by (5) and (6), respectively. The parameters of the IGBT modules used are listed in Table 1.

$$P_{PE-AC} = N_{turbine} \cdot (P_{IGBT} + P_{FWD}), \quad (5)$$

$$P_{PE-DC} = N_{turbine} \cdot (P_{IGBT} + P_{FWD}) + P_{IGBT-HVDC} + P_{FWD-HVDC} + P_{IGBT-HVAC} + P_{FWD-HVAC}, \quad (6)$$

where, $N_{turbine}$ is the total number of turbines within the OWF.

Table 1. Rated values for Parameters of the IGBTmodules used in the converters [33].

Parameter	5SNA 3600E170300	5SNA 1200G450300	5SNA 0750G650300
V_{CES} (V)	1700	4500	6500
I_C (A)	3600	1200	750
V_{CEO} (V)	2.5	2.6	2.9
R_C (mΩ)	0.055	0.07	0.07
E_{onT} (mJ)	1100	4350	6400
E_{offT} (mJ)	1600	6000	5300
V_{DO} (V)	1.85	3.2	3.2
R_D (mΩ)	0.094	0.34	0.13
E_{onD} (mJ)	1080	2730	2700

3.2. Transformer Losses

As the transformerless multilevel converter topologies are considered in the DC offshore wind configuration, the transformer losses are therefore a matter of concern for the AC offshore wind configuration. They include the losses of turbine transformers and the onshore substation transformers. The total losses of a transformer at any load level can be obtained by (7) [36],

$$P_{Trfm} = P_0 + I_L^2 \cdot \Re(Z_{pu} \times Z_{base}), \tag{7}$$

where, P_0, Z_{pu} and Z_{base} are no-load losses, p.u.and base impedances of transformer, respectively, obtained from its nameplate. I_L is transformer primary current.

3.3. Collection and Transmission Lines Losses

The longest collection line is 8 km while the length of the transmission line is 19 km. The short line model can then be used for the modeling of the cables of the collection and transmission lines. It is represented by a series RL circuit. In this case, line losses are calculated by $I^2 \cdot R$. The currents are calculated from operating wind power associated with each wind speed while resistance values are obtained from the underground cable manufacturer's catalog which is selected for rated operation. Herein, the DC resistance values at 20 °C of cables are used for the DC offshore configuration while maximum AC resistance values at 90 °C are used for the AC counterpart. In determining the resistance values, cables are assumed to be directly buried in ground.

3.4. Annual Energy Losses

The total annual energy losses can be found by integrating the losses over the Weibull probability distribution of wind speed for a cycle of a year [25]. Thus, the annual energy losses in the AC and DC offshore configurations become

$$E_{AC-losses} = \int_{v_{min}}^{v_{max}} (P_{PE-AC} + P_{Trfm} + P_{cable-AC}) \cdot f(v_w) \cdot 8760 \, \mathrm{d}v_w, \tag{8}$$

$$E_{DC-losses} = \int_{v_{min}}^{v_{max}} (P_{PE-DC} + P_{cable-DC}) \cdot f(v_w) \cdot 8760 \, \mathrm{d}v_w, \tag{9}$$

where $E_{AC-losses}$ and $E_{DC-losses}$ are the total annual energy losses in the AC and DC offshore configurations, respectively. $P_{cable-AC}$ and $P_{cable-DC}$ are the total collection and transmission lines losses in the AC and DC offshore configurations, respectively. $f(v_w)$ is the Weibull probability distribution function of occurrence of each wind speed for a year obtained using the wind farm model.

4. Economic Analysis

4.1. Major Investment Indicators Considered For Economic Assessment

NPV, LCOE and DPBP are among the major investment energy economic metrics which help the energy sector players to make wise investment decisions [8,37]. Besides, the cash follow diagrams provided contain more information about the entire projected life cycle of an project investment scenarios with yearly resolution. The business of the usual operations of the energy companies shall ideally utilize the above-mentioned techno-economic metrics with higher resolution by considering other dynamic parameters including tax, inflation and risk management components before making their multi-million $ investments. AEP figures are one of the most important parameters of a cost-benefit analysis where the revenues of the energy economic system are created. NPV indicates the difference between the present value of annual cash inflows (benefits) and annual outflows (expenditures). For the entire project lifespan of an OWF, NPV can be expressed by [8]:

$$NPV = -C_{CAPEX} + \sum_{t=1}^{T} \frac{netCashFlow(t)}{(1+r)^t}, \tag{10}$$

where C_{CAPEX} and T represents the total capital expenditures (CAPEX) and lifespan of OWF, respectively and r is the annual discount rate. The net cash flow for a year is found by subtracting the present value of outflows from the present value of annual cash inflows which includes the annualized operational expenditures (OPEX) and revenues, respectively. In other words, the outflows correspond to the OPEX in the corresponding year while the inflows are related to the AEP of the corresponding year. Revenues of investment calculation are primarily dependent on the AEP figures in energy investments. Positive NPV values represent the economically viable investment option. If there are multiple positive NPV values calculated for various investment options, the options that yield the highest NPV figure shall be selected for the investment. The LCOE is a special per unit cost energy economic metrics which characterizes the NPV of an OWF over its life-cycle and is estimated by [8]:

$$LCOE = \frac{\sum_{t=0}^{T} \frac{C_{CAPEX}(t)+C_{OPEX}(t)}{(1+r)^t}}{\sum_{t=0}^{T} \frac{netAEP}{(1+r)^t}}, \tag{11}$$

where $\forall t \in \{1..T\}$, $C_{CAPEX}(t) = 0$ and initial value of $C_{OPEX}(0) = 0$. $C_{OPEX}(t)$ indicates the OPEX for the year of t. The net AEP is the estimated amount of energy generated by the power plant annually. Pay-back period (PBP) shows the time duration in which the cumulative profit is equal to the cumulative cost. For many investment decision processes, PBP is considered one of the important economic threshold values. However, the PBP does not reflect the time value of money. Thus, using the PBP can be misleading in real life investment decisions where the discount rate is greater than zero percent. In this case, it is essential to utilize the DPBP metrics for more realistic evaluations where the time value of money is also taken in to account. The DPBP is then calculated by [8]

$$DPBP = \frac{ln\left(\frac{1}{1-\frac{r \cdot C_{CAPEX}}{NetCashFlow}}\right)}{ln(1+r)}. \tag{12}$$

The profitability can be measured by using internal rate of return (IRR) metrics that express the discount rate which makes the NPV of an investment equal to zero. The IRR is calculated by dividing the net profit of the investment by the total cost of the investment. The detailed explanation of techno-economic evaluation will be given in the following sections.

4.2. Cost Calculation for AC and DC Offshore Wind Energy Projects

The total investment cost of an OWF project includes CAPEX and OPEX. The parts of each element are expressed below.

4.3. CAPEX

The CAPEX typically have four parts [38]—(i) turbine cost, (ii) support system cost, (iii) electrical system cost, (iv) project development, management and other costs such as insurance. The cost difference in HVAC and HVDC mainly exists due to the different electrical system topologies. The following subsections provide details of each cost component.

4.3.1. Wind Turbine Cost

Wind turbine cost based on the power capacity is provided in Reference [39] for turbines ranging from 2 to 5 MW. Transportation and installation costs of turbines are considered to be 10% of the turbine cost and included into the total cost given by

$$C_{turbines} = 3.245 \cdot 10^3 ln(P) - 412.72 \quad [k€], \tag{13}$$

where, P is the installed wind power capacity. It is also assumed that this includes the cost of turbine converters and transformer. The given cost function is used both for AC and DC system turbine costs.

4.3.2. Support System Cost

The support system includes foundation and tower. Its cost mainly has three parts—(i) manufacturing, (ii) transportation and (iii) installation. The costs of transportation and installation are included into the manufacturing cost with the assumption of being 50% of the manufacturing cost. The total cost can be formulated as

$$C_{support} = 480 \cdot P(1 + 0.02(d - 8))(1 + 0.8 \cdot 10^{-6}(h(\frac{D}{2})^2 - 10^5)) \quad [k€/turbine], \tag{14}$$

where d [m] is sea depth, h[m] is hub height and D[m] is rotor diameter. Monopile foundation cost is considered for all the turbines. A sea depth of 45 m is considered; however, the soil properties are not taken into account due to the lack of publicly available data. Both AC and DC systems use the same cost function for support system.

4.3.3. Electrical System Cost

Based on the selected electrical system topology, electrical system cost components vary. Both in AC MV collection and HV transmission systems, the topology is standard AC system topology. In this study, the AC electrical system cost includes inner cable, substation, power factor correction devices and high voltage cables connecting the OWF to the nearest point of common coupling [8]. DC collection and transmission system, on the other hand, may have different configurations both in cables and components. There are two main topologies that exist in a HVDC transmission system, that is, Line-Commuted Converter (LCC) and VSC based topologies. Nowadays, the VCS based converter is the most promising technology that dominates the market [40,41].The overall electrical system cost components for the DC configuration include: (1) medium voltage DC submarine inner cables with installations; (2) onshore substation that includes converters and other necessary components; (3) high voltage DC submarine cables and their installations connecting onshore substation in the island to the mainland; (4) converters in the mainland; and (5) a grid connection unit including other substation components such as reactors.

1. *Collection system cable cost*—the wind turbines are connected to each other as well as to the onshore substation through submarine cables. The core (conductor) of the cables can be either

stranded copper or aluminum. Due to the surrounding sea environment, sufficient electrical insulation is needed around the conductor. The subsea cable insulations are made of different dielectric materials. Among the two common ones are mass impregnated paper and Cross Linked Polyethylene (XLPE) Polymeric cables [42,43]. There are additional layers exist for shielding and mechanical strength purposes. For the DC configuration, XLPE cables are mostly used with VSC topology [44] and were therefore selected for this study. For the AC configuration, 3 core XLPE type cables were selected from available manufacturer datasheets. Reference [45] provides DC cable cost formulation for different voltages. Reference [25] presents a cost function for a 30 kV voltage level cable. The cost model used is given as follows [25]:

$$C_{cable-DC/km} = A_p + B_p \cdot P_n \quad [M£/km], \tag{15}$$

where A_p and B_p are the cost constants of $-0.0256 \cdot 10^6$ and 0.0068 for 30 kV, respectively. P_n rated power of the cable [W]. The cost is converted to €/m and costs for different cross-sections of cables are calculated. The bipole 150 kV cable cost is calculated with the same formula with different constants ($A = -0.1 \cdot 10^6$ and $B = 0.0164$) given in Reference [45]. The calculated cable costs in €/m are given in Table 2.

Table 2. DC cable costs considered for collection and transmission systems.

Voltage (kV)	Topology	Cable Cross-Section (mm^2)	Price (€/m)
30	Monopole	95	50
30	Monopole	120	61
30	Monopole	185	86
30	Monopole	300	124
30	Monopole	400	147
30	Monopole	500	175
30	Monopole	630	207
30	Monopole	1000	279
30	Monopole	1400	339
30	Monopole	1600	368
150	Bipole	150	201
150	Bipole	630	479

Typical cable cross-sections were taken from a manufacturer's [46] publicly available datasheet and depending on the selected voltage and power levels, cable costs are estimated as in Table 2. The cable cross sections were selected such that they carried the maximum power output of the wind turbines. It was considered that the selected radial collector system has a single cable in a row and carries the power of minimum 3 and maximum 13 wind turbine outputs in one feeder. These numbers were determined by considering the physical layout design as well as cable cross sections ampacity levels. An additional 40 m supplementary cable for each turbine was considered as recommended in Reference [38]. The total cable cost for DC collection system was calculated as

$$C_{cable} = C_{cable-DC/km} \times l_{inner-cable} \quad [k€]. \tag{16}$$

The cost function for 3 core XLPE cables given in Reference [39] was used to calculate the cable costs as follows:

$$C_{cable-AC/km} = \alpha + \beta \times e^{\frac{\gamma \cdot I_n}{10^5}} \quad [k€/km], \tag{17}$$

where α, β and γ are constants 52.08, 75.51 and 234.34, respectively. I_n is the current ratings of the cables. Typical cable cross-sections with their current ratings were taken from two manufacturer's available data sheets [47,48].

The cables were considered to be buried under on the seabed. The burying cost in Reference [38] was used as 273 k€/km. The total burying cost for the collection system was calculated by considering all the cable lengths used in the system as

$$C_{burrying} = 273 \times l_{inner-cable} \quad [k€]. \tag{18}$$

2. *Onshore DC/DC converter substation*—one of the factors affecting the DC offshore wind system cost is converter costs. The percentage of the converters over the total cost varies based upon the system topology and transmission distance. Converter costs are found to be around 20% in References [49,50]. The DC configuration becomes more economical over the AC configuration once the converter cost is covered by the cable costs. In DC offshore wind systems, the onshore and offshore substations house the converters and a few other components such as reactors, filters and DC breakers. In addition, the offshore substations cost includes the platform cost as well. In this paper, since there were two onshore substations considered, platform cost was disregarded.

   Obtaining the exact cost figures for substation converter stations is very difficult. Reference [51] investigated many studies and proposed € 150/kW. Reference [45,52] presented 1 SEK/VA price for the converters. Reference [53] argues this is because of having different insulation levels at different voltages and proposes three different cost figures for different power ratings. Reference [52] states that this cost includes the cost of valves, filters and other necessary parts. The average of these figures given in the literature was used in this study, which is € 194.23/kVA by assuming that all the substation component costs are included. The onshore substation in the island is a DC/DC converter that steps up the voltage. It is assumed that the converter station includes a series connection of valves for the total power rating. The total price is calculated as

$$C_{substation-DC} = 194.23 \cdot P \quad [k€/km]. \tag{19}$$

3. *Onshore AC substation and power factor correction costs*—since the substation has many components including transformers, switchgeras, backup generators and so forth, the cost is considered as a lump sum that is a function of the installed wind power capacity. Based on the cost model in Reference [38], a cost of 50 k€/MW was used for the calculations. The cost models for power factor correction devices (i.e., SVC, STATCOM, shunt reactors) are given as follows [38]:

$$\begin{cases} C_{shunt-reactor} = 2,556€/MVAr \\ C_{SVC} = 6390€ + 63,900€/MVAr \\ C_{STATCOM} = 128k€/MVAr \end{cases} \tag{20}$$

   Thus, the total substation cost is found [8] by

$$C_{substation-AC} = 50[k€]/MW + C_{shunt-reactor} + C_{SVC} + C_{STATCOM}. \tag{21}$$

4. *Transmission line cost*: The total power of 100 MW and 300 MW collected from wind turbines are delivered to onshore substation with the monopole collector system in DC collection system. The DC/DC converter in onshore substation steps up the collector voltage from 30 kV to 150 kV for HV transmission system. A bipole with two conductor system given in Reference [54] is considered for the transmission system from the onshore substation on the island to the other onshore substation on the mainland. The system has 150 kV voltage and two identical cables deliver the power as an underground (1.7 km) and subsea system (17.3 km). No overhead lines are considered for the transmission system. The two cables connecting the two substations share the total power due to being a bipole system and their cross-sections were considered based on the

maximum current. The transmission cable cost that was calculated earlier was used for per km. Additional 100 km supplemental cable was considered and the total cable cost was calculated as:

$$C_{transmission-HVDC} = 2 \cdot C_{cable-DC/km} \times l_{transmission-cable} \quad [k€/km]. \tag{22}$$

Since all the transmission cables are underground and subsea cables, a burying cost of 273 k€/km given in Equation (18) was used. In this study, close laying structure of cables was considered for the bipole system. The two cables were considered to be close to each other and buried together to have a single burying cost. The literature does not present any cost model for a single core XLPE cable used in the HVAC transmission system for high power delivery. It is also difficult to get the cost information from a manufacturer due to it being sensitive information for business operations. Therefore, it was assumed that a single core cable cost is 40% of the 3-core for the same current rating because of better insulation requirements for high voltage. The HVAC transmission system includes three single core cables, hence, the total cost for transmission system cable is tripled.

5. *Onshore DC/AC converter substation*—the onshore substation on the mainland is a DC/AC substation that converts 150 kV DC to 154 kV AC national transmission voltage. Although this is a DC/AC converter, the price of € 194.23 /kVA used for the DC/DC converter in Equation (19) was used for the calculations. Many converters are connected together for the total power as considered earlier. Since the total cost is given as per power, the total cost considered with total power is in Equation (19).
6. *Grid connection cost*—although the cost of the substation in the mainland was considered earlier, it was assumed that there is an additional grid connection cost at the point of common coupling in order to be connected to the 154 kV AC national electric transmission system. The cost for both AC and DC configuration is given as a function of total delivered power in Reference [38] as

$$C_{GC} = 8.047 \times P^{1.66}. \tag{23}$$

4.3.4. Project Development, Management and Other Costs

The project development and management costs including other costs such as insurance and design costs were estimated as $280.38 per MW as given in [55,56].

4.4. OPEX

The OPEX consist of operational, maintenance, administrative, insurance premiums and royalty costs. The sum of all these costs was considered to be 1.9% of the total CAPEX per annum for 20 years lifespan of the project [57].

By considering the aforementioned individual cost models, the total OWF investment cost was calculated as follows:

$$C_{CAPEX} = C_{turbines} + C_{support} + C_{cable} + C_{burrying} + C_{substation} + C_{transmission} + C_{GC}. \tag{24}$$

5. Results and Discussion

5.1. Losses Assessment

The estimated energy losses for each part of the AC and DC configurations for selected wind farm scales are reported in Table 3. It was found that the losses in the AC configuration were slightly higher than those of the DC counterpart for the 100 MW OWF size while they were almost the same for the 300 MW size. In this category, losses are mainly contributed to by the losses of the turbine converters (P_{PE-AC}) with regard to the transformer and onshore converter losses for the AC and DC configurations, respectively. There is a significance decrease in line losses in the case of DC offshore

configuration. In this case study, the length of the collection and transmission lines are relatively shorter. The impact of further OWFs from shore on the losses was assessed in the sensitivity analysis.

Table 3. Annual Energy Losses of each components in the AC and DC Offshore Configurations.

AC Configuration	**100 MW (kWh)**	**(%)**	**300 MW (kWh)**	**(%)**
Collection cables	190,564	0.05	700,393	0.06
Transmission cable	1,422,127	0.36	3,490,676	0.30
Total line losses	1,612,692	0.41	4,191,070	0.36
Power electronics including transformer	13,256,069	3.39	39,768,206	3,39
Total energy losses	14,868,760	3.80	43,959,276	3,75
DC Configuration	**100 MW (kWh)**	**(%)**	**300 MW (kWh)**	**(%)**
Collection cables	129,018	0.03	515,944	0.04
Transmission cable	1,069,279	0.27	2,748,187	0.23
Total line losses	1,198,297	0.31	3,264,131	0.28
Power electronics	13,552,123	3.46	40,697,999	3.47
Total energy losses	14,750,420	3.77	43,962,129	3.75

5.2. Economic Assessment

Revenue of an OWF energy investment mainly depends on the annual energy production and the capacity factor of the power plant. The VWF model estimates the AEP values without considering array (wake effect), electrical and other related losses. Therefore, wind array efficiency parameters were calculated and used to generate realistic net AEP figures. Wind farm array efficiency for this study was assumed to be 96%. The net AEP was calculated by considering wake effects (e.g., 4%) and total electrical losses from the gross AEP estimated by the VWF model. Annual revenues were estimated by multiplying the net AEP and the corresponding Feed-in-Tariff (FIT). The base FIT of 7.3 USD cent/kWh represents the support mechanism which was designed for the wind investments using all exported wind turbines. In addition, the maximum FIT of 11 USD cent/kWh is provided for the investors using domestic wind turbines. The economic calculations in this study were performed in terms of US dollars. The dollar/euro parity of 1.335 is used to convert the CAPEX values to US dollars.

The estimated values for the mean wind speed, OPEX, CAPEX, annual revenues, capacity factors and the net AEP values are summarized in Table 4. This case study is considered as a reference scenario for the sensitivity analysis. The mean wind speed of the selected wind turbine at hub height of 90 m was estimated to be 7.68 m/s. The capacity factor at wind turbines output is constant for all electrical topologies (e.g., 44.7%). Final capacity factor values at the point of common coupling (PCC) that consider wake and electrical losses vary between 41.20% and 41.31% depending on the electrical topology and installed capacity. The net AEP values were estimated between 361.34 GWh and 361.19 GWh and 1,084.59 GWh for the 100 MW and 300 MW sizes, respectively, depending on the final capacity factor. Estimated annual revenue for each configuration ranges from 39.75 million $ to 39.73 million and 119.31 million $ the 100 MW and 300 MW sizes, respectively. CAPEX values were estimated to be in the range of 335.01 million $ and 998.72 million $ for the DC configuration and 300.59 million $ and 998.72 million $ for the AC configuration for the 100 MW and 300 MW sizes, respectively. For the entire project life cycle of 20 year, the OPEX values were estimated to be in the range of 6.37 and 18.98 million $ for the DC configuration and 5.71 and 17.17 million $ for the AC configuration.

Table 4. Cost–benefit analysis components of the OWF for AC and DC configurations.

	AC 100 MW	DC 100 MW	AC 300 MW	DC 300 MW
Capacity factor at PCC (%)	41.24	41.20	41.24	41.24
Net AEP (kWh/year)	361,344,935	361,194,688	1,084,598,234	1,084,598,234
Annual Revenue with base FIT (million$)	26.38	26.37	79,18	79,18
Annual Revenue with max FIT (million$)	39.75	39.73	119.31	119.31
CAPEX (million$)	300.59	335.01	903.88	998.72
OPEX (million$/20 years)	5.71	6.37	17.17	18.98

A comprehensive economic evaluation was performed by using the estimated cost-benefit analysis components. The estimated LCOEs for different discount rates are shown in Figure 4. The results reveal that the LCOE deviates from 88.34 $/MWh (AC 100 MW with 6 % discount rate) to 126.60 $/MWh (DC 100 MW with 10 % discount rate) depending on the electrical topology, interest rates and wind farm size. It can be observed that, although wind farm size is increased by three-fold, LCOEs for the AC and DC options slightly change.

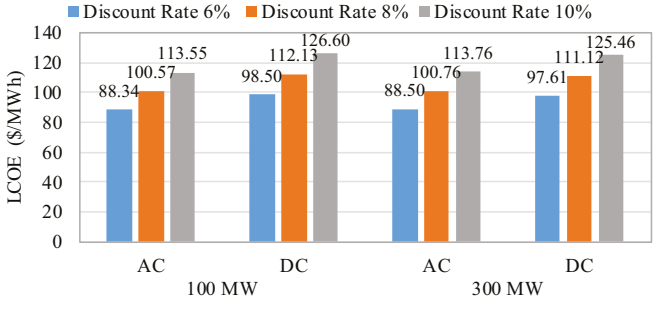

Figure 4. LCOEs of the OWFsfor AC and DC configurations for various discount rates.

Figure 5 shows the NPV distribution over the entire lifespan of the OWF. It is proved that AC and DC options for larger wind farm size (e.g., 300 MW) are delivering a better NPV performance in comparison to the 100 MW wind farm size. DPBP for the AC configuration is found to be 13 years while it is 14 years for the DC options. The one year difference is due to higher CAPEX in DC options which is mainly contributed by the converters' cost. The economic performance of the investigated electrical topologies in terms of NPV for various interest rates with the maximum FIT option is demonstrated in Figure 6. The 300 MW AC configuration under 6 % discount rate yields the best results with a NVP (i.e., 667 million$). Contrarily, the 100 MW DC option under a 10 % discount rate yields the worst performance in terms of NVP (i.e., 37 million). It is also shown that the OWF is economically viable for all interest rates considered for selected configurations and wind farm sizes. Nevertheless, the investigated OWF with both AC and DC electrical topologies for the 300 MW wind farm size is a superior investment option in case the discount rates are in the 6% range with the maximum FIT.

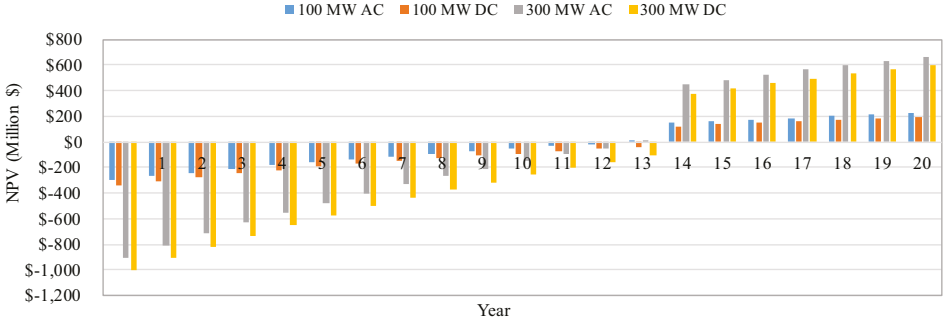

Figure 5. The discounted cash flow of the OWF in terms of years for AC and DC configurations.

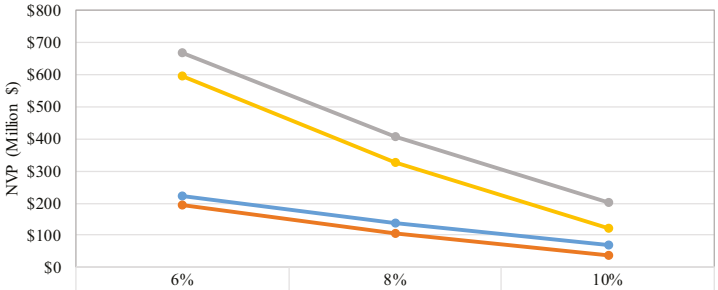

	6%	8%	10%
100 MW AC	223	136	68
100 MW DC	195	106	37
300 MW AC	667	407	203
300 MW DC	596	329	120

Figure 6. The variation of NPV of the OWF in terms of discount rates for AC and DC configurations.

5.3. Sensitivity Analysis

The evaluation was extended with a sensitivity analysis to investigate the influence of capacity factor, transmission line length and the electrical topology with the 100 MW and 300 MW wind farm sizes on the technical and economic viability of OWFs. For this purpose, three different capacity factors with various transmission line lengths ranging from 20 km to 120 km were used. Based on the critical distance of 85 km given in Reference [11] and of 80 km in Reference [21], the transmission line length of 80 km and above distances are considered further offshore locations. Consequently, electrical losses and LCOEs are observed for the estimated values.

The impact of capacity factor and distance to shore on electrical losses is depicted in Figure 7. In terms of electrical losses, the DC configuration is found to be more favorable as the wind farm size, capacity factor and line lengths increase. Losses in the AC configuration range from 3.75% to 5.86% for 45% capacity factor with the transmission line length of the reference scenario (i.e., $l = 19$ km) and 60% capacity factor with a six-fold longer transmission line, respectively. Similarly, losses in the DC configuration vary between 3.75% and 5.34% for 45% capacity factor with the line length of l and 60% with a line length of $6 \times l$, respectively. As the wind farm size, capacity factor and transmission line length increase, the difference between the AC and DC configuration losses becomes significant. It is proved that transmission line length is more sensitive in losses estimation as compared to the capacity factor.

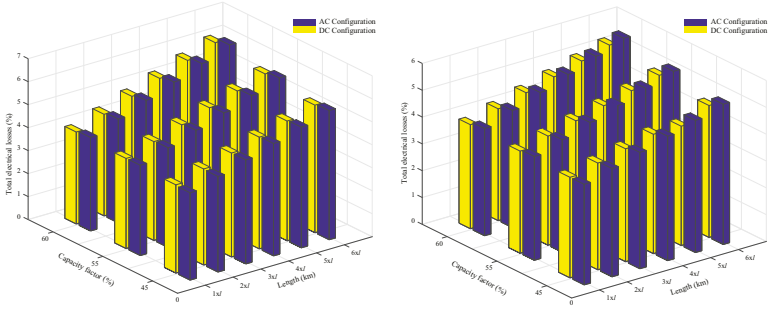

Figure 7. Losses evaluation for AC and DC configurations with respect to capacity factor and transmission line length: (**a**) 100 MW layout. (**b**) 300 MW layout.

Figure 8 illustrates the impact of capacity factor and distance to shore on LCOE based on the 6% discount rate with the maximum FIT. In terms of LCOE, the AC configuration is found to be more favorable for all cases. It is shown that the best LCOE value is estimated to be 59.90 $/MWh for the AC configuration (i.e., 100 MW wind farm size) with 60% capacity factor and the transmission line of l. The highest LCOE value is, on the other hand, estimated to be 124.15 $/MWh for the DC configuration (e.g., 100 MW wind farm size) with 45% capacity factor and a transmission line of $6 \times l$. As the wind farm size, capacity factor and distance to shore increase, the difference between the AC and DC configuration LCOEs decreases. Unlike the impact on losses, the capacity factor proved to be more sensitive in LCOE estimation as compared to transmission line length.

It must be noted that this sensitivity analysis considers climatological conditions for the offshore sites with different capacity factors by using the MERRA 2 database for the annual energy yield calculations. However, due to a lack of publicly available data regarding seabed conditions, only one type of foundation structure (e.g., monopole) was considered for the CAPEX component of the foundation cost without any detailed investigation. Considering different types of foundation structures will sway LCOE estimation.

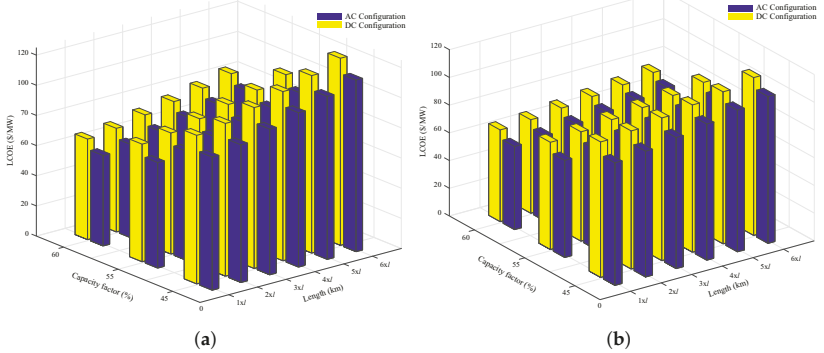

Figure 8. LCOE evaluation for AC and DC configurations with respect to capacity factor and transmission line length: (**a**) 100 MW layout. (**b**) 300 MW layout.

6. Conclusions

In this paper, the economic performance of the AC and DC configurations was investigated for examined OWF with two sizes (e.g., 100 MW and 300 MW). Annual energy yield and electrical

losses estimation for AC and DC OWF configurations were detailed. An economic analysis was performed using detailed cost models for the system components. Finally, the impact of capacity factor, transmission line length and electrical topologies on the economic performance of OWF investments was explored through the sensitivity analysis. The analysis has yielded the following conclusions:

- The studied OWF was found to be economically viable for both AC and DC configurations with 13 and 14 years of DPBPs for the AC and DC options, respectively. The estimated LCOEs for the AC and DC OWF configurations range from 88.34 $/MWh to 113.76 $/MWh and from 97.61 $/MWh to 126.60 $/MWh, respectively. LCOEs for both options slightly change even though the wind farm size was increased by three-fold.
- Losses in the AC and DC configurations range from 3.75% to 5.86% and 3.75% to 5.34%, respectively, while LCOEs vary between 59.90 $/MWh and 113.76 $/MWh for the AC configuration and 66.21 $/MWh and 124.15 $/MWh for the DC configuration.
- It was found that the transmission line length parameter is more sensitive in loss estimation while the capacity factor parameter is more sensitive in LCOE estimation.
- It was proved that the superiority of AC configuration over the DC option in terms of LCOE decreases as capacity and transmission line length increase.
- It was also shown that the advantage of DC configuration over the AC option in terms of losses increased as capacity factor and transmission line length increased.

The presented study provides a framework and methodology that can be used to verify the threshold point where LCOE of DC configuration reaches that of AC configuration for a particular wind farm. Although the techno-economic outcomes in this study are unique to the selected offshore sites, the presented methodology can be applied to other specific wind farms with various sizes using the given sensitivity analysis that may result in different break-even LCOE values.

Author Contributions: All authors contributed equally to this work.

Funding: This research received no external funding.

Conflicts of Interest: The authors declare no conflict of interest.

References

1. Enerdata. 2018 Global Energy Trends Report. Available online: http://www.enerdata.net (accessed on 28 May 2019).
2. International Energy Agency (IEA). Available online: https://www.iea.org/geco/electricity/ (accessed on 10 August 2019).
3. Saidur, R.; Islam, M.R.; Rahim, N.A.; Solangi, K.H. A review on global wind energy policy. *Renew. Sustain. Energy Rev.* **2010**, *14*, 1744–1762. [CrossRef]
4. Argin, M.; Yerci, V.; Erdogan, N.; Kucuksari, S.; Cali, U. Exploring the offshore wind energy potential of Turkey based on multi-criteria site selection. *Energy Strategy Rev.* **2019**, *23*, 33–46. [CrossRef]
5. Serrano Gonzalez, J.; Burgos Payan, M.; Riquelme Santos, J. Optimum design of transmissions systems for offshore wind farms including decision making under risk. *Renew. Energy* **2013**, *59*, 115–127. [CrossRef]
6. Global Wind Energy Council (GWEC). Global Wind Report 2018. Available online: http://www.gwec.net (accessed on 30 April 2019).
7. Salo, O.; Syri, S. What economic support is needed for Arctic offshore wind power? *Renew. Sustain. Energy Rev.* **2014**, *31*, 343–352. [CrossRef]
8. Cali, U.; Erdogan, N.; Kucuksari, S.; Argin, M. Techno-economic analysis of high potential offshore wind farm locations in Turkey. *Energy Strategy Rev.* **2018**, *22*, 325–336. [CrossRef]
9. Gardner, P. Offshore wind energy: Resources, technology and grid connection. In *First International Workshop on Feasibility of HVDC Transmission for Offshore Wind Farms*; KTH Royal Institute of Technology: Stockholm, Sweden, 2000.
10. Houghton, T.; Bell, K.R.W.; Doquet, M. Offshore transmission for wind: Comparing the economic benefits of different offshore network configurations. *Renew. Energy* **2016**, *94*, 268–279. [CrossRef]

11. Reed, G.F.; Hassan, H.A.A.; Korytowski, M.J.; Lewis, P.T.; Grainger, B.M. Comparison of HVAC and HVDC solutions for offshore wind farms with a procedure for system economic evaluation. In Proceedings of the IEEE Energytech, Cleveland, OH, USA, 21–23 May 2013; pp. 1–7.
12. Morton, A.B.; Cowdroy, S.; Hill, J.R.A.; Halliday, M.; Nicholson, G.D. AC or DC? Economics of grid connection design for offshore wind farms. In Proceedings of the 8th IEE International Conference on AC and DC Power Transmission (ACDC 2006), London, UK, 28–31 March 2006; pp. 236–240.
13. Ruddy, J.; Meere, R.; O'Donnell, T. Low Frequency AC transmission for offshore wind power: A review. *Renew. Sustain. Energy Rev.* **2016**, *56*, 75–86. [CrossRef]
14. Gonzalez, J.S.; Payan, M.B.; Santos, J.M.R.; Gonzalez-Longatt, F. A review and recent developments in the optimal wind-turbine micro-siting problem. *Renew. Sustain. Energy Rev.* **2014**, *30*, 133–144. [CrossRef]
15. Musasa, K.; Nwulu, N.I.; Gitau, M.N.; Bansal, R.C. Review on DC collection grids for offshore wind farms with high-voltage DC transmission system. *IET Power Electron.* **2017**, *10*, 2104–2115. [CrossRef]
16. Gil, M.D.P.; Domínguez-García, J.L.; Díaz-González, F.; Aragüés-Peñalba, M.; Gomis-Bellmunt, O. Feasibility analysis of offshore wind power plants with DC collection grid. *Renew. Energy* **2015**, *78*, 467–477.
17. Xu, L.; Yao, L. DC voltage control and power dispatch of a multi-terminal HVDC system for integrating large offshore wind farms. *IET Renew. Power Gener.* **2011**, *5*, 223–233. [CrossRef]
18. Kong, X.; Jia, H. Techno-Economic Analysis of SVC-HVDC Transmission System for Offshore Wind. In Proceedings of the 2011 Asia-Pacific Power and Energy Engineering Conference, Wuhan, China, 25–28 March 2011; pp. 1–5.
19. Xiang, X.; Merlin, M.M.C.; Green, T.C. Techno-Cost analysis and comparison of HVAC, LFAC and HVDC for offshore wind power connection. In Proceedings of the 12th IET International Conference on AC and DC Power Transmission (ACDC 2016), Beijing, China, 28–29 May 2016.
20. Hassan, A. Hamdan and Brian Kinsella. Using a VSC Based HVDC Application to Energize Offshore Platforms from Onshore—A Life-cycle Economic Appraisal. *Energy Procedia* **2017**, *105*, 3101–3111.
21. Eeckhout, B.V. The Economic Value of VSC HVDC Compared to HVAC for Offshore Wind Farms. Ph.D. Thesis, Katholieke Universiteit Leuven, Leuven, Belgium, 2007.
22. Elliott, D.; Bell, K.R.W.; Finney, S.J.; Adapa, R.; Brozio, C.; Yu, J.; Hussain, K. A Comparison of AC and HVDC Options for the Connection of Offshore Wind Generation in Great Britain. *IEEE Trans. Power Deliv.* **2016**, *31*, 798–809. [CrossRef]
23. Abdulrahman, A.; Santiago, B.; Omar, E.; Grain, A.; Callum, M. HVDC Transmission: Technology Review, Market Trends and Future Outlook. *Renew. Sustain. Energy Rev.* **2019**, *112*, 530–554.
24. Johnson, M.H.; Aliprantis, D.C.; Chen, H. Offshore wind farm with DC collection system. In Proceedings of the 2013 IEEE Power and Energy Conference at Illinois (PECI), Champaign, IL, USA, 22 February 2013; pp. 53–59.
25. Lakshmanan, P.; Liang, J.; Jenkins, N. Assessment of collection systems for HVDC connected offshore wind farms. *Electr. Power Syst. Res.* **2015**, *129*, 75–82. [CrossRef]
26. Ebenhoch, R. Comparative Levelized Cost of Energy Analysis. *Energy Procedia* **2015**, *80*, 108–122. [CrossRef]
27. Masters, G.M. *Renewable and Efficient Electric Power Systems*; John Wiley & Sons: Hoboken, NJ, USA, 2013
28. Cali, U. *Grid and Market Integration of Large-Scale Wind Farms Using Advanced Wind Power Forecasting: Technical and Energy Economic Aspects*; Kassel University Press GmbH: Kassel, Germany, 2011; pp. 1–156.
29. Renewables.ninja. 2017. Available online: https://www.renewables.ninja/ (accessed on 29 January 2019).
30. Staffell, I.; Pfenninger, S. Using bias-corrected reanalysis to simulate current and future wind power output. *Energy* **2016**, *114*, 1224–1239. [CrossRef]
31. Siemens. Wind Turbine SWT-4.0-130 Technical Specifications. 2015. Available online: https://www.thewindpower.net/scripts/fpdf181/turbine.php?id=957 (accessed on 25 May 2019).
32. Al Ameri, A.; Ounissa, A.; Nichita, C.; Djamal, A. Power Loss Analysis for Wind Power Grid Integration Based on Weibull Distribution. *Energies* **2017**, *10*, 463. [CrossRef]
33. ABB. HiPak IGBT Modules Data Sheet. 2014. Available online: www.abb.com/semiconductors (accessed on 12 January 2019).
34. Zhang, X.; Green, T.C. The modular multilevel converter for high step-up ratio DC–DC conversion. *IEEE Trans. Ind. Electron.* **2015**, *62*, 4925–4936. [CrossRef]

35. Gultekin, B.; Gercek, C.O.; Atalik, T.; Deniz, M.; Bicer, N.; Ermis, M.; Kose, K.N.; Ermis, C.; Ko, E.; Cadirci, I.; et al. Design and Implementation of a 154-kV±50-Mvar Transmission STATCOM Based on 21-Level Cascaded Multilevel Converter. *IEEE Trans. Ind. Appl.* **2012**, *48*, 1030–1045. [CrossRef]
36. Mamane, C. Transformer Loss Evaluation: User-Manufacturer Communications. *IEEE Trans. Ind. Appl.* **1984**, *20*, 11–15. [CrossRef]
37. Lerch, M.; De-Prada-Gil, M.; Molins, C.; Benveniste, G. Sensitivity analysis on the levelized cost of energy for floating offshore wind farms. *Sustain. Energy Technol. Assess.* **2018**, *30*, 77–90. [CrossRef]
38. Gonzalez-Rodrigue, A.G. Review of offshore wind farm cost components. *Energy Sustain. Dev.* **2017**, *37*, 10–19. [CrossRef]
39. Dicorato, M.; Forte, G.; Pisani, M.; Trovato, M. Guidelines for assessment of investment cost for offshore wind generation. *Renew. Energy* **2011**, *36*, 2043–2051. [CrossRef]
40. Wei, Q.; Wu, B.; Xu, D.; Zargari, N.R. IOP Conference Series: Earth and Environmental Science. In Proceedings of the 12th IET International Conference on AC and DC Power Transmission (ACDC 2016), Beijing, China, 28–29 May 2016.
41. Koch, H.; Retzmann, D. Connecting large offshore wind farms to the transmission network. In Proceedings of the IEEE PES T&D 2010, New Orleans, LA, USA, 19–22 April 2010.
42. Europa Cable. An Introduction to High Voltage Direct Current (HVDC) Underground Cables. Technical Brochure. Available online: www.europacable.eu (accessed on 12 January 2019).
43. ENSO. Offshore Transmission Technology. 2011. Available online: https://www.entsoe.eu (accessed on 20 February 2019).
44. Zaccone, E. High voltage underground and subsea cable technology options for future transmission in Europe. In Proceedings of the European Electricity Grid Initiative E-Highway 2050 Workshop, Brussels, Belgium, 15 April 2014.
45. Lundberg, S. *Performance Comparison of Wind Park Configurations*; Technical Report; Chalmers University of Technology: Gothenburg, Sweden, 2003.
46. ABB. HVDC Light. 2011. Available online: www.new.abb.com/docs/default-source/ewea-doc/hvdc-light.pdf (accessed on 20 February 2019).
47. BS6622/BS7835 Three Core Armoured 33kV XLPE Stranded Copper Conductors. Prysmian. 2011. Available online: www.powerandcables.com (accessed on 20 February 2019).
48. BS6622/BS7835 Three Core Armoured 33kV XLPE Stranded Copper Conductors. 6-36kV Medium Voltage Underground Power Cables XLPE Insulated Cables. 2019. Available online: www.nexans.co.uk (accessed on 20 February 2019).
49. Nieradzinska, K.; MacIver, C.; Gill, S.; Agnew, G.A.; Anaya-Lara, O.; Bell, K.R.W. Optioneering analysis for connecting Dogger Bank offshore wind farms to the GB electricity network. *Renew. Energy* **2016**, *91*, 120–129. [CrossRef]
50. Daniel Manrique, O. *Design of the HVDC Connection of a 425 MW Offshore Wind Farm to the German Network*; Technical Report; Universidad Pontificia: Madrid, Spain, 2017.
51. Stamatiou, G. Techno-Economical Analysis of DC Collection Grid for Offshore Wind Parks. Master's Thesis, The University of Nottingham, Nottingham, UK, 2010.
52. Lazaridis, L.P. Economic Comparison of HVAC and HVDC Solutions for Large Offshore Wind Farms underSpecial Consideration of Reliability. Master's Thesis, School of Electrical Engineering, KTH, Stockholm, Sweden, 2005.
53. Stamatiou, G.; Srivastava, K.; Reza, M.; Zanchetta, P. Economics of DC Wind Collection Grid as Affected by Cost of Key Components. In Proceedings of the World Renewable Energy Congress-Sweden, Linköping, Sweden, 8–13 May 2011.
54. Korompili, A.; Wu, Q.; Zhao, H. Review of VSC HVDC connection for offshore wind power integration. *Renew. Sustain. Energy Rev.* **2016**, *59*, 1405–1414. [CrossRef]
55. Heimiller, D.; Ho, J.; Moné, C.; Hand, M. 2015 Cost of Wind Energy Review. In *National Renewable Energy Laboratory/TP-6A20-66861 Technical Report*; 2017; 115p. Available online: https://www.nrel.gov/docs/fy17osti/66861.pdf (accessed on 12 July 2019) .

56. Kempton, W.; McClellan, S.; Ozkan, D. Massachusetts offshore wind future cost study. *Special Initiative on Offshore Wind*; University of Delaware: Newark, DE, USA, 2016.
57. Kim, J.-Y.; Oh, K.-Y.; Kang, K.-S.; Lee, J.-S. Site selection of offshore wind farms around the korean peninsula through economic evaluation. *Renew. Energy* **2013**, *54*, 189–195. [CrossRef]

energies

MDPI

Article

Ocean Renewable Energy Potential, Technology, and Deployments: A Case Study of Brazil

Milad Shadman [1,*], Corbiniano Silva [2], Daiane Faller [3], Zhijia Wu [1,4], Luiz Paulo de Freitas Assad [2,5], Luiz Landau [2], Carlos Levi [1] and Segen F. Estefen [1]

1 Ocean Engineering Department, Federal University of Rio de Janeiro, Rio de Janeiro 21941-914, Brazil; zhijiawu@lts.coppe.ufrj.br (Z.W.); Levi@laboceano.coppe.ufrj.br (C.L.); segen@lts.coppe.ufrj.br (S.F.E.)
2 Civil Engineering Department, Federal University of Rio de Janeiro, Rio de Janeiro 21941-907, Brazil; corbiniano@gmail.com (C.S.); luizpauloassad@gmail.com (L.P.d.F.A.); landau@lamce.coppe.ufrj.br (L.L.)
3 Center for Global Sea Level Change (CSLC), New York University Abu Dhabi (NYUAD), Abu Dhabi PO Box 129188, UAE; daianecem@gmail.com
4 China Ship Scientific Research Center (CSSRC), Wuxi, Jiangsu 214082, China
5 Meteorology Department, Federal University of Rio de Janeiro, Rio de Janeiro 21941-916, Brazil
* Correspondence: milad.shadman@lts.coppe.ufrj.br

Received: 26 July 2019; Accepted: 9 September 2019; Published: 25 September 2019

Abstract: This study, firstly, provides an up-to-date global review of the potential, technologies, prototypes, installed capacities, and projects related to ocean renewable energy including wave, tidal, and thermal, and salinity gradient sources. Secondly, as a case study, we present a preliminary assessment of the wave, ocean current, and thermal gradient sources along the Brazilian coastline. The global status of the technological maturity of the projects, their different stages of development, and the current global installed capacity for different sources indicate the most promising technologies considering the trend of global interest. In Brazil, despite the extensive coastline and the fact that almost 82% of the Brazilian electricity matrix is renewable, ocean renewable energy resources are still unexplored. The results, using oceanographic fields produced by numerical models, show the significant potential of ocean thermal and wave energy sources in the northern and southern regions of the Brazilian coast, which could contribute as complementary supply sources in the national electricity matrix.

Keywords: ocean renewable energy; ocean renewable technologies; ocean source potential; Brazilian ocean energy

1. Introduction

Only 14% of the world's primary energy matrix originates from renewable resources (based on the 2016 database), and this value is about 25% for the electrical energy sector [1]. The immediate needs to limit climate change and achieve sustainable growth are two key drivers of global energy transformation. Consequently, it is estimated that the share of renewable energy sources in the electrical energy sector will increase from 25% in 2017 to 85% in 2050 [1], in which ocean renewable energy sources including wave, tidal, thermal, and the salinity gradient will be responsible for the 4% of the total electricity generation. However, new approaches to power system planning, system and market operations, and regulations and public policy will be required to obtain that goal. As the contribution of low-carbon electricity becomes significant and it becomes the preferred energy carrier, the share of electricity consumed in the end-use sectors will need to increase from approximately 20% in 2015 to 40% in 2050 [1]. Electricity generation using coal, oil, gas, hydroelectric, nuclear, and bioenergy is predicted to decline from 2015 to 2050. On the other hand, a rapid evolution associated with the use of renewables like wind, geothermal, solar, ocean renewable energy, and concentrated solar power

(CSP) will likely be observed. International Renewable Energy Agency (IRENA) showed that the sources of renewable electricity in 2050 will be dominated by solar and wind power plants, highlighting significant growth associated with the geothermal, CSP, and ocean renewables.

Although Brazil is currently one of the world´s cleanest energy suppliers, there are some concerns associated with the country´s energy sustainability. An increasing demand for energy, mainly fossil fuels, expanding oil production, a bioenergy sector struggling with expansion, fast growth of energy-related greenhouse gas emissions, and energy efficiency performance deterioration are the current trends that put the future of the country's sustainable energy performance at risk [2].

Brazil is the world's eighth-largest economy with a population of close to 210 million and a land area expansion the size of about two times the European Union [2,3]. With a domestic energy supply of about 292.1 million tons of oil equivalent (Mtoe) in 2017, it is one of the largest energy producers in the world [4]. The Energy Research Office (EPE) of Brazil estimated a domestic electricity supply of 624.3 TWh in 2017, and this was mainly produced by the hydropower plants.

The Brazilian electrical and energy matrices are predominately based on renewable energy sources, which means that, in addition to having lower operating costs, a much lower greenhouse gas effect is emitted in association with energy production and consumption. For instance, in 2017, the total anthropogenic emissions of the Brazilian energy mix was estimated at approximately 435.8 million tons of equivalent carbon dioxide (Mt CO_2-eq), of which the transport sector emitted the largest part (199.7 Mt CO_2-eq) [4]. Based on the data presented by the International Energy Agency (IEA) [5], each Brazilian issued an average of 2.1 t CO_2-eq, considering the production and consumption of energy in 2017. This is three times less than that of a European or Chinese citizen and about seven times less than an American citizen.

By meeting almost 45% of its primary energy demand from renewable resources, Brazil has the least carbon-intensive energy sector in the world [6]. Figure 1a shows the domestic energy supply breakdown for Brazil for 2017. Petroleum and oil products, with a share of 36.4%, had the largest contribution to energy supply, followed by sugarcane biomass (17%). Natural gas (13%) and hydraulic energy were other players in the energy matrix of Brazil. Black liquor contributed 50.6% of the "other renewables" sector, followed by wind (21.3%), biodiesel (19.7%), other biomasses including rice husk, elephant grass, and vegetable oil (6.5%), charcoal industrial gas (0.4%), biogas (1.1%), and solar energy (0.4%). The Brazilian electrical matrix, as shown in Figure 1b, was dominated by hydropower resources with a contribution of approximately 65.2%. The main Brazilian hydroelectric reservoirs are located in the Paraná River basin, South region, featuring the Itaipu plant, which is the second-largest hydroelectric power plant in the world with a capacity of 14 GW [7]. The hydroelectric power plants in Brazil are mostly concentrated in the Midwest, South, and Southeast regions. Several studies have discussed the benefits and challenges of the hydroelectric plants in Brazil [7–10]. Nevertheless, the remoteness and environmental sensitivity of a large part of the remaining resources are two hurdles that constrain the continued expansion of hydroelectric plants in Brazil [6].

Brazil already has a significant contribution of renewable energy in its energy and electricity matrix; however, there is an inestimable untapped potential for energy supply from the oceans. Although nearly 80% of the Brazilian population lives near the coast, there has been no in-depth survey on the utility of ocean energy and its conversion into electricity. There have only been a handful of studies associated with the ocean renewable energy potential along the Brazilian coastline, and these have mainly focused on the wave and ocean current energy in some specific regions. Some examples of the studies related to the wave and current energy include those in [11–16], which focused on the South and Southeast regions of the Brazilian coast. Moreover, ocean thermal energy conversion (OTEC) resource evaluation of the Southern Brazilian continental shelf is presented in [17]. The EPE, through the National Energy Plan [18,19], established some general roadmaps related to the long-term plan of the Brazilian energy sector. Accordingly, the ocean energy resources, among other alternative energy sources, were suggested as a way to expand the Brazilian energy matrix in the coming decades.

This was also emphasized by the National Agency of Electric Energy through a roadmap project performed by the Center of Management and Strategic Studies of Brazil in 2017 [20].

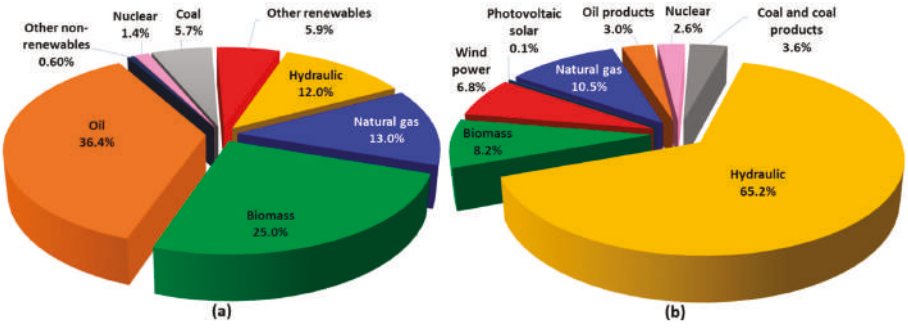

Figure 1. (**a**) Domestic Brazilian energy supply and (**b**) electrical matrix breakdown in 2017.

2. Targets, Materials, and Methods

In Brazil, mapping of the ocean renewable energy resources through a detailed survey of all resources is required to identify potential areas for exploration and, consequently, encourage the development of technologies through the implementation of socio-economically feasible and acceptable projects. Using this perspective, this article firstly presents an overview of the global potential of ocean renewable energy resources and the associated technologies for harnessing such energy. Then, in the second part, the global status of technology maturity is presented through a wide survey of projects, which are at different stages of development. This shows the current global installed capacity for different energy sources, as well as pointing out the more promising technologies through the global interest trend. The third part presents an assessment of the ocean renewable energy resources including ocean currents, waves, and thermal gradients along the Brazilian coastline. This is a preliminary effort aimed at indicating the potential energetic regions. Further detailed works are required to investigate these locations. The methodology applied in this study consists of the use of oceanographic fields produced by hydrodynamic models to estimate the potential of the energy resources. Modeling is performed for a data resolution (one regular horizontal grid) of 1/12° (~9 km). The study reveals the theoretical potential (available energy at sea and not what can be captured) of the resources as well as their seasonal and temporal variability. Finally, the main Brazilian projects are presented, and the challenges are discussed.

2.1. Study Area

The Brazilian coastline is more than 7400 km in length and is situated between 04°52′45″N (Oiapoque River) and 33°45′10″S (Chuí River). The marine areas under Brazilian jurisdiction include the Territorial Sea, with a limit of 12 nautical miles; the Exclusive Economic Zone (EEZ), with 12 to 200 nautical miles; and the Continental Shelf, which comprises the seabed that extends beyond the Territorial Sea, along the natural extension of the land territory off the continental shelf.

The extent of the Brazilian continental shelf varies along the coast, with a few kilometers (~8 km) near Bahia and up to 300 km on the coast of the State of Pará, with a range between 60 and 180 m [21,22]. The Brazilian coastline is characterized by intraseasonal fluctuations in the upper ocean circulation due to several dynamic processes, such as the local forcing dynamics, the remote forcing of winds via waveguide dynamics, the average flow instability, and the resonance as a function of the coastline geometry [23,24]. The ocean circulation is dominated by the Subtropical Turn (Equatorial South Current, SEC) and the Antarctic Circumpolar Current [25]. The SEC is responsible for transporting the water from the Benguela Current to the Brazilian platform (about 10°S and 20°S), where it passes through a fork in the North Brazil Current (NBC) and the Brazil Chain (BC) to the south. Due to this

circulation, the western margin of the tropical South Atlantic is a particularly interesting region for the observation of thermohaline circulation [21–24,26].

As illustrated in Figure 2, the study area included the Brazilian coastline inside the EEZ, which is divided into four regions A, B, C and, D, according to both hydrodynamic and atmospheric characteristics. Table 1 shows the regions and the corresponding latitudes.

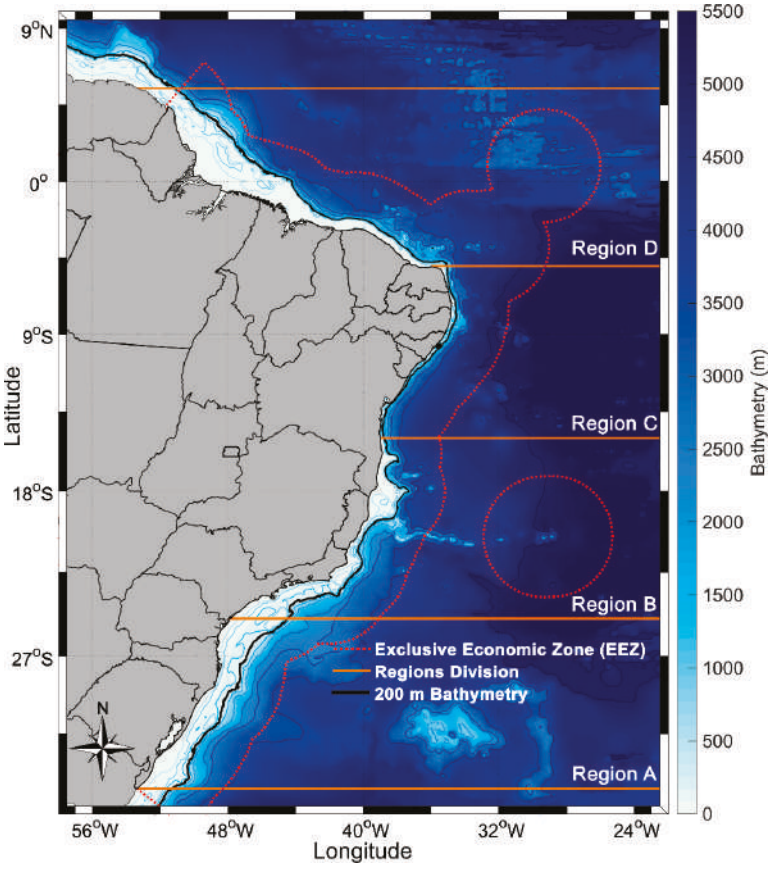

Figure 2. Brazilian coastline and the main marine areas delimited.

Table 1. Regions of the Brazilian coast considered in this study.

Regions	Latitude
A	34°S–25°S
B	25°S–15°S
C	15°S–05°S
D	05°S–05°N

2.2. Model Description

2.2.1. Ocean Current and Thermal Gradient Energy

The datasets for ocean current velocities and temperature were obtained (surface down to 5500 m) from the numerical model product available for the CMEMS (Copernicus Marine Environment Monitoring Service) center. The applied product is a high-resolution global analysis and forecasting system that uses the NEMO (3.1) ocean model [27]. It consists of part of the Operational Mercator global ocean analysis and forecast daily system, which was initiated on December 27, 2006. The dataset has one regular horizontal grid with a 1/12° (~9 km) resolution based on the tripolar ORCA grid [28], 50 vertical levels with 22 layers within the upper 100 m from the surface, bathymetry from ETOPO1 [29], and atmospheric forcings from the ECMWF (European Centre for Medium-Range Weather Forecasts). Additionally, it uses a data assimilation scheme, in which the initial conditions for numerical ocean forecasting are estimated by joint assimilation of the altimeter data, in situ temperature, salinity vertical profiles, and satellite sea surface temperature.

- Ocean current energy

Near-surface (~5 to 50 m) u and v components of velocity from January 1, 2007 to December 31, 2017 were used as a subset of the area corresponding to the Brazilian coastline (25°W–55°W and 6°N–34°S).

The ocean current power can be calculated as the amount of marine-hydrokinetic energy that flows through a unit cross-sectional area oriented perpendicular to the current direction per unit time [30] expressed as follows:

$$P = \frac{1}{2}\rho S^3, \quad (1)$$

where P is the current power density in (W/m^2), ρ is the density of seawater (defined as 1025 kg/m^3), and S is the flow speed (in m/s). In practice, only a fraction of this energy can be harnessed. The underwater turbine efficiency has a typical range from 35% to 50% [31]. Additionally, a mean peak current of more than 2 m/s is necessary for commercial power generation [32].

- Thermal gradient energy

Gridded daily seawater temperature (°C) model output with 50 vertical layers and ~9 km in horizontal resolution was used to analyze the temperature difference (ΔT (°C)) between the surface warm water and the deeper cold water. It was assumed that the superficial water intake pipe was located at about 20 m and the deepest point in the vertical depth stratification was approximately 1000 m. At specific locations (each grid cell), we calculated the gross power (P_{gross}) following the methodology described by [33,34]. The OTEC gross power can be expressed as the product of the evaporator heat load and the conversion efficiency of the gross OTEC [34]:

$$P_{gross} = \frac{Q_{cw}\rho c_p 3\varepsilon_{tg}\gamma}{16(1+\gamma)T}\Delta T^2, \quad (2)$$

$$\gamma = \frac{Q_{ww}}{Q_{cw}}, \quad (3)$$

where γ is the flow rate ratio calculated for a 10 MW OTEC plant in which $Q_{ww} = 45\ m^3/s$ and $Q_{cw} = 30\ m^3/s$ are the warm surface water and the cold deep water flow rates, respectively [35]. ΔT is the difference in temperature between the surface layers and deeper layers, and T is the absolute temperature at the surface (in Kelvin) (20 m). ρ and ε_{tg} represent the water density, which was equal to 1025 kg/m^3, and the turbo-generator efficiency fixed at 0.75, respectively. c_p is the specific heat of seawater and has a value of 4000 J.kg^{-1}.K^{-1}.

A considerable amount of the P_g is consumed to pump the large seawater flow rates through the OTEC plant. The net power P_{net} should be calculated, which is usually about 30% of the P_g [36,37]. The P_{net} can be expressed by the following equation considering $\Delta T_{design} = 20$ °C and the other losses presented in [34]:

$$P_{net} = \frac{Q_{cw}\rho c_p \varepsilon_{tg}}{8T}\left\{\frac{3\gamma}{2(1+\gamma)}\Delta T^2 - 0.18\Delta T^2{}_{design} - 0.12\left(\frac{\gamma}{2}\right)^{2.75}\Delta T^2{}_{design}\right\}. \quad (4)$$

2.2.2. Wave Energy

The wave dataset was obtained using the operational global ocean analysis and forecast system of Météo-France that is available for the CMEMS (Copernicus Marine Environment Monitoring Service) center. The model had a horizontal resolution of 1/12° (~9 km) and 3-hourly instantaneous fields of integrated wave parameters. The global wave system of Météo-France is based on the third-generation wave model MFWAM. It uses the computing code ECWAM-IFS-38R2 with a dissipation term [38]. The 2-min gridded global topography data ETOPO2/NOAA were used to generate the model's mean bathymetry. The dataset uses three years of data to estimate the wave climatology along the Brazilian coastline (between 2015 and 2018). The power density P was calculated using the significant wave height H_s and the wave energy period T_e as follows:

$$P = \frac{\rho g^2}{64\pi}{H_s}^2 T_e \quad (5)$$

where ρ and g represent the seawater density (1025 kg.m^{-3}) and gravity acceleration (9.806 m.s^{-2}), respectively; H_s is the significant height (m); and T_e is the energy wave period (s). This simplified expression uses deep-water approximation [39], which fits well most of the modeled domains; however, more sophisticated techniques as well as in situ measurements are required to precisely determine the shallow water wave climate.

2.3. Metrics

The variability of the available ocean renewable energy in time is an important issue due to its impact on the capacity factor, which, consequently, affects the economy of the ocean energy system. Two different metrics were used to address the seasonal and temporal variability of the Brazilian coastline. The seasonal variability (SV) index [40] can be expressed as follows:

$$SV = \frac{P_{S,max} - P_{s,min}}{P_{year}}, \quad (6)$$

where $P_{s,min}$ and $P_{S,max}$ are the mean wave power of the least and the most energetic seasons, respectively, and the P_{year} is the annual mean power. Greater values of SV imply a larger seasonal variability; however, it should be noted that this is the variability of the energy resources relative to their mean level on a three-month seasonal time scale [40]. The temporal variability of the energy at a site or region can be evaluated by the coefficient of variation (COV) [40], which is expressed as

$$COV(P) = \frac{SD(P(t))}{mean\ (P(t))} = \frac{\left[\overline{\left(P - \overline{P}\right)^2}\right]^{0.5}}{\overline{P}}, \quad (7)$$

where SD is the standard deviation, and the over-bar denotes the time-averaging. A COV equal to zero leads to a fictitious power time series with absolutely no variability, while $COV\ (P)$ = 1 and 2 imply that the standard deviation of the time series is equal to and twice the mean value, respectively.

3. Literature on the Issue and State-of-the-Art Technology Related to Ocean Renewable Energy

3.1. Resource Potential

Ocean renewable energy, also referred to as marine renewable energy, is defined as energy captured by technologies that utilize the seawater's motion or potential properties as the driving power or harness its heat or chemical potential. The ocean surface waves, tidal range, tidal current, ocean current, and thermal and salinity gradient are renewable sources of ocean energy that have different origins. Technologies associated with ocean energy convert these renewable energy sources into electricity or other desirable forms of energy.

Other renewable sources of energy can be exploited from the ocean environment that is excluded from the above definition. The production of biofuels from marine biomass, energy harnessing from submarine vents, and offshore wind are some examples that can be considered as forms of bioenergy, geothermal, and wind energy, respectively.

The highest level of potential is theoretical potential, which only takes into account the natural and climatic characteristic limitations. Reducing this potential due to the consideration of the technical limitations, such as the conversion efficiency and storage of electricity, results in technical potential, which varies with the development of technologies.

3.1.1. Wave Power

Temporal variations of the wave condition can be estimated by the use of long-term averages in modeling, applying global databases with reasonably long histories [41]. It can be observed that the most energetic waves exist in the region between latitudes of 30° and 60° of both hemispheres because of the extra-tropical storms [41].

Mørk et al. [42] calculated the theoretical potential of wave energy resources for areas with a wave power larger than 5 kW per meter and a lower latitude than 66.5°. Accordingly, they presented a total theoretical potential of about 3.37 TW (29,500 TWh/yr or 106.2 EJ/yr). An overall technical potential of 500 GW (around 16 EJ/yr) was estimated by Sims et al. [43], assuming an efficiency of 40% for wave energy converters installed in offshore regions with a wave power exceeding 30 kW/m. Krewitt et al. [44] presented a technical potential of 20 EJ/yr. Gunn and Stock-Williams estimated a global theoretical potential of about 2.11 TW, of which 4.6% was predicted to be extractable by deploying a specific wave energy converter (WEC) [45]. They considered the area between 30 nautical miles and the Exclusive Economic Zone (EEZ) for each region. Besides these global studies, some works have assessed the wave energy resource potential at national and regional levels in China [46,47], Italy [48], Spain [49], Ireland [50], and the USA [51].

3.1.2. Tidal Power

Tidal ranges can be forecasted accurately. The world's largest tidal ranges occur in the Bay of Fundy, Canada (17 m), the Severn River Estuary, the United Kingdom (15 m), and the Bay of Monte Saint Michel, France (13.5 m) [52]. In addition, Argentina, Australia, China, India, Russia, and South Korea also have large amounts of tidal power.

The global theoretical potential of tidal energy (tidal ranges and currents) is estimated to be in the range of 500–1000 TWh/yr (1.8–3.6 EJ/yr) [52]. Sims et al. [43] estimated that tidal currents of more than 100 TWh/yr (0.4 EJ/yr) could be converted into electrical energy if major estuaries with large tidal fluctuations could be tapped [43].

The Ocean Energy System (OES) reported the worldwide theoretical potential of tidal energy, including tidal current, to be around 7800 TWh/yr (28.1 EJ/yr) [53]. Some studies of the regional tidal energy resource potential can be found in Scotland [54], Uruguay [55], Ireland [56], Taiwan [57], and Iran [58].

3.1.3. Ocean Current Power

The ocean current is the movement of seawater in the open sea generated by forces acting upon the water, including wind, the Coriolis effect, temperature and salinity differences, and so on. Compared with tidal currents, ocean currents are generally slower, relatively constant, flow in only one direction, and fluctuate seasonally. The currents off South Africa (Agulhas/Mozambique), the Kuroshio Current (off East Asia), the Gulf Stream (off eastern North America), and the East Australian Current are locations with potential ocean currents already identified [59]. Yang et al. [60] estimated a theoretical potential of about 163 TWh/yr for the Gulf Stream system, considering the entire area of the Gulf Stream within 200 miles of the US coastline between Florida and North Carolina as the extraction region. Besides that, they calculated a technical potential of about 49 TWh/yr, assuming a power conversion efficiency of 30%. Chang et al. [61] identified suitable sites for ocean current energy extraction near the coastlines of Japan, Vietnam, Taiwan, and the Philippines. Goundar and Ahmed [62] evaluated marine current resources for Fiji, presenting a peak velocity of about 2.5 m/s.

3.1.4. Ocean Thermal Energy

The resulting temperature difference between the upper layers and the colder layers of seawater—usually at a depth of more than 1000 m—can be converted through different oceanic thermal energy conversion (OTEC) methods [63]. In practice, a minimum temperature difference of 20 °C (or K) is required for the use of the temperature gradient in the generation of electricity. The tropical latitudes (0° to 30°) in both hemispheres, including the western and eastern coasts of the Americas, many islands of the Caribbean and Pacific, and the coasts of Africa and India, are the places with the greatest potential [59]. Although there is a little variation in the temperature gradient from summer to winter, the thermal gradient feature is continuously available. It is estimated that about 44,000 TWh/yr (159 EJ/yr) to 88,000 TWh/yr (318 EJ/yr) of power could be generated through OTEC devices [34,64]. Rajagopalan and Nihous [65] estimated that an annual OTEC net power of about 7 TW could be obtained, considering the small effect on the oceanic temperature field. Thus, ocean thermal energy has the highest potential among ocean renewable energy sources. However, the energy density of OTEC systems is quite low compared with that of other sources, such as waves and tidal currents. This issue may affect the low-cost OTEC operation [63], requiring further investigation.

3.1.5. Salinity Gradient Power

The salinity gradient power (osmotic power) is the potential energy from the difference in the salt concentrations of seawater and freshwater. Energy is released due to the mixing of fresh water with seawater. The entropy of the freshwater–seawater mixture can be exploited as pressure by using the semipermeable membrane. This pressure can be converted into the desired energy form. The freshwater rivers discharging into saltwater are distributed globally, with a volume of about 44,500 km^3/yr. Assuming that only 20% of this discharge can be used for salinity gradient energy generation, the overall potential is approximately 2000 TWh/yr (7.2 EJ/yr) [44]. Skramesto et al. [66] estimated a technical potential of 1650 TWh/yr (5.9 EJ/yr) for the production of salinity gradient energy. Recently, in [67] it was shown that, practically, 625 TWh/yr of salinity gradient energy is globally extractable from river mouths. Some examples of the regional assessment of the salinity gradient potential can be found in Colombia [68], remote regions of Quebec [69], and the hypersaline Urmia Lake of Iran [70]. The potential for salinity gradient energy extraction from some major world rivers is presented in [71].

Figure 3 shows a summary of the potential of ocean renewable energy resources based on the references presented in this paper. The bars illustrate the range of estimated resource potential. Note that the technical potential of ocean current is shown as presented in [60] for the Gulf Stream.

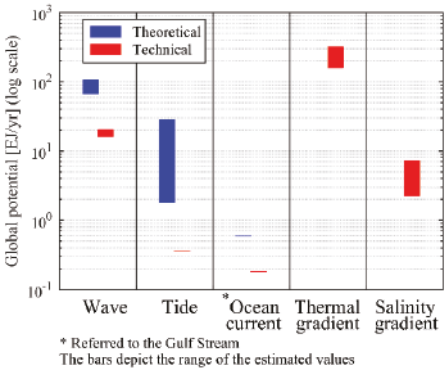

Figure 3. Summary of the global ocean renewable energy resources.

3.2. Conversion Technologies

3.2.1. Wave Energy Conversion

Currently, there are a large number of concepts and patents on the use of wave energy. As illustrated in Figure 4, the process of the wave energy conversion can be divided into three main stages: the primary conversion stage, the secondary conversion stage, and the tertiary conversion stage [72]. In the primary conversion stage, the wave converter captures the kinetic energy of the waves through wave body interactions (e.g., buoy oscillation, air flow, or water flow). The secondary conversion stage converts the body motion energy into electricity through the power take-off (PTO) system, and the tertiary stage adapts the characteristics of the produced power to the grid requirements with power electronic interfaces.

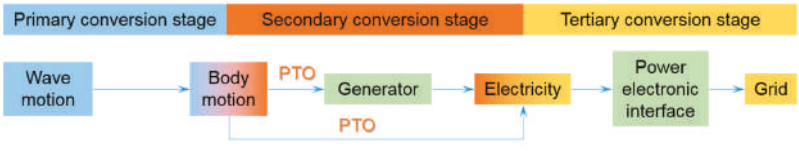

Figure 4. Main stages of wave energy conversion.

Based on the working principles of the WEC, from the primary conversion stage to the secondary conversion stage, the general categories are classified as shown in Figure 5 [72–75]:

- The oscillating water column (OWC), which compresses or decompresses the air in a chamber using the wave elevation to drive a Wells or impulse turbine to convert wave power. Depending on the location of installation, OWC devices can be fixed onshore [76–78], as shown in Figure 6a, or floating, as shown in Figure 6b [79–81].
- Wave activated bodies (WABs), which utilize the wave excitation motions between two bodies to convert wave power into electric power. According to their dimension and orientation, WABs can also be classified as *terminators* [82] (Figure 6c), positioned with large horizontal extensions perpendicular to the wave propagation direction); *attenuators* [83,84] (Figure 6d), which have a large horizontal extension parallel to the wave propagation direction; *point absorbers* [85,86] (Figure 6e), which have small dimensions compared to the predominant wavelength and are usually axisymmetric about their vertical axis; and *submerged pressure differentials* [87] (Figure 6f), which are submerged buoys with large dimensions.

- The overtopping device, which utilizes the overtopping phenomenon to the let the water fall through the turbine to converter the potential energy into electric power [88–90], as shown in Figure 6g.
- Others, describing concepts different from the above categories, e.g., the wave carpet [91] and the *rotating mass* [92,93], which uses the motion of a hull to accelerate and maintain the revolutions of a spinning mass inside.

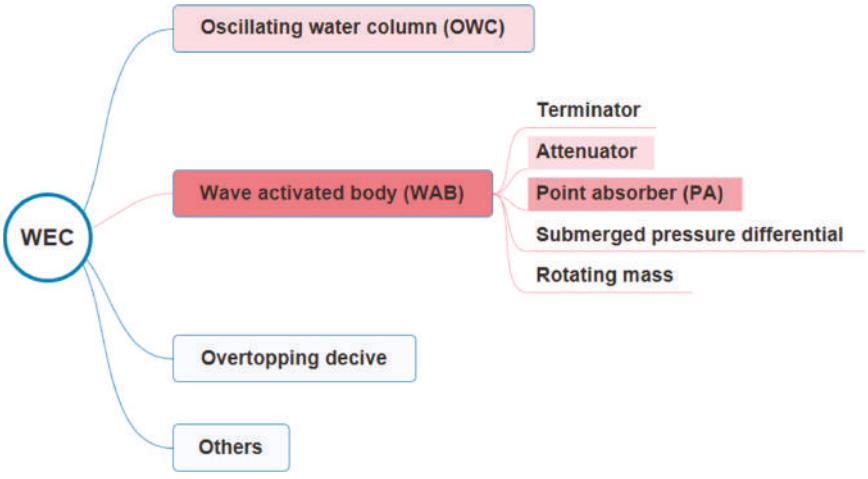

Figure 5. Categories of wave energy converter (WEC) technology.

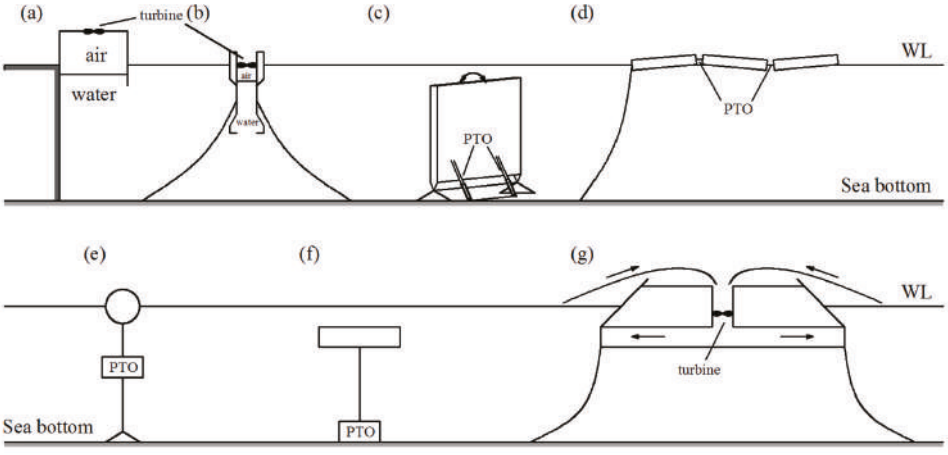

Figure 6. WEC technologies.

There are different types of PTO systems adopted for different WEC devices, e.g., pneumatic [94,95], hydraulic [96–99], direct mechanical drive [100–102], and direct electrical drive [103–105]. An elaborated description of these systems can be found in [106–108].

A time-varying wave climate in real sea may deteriorate the power quality gained from a single device. In practice, some strategies, like short-term energy storage or PTO resistance control, can be utilized to smooth energy production. However, arrays of wave energy converters are more desirable

because their cumulative energy generation will be smoother than the energy production of a single device [59]. Efficient power production is strictly dependent on the advanced control systems.

3.2.2. Tidal Range Energy Conversion

Tidal barrage power plants use the difference in the height of the water surface during ebbs and floods (tidal range) to drive common hydro turbines. The greater tidal range results in higher energy extraction by the power plant.

Figure 7 presents the principle of the tidal barrage power plant [109]. The shapes of structures are similar to dams and the structures are built in the estuary or bays to store water at high tide. A difference in water height at the internal and external sides of the dam occurs due to changes in the tidal regime. Three main tidal barrage schemes are

- Flood generation—the power production process starts as the water enters the tidal basin (flood tide);
- Ebb generation—power production starts as the water leaves the tidal basin (ebb tide);
- Two-way generation—the tidal power plant produces power during the flood and ebb tides.

The sluice gates on the barrages are utilized to control water levels and flow rates. In general, ebb generation is generally more efficient than flood generation. This is due to there being more kinetic energy in the upper half of the basin in which ebb generation operates. This is because of the effects of gravity and the second filling of the basin from inland rivers and streams connected to it via the land. The bi-directional tidal turbine generators are generally more expensive and less efficient than unidirectional tidal generators [110]. Some studies related to the tidal barrages' dynamics, power performance, and economy can be found in [111–115].

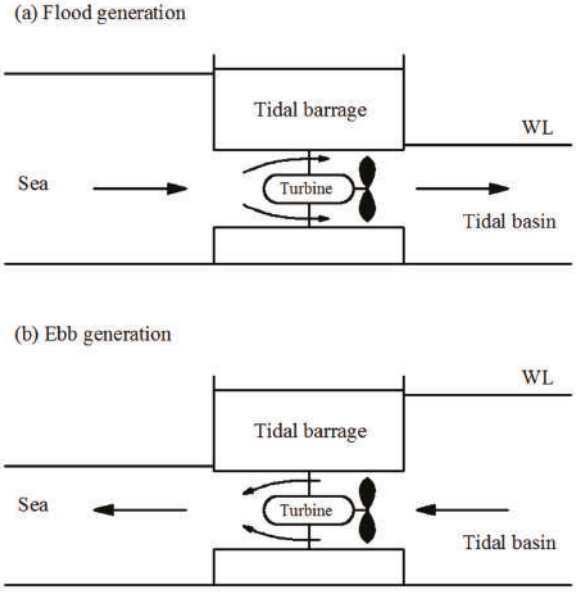

Figure 7. Tidal barrage principles.

3.2.3. Tidal Current and Ocean Current Energy Conversion

The kinetic energy of both tidal and ocean currents can be extracted with hydrokinetic turbines, which have similarities with wind turbines but are still submerged. Due to the higher density of water

compared to that of air, the blades of current turbine devices have smaller dimensions and move slower than those of wind turbines while still providing a significant amount of energy. The main difference between tidal and ocean currents is that the tidal currents have bi-directional flows in contrast to the ocean currents which are unidirectional. This has implications for the design of a tidal current turbine, which must act in both directions of the water flow [59].

The four major types of current energy conversion devices are as follows, as shown in Figure 8:

- Horizontal axis turbine [116–118]—blades, driven by current energy, rotate around the horizontal axis;
- Vertical axis turbine [119–124]—blades, driven by current energy, rotate around the vertical axis;
- Oscillating hydrofoil [125–128]—currents passing the hydrofoil result in the lift force, which can drive the motion of the hydraulic system to generate electricity;
- Venturi effect turbines [129]—harness the kinetic energy of the current by amplifying the current velocity by the Venturi effect in the strangulated section of a tube [63].

Additionally, ducted channels are utilized to induce a sub-atmospheric pressure within a constrained area and, consequently, increase the flow velocity around the rotor [130–132]. The tidal kite is a novel technology, which uses wing carrying and pushes a turbine in an "8" shaped trajectory, sweeping a large area with a relative speed of more than the local current speed [133–135]. A review of the tidal current technology is presented in [136].

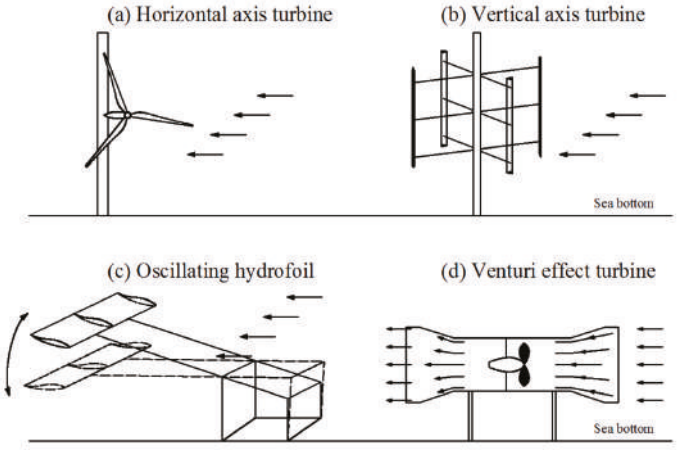

Figure 8. Primary types of tidal and ocean current energy conversion devices.

3.2.4. Ocean Thermal Energy Conversion (OTEC)

OTEC is a technology that converts the difference in temperature between the sea surface and large depths (around 1000 m) for use in heating, cooling, or to generate electricity. Closed-cycle technology requires a minimum temperature difference of 20 °C, which is possible in equatorial marine regions. Warm water from the upper layers is used to vaporize a secondary working fluid (e.g., ammonia), thus driving an electric generator. The resultant steam is then condensed by the cold water, which is brought, using pumps, from the bottom of the ocean and then discarded. Some works that studied the closed-cycle OTEC can be found in [137–139].

Open cycle technology uses the warm surface ocean water as the working fluid, which is drawn into a vacuum vessel, causing the working fluid to vaporize. The main benefit of the open cycle process is that it produces both electricity and desalinated fresh water. An investigation of the performance of a shore-based low temperature thermal desalination using an open-cycle OTEC is presented in [140]. Recently, a novel optimal open-cycle OTEC plant using multiple condensers was designed in [141].

The hybrid cycle combines both closed and open cycle technologies. Similar to the open cycle process, the warm surface water is flash-evaporated into steam. The steam is used to vaporize the ammonia working fluid of a closed-cycle loop and drives a turbine to produce electricity. Afterwards, the steam is condensed through a heat exchanger, providing desalinated water [142]. Such a cycle can realize the generation of both electricity and fresh drinking water simultaneously.

3.2.5. Salinity Gradient Energy Conversion

The salinity gradient takes advantage of the power that can be generated by the mixture of cold and salty water, for instance, at the mouth of a river that flows into the sea. There are two common methods for generating energy from the salinity gradient: pressure-retarded osmosis (PRO) [143–146] and reverse electrodialysis (RED) [147–149].

The PRO method is based on semipermeable membranes that allow only the traveling of water molecules. In this approach, water flows from the diluted solution (freshwater) to the concentrated solution (seawater) to provide a chemical potential equilibrium on both sides of the membrane. This occurs only when the pressure difference between the liquids is less than the difference in osmotic pressure. This flow of water can be used to power turbines that transform mechanical energy into electricity. The RED method is based on the transport of ions (salt) through membranes. Two fluids of different salinities (freshwater and seawater) pass through a series of specific membranes. The difference in chemical potential between membranes results in an electrical voltage. The brackish water is then discarded into the sea.

Additionally, some hybrid processes, such as the production of electricity from thermal energy using a closed-loop RED heat engine, low-energy desalination by integrating RED with desalination facilities, and the use of microbial RED cells with boosted power performance, have been proposed to facilitate energy extraction from salinity gradient resources [149,150].

3.3. Global Status of Development

3.3.1. Installed Capacity

Despite decades of development efforts, a large amount of the ocean's renewable energy sources are still untapped [151]. In the last 10 years, the use of ocean energy sources has experienced significant growth globally. Since 2009, many devices have been deployed worldwide to capture the energy from currents, tidal ranges, thermal and salinity gradients, and waves. This progress is noticeable by the gradual increase in installed capacity in some continents, as shown in Figure 9 [152], demonstrating an expansion of marine energy in the world energy matrix. Globally, this growth has more than doubled from 244 MW in 2009 to 532 MW in 2018. However, more than 90% of this operating capacity is represented by two tidal barrages in La Rance, France and Sihwa Lake, South Korea.

The contribution of Asia is led by China and South Korea, where extraordinary progress has been made since 2011, mainly because of the development of tidal barrage facilities. This is due to government support, through the adoption of economic policies, the reduction of tariffs and exemption, which includes financial subsidy policies to encourage scientific research and development, the development of new renewable energy technologies, prototype demonstration, and development of the renewable energy industry [153]. After France developed the La Rance tidal barrage, the United Kingdom led the way in terms of installation capacity followed by Spain, Sweden, the Netherlands, Norway, Portugal, and Italy. In North America, mainly in Canada and the United States, the development of these energy sources is in advanced stages, with the implementation of demonstration-scale commercial projects. Africa, Central America and the Caribbean, South America, and Oceania are in the early stages of deploying ocean resources as energy sources, with incipient projects and installed capacity.

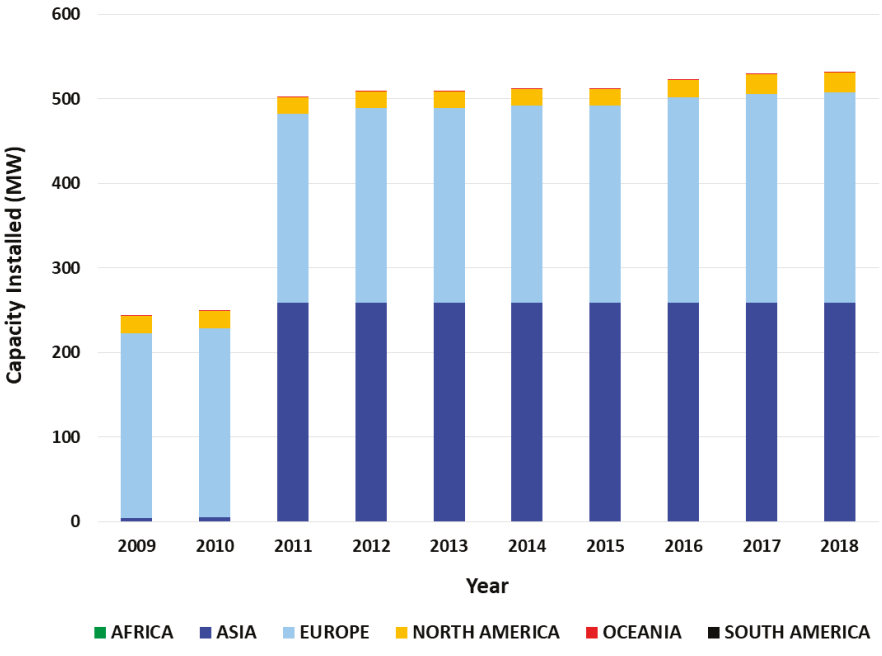

Figure 9. Marine energy: capacity installed by continents, according to the International Renewable Energy Agency (IRENA) (2019) [152].

3.3.2. Technology Status

The technology readiness level (TRL) presented by NASA has been adapted for ocean renewable energy technologies and presented by [154]. The TRL system quantifies the development of ocean energy devices from an initial stage of research and development (R&D) to industrial roll-out, which involves the mass production of off-the-shelf components and devices. Accordingly, the ocean renewable energy technologies are still at the conceptual, R&D, or demonstrative prototype stages. Nevertheless, in the case of waves and tidal currents, global commercial application is expected in the near to medium future. Based on reports, the extraction of energy from tidal ranges is still at the precommercial stage and the use of energy from tidal currents and waves is at the demonstration and prototype stages, respectively.

3.3.3. Deployed Devices

Large-scale (half- or full-scale) testing at sea is necessary for the pre-commercial stage of development. However, only a few devices have been constructed and tested at full scale. Oscillating water column devices have been employed as fixed onshore and floating offshore structures. Some examples of the fixed OWC prototypes have been deployed in Japan [155], Italy [156], Portugal [157], and Norway [158].

The Pelamis Wave power is the most mature wave-activated body device. It was installed for the first time in 2004 at the European Marine Energy Centre (EMEC) wave test site at Billia Croo. Later, its second generation, which comprised five connected sections, giving a total length of 180 m and a rated power of 750 kW, was installed at the same test site in 2010. AquaBuoy [159], Interproject Service (IPS) buoy [160], and Wave Bob [161] are examples of the wave-activated body devices that produce energy from the relative motion of two connected oscillating bodies.

Overtopping devices can be floating or fixed structures. The Wave Dragon [162] and the Seawave Slot-Cone Generator [163] are prototypes that represent overtopping with floating and fixed structures, respectively.

In contrast to the other sources, tidal energy can provide predictable and stable power to the electrical network. However, the tidal-current-generated electricity price is not yet competitive with the current wholesale prices of electricity due to the technical challenges associated with building, installing, operating, and maintaining the plant which affect the cost of the produced energy in energetic sub-sea environments [164].

Some important deployments of the horizontal axis tidal turbines are as follows: The Shetland tidal array was the first deployed tidal array. It includes three turbines of 100 kW each. Meygen, which is the largest operational tidal current array with four turbines of 1.5 MW, was developed by ANDRITZ HYDRO Hammerfest and Atlantis Resource Limited. The Sabella D10 tidal turbine has a capacity of 1 MW. The Cape Sharp Tidal project consists of two turbines of 2 MW and was developed by OpenHydro/Naval Energies.

The two largest tidal barrages are the 240 MW Rance barrage (1966) in France [165] and the 254 MW Sihwa Lake tidal barrage (2011) in South Korea [166,167]. Other countries, such as China, Russia, and the UK [168], are also focusing on tidal barrage technology. In particular, the former two countries have operated tidal barrage power plants in a mean range of 2.4 m with modern low-head turbines [169], which proves that relatively low tides (lower than 5 m, which is considered necessary for tidal barrages [170]) can also be utilized economically.

The extraction of energy from the ocean's thermal gradient is being pursued by some countries including the United States, China, Japan, France, Taiwan, South Korea, India, and the Netherlands. However, two main projects that achieved the prototype phase are the onshore Okinawa 100 kW [171,172] and Hawaii 105 kW OTEC [173] power plants. The former prototype is a hybrid OTEC, developed by Saga University, which uses mixed water/ammonia as "working fluid". It was installed in 2013 in Okinawa, Japan. The latter is a closed-cycle OTEC that was developed by Makai Ocean Engineering. It was installed and connected to the US electrical grid in 2015.

Salinity gradient power is still a concept under development [149,150]. The first PRO (pressure retarded osmosis) power plant was developed by Statkraft in 2006. The main project is a 5 kW RED pilot project that was developed by the REDStack and Fujifilm in 2005. They deployed a 50 kW RED pilot project in "Afsluitdijk" (the sea defense site and major causeway) in 2013.

3.3.4. Status of the Projects

- Project development phases

In general, numerous projects have been implemented in all continents, and some regions present a relatively high TRL compared with others. To address the current status of ocean renewable energy technologies, we integrated the data of 455 projects from five different databases as follows: OES 2019 (Ocean Energy System), EMODnet 2017 (The European Marine Observation and Data Network), UKMED 2019 (UK Marine Energy Database), and OpenEI 2019 (Open Energy Information) provided by the US Department of Energy's Marine and Hydrokinetic Technology Database and PNNL 2019 (Pacific Northwest National Laboratory) [174–178]. Note that, in some cases, mainly related to the wave and current energy, each project may include more than one device unit, forming a farm; however, the numbers that are shown in this section represent the quantity of projects and not the number of the employed technology units. Since each database classifies projects based on its defined categories, unification of the stages of the project development is required. In this work, to unify the classifications of the databases, four different categories were defined based on the "guidelines for project development in the marine energy industry" presented by the EMEC [179]. Accordingly, each marine energy project was divided into seven stages, labelled 0, 1, 2, 3, 4, 5, and 6, associated with the project development strategy, site screening, project feasibility, project design and development,

project fabrication and installation, operation and maintenance, and decommissioning, respectively. Table 2 shows a summary of the project stages.

Table 2. Stages of ocean renewable energy project development.

Project Stage	Description
Early concept	The technology is in the early stage of development. The basic principles are observed, and analytical formulations, numerical simulations, and laboratory-scale experimental tests are performed at this stage. (Stages 0, 1, and 2 based on [179]).
In planning	The technology is being used in medium- or large-scale experimental tests in a realistic working environment or in an open sea. The represents preparation for authorized consent. (Stage 3 based on [179]).
Pre-deployment	Consent is authorized by the consent authority and the company or technology developers perform activities such as site preparation, fabrication, and installation. (Stage 4 based on [179]).
Operational	The device is fully operational. In this paper, the operational system can even be connected to a local electrical grid or can provide energy for an isolated center of consumption, such as a marine lighthouse.
Decommissioned	Devices that have been removed from the water after being operational for a certain period.
Dormant	Projects that had site permission or authorized consent or were in the permitting process but were later abandoned.

- Geographical distribution of the projects

Figure 10a,b shows the geographical distribution of the projects over approximately 40 countries. It can be seen that, in terms of quantity, Europe has the largest contribution (about 60.66%), followed by North America, Asia, Oceania, Africa, Central America and the Caribbean, and South America with 17.10%, 13.35%, 5.62%, 1.64%, 0.94%, and 0.7%, respectively. As Figure 10b illustrates, the largest number of projects belong to the wave and current energy sector, and these are mostly located in Europe. Note that in this sector, the current energy projects include technologies that are utilized to harness current energy, independent of its type, including ocean and tidal currents.

It is observed that although the ocean thermal gradient has the largest potential among the energy resources, there is a very low interest in harnessing such energy. This may be due to the technical complexities and high capital cost that decelerate the development process of OTEC technology [180]. Nevertheless, it can be inferred that wave and current energy are considered to be more promising energy resources than others.

Figure 11 illustrates a summary of the global status of ocean renewable energy projects. Approximately half of the projects are in the "planning" and "pre-deployment" stages, and these projects are dominated by the current and wave energy and mostly located in Europe. This means that there will be a significant evolution in ORE deployment in the next 5 years. Europe, Asia, North America, and Africa are the regions with operational projects. Asia may lead the future in OTEC technology having a larger number of "planning" and "pre-deployment" projects compared with other regions. These projects are mostly located on the eastern coast of Asia. Tidal range energy has been harnessed commercially since 1966 (Rance River north-western France); however, to date, only a handful of operational projects have been deployed. On the other hand, wave and current energy projects, which are operational or at an earlier stage of development, represent about 65% of all projects. This implies that tidal range technology has not drawn as much serious developmental interest as wave and current technologies. This may be due to the high cost and ecological impacts of such technology [181].

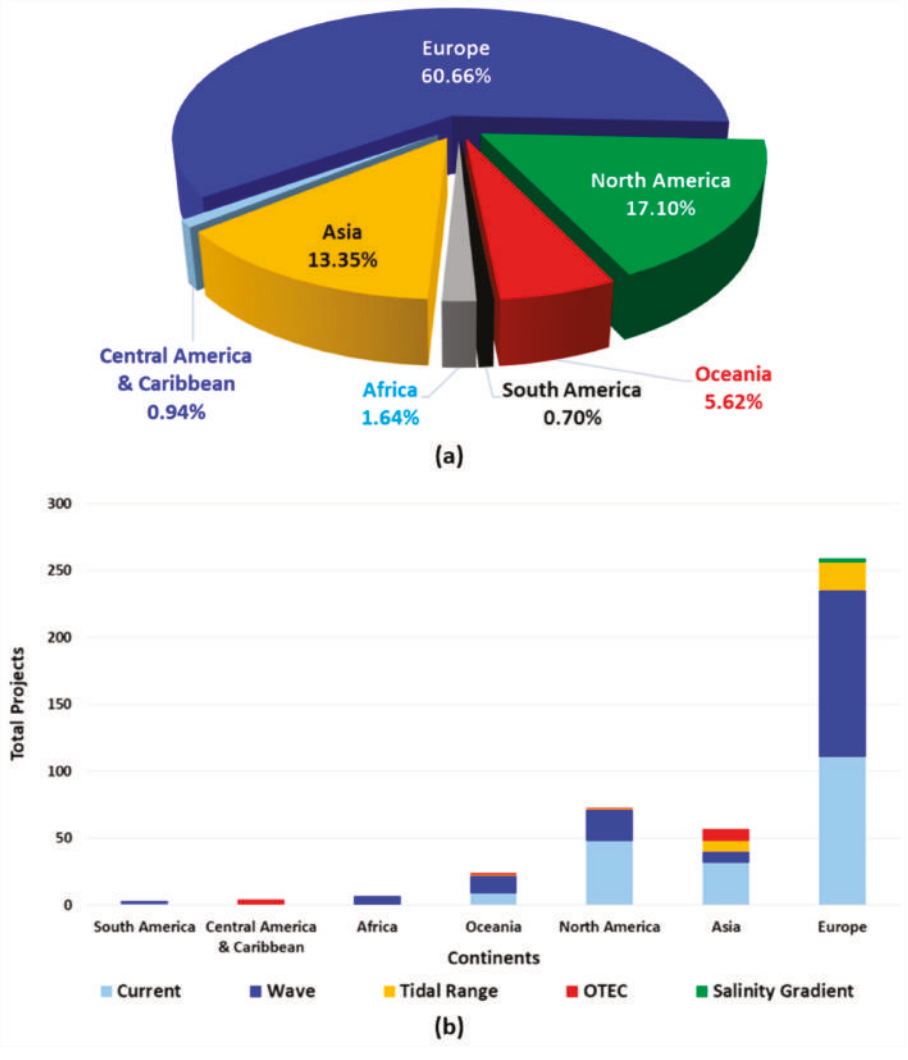

Figure 10. Distribution of the ocean renewable energy projects by (**a**) continent and (**b**) source for each continent.

- Technology distribution

The databases were used to determine the technological distribution of the projects. As Figure 12 illustrates, and as was expected, the most employed technologies are current and wave energy technologies. Current energy technologies are closest to technological maturity showing a significant convergence with the use of horizontal axis turbines. Most projects use horizontal axis turbine technology, followed by vertical axis turbines, tidal kites, and oscillatory hydrofoils. On the other hand, more technology diversity can be observed for wave energy converters, partly due to the diversity of wave resources and the complexity of harnessing wave energy. The wave energy technologies are dominated by point absorber devices followed by OWC, oscillating wave surge converters, attenuators, rotating masses, overtopping devices, and submerged pressure differential devices (see Section 3).

The OTEC technologies are limited to the use of closed and open cycle and hybrid systems with a tendency of deploying the closed cycle method. Tidal range energy is traditionally harnessed using tidal barrages installed in the estuaries, but this method is associated with important environmental issues. The use of tidal lagoons has been proposed and developed in the UK since 2008 as an alternative to reducing such environmental issues [168]. The technology for extracting the salinity gradient energy is still in the conceptual stage of development, and its evolution is highly dependent on membrane enhancement, which will be responsible for 50% to 80% of the total cost [182].

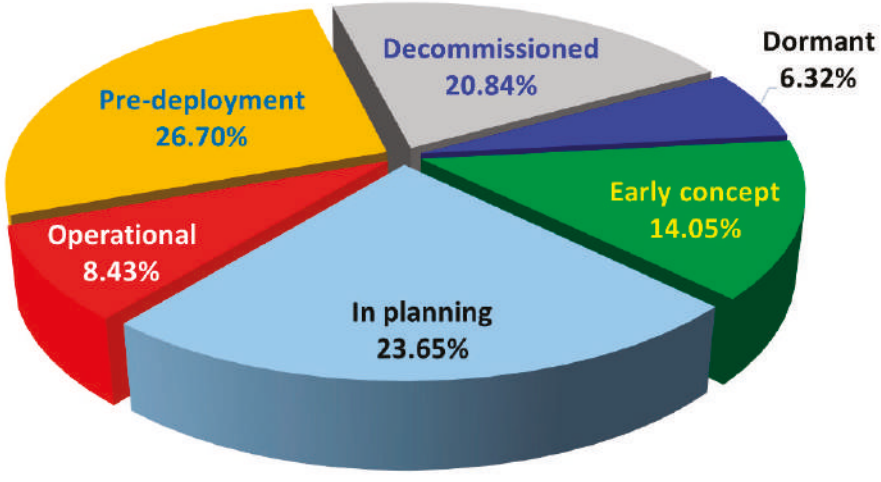

Figure 11. Global status of the ocean renewable energy projects.

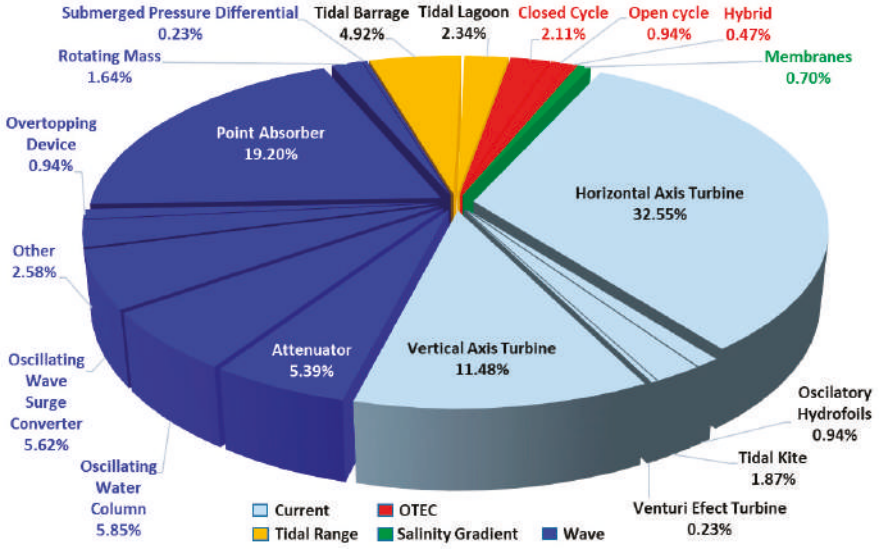

Figure 12. Technology distribution among projects.

4. Case Study of Brazil

4.1. Resource Assessment Results

4.1.1. Ocean Current Energy

Figures 13 and 14 show the spatial variation of the ocean current resources along the Brazilian coast in terms of the annual and seasonal average current speed (m/s) and power density (W/m^2). As shown in Figure 13, the maximum annual average can be observed in the north equatorial margin of Brazil with a velocity of 1.52 m/s. This region is influenced by the NBC. These regions are located at a distance of between 120 and 300 km of the coastline. The same pattern can be observed considering the seasonal distribution. A maximum speed value of 1.67 m/s occurs during autumn. It can be seen that the speed values barely reach 2 m/s, which is recommended for commercial ocean current energy extraction [32]. The current speed values are not significant (less than 0.7 m/s) for the regions A and B. They occur due to the BC flow and are higher during the spring. Figure 14 shows the power density (W/m^2), calculated using Equation (1), across the Brazilian coastline. As expected, following the speed values, region D represents the most energetic area, and power density values higher than 500 W/m^2 can be observed for some areas. Table 3 contains the average values of the seasonal mean power as well as the *SV* and *COV* values. The seasonal average values for regions D and C show that, in contrast to the regions A and B, the current power density is higher during austral autumn and winter compared to austral summer and spring. This is due to the seasonal climatological behavior of the NBC [25]. The fact that the power density of the region D is significantly higher than that of other regions indicates that the values of *SV* and *COV* are less important when the objective is to determine the best region for exploring the ocean current energy. However, these values are important for techno-economic studies of the corresponding energy extracting technologies in the North region.

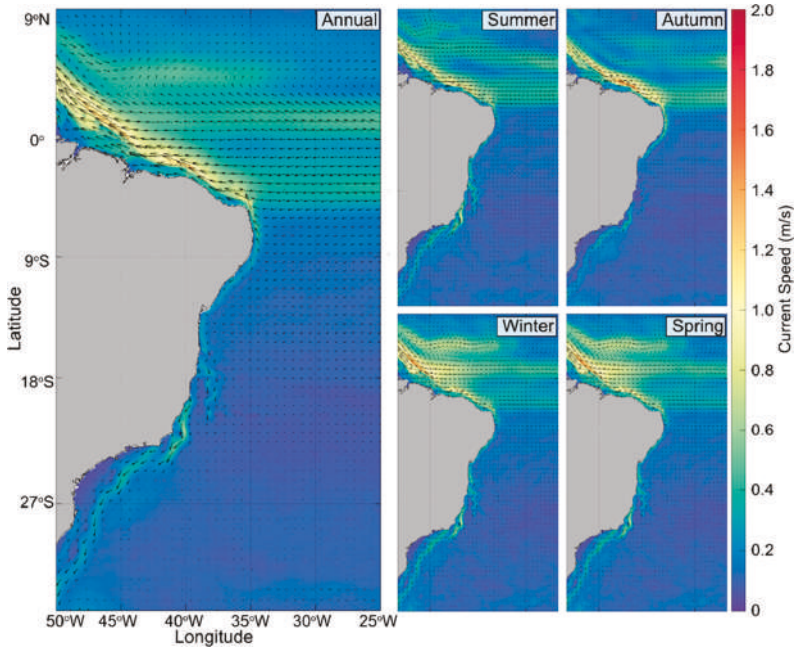

Figure 13. Annual and seasonal (summer, autumn, winter, and spring) mean surface current speed (m/s) at the Brazilian coastline between January 1, 2007 and December 31, 2017.

Table 3. Average values of the ocean current power density (W/m^2), standard deviation (±), seasonal variability (SV), and coefficient of variation (COV) for each coastline region—A, B, C and D—for each season (summer, autumn, winter, and spring) between January 1, 2007 and December 31, 2017.

Region/Season	Power Density (W/m^2) ± Standard Deviation				*SV*	*COV*
	Summer	**Autumn**	**Winter**	**Spring**		
A	98.9 (±3.3)	73.67 (±2.12)	74.35 (±2.12)	97.85 (±2.7)	0.269	0.951
B	362.76 (±9.9)	90.06 (±3.83)	167.37 (±5.6)	280.25 (±7.8)	0.609	1.994
C	193.93 (±3.84)	399.93 (±11.1)	379.137 (±11.06)	216.36 (±5.06)	0.426	1.460
D	788.21(±39.15)	1416.64 (±58.28)	1240.21 (±58.82)	1103.4 (±52.3)	0.514	1.333

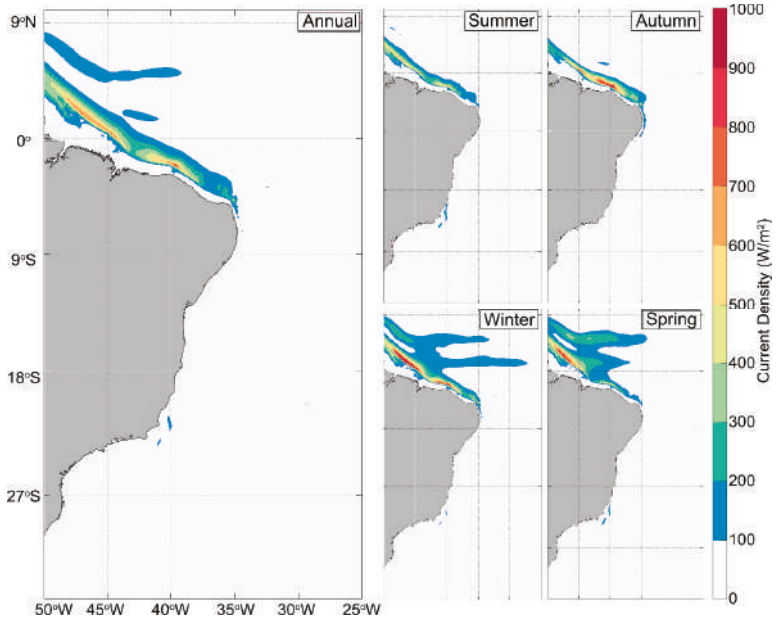

Figure 14. Annual and seasonal (summer, autumn, winter, and spring) mean power density (W/m^2) at the Brazilian coastline between January 1, 2007 and December 31, 2017.

4.1.2. Wave Energy

Figure 15 shows the average annual and seasonal wave power density values. The hindcast shows the variability of the energy resource and provides a holistic view of the wave climate along the Brazilian coast. It can be observed that the most energetic wave areas are located near the regions A and B coasts with a power value between 20 and 25 kW/m. This is intensified during the autumn and winter seasons. This fact is directly related to the increase in the occurrence of extratropical cyclones that generate larger waves that propagate toward these Brazilian regions. The nearshore areas of region A (areas with a water depth of less than 100 m) have values close to 20 kW/m for almost the entire year. This is mainly due to the preponderance of south winds combined with the shoreline orientation that induces strong swells near the coast. The average values of the *SV* and *COV* related to the wave power were calculated and are illustrated in Table 4 for five different bathymetries of 25, 50, 100, 150, and 200 m along the Brazilian coast. It can be observed that, independently of the water depth, the seasonal variability (SV) of the regions A and B is always smaller than that of the regions D and C. On the other hand, the minimum *COV* occurs in the region C, while the region D has a

greater *COV* than the other regions. However, the differences between the *COV* values of the region C, when compared with those in the regions A and B, are small and decrease as the water depth increases from 25 to 200 m. The region C has the smallest wave power variability during the year, which may lead to a higher capacity factor, while the regions A and B are the areas with the most energetic waves, allowing the deployment of the devices with higher installed capacity. A trade-off between the WEC nominal power and capacity factor as well as other local characteristics such as water depth should be considered to determine the proper locations for deploying wave farms.

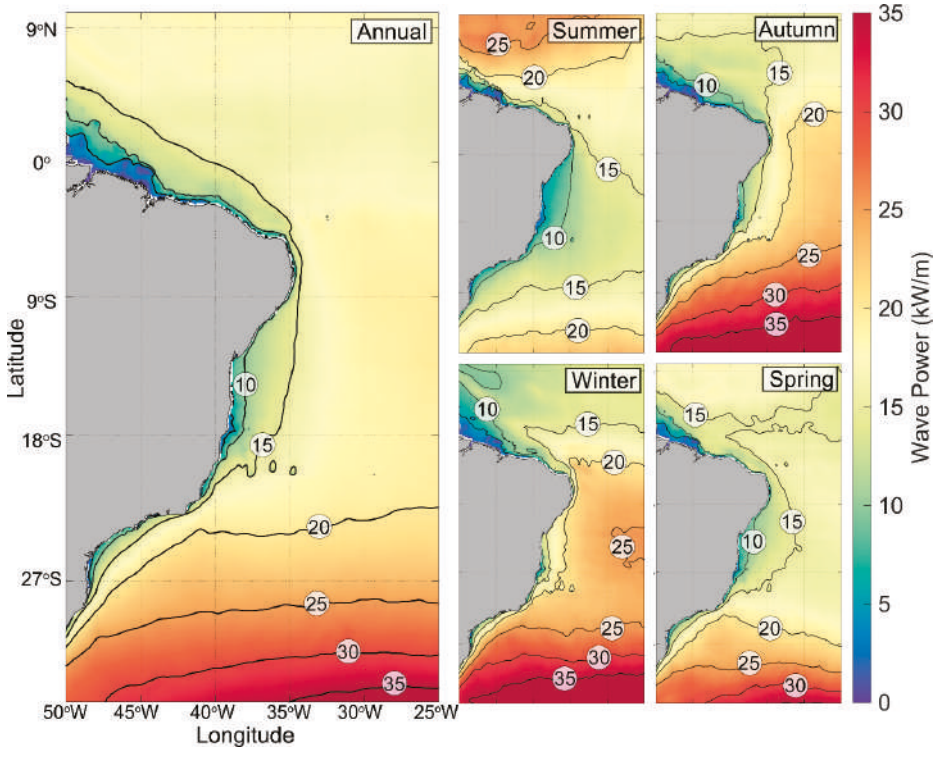

Figure 15. Annual and seasonal (summer, autumn, winter and spring) mean wave power density (k W/m^2) at the Brazilian coastline between January 1, 2015 and December 31, 2017.

Table 4. Average values of wave seasonal variability (SV) and coefficient of variation (COV) considering five different bathymetries (25, 50, 100, 150 and 200 m) for each region—A, B, C and D—between January 1, 2015 and December 31, 2017.

Region \ Bathymetry	25		50		100		150		200	
	SV	*COV*	*SV*	*COV*	*SV*	*COV*	*SV*	*COV*	*SV*	*COV*
A	0.467	0.533	0.431	0.334	0.482	0.303	0.502	0.285	0.509	0.258
B	0.637	0.515	0.619	0.350	0.595	0.294	0.596	0.283	0.615	0.287
C	0.845	0.375	0.865	0.302	0.856	0.305	0.852	0.274	0.781	0.250
D	0.748	0.685	0.929	0.464	0.929	0.432	0.744	0.301	0.833	0.296

The available wave power for the Brazilian coastline was calculated at an average distance of 128 km from the coast (Table 5). Accordingly, a total available wave power of approximately 91.8 GW was estimated considering a total coastline length of about 7491 km (an approximate value without coastline details). It should be noted that this value is an estimation of the theoretical potential of

the Brazilian wave power. In practice, only a fraction of this value can be extracted by the wave energy devices, which depends on different issues such as technical challenges, environmental impacts, economy, deferent use of the sea area, and social impacts. Nevertheless, only one-fifth of this potential is equal to approximately 35% of the Brazilian electricity demand in 2017 [183].

Table 5. Available wave power of the Brazilian coastline.

Parameters	Regions			
	A	B	C	D
Length (km)	~1250	~1952	~1452	~2837
Average power (kW/m)	21.1	12.4	13.8	7.4
Total power (GW)	26.4	24.2	20.1	21.0

4.1.3. Ocean Thermal Energy

Figure 16a shows the annual average ΔT (°C) between the water depth of 20 and 1000 m along the Brazilian coast. The results show that, except for the extreme South below 27 °S, the yearly average ΔT is always about 20 °C or higher along the Brazilian coast. The average gross power of a 10 MW OTEC plant (see Section 2.2.1) was calculated for 12 locations along the coastline. The selected points were located approximately at a distance between 30 and 200 km to the shore and had an annual average ΔT at between 20 and 1000 m of water depth of more than 20 °C. Figure 16b illustrates the annual variation in the gross power for the considered points. A greater average annual gross power, represented by the red solid line, can be observed for the regions D and C comparing to the regions A and B. Moreover, the results show smoother power production for the regions D and C comparing to the regions A and B. Table 6 shows the characteristics of the selected points as well as the P_{gross} and P_{net}.

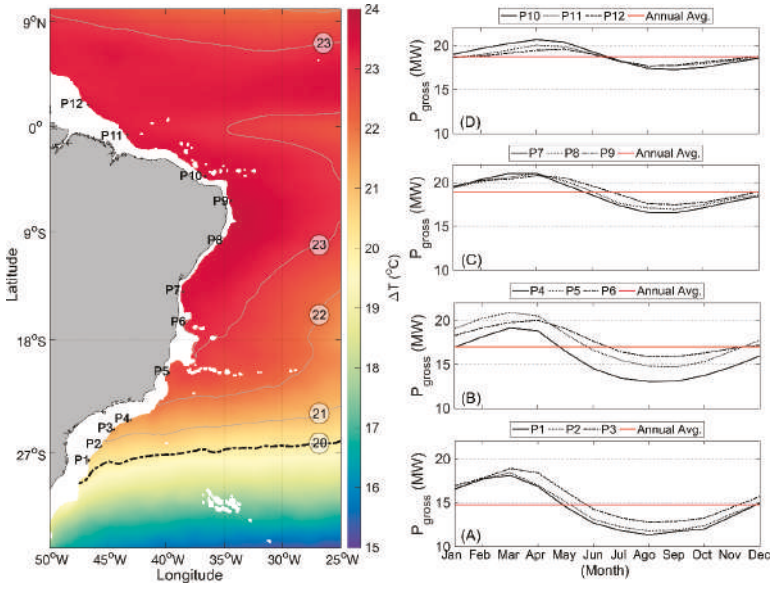

Figure 16. (**a**) Annual mean ΔT (°C) between 20 and 1000 m and (**b**) the annual ocean thermal energy conversion (OTEC) Gross Power Density (P_G in MW) at a depth of 1000 m considering the period between January 1, 2007 and December 31, 2017.

Figure 17 illustrates the seasonal mean ΔT (°C) between the water depths of 20 and 1000 m, for a bathymetry of 1000 m, across the Brazilian coastline. The black line represents a ΔT of 20 °C. It can be observed that, for the regions A and B, the water depth in which the mean ΔT = 20 °C is achieved, varies between 500 m in summer and 700–1000 m in other seasons. On the other hand, in the regions D and C, a mean ΔT of 20 °C can be reached in a water depth of about 500–700 m throughout the year. From a technical point of view, less structural challenges would be expected when bringing the cold water from a depth of 500 m rather than from 1 km.

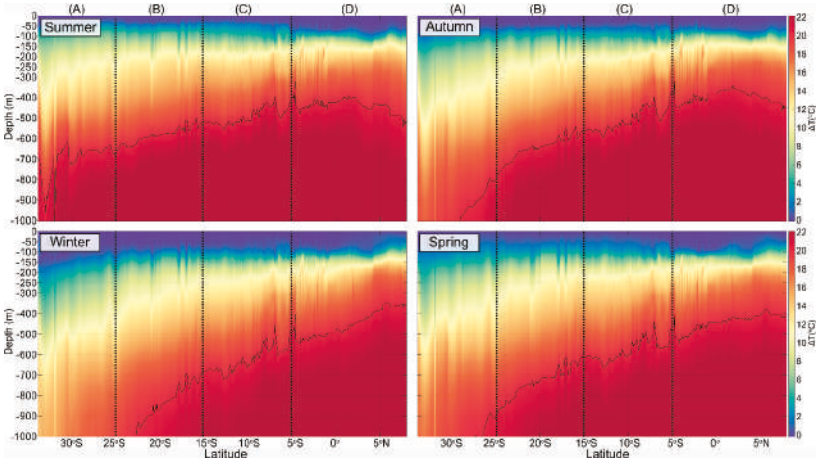

Figure 17. Seasonal (summer, autumn, winter, and spring) mean ΔT (°C) between 20 and 1000 m for the bathymetry of 1000 m (for regions A, B, C and D) across the Brazilian coastline latitude considering the period between January 1, 2007 and December 31, 2017. The black line corresponds to a ΔT of 20 °C.

Table 6. Gross and net power estimation for the selected points along the Brazilian coastline.

Regions	Points	Lat/Lon	Bathymetry (~m)	ΔT (°C)	Annual Average P_{gross} (MW)	Annual Average P_{net} (MW)
A	P1	27.6666°S 46.5833°W	1396	20.17	14.32	10.12
	P2	26.5833°S 45.5833°W	1409	20.37	14.58	10.39
	P3	25.3333°S 44.5000°W	1000	20.98	15.42	11.23
B	P4	24.4167°S 43.0833°W	1396	21.16	15.67	11.49
	P5	20.8333°S 39.7500°W	1422	22.43	17.53	13.36
	P6	16.6667°S 38.4167°W	1005	22.59	17.71	13.55
C	P7	14.1667°S 38.5833°W	1948	23.21	18.88	14.51
	P8	9.9167°S 35.2500°W	2012	23.33	18.84	16.69
	P9	6.5000°S 34.4167°W	2764	23.54	19.15	15.00
D	P10	4.3333°S 36.6667°W	1945	23.37	18.86	14.72
	P11	0.8333°S 43.3333°W	2337	23.29	18.71	14.57
	P12	1.6667°N 46.6667°W	1463	23.24	18.63	14.50

4.2. Deployments in Brazil

The first deployment of an ocean renewable energy converter in Brazil occurred in 1934 when the French engineer Georges Claude used an ocean thermal energy source to produce ice for the residents of Rio de Janeiro. His plant ran into problems and stopped working off the coast of Rio de Janeiro due to fatigue of its long intake tubes [184]. Studies associated with ocean renewable energy in Brazil began in 2001 at the Federal University of Rio de Janeiro (UFRJ), focusing on wave and tidal energy. Some other universities have also started working in this field, such as the Federal University of Maranhão (UFMA), the Federal University of Santa Catarina (UFSC), the Federal University of Pará (UFPA), and the Federal University of Itajubá (UNIFEI).

There are three main ocean renewable energy projects being carried out in Brazil with different technology readiness levels. The first one is the COPPE (The Alberto Luiz Coimbra Institute for Graduate Studies and Research in Engineering) hyperbaric wave converter developed by the UFRJ, which has reached the prototype stage. A full-scale single device of the technology was installed in 2011 in Pecém port of Ceará state located in the northeast of Brazil. The device was decommissioned after 6 months of operation due to the port extension project. The second project is a nearshore wave energy converter, also developed by the UFRJ, which will be installed in relatively shallow water (water depth of 25–30 m) off the Rio de Janeiro coast. The technology is at the R&D stage and is undergoing medium-scale laboratory tests. The last project is the tidal range project of the Bacanga River estuary located in São Luís of Maranhão state in North Brazil. Although the discussion about the tidal energy extraction in this region is relatively old, the project is still at an early stage of development as it is waiting for finance. The following sections describe the characteristics and statuses of the mentioned projects.

4.2.1. COPPE Hyperbaric Wave Converter

As illustrated in Figure 18, this device is composed of a floating body connected to the pumping modules, a hydrodynamic accumulator, a hyperbaric chamber, and a generating unit. The vertical motion of the floating body due to the wave body interactions drives the pump actuator which displaces the water inside the closed circuit to a hydro-pneumatic accumulator. The accumulator is connected to a hyperbaric chamber, which has previously been pressurized. Then, the pressurized water drives a hydraulic turbine coupled to an electrical generator. The hyperbaric chamber works as an energy storage system, which smooth the power fluctuations due to the oscillatory nature of sea waves. The applied pressure is in the range of 250−400 m of water column (m.wc) [185].

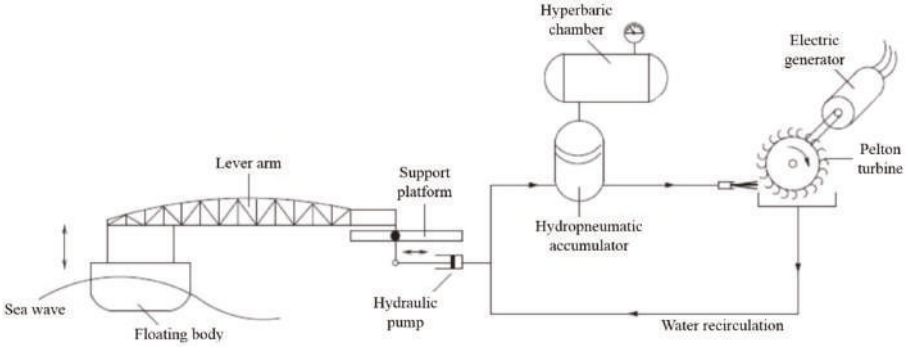

Figure 18. A schematic of the COPPE/UFRJ (Federal University of Rio de Janeiro) hyperbaric wave converter [185].

Additionally, a discrete control scheme was applied to the system to improve power production by adjusting the PTO parameters without wave measurement [186]. The experimental tests were

performed at the Ocean Technology Laboratory (LabOceano) of the UFRJ. Figure 19 shows the medium-scale model at a ratio of 1:10 which was tested under regular and irregular wave conditions corresponding to the predominant wave climate at the location of installation [187,188]. As a result of the experimental tests, a capture width ratio of between 19% and 36% was observed for the wave energy converter.

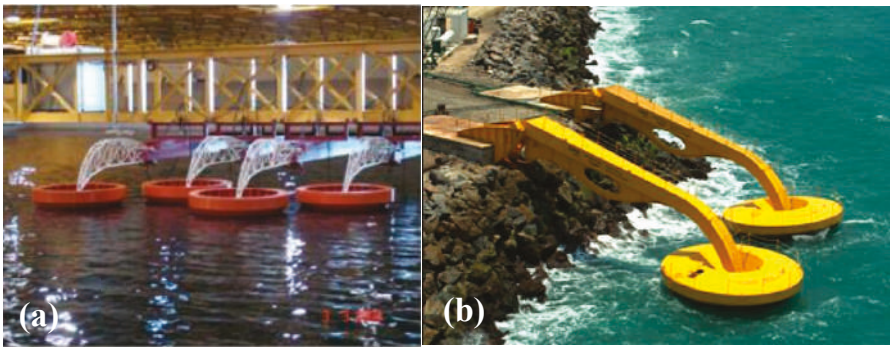

Figure 19. COPPE hyperbaric wave converter: (**a**) medium-scale model with a ratio of 1:10 at LabOceano [187]: (**b**) installed full-scale prototype.

A full-scale prototype with a capacity of 100 kW was deployed at the Pecém port in Northeast Brazil (Figure 19b). The device was installed on two concrete bases, 12 m in length, built on a breakwater. The oscillating part, which consists of a floater, 10 m in diameter, and a mechanical arm, 22 m in length, is connected to two skids mounted on the concrete bases.

4.2.2. COPPE Nearshore WEC

The system is a point absorber WEC type with a capacity of 50 kW that consists of an oscillating body and a bottom-mounted support structure. The oscillating part is a floating conical cylinder which is allowed to move only in the heave direction (Figure 20). The fixed structure consists of four columns with very small diameters relative to the wavelengths (no diffraction). The structure is mounted on the seabed through a concrete base. Eight roller bearings facilitate oscillation of the buoy in the vertical direction (heave). They are placed on the top and bottom of the cylindrical section.

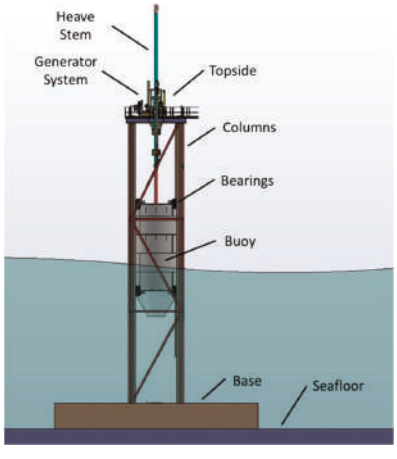

Figure 20. Components of the COPPE nearshore WEC.

The PTO system is located on the topside deck and consists of a gearbox and a rotational generator (Figure 21). The vertical motion of the buoy is transferred through a central rod (heave stem) to the gearbox. Then, the pulley converts the vertical movement into rotation that is adequate for the electrical generator. A backstop system unifies the rotation direction using freewheels. This implies that the buoy can drive the PTO system either upwards or downwards. A solid cylindrical flywheel is used to amplify the rotational inertia as well as smooth the delivered energy to the generator. Additionally, the PTO system includes a gearbox that multiplies the rotational speed so that it is adequate for power generation.

The location that has been considered for installation of the WEC is near to a small island called "Ilha Rasa". The location's water depth is about 20 m, and its distance from shore (Copacabana beach, Rio de Janeiro, Brazil) is about 14 km. The predominant wave climate of the region is a peak period of $T_p = 9.6$ s and a significant height of $H_s = 1.33$ m. Shadman et al. [189] showed that a very large buoy is required to maximize the power absorption in a region like nearshore Rio de Janeiro, where the predominate wave periods are beyond 7 s. This might lead to higher costs, which could make the project economically infeasible. Hence, a specific control called "latching", presented originally by Budal and Falnes [190], was applied on the WEC to overcome this challenge. Latching is a mechanical control method that tunes the natural period of the buoy to the predominate wave period of the sea site by halting and releasing the buoy at its motion extremum. As a result, larger buoy motion amplitude and velocities can be achieved, leading to higher power production. Eventually, the latching control enables a smaller buoy with a smaller natural period to be tuned with such a wave climate [191]. A hydraulic system is designed and tested for latching the oscillating buoy.

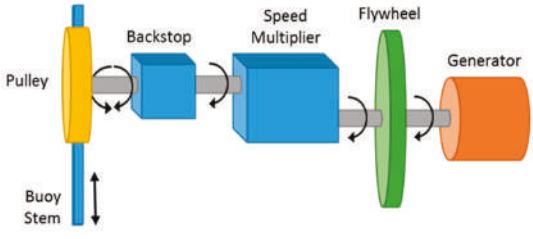

Figure 21. Schematic view of the power take-off (PTO) system.

Experimental tests of small-scale models, shown in Figure 22, were performed in a wave and current channel (LOC) at the COPPE/UFRJ. The hydrodynamic behavior of the buoy was studied by applying different modeling scales including 1:17, 1:20, 1:30, and 1:40. Additionally, a strategy was developed to investigate the effect of latching control on the WEC.

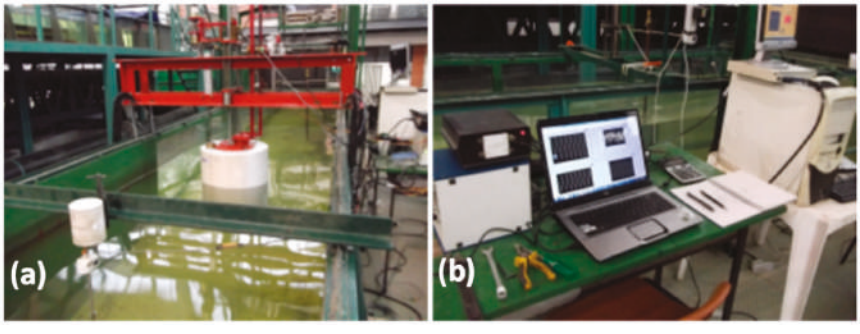

Figure 22. Experimental tests of the COPPE nearshore WEC in a wave channel: (**a**) 1:17 scaled model, (**b**) instruments for data acquisition.

4.2.3. Tidal Power Plant of the Estuary of Bacanga

The largest tidal ranges in Brazil are located on the North coast including the coastal areas of Maranhão, Pará, and Amapá. For instance, a tidal energy potential of 22 TWh/year has been estimated for Maranhão state [192]. Some studies have addressed the exploitation of such energy in Brazil [193,194]. As Figure 23a illustrates, the Bacanga basin is 10,219 ha in size, which includes the estuarine body of water and the Bacanga lake. The reservoir capacity is about 40 million cubic meters at an elevation of +4.5 m, corresponding to the spring tide level [192]. As shown in Figure 23b, the dam includes an 800 m embankment rock which is filled with clay material. Additionally, the dam has two sluice gate systems types of radial and stop-log that were installed in 1974 and 1980, respectively. There are three radial sluice gates with widths of approximately 12.5 m. In the case of a fully open gate, a water height level of 4.5 m is registered for each radial gate. This value is about 3 m for the stop-log gates, which are flat and operate vertically, with widths of 2.85 m.

Figure 23. (**a**) The Bacanga Estuary, and (**b**) aerial image of the radial and stop-log sluice gates [192].

Considering some restrictions, including a reservoir water level limit of +2.5 m, Neto et al. [192] proposed a new model for the tidal power plant in which the three radial sluice gates were replaced by the modern and appropriate version for automatic operation, which excluded the necessity of using stop-log type gates to control the reservoir maximum limit. Considering the Kaplan turbine with double regulation provided by ANDRITZ HYDRO [195], they estimated an annual energy production of slightly larger than 14 GWh/yr for the power plant.

5. Discussion and Open Question

The present cost of ocean renewable energy cannot complete with that of grid-connected renewables. The alternative, nowadays, in addition to the development of more optimized projects, is to look for new markets where electricity generation options are either scarce or expensive, for example the oil and gas industry, aquaculture, defense, and the demands from isolated communities. In the particular case of Brazil, there is a concentration of power generation, mostly from hydroelectric plants, located in the South and Southeast regions. It has been demonstrated that a significant amount of ocean renewable energy featuring an ocean thermal gradient is located in the regions D and C (see Figure 2). In these regions, an annual electricity production of 0.8 TWh per year has been calculated, considering only six OTEC plants with 10 MW installed power, as presented in this paper. Accordingly, considering an annual average of 15 MW, 20 OTEC plants would be sufficient to supply approximately 10% of the total residential electricity consumption of the Northeast region of Brazil, which was estimated to be approximately 27.059 TWh in 2017 [183]. This implies that such renewable energy resources could be harnessed as a supplementary alternative for these regions, especially when there is a power generation drop due to seasonal rain shortage. Additionally, the low seasonal and temporal variability of the ocean renewable resources along the Brazilian coast could provide stable power production throughout the year, with substantial capacity. The supply chain associated with ocean renewable technologies is still incipient worldwide. The increasing prototype deployments may

promote the association of local supply chains with the global suppliers of specific equipment such as submarine cables, electrical connectors, turbines, and generators. In Brazil, the supply chain would consist of companies already operating in the offshore oil and gas sector. This is a very robust sector, which will be able to meet the demands of the ocean renewable energy sector. The synergy of the long-established offshore oil and gas sector and the new ocean renewable energy sources could represent a crucial factor for the success of the new industry. Updated technologies must be incorporated, especially digital ones associated with artificial intelligence, control, and robotics to provide competitive services for inspection and maintenance, reducing the operational costs. New materials, such as the composites associated with innovative floating structures and installation methods, can also contribute to the competitiveness of the new sector in terms of the electricity cost. In Brazil, the large number of hydropower plants and the complex grid system also present opportunities for the implementation of ocean renewable energy sources. Hydropower plants could be designed as storage components of the whole electrical system, combining a better water supply with clean and efficient power generation throughout the country. The substitution of oil and gas-based power plants for ocean renewables would modify the national energy matrix substantially, reinforcing sustainably oriented electricity generation.

6. Conclusions

This paper, as a preliminary approach, has presented an assessment of ocean renewable energy resources, including wave, ocean current and thermal gradient energy, along the Brazilian coastline. The results show considerable ocean currents, thermal gradients, and wave energy in the regions D, C and A, respectively. A maximum annual average velocity of 1.52 m/s, which represents a power density of approximately 500 W/m^2, was observed for the ocean current energy in the region D near the equatorial margin of Brazil. However, the distance of the resource to the coastline, between 120 and 300 km, is an obstacle to its commercialization. The total theoretical potential of wave energy is estimated to be 91.8 GW along the coastline. The most energetic waves occur in the region A, following by the regions C, B, and D, with average power values of 21.1, 13.8, 12.4, and 7.4 kW/m, respectively. In the region C, the wave resource has the least temporal variability compared with the other regions; nevertheless, the differences are small, and they decrease with an increasing water depth. The results revealed an annual average ocean thermal gradient, between the water depths of 20 and 1000 m, of more than 20 °C for latitudes above 27°S. A mean thermal gradient of 20 °C between the upper layers and water depth between 500 and 700 m can be achieved throughout the year in the regions D and C. This could facilitate the process of bringing cold water from the deep sea, compared with the usual water depth of 1000 m.

The paper also presented an overview of the potential technologies and their statuses of development related to ocean renewable energy sources worldwide. Although available studies indicate different values for the global resource potential, they converge in presenting the ocean thermal gradient as being the most energetic resource followed by waves, salinity gradients, and tides. The TRL and the status of the current projects imply that the global interest tends toward tidal current and wave devices.

Large-scale installations, learning-curves, and innovation are necessary to make the cost of energy competitive with solar and onshore wind energy production. About 27% of the current projects are at the pre-deployment phase and, optimistically, will be deployed in the open sea in the next three years. Apart from tidal range technology, which is already close to the commercialization stage, research, development, and demonstration projects have been led by universities and startups, mostly by taking advantage of public financing. Nevertheless, in the last five years, large industry players and utilities have started carrying out activities and financing in the sector. This is an important step towards speeding up technology commercialization due to the new players' capability to execute utility-scale projects.

Author Contributions: Conceptualization, M.S.; Formal analysis, M.S. and D.F.; Methodology, M.S. and D.F.; Project administration, M.S.; Resources, L.P.d.F.A.; Software, D.F.; Supervision, L.L., C.L. and S.F.E.;

Visualization, C.S. and Z.W.; Writing—original draft, M.S., C.S. and Z.W.; Writing—review & editing, L.P.d.F.A., L.L., C.L. and S.F.E.

Funding: This research received no external funding.

Acknowledgments: The authors acknowledge CNPq, the Ministry of Science, Technology, Innovation and Communication/Brazil, for supporting the research activities of the authors. Additionally, the first author highly appreciates the Instituto Nacional de Ciência e Tecnologia—Energias Oceânicas e Fluviais (INEOF) for supporting his research activities. The third author acknowledges David Holland and the Center for Global Sea Level Change from New York University Abu Dhabi for supporting her research work.

Conflicts of Interest: The authors declare no conflict of interest.

References

1. International Renewable Energy Agency (IRENA). *Global Energy Transformation: A Roadmap to 2050*; International Renewable Energy Agency: Abu Dhabi, UAE, 2018.
2. Luomi, M. *Sustainable Energy in Brazil: Reversing Past Achievements or Realizing Future Potential*; The Oxford Institute for Energy Studies: Oxford, UK, 2014; Volume SP-34, ISBN 978-1-78467-005-4.
3. International Monetary Fund (IMF). IMF Country Information. Available online: https://www.imf.org/en/Countries (accessed on 1 June 2019).
4. Empresa de Pesquisa Energética (EPE). *Brazilian Energy Balance—Summary Report: Year Base 2017*; Empresa de Pesquisa Energética: Rio de Janeiro, Brazil, 2018.
5. International Energy Agency. *World Energy Outlook 2016*; International Energy Agency: Paris, France, 2016.
6. International Energy Agency. *World Energy Outlook 2017*; International Energy Agency: Paris, France, 2017.
7. Dias, V.S.; da Luz, M.P.; Medero, G.M.; Nascimento, D.T.F. An overview of hydropower reservoirs in Brazil: Current situation, future perspectives and impacts of climate change. *Water* **2018**, *10*, 592. [CrossRef]
8. Von Sperling, E. Hydropower in Brazil: Overview of positive and negative environmental aspects. *Energy Procedia* **2012**, *18*, 110–118. [CrossRef]
9. Reggiani, M.C.P. Hydropower in Brazil-Development and Challenges. Master's thesis, Norwegian University of Science and Technology, NTNU, Trondheim, Norway, December 2015. [CrossRef]
10. Rocha Lessa, A.C.; Dos Santos, M.A.; Lewis Maddock, J.E.; Dos Santos Bezerra, C. Emissions of greenhouse gases in terrestrial areas pre-existing to hydroelectric plant reservoirs in the Amazon: The case of Belo Monte hydroelectric plant. *Renew. Sustain. Energy Rev.* **2015**, *51*, 1728–1736. [CrossRef]
11. Beserra, E.R.; Mendes, A.; Estefen, S.F.; Parente, C.E. Wave climate analysis for a wave energy conversion application in Brazil. In Proceedings of the ASME 2007 26th International Conference on Offshore Mechanics and Arctic Engineering, San Diego, CA, USA, 10–15 June 2007; pp. 897–902.
12. Oleinik, P.H.; Marques, W.C.; Kirinus, E.D.P. Estimate of the wave climate on the most energetic locations of the south-southeastern Brazilian shelf. *Defect Diffus. Forum* **2017**, *370*, 130–140. [CrossRef]
13. Kirinus, E.D.P.; Marques, W.C. Viability of the application of marine current power generators in the south Brazilian shelf. *Appl. Energy* **2015**, *155*, 23–34. [CrossRef]
14. Kirinus, E.D.P.; Oleinik, P.H.; Costi, J.; Marques, W.C. Long-term simulations for ocean energy off the Brazilian coast. *Energy* **2018**, *163*, 364–382. [CrossRef]
15. Martins, J.C.; Goulart, M.M.; Gomes, M.N.; Souza, J.A.; Rocha, L.A.O.; Isoldi, L.A.; Santos, E.D. Geometric evaluation of the main operational principle of an overtopping wave energy converter by means of Constructal Design. *Renew. Energy* **2018**, *118*, 727–741. [CrossRef]
16. Barbosa, D.V.E.; Santos, A.L.G.; Santos, E.D.; Souza, J.A. International journal of heat and mass transfer overtopping device numerical study: Openfoam solution verification and evaluation of curved ramps performances. *Int. J. Heat Mass Transf.* **2019**, *131*, 411–423. [CrossRef]
17. Jung, J.Y.; Lee, H.S.; Kim, H.J.; Yoo, Y.; Choi, W.Y.; Kwak, H.Y. Thermoeconomic analysis of an ocean thermal energy conversion plant. *Renew. Energy* **2016**, *86*, 1086–1094. [CrossRef]
18. Empresa de Pesquisa Energética (EPE). *Plano Nacional de Energia—PNE 2030*; Empresa de Pesquisa Energética: Rio de Janeiro, Brazil, 2007.
19. Empresa de Pesquisa Energética (EPE). Plano Nacional de Energia—2050. Available online: http://www.epe.gov.br/pt/publicacoes-dados-abertos/publicacoes/Plano-Nacional-de-Energia-2050 (accessed on 18 April 2019).

20. Agência Nacional de Energia Elétrica (ANEEL). *Volume 3–8 Evolução Tecnológica Nacional no Segmento Geração de Energia Elétrica e Armazenamento de Energia*; Agência Nacional de Energia Elétrica: Brasília, Brazil, 2017.
21. Schmitz, W.J., Jr. On the interbasin-scale thermohaline circulation. *Rev. Geophys.* **1995**, *33*, 151–173. [CrossRef]
22. Stramma, L.; England, M. On the water masses and mean circulation of the South Atlantic Ocean. *J. Geophys. Res. Ocean.* **1999**, *104*, 20863–20883. [CrossRef]
23. Schott, F.A.; Dengler, M.; Zantopp, R.; Stramma, L.; Fischer, J.; Brandt, P. The shallow and deep western boundary circulation of the South Atlantic at 5°–11° S. *J. Phys. Oceanogr.* **2005**, *35*, 2031–2053. [CrossRef]
24. Rodrigues, R.R.; Rothstein, L.M.; Wimbush, M. Seasonal variability of the South Equatorial Current bifurcation in the Atlantic Ocean: A numerical study. *J. Phys. Oceanogr.* **2007**, *37*, 16–30. [CrossRef]
25. Peterson, R.G.; Stramma, L. Upper-level circulation in the South Atlantic Ocean. *Prog. Oceanogr.* **1991**, *26*, 1–73. [CrossRef]
26. Soutelino, R.G.; Da Silveira, I.C.A.; Gangopadhyay, A.; Miranda, J.A. Is the Brazil Current eddy-dominated to the north of 20° S? *Geophys. Res. Lett.* **2011**, *38*, 1–5. [CrossRef]
27. Madec, G. *NEMO Ocean Engine*; Note du Pôle Modélisation, Institut Pierre-Simon Laplace: Paris, France, 2011; pp. 1–332.
28. Madec, G.; Imbard, M. A global ocean mesh to overcome the North Pole singularity. *Clim. Dyn.* **1996**, *12*, 381–388. [CrossRef]
29. Amante, C.; Eakins, B.W. *Arc-minute global relief model: procedures, data sources and analysis. NOAA Technical Memorandum NESDIS NGDC-24*; National Geophysical Data Center NOAA: Boulder, CO, USA, 2018.
30. Lowcher, C.F.; Muglia, M.; Bane, J.M.; He, R.; Gong, Y.; Haines, S.M. Marine hydrokinetic energy in the gulf stream off North Carolina: An assessment using observations and ocean circulation models. In *Marine Renewable Energy: Resource Characterization and Physical Effects*; Yang, Z., Copping, A., Eds.; Springer International Publishing: Cham, Switzerland, 2017; pp. 237–258, ISBN 978-3-319-53534-0.
31. Myers, L.; Bahaj, A.S. Power output performance characteristics of a horizontal axis marine current turbine. *Renew. Energy* **2006**, *31*, 197–208. [CrossRef]
32. Batten, W.M.J.; Bahaj, A.S.; Molland, A.F.; Chaplin, J.R. The prediction of the hydrodynamic performance of marine current turbines. *Renew. Energy* **2008**, *33*, 1085–1096. [CrossRef]
33. Nihous, G.C. An order-of-magnitude estimate of ocean thermal energy conversion resources. *J. Energy Resour. Technol.* **2005**, *127*, 328. [CrossRef]
34. Nihous, G.C. A preliminary assessment of ocean thermal energy conversion resources. *J. Energy Resour. Technol.* **2007**, *129*, 10. [CrossRef]
35. Devis-Morales, A.; Montoya-Sánchez, R.A.; Osorio, A.F.; Otero-Díaz, L.J. Ocean thermal energy resources in Colombia. *Renew. Energy* **2014**, *66*, 759–769. [CrossRef]
36. Nihous, G.C. Conceptual design of a small open-cycle OTEC plant for the production of electricity and fresh water in a Pacific Island. In Proceedings of the International Conference on Ocean Energy Recovery, Honolulu, HI, USA, 28–30 November 1989.
37. Vega, L.A.; Nihous, G.C. Design of a 5 MWe OTEC pre-commercial plant. In Proceedings of the Oceanology International'94 Conference, Brighton, UK, 8–11 March 1994.
38. Ardhuin, F.; Rogers, E.; Babanin, A.; Filipot, J.-F.; Magne, R.; Roland, A.; Van Der Westhuysen, A.; Queffeulou, P.; Lefevre, J.-M.; Aouf, L.; et al. Semi-empirical dissipation source functions for ocean waves: Part I, definition, calibration and validation. *J. Phys. Oceanogr.* **2010**, *40*, 1917–1941. [CrossRef]
39. Nielsen, P. *Coastal and Estuarine Processes, Advanced Series on Ocean Engineering*, 29th ed.; World Scientific: Singapore, 2009; Volume 29, ISBN 978-981-283-711-0.
40. Cornett, A. A global wave energy resource assessment. *Proc. ISOPE* **2008**, *8*, 318–326.
41. Barstow, S.F.; Mørk, G.; Lønseth, L.; Mathisen, J.P. WorldWaves wave energy resource assessments from the deep ocean to the coast. *J. Energy Power Eng.* **2011**, *5*, 730–742.
42. Mork, G.; Barstow, S.; Kabuth, A.; Pontes, M.T. Assessing the global wave energy potential. In Proceedings of the ASME 2010 29th International Conference on Ocean, Offshore and Arctic Engineering, Shanghai, China, 6–11 June 2010; pp. 447–454.
43. Sims, R.E.H.; Schock, R.N.; Adegbululgbe, A.; Fenhann, J.; Konstantinaviciute, I.; Moomaw, W.; Nimir, H.B.; Schlamadinger, B.; Torres-Martínez, J.; Turner, C.; et al. Energy supply. In *Climate Change 2007: Mitigation. Contribution of Working Group III to the Fourth Assessment Report of the Intergovernmental Panel on Climate Change*; Cambridge University Press: Cambridge, UK; New York, NY, USA, 2007; pp. 252–322, ISBN 978-0-511-54601-3.

44. Krewitt, W.; Nienhaus, K.; Kleßmann, C.; Capone, C.; Stricker, E.; Graus, W.; Hoogwijk, M.; Supersberger, N.; von Winterfeld, U.; Samadi, S. *Role and Potential of Renewable Energy and Energy Efficiency for Global Energy Supply*, 18th ed.; German Federal Environment Agency: Dessau-Roßlau, German, 2009; Volume 18.
45. Izadparast, A.H.; Niedzwecki, J.M. Estimating the potential of ocean wave power resources. *Ocean Eng.* **2011**, *38*, 177–185. [CrossRef]
46. Wu, S.; Liu, C.; Chen, X. Offshore wave energy resource assessment in the East China Sea. *Renew. Energy* **2015**, *76*, 628–636. [CrossRef]
47. Mirzaei, A.; Tangang, F.; Juneng, L. Wave energy potential assessment in the central and southern regions of the South China Sea. *Renew. Energy* **2015**, *80*, 454–470. [CrossRef]
48. Mentaschi, L.; Besio, G.; Cassola, F.; Mazzino, A. Performance evaluation of Wavewatch III in the Mediterranean Sea. *Ocean Model.* **2015**, *90*, 82–94. [CrossRef]
49. Silva, D.; Bento, A.R.; Martinho, P.; Soares, C.G. High resolution local wave energy modelling in the Iberian Peninsula. *Energy* **2015**, *91*, 1099–1112. [CrossRef]
50. Penalba, M.; Ulazia, A.; Ibarra-berastegui, G.; Ringwood, J.; Sáenz, J. Wave energy resource variation off the west coast of Ireland and its impact on realistic wave energy converters' power absorption. *Appl. Energy* **2018**, *224*, 205–219. [CrossRef]
51. Ahn, S.; Haas, K.A.; Neary, V.S. Wave energy resource classification system for US coastal waters. *Renew. Sustain. Energy Rev.* **2019**, *104*, 54–68. [CrossRef]
52. Kerr, D. Marine energy. *Philos. Trans. R. Soc. A Math. Phys. Eng. Sci.* **2007**, *365*, 971–992. [CrossRef] [PubMed]
53. Ocean Energy Systems (OES). Tidal & Currents. Available online: https://www.ocean-energy-systems.org/about-oes/what-is-ocean-energy/tidal-currents/ (accessed on 18 April 2019).
54. Neill, S.P.; Vögler, A.; Goward-Brown, A.J.; Baston, S.; Lewis, M.J.; Gillibrand, P.A.; Waldman, S.; Woolf, D.K. The wave and tidal resource of Scotland. *Renew. Energy* **2017**, *114*, 3–17. [CrossRef]
55. Alonso, R.; Jackson, M.; Santoro, P.; Fossati, M.; Solari, S.; Teixeira, L. Wave and tidal energy resource assessment in Uruguayan shelf seas. *Renew. Energy* **2017**, *114*, 18–31. [CrossRef]
56. Lewis, M.; Neill, S.P.; Robins, P.E.; Hashemi, M.R. Resource assessment for future generations of tidal-stream energy arrays. *Energy* **2015**, *83*, 403–415. [CrossRef]
57. Chen, W.B.; Liu, W.C.; Hsu, M.H. Modeling assessment of tidal current energy at Kinmen Island, Taiwan. *Renew. Energy* **2013**, *50*, 1073–1082. [CrossRef]
58. Rashid, A. Status and potentials of tidal in-stream energy resources in the southern coasts of Iran: A case study. *Renew. Sustain. Energy Rev.* **2012**, *16*, 6668–6677. [CrossRef]
59. Lewis, A.; Estefen, S.; Huckerby, J.; Lee, K.S.; Musial, W.; Pontes, T.; Torres-Martinez, J. Ocean energy. In *IPCC Special Report on Renewable Energy Sources and Climate Change Mitigation*; Edenhofer, O., Pichs-Madruga, R., Sokona, Y., Seyboth, K., Matschoss, P., Kadner, S., Zwickel, T., Eickemeie, P., Hansen, G., Schlömer, S., et al., Eds.; Cambridge University Press: Cambridge, UK; New York, NY, USA, 2011; pp. 497–534.
60. Yang, X.; Haas, K.A.; Fritz, H.M. Evaluating the potential for energy extraction from turbines in the gulf stream system. *Renew. Energy* **2014**, *72*, 12–21. [CrossRef]
61. Chang, Y.C.; Chu, P.C.; Tseng, R.S. Site selection of ocean current power generation from drifter measurements. *Renew. Energy* **2015**, *80*, 737–745. [CrossRef]
62. Goundar, J.N.; Ahmed, M.R. Marine current energy resource assessment and design of a marine current turbine for Fiji. *Renew. Energy* **2014**, *65*, 14–22. [CrossRef]
63. Mofor, L.; Goldsmith, J.; Jones, F. *Ocean Energy: Technology Readiness, Patents, Deployment Status and Outlook*; International Renewable Energy Agency (IRENA): Abu Dhabi, UAE, 2014.
64. Pelc, R.; Fujita, R.M. Renewable energy from the ocean. *Mar. Policy* **2002**, *26*, 471–479. [CrossRef]
65. Rajagopalan, K.; Nihous, G.C. An assessment of global ocean thermal energy conversion resources with a high-resolution ocean general circulation model. *J. Energy Resour. Technol.* **2013**, *135*, 041202. [CrossRef]
66. Skråmestø, Ø.S.Ø.; Skilhagen, S.S.E.; Nielsen, W.K.W. Power production based on osmotic pressure. *Waterpower XVI* **2009**, 1–9. Available online: https://www.statkraft.com/globalassets/old-contains-the-old-folder-structure/documents/waterpower_xvi_-_power_production_based_on_osmotic_pressure_tcm21-4795.pdf (accessed on 18 April 2019).
67. Alvarez-Silva, O.A.; Osorio, A.F.; Winter, C. Practical global salinity gradient energy potential. *Renew. Sustain. Energy Rev.* **2016**, *60*, 1387–1395. [CrossRef]

68. Alvarez-Silva, O.A.; Osorio, A.F. Salinity gradient energy potential in Colombia considering site specific constraints. *Renew. Energy* **2015**, *74*, 737–748. [CrossRef]
69. Maisonneuve, J.; Pillay, P.; La, C.B. Osmotic power potential in remote regions of Quebec. *Renew. Energy* **2015**, *81*, 62–70. [CrossRef]
70. Emdadi, A.; Gikas, P.; Farazaki, M.; Emami, Y. Salinity gradient energy potential at the hyper saline Urmia Lake—ZarrinehRud River system in Iran. *Renew. Energy* **2016**, *86*, 154–162. [CrossRef]
71. Helfer, F.; Lemckert, C.; Anissimov, Y.G. Osmotic power with Pressure Retarded Osmosis: Theory, performance and trends—A review. *J. Membr. Sci.* **2014**, *453*, 337–358. [CrossRef]
72. Rusu, E.; Venugopal, V. *Offshore Renewable Energy—Ocean Waves, Tides, and Offshore Wind*; Rusu, E., Venugopal, V., Eds.; MDPI: Basel, Switzerland, 2019; ISBN 978-3-03897-593-9.
73. Li, Y.; Yu, Y.H. A synthesis of numerical methods for modeling wave energy converter-point absorbers. *Renew. Sustain. Energy Rev.* **2012**, *16*, 4352–4364. [CrossRef]
74. EMEC European Marine Energy Centre Ltd. Wave Devices. Available online: http://www.emec.org.uk/marine-energy/wave-devices/ (accessed on 18 April 2019).
75. López, I.; Andreu, J.; Ceballos, S.; Martínez De Alegría, I.; Kortabarria, I. Review of wave energy technologies and the necessary power-equipment. *Renew. Sustain. Energy Rev.* **2013**, *27*, 413–434. [CrossRef]
76. Heath, T.V. A review of oscillating water columns. *Philos. Trans. R. Soc. A Math. Phys. Eng. Sci.* **2012**, *370*, 235–245. [CrossRef] [PubMed]
77. Ning, D.Z.; Wang, R.Q.; Zou, Q.P.; Teng, B. An experimental investigation of hydrodynamics of a fixed OWC Wave Energy Converter. *Appl. Energy* **2016**, *168*, 636–648. [CrossRef]
78. Fernandes, M.P.; Vieira, S.M.; Henriques, J.C.; Valério, D.; Gato, L.M. Short-term prediction in an Oscillating Water Column using Artificial Neural Networks. In Proceedings of the 2018 International Joint Conference on Neural Networks (IJCNN), Rio de Janeiro, Brazil, 8–13 July 2018; pp. 1–7.
79. Bull, D.; Jenne, D.S.; Smith, C.S.; Copping, A.E.; Copeland, G. Levelized cost of energy for a Backward Bent Duct Buoy. *Int. J. Mar. Energy* **2016**, *16*, 220–234. [CrossRef]
80. Sheng, W. Motion and performance of BBDB OWC wave energy converters: I, hydrodynamics. *Renew. Energy* **2019**, *138*, 106–120. [CrossRef]
81. Falcão, A.F.O.; Henriques, J.C.C. Model-prototype similarity of oscillating-water-column wave energy converters. *Int. J. Mar. Energy* **2014**, *6*, 18–34. [CrossRef]
82. Dias, F.; Renzi, E.; Gallagher, S.; Sarkar, D.; Wei, Y.; Abadie, T.; Cummins, C.; Rafiee, A. Analytical and computational modelling for wave energy systems: The example of oscillating wave surge converters. *Acta Mech. Sin.* **2017**, *33*, 647–662. [CrossRef] [PubMed]
83. Yemm, R.; Pizer, D.; Retzler, C.; Henderson, R. Pelamis: Experience from concept to connection. *Philos. Trans. R. Soc. A Math. Phys. Eng. Sci.* **2012**, *370*, 365–380. [CrossRef]
84. Zheng, S.; Zhang, Y. Analytical study on hydrodynamic performance of a raft-type wave power device. *J. Mar. Sci. Technol.* **2017**, *22*, 620–632. [CrossRef]
85. Olaya, S.; Bourgeot, J.M.; Benbouzid, M. Optimal control for a self-reacting point absorber: A one-body equivalent model approach. In Proceedings of the 2014 International Power Electronics and Application Conference and Exposition, Shanghai, China, 5–8 November 2014; pp. 1–6.
86. Todalshaug, J.H.; Ásgeirsson, G.S.; Hjálmarsson, E.; Maillet, J.; Möller, P.; Pires, P.; Guérinel, M.; Lopes, M. Tank testing of an inherently phase-controlled wave energy converter. *Int. J. Mar. Energy* **2016**, *15*, 68–84. [CrossRef]
87. Sergiienko, N.Y.; Cazzolato, B.S.; Ding, B.; Arjomandi, M. Three-tether axisymmetric wave energy converter: Estimation of energy delivery. In Proceedings of the 3rd Asian Wave and Tidal Energy Conference (AWTEC 2016), Singapore, 24–28 October 2016; pp. 163–171.
88. Kofoed, J.P.; Frigaard, P.; Friis-Madsen, E.; Sørensen, H.C. Prototype testing of the wave energy converter wave dragon. *Renew. Energy* **2006**, *31*, 181–189. [CrossRef]
89. Musa, M.A.; Maliki, A.Y.; Ahmad, M.F.; Sani, W.N.; Yaakob, O.; Samo, K.B. Numerical simulation of wave flow over the overtopping breakwater for energy conversion (OBREC) device. *Procedia Eng.* **2017**, *194*, 166–173. [CrossRef]
90. Liu, Z.; Shi, H.; Cui, Y.; Kim, K. Experimental study on overtopping performance of a circular ramp wave energy converter. *Renew. Energy* **2017**, *104*, 163–176. [CrossRef]

91. Alam, M.R. Nonlinear analysis of an actuated seafloor-mounted carpet for a high-performance wave energy extraction. *Proc. R. Soc. A Math. Phys. Eng. Sci.* **2012**, *468*, 3153–3171. [CrossRef]
92. Durand, M.; Babarit, A.; Pettinotti, B.; Quillard, O.; Toularastel, J.L.; Clément, A.H. Experimental validation of the performances of the SEAREV wave energy converter with real time latching control. In Proceedings of the 7th European Wave and Tidal Energy Conference, Porto, Portugal, 11–13 September 2007; pp. 1–8.
93. Zhang, Z.; Chen, B.; Nielsen, S.R.K.; Olsen, J. Gyroscopic power take-off wave energy point absorber in irregular sea states. *Ocean Eng.* **2017**, *143*, 113–124. [CrossRef]
94. Camporeale, S.M.; Filianoti, P.; Torresi, M. Performance of a Wells turbine in an OWC device in comparison to laboratory tests. In Proceedings of the 9th European Wave and Tidal Energy Conference (EWTEC), Southampton, UK, 5–9 September 2011; p. 9.
95. Carrelhas, A.A.D.; Gato, L.M.C.; Henriques, J.C.C.; Falcão, A.F.O.; Varandas, J. Test results of a 30 kW self-rectifying biradial air turbine-generator prototype. *Renew. Sustain. Energy Rev.* **2019**, *109*, 187–198. [CrossRef]
96. António, F.D.O. Phase control through load control of oscillating-body wave energy converters with hydraulic PTO system. *Ocean Eng.* **2008**, *35*, 358–366.
97. Zhang, D.; Li, W.; Ying, Y.; Zhao, H.; Lin, Y.; Bao, J. Wave energy converter of inverse pendulum with double action power take off. *Proc. Inst. Mech. Eng. Part C J. Mech. Eng. Sci.* **2013**, *227*, 2416–2427. [CrossRef]
98. Gaspar, J.F.; Calvário, M.; Kamarlouei, M.; Soares, C.G. Design tradeoffs of an oil-hydraulic power take-off for wave energy converters. *Renew. Energy* **2018**, *129*, 245–259. [CrossRef]
99. Zhang, H.; Xu, D.; Ding, R.; Zhao, H.; Lu, Y.; Wu, Y. Embedded Power Take-Off in hinged modularized floating platform for wave energy harvesting and pitch motion suppression. *Renew. Energy* **2019**, *138*, 1176–1188. [CrossRef]
100. Albert, A.; Berselli, G.; Bruzzone, L.; Fanghella, P. Mechanical design and simulation of an onshore four-bar wave energy converter. *Renew. Energy* **2017**, *114*, 766–774. [CrossRef]
101. Liang, C.; Ai, J.; Zuo, L. Design, fabrication, simulation and testing of an ocean wave energy converter with mechanical motion rectifier. *Ocean Eng.* **2017**, *136*, 190–200. [CrossRef]
102. Yin, X.; Li, X.; Boontanom, V.; Zuo, L. Mechanical motion rectifier based efficient power takeoff for ocean wave energy harvesting. In Proceedings of the ASME 2017 Dynamic Systems and Control Conference, Fairfax, VA, USA, 11–13 October 2017; p. 5.
103. Mueller, M.A. Electrical generators for direct drive wave energy converters. *IEE Proc. Gener. Transm. Distrib.* **2002**, *149*, 446. [CrossRef]
104. Polinder, H.; Mueller, M.A.; Scuotto, M.; Goden de Sousa Prado, M. Linear generator systems for wave energy conversion. In Proceedings of the 7th European Wave and Tidal Energy Conference, Porto, Portugal, 11–13 September 2007.
105. Li, W.; Isberg, J.; Engström, J.; Waters, R.; Leijon, M. Parametric study of the power absorption for a linear generator wave energy converter. *J. Ocean Wind Energy* **2015**, *2*, 248–252. [CrossRef]
106. Ozkop, E.; Altas, I.H. Control, power and electrical components in wave energy conversion systems: A review of the technologies. *Renew. Sustain. Energy Rev.* **2017**, *67*, 106–115. [CrossRef]
107. Pecher, A.; Kofoed, J.P. Erratum to: Handbook of ocean wave energy. In *Ocean Engineering & Oceanography*; Pecher, A., Kofoed, J.P., Eds.; Springer: Cham, Switzerland, 2017; p. E1, ISBN 9783319398884.
108. Wang, L.; Isberg, J.; Tedeschi, E. Review of control strategies for wave energy conversion systems and their validation: The wave-to-wire approach. *Renew. Sustain. Energy Rev.* **2018**, *81*, 366–379. [CrossRef]
109. Alternative Energy Tutorials. Tidal Barrage Generation. Available online: http://www.alternative-energy-tutorials.com/tidal-energy/tidal-barrage.html (accessed on 18 April 2019).
110. Waters, S.; Aggidis, G. Tidal range technologies and state of the art in review. *Renew. Sustain. Energy Rev.* **2016**, *59*, 514–529. [CrossRef]
111. Xia, J.; Falconer, R.A.; Lin, B.; Tan, G. Estimation of annual energy output from a tidal barrage using two different methods. *Appl. Energy* **2012**, *93*, 327–336. [CrossRef]
112. Li, Y.; Pan, D.Z. The ebb and flow of tidal barrage development in Zhejiang Province, China. *Renew. Sustain. Energy Rev.* **2017**, *80*, 380–389. [CrossRef]
113. Angeloudis, A.; Falconer, R.A. Sensitivity of tidal lagoon and barrage hydrodynamic impacts and energy outputs to operational characteristics. *Renew. Energy* **2017**, *114*, 337–351. [CrossRef]

114. Angeloudis, A.; Kramer, S.C.; Avdis, A.; Piggott, M.D. Optimising tidal range power plant operation. *Appl. Energy* **2018**, *212*, 680–690. [CrossRef]
115. Harcourt, F.; Angeloudis, A.; Piggott, M.D. Utilising the flexible generation potential of tidal range power plants to optimise economic value. *Appl. Energy* **2019**, *237*, 873–884. [CrossRef]
116. Keysan, O.; McDonald, A.S.; Mueller, M. A direct drive permanent magnet generator design for a tidal current turbine (SeaGen). In Proceedings of the 2011 IEEE International Electric Machines & Drives Conference (IEMDC), Niagara Falls, ON, Canada, 15–18 May 2011; pp. 224–229.
117. Shirasawa, K.; Tokunaga, K.; Iwashita, H.; Shintake, T. Experimental verification of a floating ocean-current turbine with a single rotor for use in Kuroshio currents. *Renew. Energy* **2016**, *91*, 189–195. [CrossRef]
118. Seo, J.; Yi, J.; Park, J.; Lee, K. Review of tidal characteristics of Uldolmok Strait and optimal design of blade shape for horizontal axis tidal current turbines. *Renew. Sustain. Energy Rev.* **2019**, *113*, 109273. [CrossRef]
119. Li, Y.; Calisal, S.M. Three-dimensional effects and arm effects on modeling a vertical axis tidal current turbine. *Renew. Energy* **2010**, *35*, 2325–2334. [CrossRef]
120. Jing, F.; Sheng, Q.; Zhang, L. Experimental research on tidal current vertical axis turbine with variable-pitch blades. *Ocean Eng.* **2014**, *88*, 228–241. [CrossRef]
121. Fernandes, A.C.; Bakhshandeh Rostami, A. Hydrokinetic energy harvesting by an innovative vertical axis current turbine. *Renew. Energy* **2015**, *81*, 694–706. [CrossRef]
122. Wang, S.Q.; Xu, G.; Zhu, R.Q.; Wang, K. Hydrodynamic analysis of vertical-axis tidal current turbine with surging and yawing coupled motions. *Ocean Eng.* **2018**, *155*, 42–54. [CrossRef]
123. Chen, B.; Su, S.; Viola, I.M.; Greated, C.A. Numerical investigation of vertical-axis tidal turbines with sinusoidal pitching blades. *Ocean Eng.* **2018**, *155*, 75–87. [CrossRef]
124. Gorle, J.M.R.; Chatellier, L.; Pons, F.; Ba, M. Modulated circulation control around the blades of a vertical axis hydrokinetic turbine for flow control and improved performance. *Renew. Sustain. Energy Rev.* **2019**, *105*, 363–377. [CrossRef]
125. Kinsey, T.; Dumas, G.; Lalande, G.; Ruel, J.; Méhut, A.; Viarouge, P.; Lemay, J.; Jean, Y. Prototype testing of a hydrokinetic turbine based on oscillating hydrofoils. *Renew. Energy* **2011**, *36*, 1710–1718. [CrossRef]
126. Ma, P.; Yang, Z.; Wang, Y.; Liu, H.; Xie, Y. Energy extraction and hydrodynamic behavior analysis by an oscillating hydrofoil device. *Renew. Energy* **2017**, *113*, 648–659. [CrossRef]
127. Wang, Y.; Huang, D.; Han, W.; YangOu, C.; Zheng, Z. Research on the mechanism of power extraction performance for flapping hydrofoils. *Ocean Eng.* **2017**, *129*, 626–636. [CrossRef]
128. Filippas, E.S.; Gerostathis, T.P.; Belibassakis, K.A. Semi-activated oscillating hydrofoil as a nearshore biomimetic energy system in waves and currents. *Ocean Eng.* **2018**, *154*, 396–415. [CrossRef]
129. Chaudhari, C.D.; Waghmare, S.A.; Kotwal, A. Numerical analysis of venturi ducted horizontal axis wind turbine for efficient power generation. *Int. J. Mech. Eng. Comput. Appl.* **2013**, *1*, 90–93.
130. Khan, M.J.; Bhuyan, G.; Iqbal, M.T.; Quaicoe, J.E. Hydrokinetic energy conversion systems and assessment of horizontal and vertical axis turbines for river and tidal applications: A technology status review. *Appl. Energy* **2009**, *86*, 1823–1835. [CrossRef]
131. Belloni, C.S.K.; Willden, R.H.J.; Houlsby, G.T. An investigation of ducted and open-centre tidal turbines employing CFD-embedded BEM. *Renew. Energy* **2017**, *108*, 622–634. [CrossRef]
132. Tampier, G.; Troncoso, C.; Zilic, F. Numerical analysis of a diffuser-augmented hydrokinetic turbine. *Ocean Eng.* **2017**, *145*, 138–147. [CrossRef]
133. Tsao, C.C.; Han, L.; Jiang, W.T.; Lee, C.C.; Lee, J.S.; Feng, A.H.; Hsieh, C. Marine current power with cross-stream active mooring: Part I. *Renew. Energy* **2017**, *109*, 144–154. [CrossRef]
134. Tsao, C.C.; Han, L.; Jiang, W.T.; Lee, C.C.; Lee, J.S.; Feng, A.H.; Hsieh, C. Marine current power with cross-stream active mooring: Part II. *Renew. Energy* **2018**, *127*, 1036–1051. [CrossRef]
135. Minesto. The Future of Renewable Energy. Available online: https://minesto.com/our-technology (accessed on 18 April 2019).
136. Qian, P.; Feng, B.; Liu, H.; Tian, X.; Si, Y.; Zhang, D. Review on configuration and control methods of tidal current turbines. *Renew. Sustain. Energy Rev.* **2019**, *108*, 125–139. [CrossRef]
137. Faizal, M.; Ahmed, M.R. Experimental studies on a closed cycle demonstration OTEC plant working on small temperature difference. *Renew. Energy* **2013**, *51*, 234–240. [CrossRef]

138. Aydin, H.; Lee, H.S.; Kim, H.J.; Shin, S.K.; Park, K. Off-design performance analysis of a closed-cycle ocean thermal energy conversion system with solar thermal preheating and superheating. *Renew. Energy* **2014**, *72*, 154–163. [CrossRef]
139. Yang, M.H.; Yeh, R.H. Analysis of optimization in an OTEC plant using organic Rankine cycle. *Renew. Energy* **2014**, *68*, 25–34. [CrossRef]
140. Mutair, S.; Ikegami, Y. Design optimization of shore-based low temperature thermal desalination system utilizing the ocean thermal energy. *J. Sol. Energy Eng.* **2014**, *136*, 041005. [CrossRef]
141. Kim, A.S.; Kim, H.J.; Lee, H.S.; Cha, S. Dual-use open cycle ocean thermal energy conversion (OC-OTEC) using multiple condensers for adjustable power generation and seawater desalination. *Renew. Energy* **2016**, *85*, 344–358. [CrossRef]
142. Octaviani, F.; Muslim, M.; Buwono, A.; Faturachman, D. Study of ocean thermal energy conversion (OTEC) generation as project of power plant in West Sumatera-Indonesia. *Recent Adv. Renew. Energy Sources* **2016**, *10*, 64–68.
143. Thorsen, T.; Holt, T. The potential for power production from salinity gradients by pressure retarded osmosis. *J. Membr. Sci.* **2009**, *335*, 103–110. [CrossRef]
144. Han, G.; Zhang, S.; Li, X.; Chung, T.S. Progress in pressure retarded osmosis (PRO) membranes for osmotic power generation. *Prog. Polym. Sci.* **2015**, *51*, 1–27. [CrossRef]
145. Altaee, A.; Zhou, J.; Alanezi, A.A.; Zaragoza, G. Pressure retarded osmosis process for power generation: Feasibility, energy balance and controlling parameters. *Appl. Energy* **2017**, *206*, 303–311. [CrossRef]
146. Altaee, A.; Cipolina, A. Modelling and optimization of modular system for power generation from a salinity gradient. *Renew. Energy* **2019**, *141*, 139–147. [CrossRef]
147. Veerman, J.; Saakes, M.; Metz, S.J.; Harmsen, G.J. Electrical power from sea and river water by reverse electrodialysis: A first step from the laboratory to a real power plant. *Environ. Sci. Technol.* **2010**, *44*, 9207–9212. [CrossRef] [PubMed]
148. Avci, A.H.; Tufa, R.A.; Fontananova, E.; Di, G.; Curcio, E. Reverse Electrodialysis for energy production from natural river water and seawater. *Energy* **2018**, *165*, 512–521. [CrossRef]
149. Tufa, R.A.; Pawlowski, S.; Veerman, J.; Bouzek, K.; Fontananova, E.; Velizarov, S.; Goulão, J.; Nijmeijer, K.; Curcio, E. Progress and prospects in reverse electrodialysis for salinity gradient energy conversion and storage. *Appl. Energy* **2018**, *225*, 290–331. [CrossRef]
150. Mei, Y.; Tang, C.Y. Recent developments and future perspectives of reverse electrodialysis technology: A review. *Desalination* **2018**, *425*, 156–174. [CrossRef]
151. Renewable Energy Policy Network for the 21st Century (REN21). *Renewable 2018: Global Status Report*; REN21: Paris, France, 2018.
152. International Renewable Energy Agency (IRENA). *Renewable Energy Capacity Statistics 2019*; IRENA: Abu Dhabi, UAE, 2019.
153. Wang, S.; Yuan, P.; Li, D.; Jiao, Y. An overview of ocean renewable energy in China. *Renew. Sustain. Energy Rev.* **2011**, *15*, 91–111. [CrossRef]
154. Neill, S.P.; Hashemi, M.R. Introduction. *Fundam. Ocean Renew. Energy* **2018**, *1990*, 1–30.
155. Ohneda, H.; Igarashi, S.; Shinbo, O.; Sekihara, S.; Suzuki, K.; Kubota, H.; Morita, H. Construction procedure of a wave power extracting caisson breakwater. In Proceedings of the 3rd Symposium on Ocean Energy Utilization, Tokyo, Japan, 22–23 January 1991; pp. 171–179.
156. Arena, F.; Romolo, A.; Malara, G.; Ascanelli, A. On design and building of a U-OWC wave energy converter in the Mediterranean Sea: A case study. In Proceedings of the ASME 2013 32nd International Conference on Ocean, Offshore and Arctic Engineering, Nantes, France, 9–14 June 2013; Volume 8.
157. Falcão, A.D.O. The shoreline OWC wave power plant at the Azores. In Proceedings of the 4th European Wave Energy Conference, Aalborg, Denmark, 4–6 December 2000; pp. 42–48.
158. Bønke, K.; Ambli, N. Prototype wave power stations in Norway. In Proceedings of the Utilization of Ocean Waves—Wave to Energy Conversion, San Diego, CA, USA, 16–17 June 1986; pp. 34–35.
159. Weinstein, A.; Fredrikson, G.; Parks, M.J.; Nielsen, K. AquaBuOY-the offshore wave energy converter numerical modeling and optimization. In Proceedings of the Oceans '04 MTS/IEEE Techno-Ocean '04, Kobe, Japan, 9–12 November 2004; pp. 1988–1995.
160. Salter, S.H.; Lin, C.-P. Wide tank efficiency measurements on a model of the sloped IPS buoy. In Proceedings of the 3rd European Wave Energy Conference, Patras, Greece, 30 September–2 October 1998; pp. 200–206.

161. Weber, J.; Mouwen, F.; Parish, A.; Robertson, D. Wavebob—Research & development network and tools in the context of systems engineering. In Proceedings of the 8th European Wave and Tidal Energy Conference, Uppsala, Sweden, 7–10 September 2009; pp. 416–420.
162. Tedd, J.; Peter Kofoed, J. Measurements of overtopping flow time series on the Wave Dragon, wave energy converter. *Renew. Energy* **2009**, *34*, 711–717. [CrossRef]
163. Vicinanza, D.; Frigaard, P. Wave pressure acting on a seawave slot-cone generator. *Coast. Eng.* **2008**, *55*, 553–568. [CrossRef]
164. Magagna, D.; Margheritini, L. *Workshop on Identification of Future Emerging Technologies in the Wind Power Sector*; European Commission, Publications Official of the European Union: Luxembourg, 2018; ISBN 9789279925870. [CrossRef]
165. World Energy Council. *2010 Survey of Energy Resources*; World Energy Council: London, UK, 2010.
166. Bae, Y.H.; Kim, K.O.; Choi, B.H. Lake Sihwa tidal power plant project. *Ocean Eng.* **2010**, *37*, 454–463. [CrossRef]
167. Worldsteel Association. Sihwa Tidal Power Station Worldsteel HR. Available online: https://stories.worldsteel.org/infrastructure/large-scale-tidal-power-reliant-steel/attachment/sihwa-tidal-power-station-worldsteel-hr/ (accessed on 1 March 2019).
168. Hooper, T.; Austen, M. Tidal barrages in the UK: Ecological and social impacts, potential mitigation, and tools to support barrage planning. *Renew. Sustain. Energy Rev.* **2013**, *23*, 289–298. [CrossRef]
169. Hammar, L.; Ehnberg, J.; Mavume, A.; Cuamba, B.C.; Molander, S. Renewable ocean energy in the Western Indian Ocean. *Renew. Sustain. Energy Rev.* **2012**, *16*, 4938–4950. [CrossRef]
170. Hammons, T.J.; Member, S. Tidal power. *Proc. IEEE* **1993**, *81*, 419–433. [CrossRef]
171. Kobayashi, H.; Jitsuhara, S.; Uehara, H. The present status and features of OTEC and recent aspects of thermal energy conversion technologies. In Proceedings of the 24th Meeting of the UJNR Marine Facilities Panel, Honolulu, HI, USA, 4–12 November 2001.
172. Uehara, H. The present status and future of ocean thermal energy conversion. *Int. J. Sol. Energy* **1995**, *16*, 217–231. [CrossRef]
173. Makai Ocean Engineering. Ocean Thermal Energy Conversion. Available online: https://www.makai.com/ocean-thermal-energy-conversion/ (accessed on 9 May 2019).
174. Ocean Energy System (OES). Offshore Installations Worldwide. Available online: https://www.ocean-energy-systems.org/ocean-energy-in-the-world/gis-map/ (accessed on 18 April 2019).
175. EMODnet—The European Marine Observation and Data Network. The European Marine Observation and Data Network. Available online: https://ec.europa.eu/maritimeaffairs/atlas/maritime_atlas/#lang=EN;p=w;bkgd=5;theme=2:0.75;c=1253866.2175874896,7033312.218247008;z=4 (accessed on 1 April 2019).
176. RenewableUK. UK Marine Energy Database (UKMED). Available online: https://www.renewableuk.com/page/UKMED2/UK-Marine-Energy-Database.htm (accessed on 3 April 2019).
177. National Renewable Energy Laboratory NREL. Marine and Hydrokinetic Technology Database. Available online: https://openei.org/wiki/Marine_and_Hydrokinetic_Technology_Database (accessed on 3 March 2019).
178. Pacific Northwest National Laboratory (PNNL). Energy, U.S.D. of Ocean Energy Systems (OES); Wind, I. TETHYS: Marine Energy Content. Available online: https://tethys.pnnl.gov/map-viewer-marine-energy (accessed on 18 April 2019).
179. EMEC (European Marine Energy Centre). *Guidelines for Project Development in the Marine Energy Industry*; EMEC: Stromness, Scotland, 2009.
180. International Renewable Energy Agency (IRENA). *Ocean Thermal Energy Conversion: Technology Brief*; IRENA: Abu Dhabi, UAE, 2014.
181. International Renewable Energy Agency (IRENA). *Tidal Energy: Technology Brief*; IRENA: Abu Dhabi, UAE, 2014.
182. International Renewable Energy Agency (IRENA). *Salinity Gradient Energy: Technology Brief*; IRENA: Abu Dhabi, UAE, 2014.
183. EPE. *Anuário Estatístico de Energia Elétrica 2018 no Ano Base de 2017*; EPE: Rio de Janeiro, Brazil, 2018.
184. Hammar, L.; Gullström, M.; Dahlgren, T.G.; Asplund, M.E.; Goncalves, I.B.; Molander, S. Introducing ocean energy industries to a busy marine environment. *Renew. Sustain. Energy Rev.* **2017**, *74*, 178–185. [CrossRef]

185. Garcia-rosa, P.B.; Paulo, J.; Soares, V.; Lizarralde, F.; Estefen, S.F.; Machado, I.R.; Watanabe, E.H. Wave-to-wire model and energy storage analysis of an ocean wave energy hyperbaric converter. *IEEE J. Ocean. Eng.* **2014**, *39*, 1–12. [CrossRef]
186. Costa, P.R.; Garcia-Rosa, P.B.; Estefen, S.F. Phase control strategy for a wave energy hyperbaric converter. *Ocean Eng.* **2010**, *37*, 1483–1490. [CrossRef]
187. Estefen, S.F.; Esperança, P.T.T.; Ricarte, E.; da Costa, P.R.; Pinheiro, M.M.; Clemente, C.H.P.; Franco, D.; Melo, E.; de Souza, J.A. Experimental and numerical studies of the wave energy hyperbaric device for electricity production. In Proceedings of the ASME 2008 27th International Conference on Offshore Mechanics and Arctic Engineering, Estoril, Portugal, 15–20 June 2008; pp. 811–818.
188. Estefen, S.F.; da Costa, P.R.; Ricarte, E.; Pinheiro, M.M. Wave energy hyperbaric device for electricity production. In Proceedings of the ASME 2007 26th International Conference on Offshore Mechanics and Arctic Engineering, San Diego, CA, USA, 10–15 June 2007; pp. 627–633.
189. Shadman, M.; Estefen, S.F.; Rodriguez, C.A.; Nogueira, I.C.M. A geometrical optimization method applied to a heaving point absorber wave energy converter. *Renew. Energy* **2018**, *115*, 533–546. [CrossRef]
190. Budal, K.; Falnes, J. Interacting point absorbers with controlled motion. In *Power from Sea Waves*; Count, B.M., Ed.; Academic Press: London, UK, 1980; pp. 129–142.
191. Budal, K.; Falnes, J.; Iversen, L.C.; Lillebekker, P.M.; Oltedal, G.; Hals, T.; Onshus, T.; Hoy, A. The Norwegian wave-power buoy project. In Proceedings of the 2nd International Symposium on Wave Energy Utilization, Trondheim, Norway, 22–24 June 1982; pp. 323–344.
192. Neto, P.B.L.; Saavedra, O.R.; de Souza Ribeiro, L.A. Analysis of a tidal power plant in the estuary of Bacanga in Brazil taking into account the current conditions and constraints. *IEEE Trans. Sustain. Energy* **2017**, *8*, 1187–1194. [CrossRef]
193. Ferreira, R.M.; Estefen, S.F. Alternative concept for tidal power plant with reservoir restrictions. *Renew. Energy* **2009**, *34*, 1151–1157. [CrossRef]
194. Leite Neto, P.B.; Saavedra, O.R.; Souza Ribeiro, L.A. Optimization of electricity generation of a tidal power plant with reservoir constraints. *Renew. Energy* **2015**, *81*, 11–20. [CrossRef]
195. Aggidis, G.A.; Feather, O. Tidal range turbines and generation on the Solway Firth. *Renew. Energy* **2012**, *43*, 9–17. [CrossRef]

MDPI
St. Alban-Anlage 66
4052 Basel
Switzerland
Tel. +41 61 683 77 34
Fax +41 61 302 89 18
www.mdpi.com

Energies Editorial Office
E-mail: energies@mdpi.com
www.mdpi.com/journal/energies

MDPI
St. Alban-Anlage 66
4052 Basel
Switzerland

Tel: +41 61 683 77 34
Fax: +41 61 302 89 18

www.mdpi.com

ISBN 978-3-03928-529-7